Hydrodynamic Modelling of Fluidised Bed Spray Granulation

Mathijs Goldschmidt

2001

Ph.D. thesis
University of Twente

Twente University **Press**

Also available in print:
www.tup.utwente.nl/uk/catalogue/technical/granulation

Hydrodynamic Modelling of Fluidised Bed Spray Granulation

The research reported in this thesis was financially supported by Unilever Research. It was part of the research programs of the J.M. Burgers Centre for Fluid Dynamics, the Dutch research school for process technology (OSPT), the Process technology Institute Twente (PIT) and the Twente Institute of Mechanics (TIM).

Samenstelling promotiecommissie:

Prof.dr.ir. J.H.A. de Smit, voorzitter	Universiteit Twente
Prof.dr.ir. J.A.M. Kuipers, promotor	Universiteit Twente
Prof.dr.ir. W.P.M. van Swaaij, promotor	Universiteit Twente
Prof.dr. M.J. Hounslow	University of Sheffield, Groot-Brittannië
Prof.dr. O. Simonin	I.N.P.T., Frankrijk
Prof.dr. W.J. Briels	Universiteit Twente
Prof.dr.ir. G.F. Versteeg	Universiteit Twente
Prof.dr.ir. M.M.C.G. Warmoeskerken	Universiteit Twente
Dr.ir. R. Boerefijn, referent	Unilever Research
Dr. J.P. van der Weele, deskundige	Universiteit Twente

Twente University **Press**

Publisher: Twente University Press, P.O. Box 217, 7500 AE Enschede, the Netherlands, www.tup.utwente.nl

Print: Grafisch Centrum Twente, Enschede

ISBN 9036516374

HYDRODYNAMIC MODELLING OF FLUIDISED BED SPRAY GRANULATION

PROEFSCHRIFT

ter verkrijging van
de graad van doctor aan de Universiteit Twente,
op gezag van de rector magnificus,
prof.dr. F.A. van Vught,
volgens besluit van het College voor Promoties
in het openbaar te verdedigen
op vrijdag 31 augustus 2001 te 15.00 uur

door

Mathijs Joseph Vincent Goldschmidt
geboren op 14 mei 1973
te Almelo

Dit proefschrift is goedgekeurd door de promotoren

Prof.dr.ir. J.A.M. Kuipers

en

Prof.dr.ir. W.P.M. van Swaaij

aan mijn ouders
aan allen op wier werk
ik heb kunnen bouwen

to my parents
to all on whose work
I have been able to build

Contents

3. COMPARISON AND VALIDATION OF A 3D HARD-SPHERE DISCRETE PARTICLE MODEL AND A TWO-FLUID CONTINUUM MODEL

4. COMPARISON OF THE KINETIC THEORY OF GRANULAR FLOW WITH 3D HARD-SPHERE DISCRETE PARTICLE SIMULATIONS

5. MULTI-FLUID CONTINUUM MODELLING OF DENSE GAS-FLUIDISED BEDS: DERIVATION OF KINETIC THEORY CLOSURE RELATIONS

6. DIGITAL IMAGE ANALYSIS OF BED EXPANSION AND SEGREGATION DYNAMICS IN DENSE GAS-FLUIDISED BEDS

7. DISCRETE PARTICLE MODELLING OF FLUIDISED BED SPRAY GRANULATION

8. GENERAL CONCLUSIONS AND OUTLOOK

Summary

Fluidised bed spray granulation is an important powder production process with several key advantages compared to other powder production processes, such as spray drying or high shear granulation. The most characteristic and essential part of the spray granulation process is wetting of particles in a gas-fluidised bed by an atomised liquid and the induced size enlargement of primary particles to granules. Thorough understanding of hydrodynamics and growth mechanisms prevailing in spray granulation processes is a prerequisite for process design and attaining proper control over the powder product characteristics. To date, a lot of research has focussed on modelling and understanding of the separate particle growth mechanisms (wetting, agglomeration, layering, breakage and consolidation) which have been integrated into population balance models. However, hydrodynamic models that capture the effect of process design and operation conditions on powder characteristics are not yet available.

In this thesis a multi-level modelling approach for fundamental hydrodynamic modelling of the complex multi-phase flow in fluidised bed spray granulation processes is adopted. A novel discrete element spray granulation model, capturing the key features of fluidised bed dynamics, liquid-solid contacting and agglomeration, is presented. This model computes the motion of every individual particle and droplet in the system, considering the gas phase as a continuum. Hereby, micro-scale processes such as particle-particle collision, droplet-particle coalescence and agglomeration are directly taken into account by simple closure models. The great potential of hydrodynamic models to predict the influence of several key process conditions such as fluidisation velocity, spray rate and spray pattern on powder product characteristics is demonstrated for a batch granulation process containing 50,000 primary particles, whereby a qualitative comparison with experimental results is made. Since the number of particles that can be handled in discrete element simulations is limited by computational resources, application of this type of model is limited to small laboratory scale systems. Therefore, the developed discrete element spray granulation model should be considered as a valuable learning tool which can be applied to gain more insight into particle growth mechanisms required for

engineering scale modelling of the granulation process. An outlook on how to proceed towards engineering scale continuum modelling of fluidised bed spray granulation is presented in the final chapter of the thesis.

Since bubbles play a dominant role in particle mixing, segregation and elutriation in dense gas-fluidised beds such as encountered in fluidised bed spray granulation processes, the research in this thesis focuses on the correctness of bubble dynamics predicted by fundamental hydrodynamic models for gas-fluidised beds. Using a two-fluid continuum model with closure laws according to the kinetic theory of granular flow, it is demonstrated that the hydrodynamic behaviour of homogeneously aerated gas-fluidised beds strongly depends on the amount of energy dissipated in non-ideal particle collisions. The more energy is dissipated, the more bubbles are formed and the stronger pressure fluctuations are observed due to the tendency of inelastic particles to contract in high-density clusters. These results are consistent with results obtained from more detailed discrete particle simulations reported by Hoomans et al. (1996, 1998a). Furthermore, due to the tendency of inelastic particles to contract in high-density clusters and the strong non-linear dependency of the particle pressure on the solids volume fraction, the numerical stability of classical multi-phase versions of the SIMPLE algorithm for continuum hydrodynamic models is adversely affected by energy dissipation. Therefore, a more stable, modified SIMPLE algorithm that takes the compressibility of the suspended particulate phase more directly into account is presented.

A critical comparison of bubble patterns, time-averaged particle distributions and bed expansion dynamics, obtained from two-fluid continuum simulations, three-dimensional hard-sphere discrete particle simulations and digital image analysis of experimental results, is presented. In all cases the discrete particle model gives closer resemblance with experimental data. The main difference between the models is caused by neglect of particle rotation in the kinetic theory closure laws, applied in the continuum model. Mechanical energy balance analysis proves to be a valuable tool to study the effect of particle-particle, particle-wall and gas-particle interactions on fluidised bed dynamics. It demonstrates that, though the total amount of rotational energy in the simulated system is relatively low, mechanical energy dissipation is dominated by sliding friction. Thus particle rotation may not be ignored and it is shown how the agreement between both models can be significantly improved by the introduction of an effective coefficient of restitution, which incorporates the effect of additional energy dissipation due to frictional interactions in the kinetic theory closures for the continuum model.

A critical comparison between experiments and modelling results is given by analysis of the bed expansion dynamics. Though both models predicted the right fluidisation regime and trends in bubble sizes, the predicted bed expansion dynamics differ significantly from experimental results. Visual observation of the experiments makes clear that the differences are mainly caused by the formation of densely packed regions in which no particle vibration is observed. Formation of such regions does not occur in the simulations and it is concluded that long-term particle contacts and multiple particle interactions most likely cause the gap between modelling results and experiments.

A first step towards linking different modelling levels is made using a newly developed sampling technique, which enables critical assessment of the assumptions underlying the kinetic theory of granular flow, generally applied in continuum models, with more detailed discrete particle models. Excellent agreement with the kinetic theory assumptions is obtained for elastic particles. The individual particle velocity distribution in a dense gas-fluidised bed is isotropic and Maxwellian and a good fit of the collision velocity distribution and the collision frequency is obtained, using the radial distribution function proposed by Carnahan and Starling (1969). However, for inelastic and rough particles an anisotropic Maxwellian velocity distribution is obtained. It is concluded that the formation of dense particle clusters disturbs spatial homogeneity and results in collisional anisotropy. Analysis of the impact velocity distribution shows that, in dense gas-fluidised beds, not all impact angles are of equal likelihood. The observed anisotropy becomes more pronounced with increasing degree of inelasticity of the particles.

To model fluidisation and segregation dynamics of particulate mixtures in engineering scale gas-fluidised beds, multi-fluid continuum models need to be developed. In Goldschmidt et al. (2001b) it was demonstrated that a multi-fluid model with existing kinetic theory closure relations predicts far to fast segregation in comparison with experimental results. Therefore the derivation of a novel set of kinetic theory closure relations and a multi-fluid model in which they are incorporated is presented in this thesis. The main difference between the new kinetic theory closure model and the existing model derived by Manger (1996) and Mathiesen (1997) is that segregation is no longer possible in the first (equilibrium) approximation to the particle velocity distribution, but is introduced as a higher order (non-equilibrium) effect. Since the new theory seems to give a more physical picture for dense particulate systems in which the collision frequency is very high, it is expected that the new multi-fluid model will predict more realistic segregation rates, though this remains to be proven.

One of the most crucial steps in the development of fundamental hydrodynamic models is the validation of these models with accurate, detailed experimental data. Therefore a whole-field, non-intrusive digital image analysis technique has been developed which enables simultaneous measurement of bed expansion and segregation dynamics of coloured particles in dense gas-fluidised beds. The development, calibration and accuracy of the technique are discussed in detail. The image analysis technique traces bubbles and voidage waves accurately, whereas the mixture composition in a fluidised bed can be determined within 10%. Experiments have been carried out with 1.5 mm and 2.5 mm coloured glass beads, for which particle-particle and particle-wall collision parameters are accurately known. They have been performed in pseudo two-dimensional laboratory scale fluidised beds with a simple rectangular geometry and well-defined gas inflow conditions. An extensive set of results obtained with both mono-disperse systems and binary mixtures, suitable for critical validation of fundamental hydrodynamic models, is presented.

All conclusions regarding the current ‘state of the art’ in hydrodynamic modelling of dense gas-fluidised beds and spray granulation processes are summarised by topic in the concluding chapter of the thesis. Challenges for future research are indicated and a priority amongst them is suggested.

Samenvatting

Wervelbedsproeigranulatie is een belangrijk poederproduktieproces met verscheidene voordelen ten opzichte van alternatieve poederproduktieprocessen, zoals sproeidrogen en 'high shear' granulatie. Het meest karakteristieke en essentiële aspect van het sproeigranulatieproces is de bevochtiging van het poeder in een wervelbed door een geatomiseerde vloeistof en de resulterende groei van primaire deeltjes tot granules. Grondig begrip van de hydrodynamica en de groeimechanismen die het sproeigranulatieproces beheersen is een vereiste voor het procesontwerp en het verkrijgen van goede controle over de eigenschappen van het poedervormige produkt. Veel onderzoek heeft zich tot op heden gericht op het begrijpen en modelleren van de verschillende deeltjesgroeimechanismen (bevochtiging, agglomeratie, laagvorming, breuk en consolidatie) die geïntegreerd zijn in populatiebalansmodellen. Hydrodynamische modellen die het effect van procesontwerp en operatiecondities op de poedereigenschappen beschrijven zijn echter nog niet beschikbaar.

In dit proefschrift wordt een gelaagde modelleringsaanpak aangewend voor fundamentele hydrodynamische modellering van de complexe meerfasenstroming in wervelbedsproeigranulatieprocessen. Een nieuw discrete elementen sproeigranulatie-model dat de belangrijkste verschijnselen van wervelbed stromingsdynamica, vloeistof-vast interactie en agglomeratie in acht neemt, wordt gepresenteerd. Dit model berekent de beweging van ieder individueel poederdeeltje en vloeistofdruppeltje in het systeem, waarbij de gasfase als een continuüm wordt beschouwd. Hierbij worden microscopische fenomenen zoals deeltje-deeltje botsingen, deeltje-druppeltje coalescenties en agglomeraties direct beschreven met eenvoudige sluitingsmodellen. Het grote potentieel van hydrodynamische modellen voor de beschrijving van de invloed van verschillende essentiële proces condities, zoals de fluidisatie snelheid, de sproeisnelheid en het sproeipatroon, op karakteristieke eigenschappen van het poedervormige produkt wordt gedemonstreerd middels simulaties van een 'batch' sproeigranulatieproces met 50.000 primaire deeltjes, waarbij een kwalitatieve vergelijking met experimentele resultaten wordt gemaakt. Aangezien het aantal deeltjes dat kan worden meegenomen in discrete

elementen simulaties wordt begrensd door de beschikbare computer capaciteit, blijft de toepassing van dit soort modellen beperkt tot kleine systemen op laboratorium schaal. Het ontwikkelde discrete elementen sproeigranulatiemodel moet daarom gezien worden als een waardevol leermodel bij de ontwikkeling van deeltjesgroei-modellen die bruikbaar zijn voor de modellering van sproeigranulatieprocessen op industriële schaal. Een vooruitblik op de ontwikkeling van continuümmodellen die toepasbaar zijn op industriële schaal wordt gepresenteerd in het laatste hoofdstuk.

Aangezien bellen een dominante rol spelen in deeltjes menging, segregatie en elutriatie in dicht gepakte, gas-gefluïdiseerde wervelbedden, zoals toegepast in wervelbed-sproeigranulatie, concentreert het in dit proefschrift hoofdzakelijk gepresenteerde onderzoek zich op de correctheid van de beschrijving van de bellendynamica door hydrodynamische wervelbedmodellen. Met behulp van een 'two-fluid' continuümmodel met sluitings-vergelijkingen ontleend aan de kinetische theorie voor granulaire stromingen, wordt aangetoond dat het stromingsgedrag van homogeen beluchte wervelbedden sterk af hangt van de hoeveelheid mechanische energie die gedissipeerd wordt in niet-ideale deeltjes botsingen. Des te meer energie er gedissipeerd wordt, des te meer bellen er gevormd worden en des te sterkere drukfluctuaties er worden waargenomen ten gevolge van de tendens die inelastische deeltjes tonen om samen te trekken in clusters met een hoge deeltjesdichtheid. Deze resultaten zijn consistent met resultaten gerapporteerd door Hoomans e.a. (1996, 1998a) met gedetailleerdere discrete deeltjes modellen. Verder wordt de numerieke stabiliteit van de klassieke meerfasen versies van het SIMPLE algoritme voor continuüm modellen negatief beïnvloed door het samentrekken van inelastische deeltjes in clusters met een hoge deeltjes dichtheid en het sterke niet-lineaire verband tussen deeltjesvolumefractie en deeltjesdruk. Daarom wordt in dit proefschrift een stabieler, gemodificeerd SIMPLE algoritme gepresenteerd dat de compressibiliteit van de gesuspendeerde deeltjesfase veel directer in acht neemt.

Een kritische vergelijking van bellen patronen, tijdsgemiddelde deeltjesverdelingen en bedexpansiedynamica, verkregen met 'two-fluid' continuümsimulaties, driedimensionale, harde-bollen discrete deeltjes simulaties en digitale beeldanalyse van experimenten, wordt gepresenteerd. Bij alle vergelijkingen geeft het discrete deeltjes model de beste overeenstemming. Het belangrijkste verschil tussen de modellen wordt veroorzaakt door de verwaarlozing van deeltjesrotatie in de kinetische theorie sluitingen, toegepast in het continuümmodel. De mechanische energiebalans blijkt een waardevol hulpmiddel te zijn bij het bestuderen van de effecten van deeltjes-deeltjes, deeltjes-wand en deeltjes-gas interacties op de stromingsdynamica van wervelbedden. Energiebalans analyses

demonstreren dat, ondanks dat de totale rotationele energie relatief laag is, de meeste mechanische energie wordt gedissipeerd door frictie bij het langs elkaar slippen van de deeltjesoppervlakken tijdens een botsing. Daarom mag rotatie niet verwaarloosd worden en wordt in dit proefschrift aangetoond dat de overeenkomst tussen de beide modellen sterk verbeterd kan worden door de introductie van een effectieve restitutiecoëfficiënt, die het effect van additionele energiedissipatie door frictie in acht neemt in de kinetische theorie sluitingen voor het continuümmodel.

Een kritische vergelijking tussen experimenten en modelleringsresultaten kan gemaakt worden op basis van de bedexpansiedynamica. Hoewel beide modellen het juiste fluidisatie regime en de juiste trends in de belgrootte voorspellen, verschilt de gesimuleerde bedexpansiedynamica significant van de experimentele resultaten. Uit visuele observatie van de experimenten blijkt dat de verschillen hoofdzakelijk veroorzaakt worden door de vorming van dicht gepakte gebieden waarbinnen geen deeltjesvibraties waarneembaar zijn. De vorming van zulke gebieden vindt in de simulaties niet plaats. Er wordt geconcludeerd dat het gat tussen de modellen en de experimenten hoogst waarschijnlijk veroorzaakt wordt door langdurige deeltjescontacten en gelijktijdige contacten tussen meerdere deeltjes die niet worden meegenomen in de modellering.

Een eerste stap in de richting van het koppelen van de verschillende modelleringsniveaus wordt gemaakt middels de ontwikkeling van een nieuwe analysetechniek die het mogelijk maakt om de aannames die ten grondslag liggen aan de kinetische theorie voor granulaire stroming, toegepast voor continuümmodellen, te verifiëren met behulp van gedetailleerdere discrete deeltjes modellen. Voor elastische deeltjes wordt een zeer goede overeenkomst met de kinetische theorie gevonden. De individuele deeltjessnelheids-verdeling in een dicht gepakt wervelbed is isotroop en Maxwells en een goede fit van de botssnelheidsverdeling en de botsfrequentie wordt verkregen met de radiële-distributiefunctie van Carnahan en Starling (1969). Voor elastische en ruwe deeltjes wordt daarentegen een anisotrope, Maxwellse snelheidsverdeling verkregen. Er wordt geconcludeerd dat de vorming van dicht gepakte deeltjesclusters de ruimtelijke homogeniteit verstoort en zodoende resulteert in anisotropie. Analyse van de botssnelheidsverdeling toont aan dat, in dicht gepakte wervelbedden, niet alle botshoeken even waarschijnlijk zijn. De waargenomen anisotropie wordt sterker naar mate de inelasticiteit van de deeltjes toeneemt.

Voor de modellering van het fluïdisatie- en segregatiegedrag van deeltjesmengsels in industriële wervelbedden dienen 'multi-fluid' continuümmodellen ontwikkeld te worden. In Goldschmidt e.a. (2001b) werd aangetoond dat een 'multi-fluid' model met bestaande sluitingsvergelijkingen, afgeleid volgens de kinetische theorie voor granulaire stromingen, veel te snelle segregatie voorspeld in vergelijking met experimenten. Daarom worden de afleiding van een nieuwe set kinetische theorie sluitingsvergelijkingen en een 'multi-fluid' model waarin deze worden gebruikt in dit proefschrift gegeven. Het belangrijkste verschil tussen de nieuwe sluitingsvergelijkingen en de bestaande set afgeleid door Manger (1996) en Mathiesen (1997), is het feit dat segregatie niet langer mogelijk is in de eerste (evenwichts) benadering voor de deeltjes snelheid verdeling, maar wordt geïntroduceerd als een hogere orde (niet-evenwichts) effect. Aangezien de nieuwe theorie een beter beeld lijkt te geven van de fysica voor dicht gepakte deeltjesstromingen waarin de botsfrequentie erg hoog is, is het te verwachten dat het nieuwe model realistischer segregatie snelheden zal geven, alhoewel dit nog aangetoond dient te worden.

Een van de meest cruciale stappen in de ontwikkeling van fundamentele hydrodynamische modellen is de validatie van deze modellen met nauwkeurige, gedetailleerde experimentele data. Daarom is er een digitale beeldanalyse techniek ontwikkeld waarmee bedexpansie- en segregatiedynamica in een wervelbed simultaan bestudeerd kunnen worden. De ontwikkeling, calibratie en nauwkeurigheid van deze techniek worden in detail besproken. De beeldanalysetechniek is in staat bellen en porositeitsgolven nauwkeurig te traceren, waarbij de mengselsamenstelling in het wervelbed binnen 10% nauwkeurig bepaald kan worden. Experimenten zijn uitgevoerd met 1,5 mm en 2,5 mm gekleurde glasparels, waarvoor de deeltjes-deeltjes en deeltjes-wand botsparameters nauwkeurig gemeten waren. Deze experimenten werden verricht in een pseudo-tweedimensionaal laboratorium schaal wervelbed met een simpele rechthoekige geometrie en goed gecontroleerde gas-instroomcondities. Een uitgebreid overzicht van de experimentele resultaten met mono-disperse systemen en binaire mengsels, geschikt voor kritische validatie van fundamentele hydrodynamische modellen, wordt gepresenteerd.

De conclusies met betrekking tot de huidige stand van zaken op het gebied van de hydrodynamische modellering van wervelbedden en wervelbedsproeigranulatoren worden in the laatste hoofdstuk van het proefschrift per onderwerp samengevat. Tevens worden de uitdagingen voor toekomstig onderzoek behandeld en worden de prioriteiten aangegeven.

Chapter 1.

General introduction

Abstract

The fluidised bed spray granulation process is briefly introduced. All essential steps of the size enlargement mechanism and the hydrodynamic aspects of the process are pointed out. The current state of the art of spray granulation and dense gas-fluidised bed modelling is discussed. The research objectives are presented, whereafter this chapter is concluded with an outline of the thesis.

1. The fluidised bed spray granulation process

Fluidised bed spray granulation is an important powder production process with several key advantages compared to other powder production processes, such as spray drying or high-shear granulation. The process was first described by Wurster (1960) for pharmaceutical application, based upon his earlier work on air suspension coating. The most characteristic and essential part of spray granulation is the wetting of particles in a gas-fluidised bed by an atomised liquid feed (solution, suspension or melt) and the induced size enlargement of primary particles to granules. A graphical representation of a spray granulation process is given in figure 1.1. The process is commonly used for the production of granules for agricultural, pharmaceutical and other fine chemical applications, as it combines good control over composition and structural properties of the powder. Fluidised bed spray granulation is often selected for its flexibility and the great cost saving potential, because all essential steps of the granulation process can be performed in one single apparatus. Reviews signifying the interest of this type of granulation process are given by Kristensen and Schaeffer (1987), Banks and Aulton (1991) and Nienow (1995). More background information on size enlargement by granulation processes can be found in the books by Pietsch (1992) and Ennis and Litster (1997).

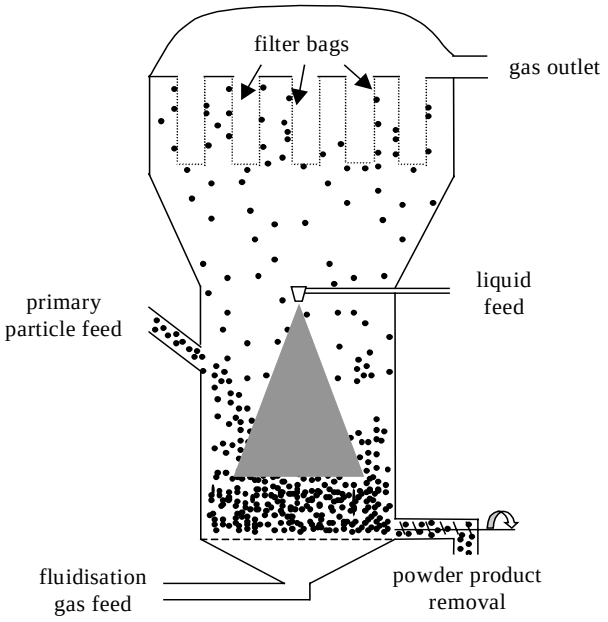

Figure 1.1. Schematic representation of a spray granulation process.

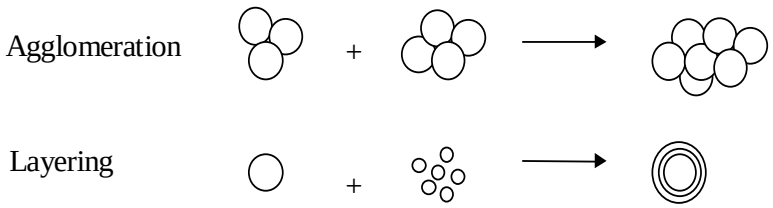

Figure 1.2. Growth mechanisms encountered in granulation processes

Thorough understanding of the hydrodynamics and the mechanisms prevailing in the spray granulation process is a prerequisite for understanding the process and attaining control over the powder characteristics. The mechanisms of granulation are often distinguished as *wetting* (or nucleation), progressive *growth* by a sequence of binary collisions, *breakage* and *consolidation*. Two different growth mechanisms are distinguished (see figure 1.2): *agglomeration* of existing granules of approximately the same size and *layering* of small (primary) particles onto previously formed granules or wetted particles. It is virtually impossible to expect that these mechanisms will occur singly or sequentially. Many granulator design and operation parameters such as mode of operation (batch or continuous), fluidisation velocity, reactor geometry, positioning of the nozzles, type of nozzle, liquid feed rate, operating temperature, etc. will influence these mechanisms and consequently the powder characteristics. Some typical granules produced by spray granulation are shown in figure 1.3. Both pictures show liquid bridges holding the primary particles together, whereas the enlargement on the right clearly shows signs of breakage.

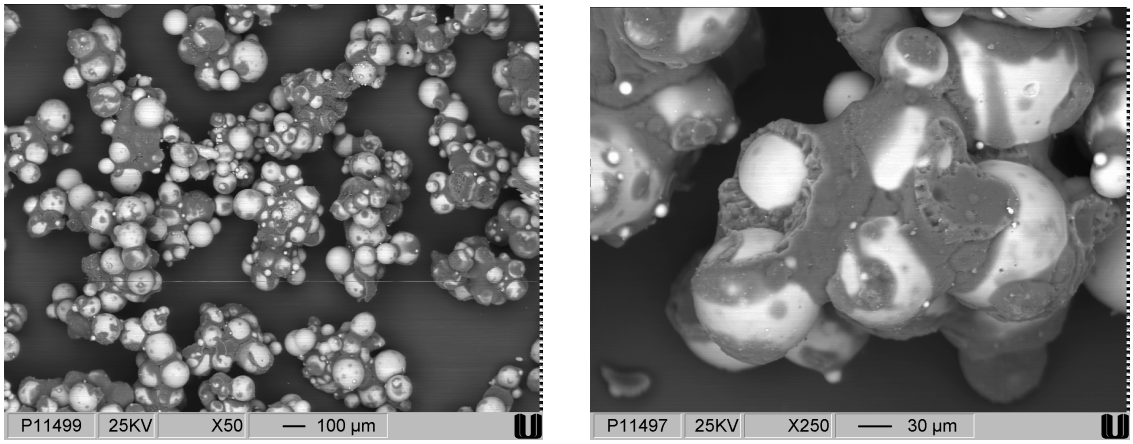

Figure 1.3. SEM photographs of granules composed of glass ballotini and poly-ethylene glycol (PEG) binder.

2. Modelling of spray granulation processes

For granulation processes, size distribution is an important, if not the most important, property. To model the evolution of the granule size distribution within the process, granule growth and breakage mechanisms can be integrated into population balance models. The population balance is basically a statement of continuity for particulate systems, that accounts for the mechanisms that change a particle property by kinetic expressions. An in-depth treatment of population balance methods is given by Randolph and Larson (1991). With respect to granulation processes, population balances have been successfully applied to provide insight into the mechanisms by which particles grow (Waldie et al., 1987; Hounslow, 1998; Cryer, 1999; Lee and Matsoukas, 2000). The use of population balance modelling has however been hampered because the kinetic parameters required for the models have proven difficult to predict and are very sensitive to operating conditions and material properties (Boerefijn et al., 2001). Therefore, though population balance models are a useful tool to gain more insight into experimental observations, they (on their own) are not sufficient for the a-priori design and scale-up of fluidised bed granulation processes.

To the author's knowledge, fundamental hydrodynamic models that capture the key features of fluidised bed hydrodynamics, liquid-solid contacting and agglomeration in one model, have not been developed so far. This can be attributed to the inherent complexity of the multi-phase hydrodynamics and contact mechanics involved. A wide range of length and associated temporal scales needs to be covered. The mixing patterns that determine the particle circulation rate in the fluidised bed and the refreshment of particles in the wetting zone typically take place on the macroscopic length scale determined by the size of the apparatus and time scales of several seconds are involved. Particle-particle collisions and coalescence of droplets with particles on the other hand are quasi-instantaneous processes taking place on a microscopic length scale determined by particle and droplet sizes and velocities. However, the size enlargement mechanisms presented in the previous paragraph are highly affected by fluidised bed dynamics and liquid-solid contacting in the wetting zone. Therefore there is a great need for models that can take the effects of both hydrodynamics and contact mechanics on powder characteristics into account in an integrated approach.

Because of the large differences in time and length scales involved, models capable of capturing all details of the contact mechanics and the full system hydrodynamics at the same time may be out of reach for the next couple of decades. Therefore a multi-level

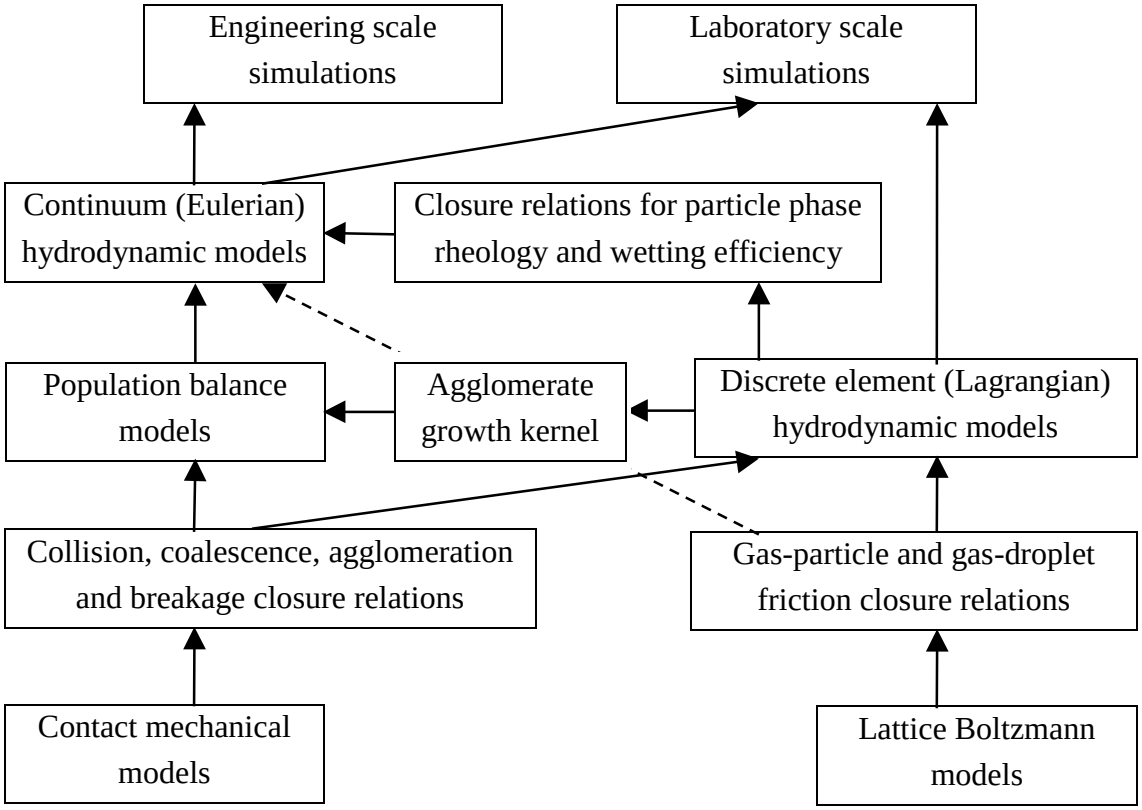

Figure 1.4. Multi-level modelling strategy for modelling of spray granulation processes.

modelling strategy to model spray granulation processes is proposed, as presented in figure 1.4. This figure shows how detailed hydrodynamic and contact mechanical models can be applied to develop closure relations required by higher level (engineering scale) models, capable of modelling the systems and industrial processes of interest. Key issues in such a multi-level modelling strategy are the validation of all models with appropriate experiments, the verification of closure theories applied for higher level models with more detailed (lower level) models and the development of (statistical) techniques to derive new closure relations from the lower level models. Figure 1.4. represents the main research strategy upon which this thesis is based, *'Linking granular dynamics to engineering scale continuum modelling'*. It should be noted that the interaction between the models is not as much one way as the figure suggests, higher level hydrodynamic models for example can also be applied to generate insight in the characteristic collision speeds and angles, which are required to describe the contact mechanics.

3. Hydrodynamic modelling of dense gas-fluidised beds

Granular products from fluidised beds generally belong to group B or group D particles according to Geldart's powder classification (Geldart, 1973). However, in batch granulation, the bed may initially consist of group A powder. For granulation, fluidised beds are typically operated in the bubbling or dense turbulent regime in the range of 1.5 to 10 times the minimum fluidisation velocity. For batch granulation the gas velocity may need to be increased significantly during operation to maintain the velocity in this range as the particle size increases. For group B and D particles, nearly all excess gas flows through the bed as bubbles. The flow of bubbles controls particle mixing, segregation, attrition and elutriation. Therefore accurate prediction of bubble dynamics in dense gas-fluidised beds is a key issue in the development of hydrodynamic models for spray granulation processes and the current state of the art in dense gas-fluidised bed modelling is discussed in this paragraph.

Nowadays gas-fluidised beds find a widespread application in the petroleum, chemical, metallurgical and energy industries. The objective of much fluidisation research has been the prediction of the performance of industrial beds (Yates, 1983; Davidson et al., 1985; Kunii and Levenspiel, 1991). Despite significant efforts, the complex hydrodynamics of these systems is still not fully understood. Scale-up of small laboratory units to engineering scale equipment is still troublesome. This is mainly due to the inherent complexity of dense gas-particle flows, which in its turn can be related to particle-particle and particle-wall interaction on the one hand and gas-particle interaction on the other hand.

Thanks to the enormous increase in computer power and algorithm development fundamental hydrodynamic modelling of multi-phase reactors has recently come within reach. In the last decade significant research efforts have been made to develop detailed micro balance models to study the complex hydrodynamics of gas-fluidised beds (Gidaspow, 1994; Simonin, 1996; Enwald et al., 1996; Kuipers and Van Swaaij, 1998; Goldschmidt et al., 2000). Broadly speaking two different types of hydrodynamic models can be distinguished, Eulerian (continuum) models and Lagrangian (discrete element) models. Both consider the gas phase as a continuum. The flow fields at sub-particle level are not resolved and empirical equations are applied for fluid-particle drag. Owing to the continuum description of the particulate suspension, Eulerian models require additional closure laws to describe particle-particle and/or particle-wall interactions. In most recent continuum models constitutive relations according to the kinetic theory of granular flow

have been incorporated. This theory is basically an extension of the classical kinetic theory of gases (Chapman and Cowling, 1970) to dense particulate flows, that takes non-ideal particle-particle collisions and gas-particle drag into account. Discrete particle models on the other hand do not require additional closure equations for the suspended particulate phase since they compute the motion of every individual particle, taking collisions and external forces acting on the particles directly into account. However, the number of particles that these models can handle (i.e. typically less than 10^6) is orders of magnitude lower than that encountered in most (industrial) fluidised beds. Therefore continuum models constitute a more natural choice for hydrodynamic modelling of engineering scale systems, whereas discrete particle models in accordance with the multi-level modelling strategy can be applied as a valuable research tool to verify and further develop closure laws for these continuum models.

In many industrial dense gas-fluidised bed processes, e.g. fluid bed spray granulation and gas-phase polymerisation, mixtures of particles with different physical properties are used. When particles differ in size and/or density, segregation (see figure 1.5) may occur. Segregation is most marked at low gas velocities when there is appreciable particle density difference. Even a strongly segregating system, however, can be fairly well mixed if the gas velocity is increased sufficiently, although it can be difficult to remove the last traces of segregation.

Accurate prediction of segregation is required to improve the design, operation and scale-up of gas-fluidised bed processes. Discrete particle models are well suited to model

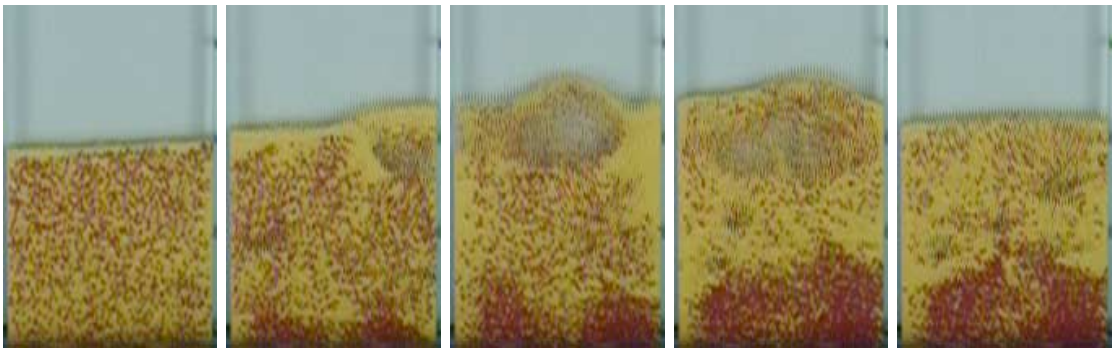

Figure 1.5. Experimental observations of size driven segregation of a binary mixture of coloured glass beads (fluidisation starts at t = 0 s).

segregation, since they offer the possibility to specify the physical properties of each individual fluidised particle. The ability of discrete particle models to predict segregation in dense gas-fluidised beds has been demonstrated by Hoomans et al. (1998c, 2000b). They observed a strong influence of the particle-particle collision parameters on bubble dynamics and subsequent segregation rates. To model segregation in engineering scale fluidised beds, multi-fluid continuum models need to be developed. Mathiessen et al. (2000) successfully modelled axial segregation in a laboratory scale riser, using a multi-fluid continuum model. In riser flows kinetic momentum transfer is the dominant momentum transfer mechanism. In dense gas-fluidised beds, on the contrary, collisional momentum transfer dominates the bubble flow patterns. The ability of multi-fluid models to capture segregation phenomena in dense gas-fluidised beds remains to be demonstrated.

One of the most important aspects of hydrodynamic model development is the careful validation of the model predictions with well-defined experiments. Though a lot has been reported on particle mixing and segregation in dense gas-fluidised beds (Rowe and Nienow, 1976; Hoffmann and Romp, 1991; Wang and Chou, 1995), hardly any information can be found on the spatial distribution and rate of segregation (Yang and Keairns, 1982; Agarwal et al., 1996; Gilbertson and Eames, 2001). Combined measurements of segregation and bubble dynamics performed with particles with well-defined properties (size, shape, density and collision properties) in a set-up with a well-defined bed geometry and gas inflow on short time scales that can currently be handled by fundamental hydrodynamic models are not yet available. Clearly, for thorough validation of these models this kind of information is required.

4. Research objectives

The research presented in this thesis has been performed as part of a bigger research program, focussed on the development of fundamental models to predict the influence of process design and material properties on product characteristics for engineering scale granulation processes. The main objective of the research presented in this thesis has been the development and validation of a fundamental hydrodynamic model, which accurately predicts the behaviour of particle mixtures in engineering scale gas-fluidised beds.

Because dense gas-fluidised bed dynamics are mainly determined by the bubble flow patterns, special attention needed to be paid to the prediction of bubble dynamics by fundamental hydrodynamic models. To validate the models new measurements had to be performed. Experiments suitable for model validation, which requires all particle properties including the collision parameters, bed geometry and gas inflow conditions in the bed to be accurately known, had not yet been reported. Also the key assumptions underlying the kinetic theory closure laws, which are nowadays widely applied in engineering scale two-fluid continuum models, needed to be verified with more detailed granular dynamics simulations. Where possible, improvements to the kinetic theory had to be indicated and implemented within the continuum model.

To enable the simulation of segregation phenomena in engineering scale gas-fluidised beds, a multi-fluid continuum model had to be developed, implemented and validated. Special attention needed to be paid to the development of an efficient numerical method to solve the model, since accurate validation and simulation of engineering scale systems requires high spatial resolution and relatively long simulations (up to 1 minute). Since hardly any experimental data on segregation rates and spatial distribution of segregation patterns was available, a non-intrusive measurement method capable of simultaneously measuring these segregation phenomena and the bed dynamics from which they result needed to be developed to obtain accurate experimental data.

Finally, to study the influence of operation conditions and particle properties on fluidised bed spray granulation processes hydrodynamic models for spray granulation processes needed to be developed. These models should be able to capture the essential features of the gas fluidised bed (bubble flow pattern and segregation phenomena) and the particle growth mechanisms (liquid-solid contacting and agglomeration) within the same modelling framework.

5. Outline of the thesis

Chapter 2 focuses on the sensitivity of dense gas-fluidised bed hydrodynamics to particle-particle collision parameters, such as the coefficient of restitution. Special attention is paid to a new, more stable numerical solution method for two-fluid continuum models with closure equations according to the kinetic theory of granular flow. It is demonstrated that the hydrodynamic behaviour of homogeneously aerated, dense gas-fluidised beds strongly depends on the amount of energy dissipated in non-

ideal particle collisions. The observed dependence is consistent with earlier observations from discrete particle simulations (Hoomans et al., 1996, 1998a). It is therefore concluded that, in order to obtain realistic bed dynamics from fundamental hydrodynamic models, it is of prime importance to correctly take the effect of energy dissipation due to non-ideal particle collisions into account. Consequently, to validate these hydrodynamic models, there is a great need for experiments in dense gas-fluidised beds with well-defined bed geometry and accurately controlled gas inflow conditions, but especially with particle properties for which besides density, size and shape, all collision parameters are accurately known.

In **chapter 3** a critical comparison between the two fluid model, a 3D hard-sphere discrete particle model and experiments performed in a pseudo two-dimensional gas-fluidised bed is made. The discrete particle model shows superior resemblance with the experimental results, though bed expansion dynamics predicted by both models differ significantly from experimental results. Alternative gas-particle drag models result in considerably different bed dynamics, but the gap between model and experimental results can not be closed. The main difference between the models is caused by the neglect of particle rotation in the kinetic theory closure equations embedded in the two-fluid model. Energy balance analyses demonstrate that over 80% of the total kinetic energy is dissipated by sliding friction. It is shown that introduction of an effective coefficient of restitution, that incorporates the additional dissipation due to frictional interactions in the two-fluid model, significantly improves the degree of agreement between both models.

A further evaluation of several key assumptions underlying the framework of the kinetic theory of granular flow is performed in **chapter 4**. In this chapter a novel technique to sample particle velocity distributions and collision dynamics from dynamic discrete particle simulations of intrinsically unsteady, non-homogeneous systems, such as fluidised beds and granulation processes, is presented. Discrete particle simulations with ideal particle collision parameters show excellent agreement with the kinetic theory of granular flow. The individual particle velocity distribution is isotropic and Maxwellian and a good fit is obtained for the collision velocity distribution function and the collision frequency. However, for inelastic and rough particles an anisotropic Maxwellian velocity distribution is obtained. It is concluded that the formation of dense particulate clusters disturbs spatial homogeneity and results in collisional anisotropy. The observed anisotropy becomes more pronounced when the degree of inelasticity increases.

In **chapter 5** a novel kinetic theory closure model for multi-component granular mixtures is presented. In earlier publications (Goldschmidt et al., 2001a, 2001b) the segregation process in dense gas-fluidised beds was modelled using a multi-fluid model with kinetic theory closure relations derived by Manger (1996) and Mathiesen (1997). The sensitive dynamic equilibrium between segregation and mixing of a binary mixture of particles in a dense gas-fluidised bed proved to be a severe test case for the fundamental hydrodynamic model, since bubble dynamics and momentum transfer between particles of different species have to be modelled correctly. Though segregation phenomena could be predicted, the segregation rates were far too high compared to experimental results obtained from non-intrusive digital image analysis measurements. This raised doubts regarding the representation of particle-particle interactions in the model. A more in-depth analysis of the derivations presented by Manger (1996) raised even more serious doubts on the starting points of the derivation. In Manger's derivation it is assumed that, in first approximation, the velocities of all particulate species are Maxwellian distributed around different mean velocities for all particle kinds. As a result the kinetic theory closure model allows for segregation in the first (equilibrium) approximation to the particle velocity distribution, whereas segregation (separation of species) is a non-equilibrium phenomenon. Therefore the derivation of a new set of kinetic theory closure relations for multi-component particulate mixtures was found necessary. The outline of the derivation of this new kinetic theory closure model and the key equations resulting from the tedious derivation are presented in chapter 5.

In **chapter 6** a non-intrusive digital image analysis technique to study bed dynamics and segregation phenomena in dense gas-fluidised beds is presented. The set-up, calibration and accuracy of the measurement method are discussed. Experiments carried out in a pseudo two-dimensional experimental rig with spherical glass beads, for which all particle properties have been accurately determined, are presented. Bed expansion dynamics are studied for two different mono-disperse systems at three different fluidisation velocities and several bed heights. The full power of the digital image analysis technique is demonstrated by experiments carried out with binary mixtures of coloured glass beads. The developed digital image analysis technique enables the non-intrusive measurement and quantification of bed dynamics and consequent segregation rates, all at the same time. The measured segregation rates and bed dynamics obtained for binary mixtures with various mixture compositions at several fluidisation velocities and bed heights are presented. Also some snapshots of segregation patterns, that demonstrate the spatial inhomogeneity of the observed segregation phenomena, are shown.

A new discrete element spray granulation model that captures the key features of fluidised bed hydrodynamics, liquid-solid contacting and agglomeration is presented in **chapter 7**. The model computes the motion of every individual particle and droplet in the system, whereas the gas phase is considered as a continuum. The hydrodynamic behaviour of a batch granulation process containing 50.000 primary particles is simulated, whereby micro scale processes such as particle-particle collisions, droplet-particle coalescence and agglomeration are directly taken into account by simple closure models. The simulations demonstrate the great potential of the model to predict the influence of several key process conditions such as fluidisation velocity, spray rate and spray pattern on powder product characteristics. In all performed simulations droplet-particle coalescence and agglomeration took place in the freeboard and at the top of the bed throughout the batch runs. Particle growth was dominated by layering, whereas agglomeration of equally size particles and bed penetration by droplets or wetted particles rarely occurred. Also severe size segregation was observed in the simulations. Big granules mainly remained at the bottom of the bed, while above the spray nozzle mainly primary particles were detected. Furthermore, a low particle concentration was observed in the spray zone, because particles are catapulted into the bed as soon as a droplet hits them.

Chapter 8 summarises the main conclusions of the thesis. Challenges for future fluidised bed and spray granulation research are discussed and a priority amongst the subjects to be studied is presented. The chapter finishes with an outlook on the development of engineering scale continuum models for fluidised bed spray granulation processes.

Chapter 2.

Two-fluid continuum modelling of dense gas-fluidised beds: effect of coefficient of restitution on bed dynamics

Abstract

In this chapter a two-fluid continuum model with constitutive equations according to the kinetic theory of granular flow is presented. Special attention is paid to a new numerical solution method, which increases the numerical stability of two-fluid simulations with kinetic theory closures. The model is applied to study the influence of the coefficient of restitution on bubble formation and bed dynamics. It is demonstrated that the hydrodynamic behaviour of homogeneously aerated gas-fluidised beds strongly depends on the amount of energy dissipated in non-ideal particle encounters. The more energy is dissipated, the more bubbles are formed due to the tendency of inelastic particles to contract in high-density clusters. Since bubbles dominate the hydrodynamic behaviour of dense gas-fluidised beds, the coefficient of restitution directly influences particle mixing and bed dynamics. A strong increase in the intensity of pressure drop fluctuations is observed when the amount of energy dissipated in collisions increases.

The observed dependence of gas-fluidised bed dynamics on the particle collision parameters is consistent with earlier results obtained from more detailed discrete particle simulations by Hoomans et al. (1996, 1998a). It is therefore concluded that, in order to obtain realistic bed dynamics from fundamental hydrodynamic models, it is of prime importance to correctly take the effect of energy dissipation due to non-ideal particle-particle encounters into account. Further, to validate these fundamental hydrodynamic models, there is a great need for experiments in systems with a well-defined geometry and accurately controlled inflow conditions, but especially with particles for which besides density, size and shape all collision parameters are accurately known.

Parts of this chapter are based on the paper:

Goldschmidt M.J.V., Kuipers J.A.M., Van Swaaij W.P.M., 2001, Hydrodynamic modelling of dense gas-fluidised beds using the kinetic theory of granular flow: effect of the coefficient of restitution on bed dynamics, *Chem. Eng. Sci.*, **56**, 571-578

1. Introduction

In the last decade considerable progress has been made in the area of hydrodynamic modelling of gas-fluidised suspensions. Broadly speaking two different classes of models can be distinguished, continuum (Eulerian) models and discrete particle (Lagrangian) models. Discrete particle models solve the Newtonian equations of motion for each individual particle, taking into account the effects of particle collisions and forces acting on the particle by the gas. Particle collisions are described by collision laws, that account for energy dissipation due to non-ideal particle interactions by means of the empirical coefficients of restitution and friction (hard-sphere approach, Hoomans et al., 1996) or an empirical spring stiffness, a dissipation constant and a friction coefficient (soft-sphere approach, Tsuji et al., 1993). The role of these collision parameters has been reported by several workers with respect to bubble formation and segregation in dense fluidised beds (Hoomans et al., 1996, 1998a; Hoomans 2000a) and cluster formation in risers (Hoomans et al., 1998b; Ouyang and Li, 1999).

Eulerian models consider the gas phase and the particulate phase to be continuous and fully interpenetrating. The equations employed are a generalisation of the Navier-Stokes equations for interacting continua. Owing to the continuum representation of the particulate phase, Eulerian models require additional closure laws to describe the rheology of the fluidised particles. In most recent continuum models constitutive equations according to the kinetic theory of granular flow are incorporated. This theory is basically an extension of the classical kinetic theory to dense particle flow, which provides explicit closures that take energy dissipation due to non-ideal particle-particle collisions into account by means of the coefficient of restitution. An extreme, unrealistic, sensitivity of Eulerian models due to inelastic particle-particle collisions has been reported by several authors for simulations of riser flow (Pita and Sundaresan, 1991; Nieuwland et al., 1996). More recent research (Hrenya and Sinclair, 1997; Detamore et al., 2001) indicates that the extreme sensitivity of the model to the coefficient of restitution is most likely caused by the neglect of gas phase turbulence, which is important in (dilute) riser flow, but may be neglected in dense gas-fluidised beds. In this study a two-dimensional two-fluid continuum model will be applied to study the influence of the coefficient of restitution on the hydrodynamics of dense gas-fluidised beds, where particle collisions dominate the hydrodynamic behaviour.

2. The two-fluid continuum model

2.1. Governing equations

In the two-fluid continuum model the gas phase and the suspended particulate phase are considered to be continuous and fully interpenetrating. For engineering scale fluidised beds this type of modelling can be justified due to the huge number of particles (typically 10^9-10^{12}) present in the system of interest. The conservation equations employed in the models can in fact be seen as a generalisation of the Navier-Stokes equations for interacting continua. The non-steady continuity and momentum equations for gas (*g*) and solid (*s*) are given by:

$$\frac{\partial}{\partial t}(\varepsilon_g \rho_g) + \nabla \cdot (\varepsilon_g \rho_g \bar{u}_g) = 0 \tag{2.1}$$

$$\frac{\partial}{\partial t}(\varepsilon_s \rho_s) + \nabla \cdot (\varepsilon_s \rho_s \bar{u}_s) = 0 \tag{2.2}$$

$$\frac{\partial}{\partial t}(\varepsilon_g \rho_g \bar{u}_g) + \nabla \cdot (\varepsilon_g \rho_g \bar{u}_g \bar{u}_g) = -\varepsilon_g \nabla P_g - \nabla \cdot (\varepsilon_g \bar{\bar{\tau}}_g) - \beta(\bar{u}_g - \bar{u}_s) + \varepsilon_g \rho_g \bar{g} \tag{2.3}$$

$$\frac{\partial}{\partial t}(\varepsilon_s \rho_s \bar{u}_s) + \nabla \cdot (\varepsilon_s \rho_s \bar{u}_s \bar{u}_s) = -\varepsilon_s \nabla P_g - \nabla P_s - \nabla \cdot (\varepsilon_s \bar{\bar{\tau}}_s) + \beta(\bar{u}_g - \bar{u}_s) + \varepsilon_s \rho_s \bar{g} \tag{2.4}$$

These conservation equations describe the mean motion of the gas-solid two-phase system. For an extensive discussion on the derivation of these equations the interested reader is referred to the work of Anderson and Jackson (1967), Ishii (1975), Gidaspow (1994), Enwald et al. (1996) and Jackson (1997). Further, in chapter 5 it is demonstrated how the continuity equation and momentum equation for the solids phase can be derived within the framework of the kinetic theory of granular flow.

2.2. Constitutive equations

The gas phase density is related to the temperature and the pressure by the ideal gas law:

$$\rho_g = \frac{M_g}{RT_g} P_g \tag{2.5}$$

For the particulate phase a constant density is assumed. In the dense regime (ε_g < 0.80) the inter-phase momentum transfer coefficient can be obtained from the well-know Ergun equation (Ergun, 1952):

$$\beta = 150\frac{(1-\varepsilon_f)^2}{\varepsilon_f}\frac{\mu_f}{(\phi_s d_p)^2} + 1.75(1-\varepsilon_f)\frac{\rho_f}{\phi_s d_p}\left|\bar{u}_f - \bar{u}_s\right| \tag{2.6}$$

In more dilute regimes (ε_g > 0.80) the inter-phase momentum transfer coefficient has been derived from the correlation of Wen and Yu (1966):

$$\beta = \frac{3}{4}C_d(1-\varepsilon_f)\frac{\rho_f}{\phi_s d_p}\left|\bar{u}_f - \bar{u}_s\right|\varepsilon_f^{-1.65} \tag{2.7}$$

Though most two-fluid models nowadays apply this gas-particle drag model, there is no general consensus about the modelling of gas-particle momentum transfer. Two alternative drag models will be presented in chapter 3, where a detailed comparison of the two-fluid model to experimental data is made. A more extensive overview of drag models is presented by Enwald et al. (1996).

Owing to the continuum representation of the particulate phase the two-fluid continuum model requires additional closure laws to describe the rheology of the fluidised particles. Experiments by Schügerl et al. (1961) indicated that fluidised suspensions exhibit approximate Newtonian behaviour. In early two-fluid models (e.g. Tsuo and Gidaspow, 1990; Kuipers et al., 1992a), as a first approximation a constant viscosity estimated from those experiments was applied. The solids phase pressure, that prevents particles from reaching impossibly low values of void fraction, was modelled as:

$$\nabla P_s = G_s \nabla \varepsilon_f \tag{2.8}$$

Thereby the solids phase elasticity modulus (G_s) was taken from simple theory of powder compaction (Orr, 1966).

2.2.1. Kinetic theory of granular flow

In most recent two-fluid continuum models (e.g. Gidaspow, 1994; Balzer et al., 1995; Nieuwland et al., 1996) constitutive equations according to the kinetic theory of granular

flow (KTGF) are incorporated. This theory describes the dependence of the rheologic properties of the fluidised particles on local particle concentration and the fluctuating motion of the particles owing to particle-particle collisions. In the KTGF the actual particle velocity ($\overline{c}_p$) is decomposed in a local mean solids velocity ($\overline{u}_s$) and a random fluctuating velocity component ($\overline{C}_p$) according to:

$$\overline{c}_p = \overline{u}_s + \overline{C}_p \tag{2.9}$$

Associated with the random motion of the particles, analogous to the definition of the temperature of a gas in the classical kinetic theory, the granular temperature θ for an ensemble of particles is defined as:

$$\theta = \frac{1}{3} < \overline{C}_p \cdot \overline{C}_p > \tag{2.10}$$

where the brackets denote ensemble averaging. The variation of the particle velocity fluctuations is described with a separate conservation equation, the so-called granular temperature equation:

$$\frac{3}{2}\left[\frac{\partial}{\partial t}(\varepsilon_s \rho_s \theta) + \nabla \cdot (\varepsilon_s \rho_s \theta \ \overline{u}_s)\right] = -(P_s \overline{\overline{I}} + \varepsilon_s \overline{\overline{\tau}}_s) : \nabla \overline{u}_s - \nabla \cdot (\varepsilon_s q_s) - 3\beta\theta - \gamma \tag{2.11}$$

For the derivation of this conservation equation and the subsequent constitutive equations the interested reader is referred to the books by Chapman and Cowling (1970) and Gidaspow (1994) and the papers by Jenkins and Savage (1983), Ding and Gidaspow (1990) and Nieuwland et al. (1996). A more detailed discussion on the derivation of kinetic theory closure models can also be found in chapter 5, where the derivation of a kinetic theory closure model for multi-component particle mixtures is presented. In this chapter the constitutive equations derived by Nieuwland et al. (1996) have been applied for the particle phase rheology. These equations are listed in table 2.1.

Within the kinetic theory of granular flow a single parameter collision model is applied to describe particle-particle collision dynamics. This collision model relates the impact velocity between particles 1 and 2 ($\overline{c}_{12} = \overline{c}_1 - \overline{c}_2$) to the rebound velocity ($\overline{c}'_{12}$) by the definition of the coefficient of (normal) restitution:

Table 2.1. Constitutive equations according to the kinetic theory of granular flow.

Particulate pressure:

$$P_s = \left[1 + 2\left(1 + e_n\right)\varepsilon_s g_0\right]\varepsilon_s \rho_s \theta \tag{2.1.1}$$

Newtonian stress-tensor (solids phase):

$$\bar{\bar{\tau}}_s = -\left[\left(\lambda_s - \frac{2}{3}\mu_s\right)(\nabla \cdot \bar{u}_s)\bar{\bar{I}} + \mu_s\left((\nabla \bar{u}_s) + (\nabla \bar{u}_s)^T\right)\right] \tag{2.1.2}$$

Bulk viscosity:

$$\lambda_s = \frac{4}{3}\varepsilon_s \rho_s d_p g_0 \left(1 + e_n\right)\sqrt{\frac{\theta}{\pi}} \tag{2.1.3}$$

Shear viscosity:

$$\mu_s = 1.01600\frac{5}{96}\pi\rho_s d_p\sqrt{\frac{\theta}{\pi}}\frac{(1 + \frac{8}{5}\frac{(1+e_n)}{2}\varepsilon_s g_0)(1 + \frac{8}{5}\varepsilon_s g_0)}{\varepsilon_s g_0} + \frac{4}{5}\varepsilon_s \rho_s d_p g_0 \left(1 + e_n\right)\sqrt{\frac{\theta}{\pi}} \tag{2.1.4}$$

Pseudo-Fourier fluctuating kinetic energy flux:

$$\bar{q}_s = -\kappa_s \nabla\theta \tag{2.1.5}$$

Pseudo-thermal conductivity:

$$\kappa_s = 1.02513\frac{75}{384}\pi\rho_s d_p\sqrt{\frac{\theta}{\pi}}\frac{(1 + \frac{12}{5}\frac{(1+e_n)}{2}\varepsilon_s g_0)(1 + \frac{12}{5}\varepsilon_s g_0)}{\varepsilon_s g_0} + 2\varepsilon_s \rho_s d_p g_0 \left(1 + e_n\right)\sqrt{\frac{\theta}{\pi}} \tag{2.1.6}$$

Dissipation of fluctuating kinetic energy due to inelastic particle-particle collisions:

$$\gamma = 3\left(1 - e_n^2\right)\varepsilon_s^2 \rho_s g_0 \theta\left[\frac{4}{d_p}\sqrt{\frac{\theta}{\pi}} - (\nabla \cdot \bar{u}_s)\right] \tag{2.1.7}$$

$$\vec{c}'_{12} \cdot \vec{k} = -e_n(\vec{c}_{12} \cdot \vec{k}) \tag{2.12}$$

in which $\vec{k}$ is the unit vector directed in the normal direction from the centre of particle 1 to the centre of particle 2. Most kinetic theory derivations assume the particles to be smooth and spherical, so particle rotation and velocity changes in the tangential impact direction can be neglected. The validity and consequences of these assumptions will be addressed in chapter 4, where a 3D discrete particle model is applied to verify the kinetic theory closure model.

3. Numerical solution method

Due to the tendency of inelastic particles to contract in high-density clusters and the strong non-linearity of the particle pressure near the maximum packing density, special care has to be paid to the numerical implementation of the model equations. Most 'classic' constant property two-fluid models are solved using computational methods based on the Implicit Continuous Eulerian (ICE) method pioneered by Harlow and Amsden (1974, 1975). The implementation is based on a finite difference technique and the algorithms closely resemble the SIMPLE algorithm (Patankar and Spalding, 1972), whereby a staggered grid is employed to reduce numerical instability. A detailed discussion on the application of this numerical technique to two-fluid models for gas-fluidised beds is presented by Kuipers et al. (1993).

In principle this numerical solution method can be straight forwardly applied to 'modern' two-fluid models with closure laws according to the kinetic theory of granular flow. However, when doing so, the numerical stability of the two-fluid model is highly affected by the value of the coefficient of restitution. Problems that can be handled with acceptable time steps of 10^{-4} s for ideal particles (e_n = 1) require time steps of 10^{-5} s when the coefficient of restitution is taken to be 0.97 and unacceptably small time steps of 10^{-6} s have to be taken when the coefficient of restitution is reduced below 0.93. This extreme sensitivity to the value of the coefficient of restitution is caused by the fact that particle volume fractions at the next time level are estimated without taking into account the strong non-linear dependence of the particle pressure on the particle volume fraction. A new numerical algorithm, that which estimates the new particle volume fraction taking the compressibility of the particulate phase more directly into account, is presented in this paragraph.

3.1. Discretisation of the governing equations

The set of conservation equations, supplemented with the constitutive equations, boundary and initial conditions can not be solved analytically and a numerical method must be applied to obtain an approximate solution. Therefore the domain of interest is divided into a number of fixed Eulerian cells through which the gas-solid dispersion moves. A standard finite difference technique is applied to discretise the governing equations. The cells are labelled by indices i, j and k located at their centres and a staggered grid configuration is applied. According to this configuration the scalar variables are defined at the cell centres whereas the velocities are defined at the cell faces, as indicated in figure 2.1. Further different control volumes have to be applied for mass and granular energy conservation on the one hand and the momentum conservation equations on the other hand. The control volumes for mass and granular energy conservation coincide with the Eulerian cells, whereas the control volumes for momentum conservation in all three directions are shifted half a cell with respect to the Eulerian cells.

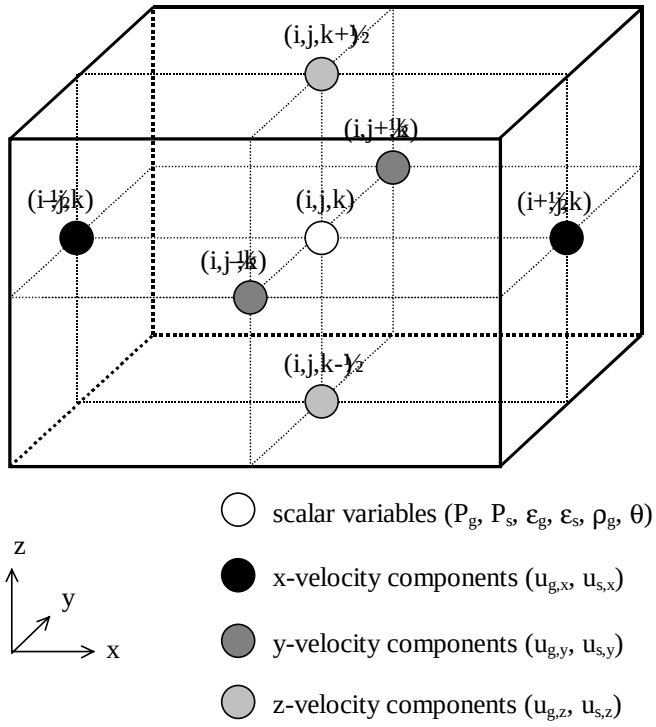

Figure 2.1. Positions at which the key variables are evaluated for a typical computational cell in the staggered grid configuration.

Applying first order time differencing and fully implicit treatment of the convective fluxes the discretised form of continuity equation for the gas phase (equation 2.1) becomes:

$$\left(\varepsilon_g \rho_g\right)_{i,j,k}^{n+1} - \left(\varepsilon_g \rho_g\right)_{i,j,k}^{n} + \frac{\delta t}{\delta x}\left\{\left\langle \varepsilon_g \rho_g u_{g,x}\right\rangle_{i+\frac{1}{2},j,k}^{n+1} - \left\langle \varepsilon_g \rho_g u_{g,x}\right\rangle_{i-\frac{1}{2},j,k}^{n+1}\right\} + \frac{\delta t}{\delta y}\left\{\left\langle \varepsilon_g \rho_g u_{g,y}\right\rangle_{i,j+\frac{1}{2},k}^{n+1} - \left\langle \varepsilon_g \rho_g u_{g,y}\right\rangle_{i,j-\frac{1}{2},k}^{n+1}\right\} + \frac{\delta t}{\delta z}\left\{\left\langle \varepsilon_g \rho_g u_{g,z}\right\rangle_{i,j,k+\frac{1}{2}}^{n+1} - \left\langle \varepsilon_g \rho_g u_{g,z}\right\rangle_{i,j,k-\frac{1}{2}}^{n+1}\right\} = 0 \qquad (2.13)$$

where n and n+1 represents the old and the new time level respectively. The solids phase continuity equation is discretised in an exactly analogue manner and can be obtained from equation 2.13 by replacing subscript g by s. For the discretisation of all convective mass, momentum and fluctuating kinetic energy fluxes the second order accurate Barton scheme (Centrella and Wilson, 1984; Hawley et al., 1984) is applied. A schematic representation of this scheme for the convective transport of a quantity D (e.g. $\varepsilon_g \rho_g$) by a velocity $V_{i+1/2}$ (e.g. $u_{g,x}$) is given in figure 2.2.

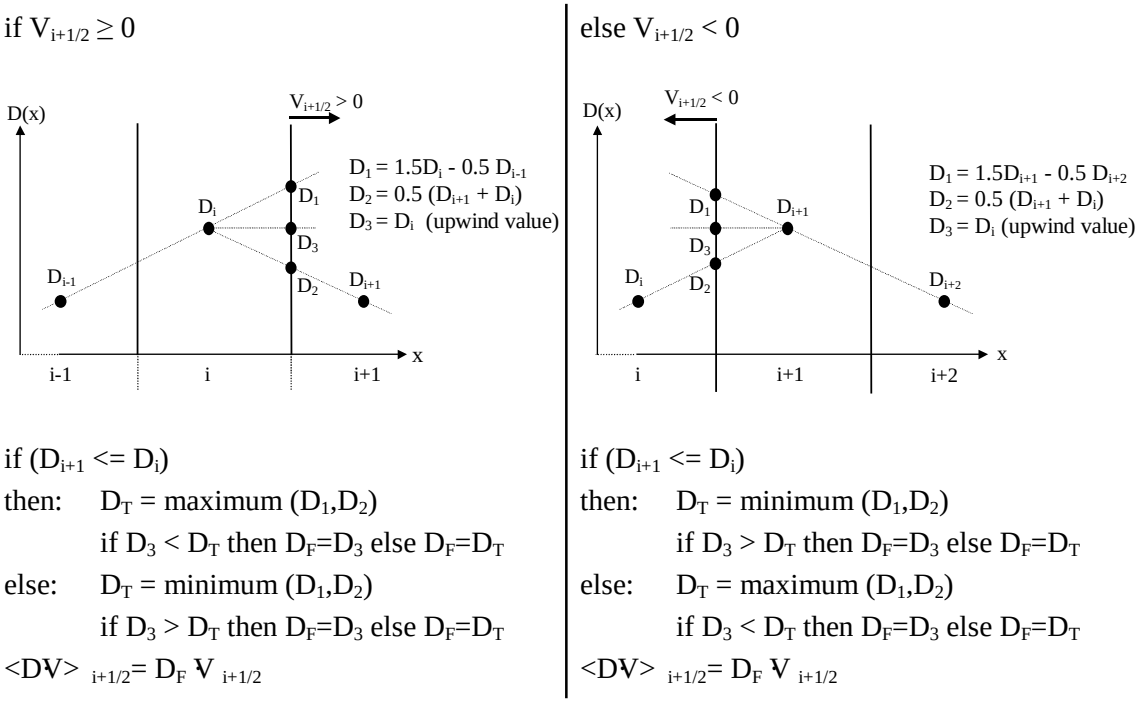

Figure 2.2. Schematic representation of the Barton scheme for the convective flux of a quantity D by velocity $V_{i+1/2}$ in the x-direction.

In the discretisation of the momentum equations the terms associated with the gas and solids pressure gradients have been treated fully implicitly. The inter-phase momentum transfer term is treated in a linear implicit fashion and all other terms are treated explicitly. The discretisation of the solids phase momentum equation for the *x*-direction is given by:

$$\begin{aligned}\left(\varepsilon_s\rho_s u_{s,x}\right)^{n+1}_{i+\frac{1}{2},j,k} = {} & A^n_{i+\frac{1}{2},j,k} - \left(\varepsilon_s\right)^{n+1}_{i+\frac{1}{2},j,k}\frac{\delta t}{\delta x}\left\{\left(P_g\right)^{n+1}_{i+1,j,k} - \left(P_g\right)^{n+1}_{i,j,k}\right\} - \frac{\delta t}{\delta x}\left\{\left(P_s\right)^{n+1}_{i+1,j,k} - \left(P_s\right)^{n+1}_{i,j,k}\right\} \\ & + \delta t\beta^n_{i+\frac{1}{2},j,k}\left(u_{g,x} - u_{s,x}\right)^{n+1}_{i+\frac{1}{2},j,k}\end{aligned} \tag{2.14}$$

where momentum convection, viscous interaction and gravity have been collected in the explicit term A^n. The solids momentum equations for the *y*- and *z*-direction are discretised in a similar manner, and given by:

$$\begin{aligned}\left(\varepsilon_s\rho_s u_{s,y}\right)^{n+1}_{i,j+\frac{1}{2},k} = {} & B^n_{i,j+\frac{1}{2},k} - \left(\varepsilon_s\right)^{n+1}_{i,j+\frac{1}{2},k}\frac{\delta t}{\delta y}\left\{\left(P_g\right)^{n+1}_{i,j+1,k} - \left(P_g\right)^{n+1}_{i,j,k}\right\} - \frac{\delta t}{\delta y}\left\{\left(P_s\right)^{n+1}_{i,j+1,k} - \left(P_s\right)^{n+1}_{i,j,k}\right\} \\ & + \delta t\beta^n_{i,j+\frac{1}{2},k}\left(u_{g,y} - u_{s,y}\right)^{n+1}_{i,j+\frac{1}{2},k}\end{aligned} \tag{2.15}$$

$$\begin{aligned}\left(\varepsilon_s\rho_s u_{s,z}\right)^{n+1}_{i,j,k+\frac{1}{2}} = {} & C^n_{i,j,k+\frac{1}{2}} - \left(\varepsilon_s\right)^{n+1}_{i,j,k+\frac{1}{2}}\frac{\delta t}{\delta z}\left\{\left(P_g\right)^{n+1}_{i,j,k+1} - \left(P_g\right)^{n+1}_{i,j,k}\right\} - \frac{\delta t}{\delta z}\left\{\left(P_s\right)^{n+1}_{i,j,k+1} - \left(P_s\right)^{n+1}_{i,j,k}\right\} \\ & + \delta t\beta^n_{i,j,k+\frac{1}{2}}\left(u_{g,z} - u_{s,z}\right)^{n+1}_{i,j,k+\frac{1}{2}}\end{aligned} \tag{2.16}$$

The momentum equations for the gas-phase can simply be obtained from these equations by replacing the subscripts *s* by *g* and dropping the terms concerning the particle pressure gradient.

The granular energy equation is solved in a fully implicit manner. The solution of the equation however proceeds through a separate iterative procedure that solves the granular temperature equations for the whole computational domain when this is required by the main solution procedure discussed in the next paragraph. In this separate iterative procedure the terms regarding convective transport and generation of fluctuating kinetic energy by viscous shear are explicitly expressed in terms of the most recently obtained granular temperature θ^*. The granular energy dissipation term is treated in a semi-implicit manner whereas all other terms are treated fully implicitly. The applied discretisation of the granular temperature equation is given by:

$$
\begin{aligned}
\frac{3}{2}\left(\varepsilon_s\rho_s\theta\right)_{i,j,k}^{n+1} = \frac{3}{2}\left(\varepsilon_s\rho_s\theta\right)_{i,j}^{n} + D_{i,j,k}^{*} - \delta t\left(P_s\right)_{i,j,k}^{n+1}\Bigg[& \frac{1}{\delta x}\left\{\left(u_{s,x}\right)_{i+\frac{1}{2},j,k}^{*} - \left(u_{s,x}\right)_{i-\frac{1}{2},j,k}^{*}\right\} \\
& + \frac{1}{\delta y}\left\{\left(u_{s,y}\right)_{i,j+\frac{1}{2},k}^{*} - \left(u_{k,y}\right)_{i,j-\frac{1}{2},k}^{*}\right\} + \frac{1}{\delta z}\left\{\left(u_{s,z}\right)_{i,j,k+\frac{1}{2}}^{*} - \left(u_{k,y}\right)_{i,j,k-\frac{1}{2}}^{*}\right\}\Bigg] \\
& + \frac{\delta t}{\delta x}\left\{\left(\varepsilon_s\kappa_s\right)_{i+\frac{1}{2},j,k}^{*}\frac{1}{\delta x}\left\{\theta_{i+1,j,k}^{n+1} - \theta_{i,j,k}^{n+1}\right\} - \left(\varepsilon_s\kappa_s\right)_{i-\frac{1}{2},j,k}^{*}\frac{1}{\delta x}\left\{\theta_{i,j,k}^{n+1} - \theta_{i-1,j,k}^{n+1}\right\}\right\} \\
& + \frac{\delta t}{\delta y}\left\{\left(\varepsilon_s\kappa_s\right)_{i,j+\frac{1}{2},k}^{*}\frac{1}{\delta y}\left\{\theta_{i,j+1,k}^{n+1} - \theta_{i,j,k}^{n+1}\right\} - \left(\varepsilon_s\kappa_s\right)_{i,j-\frac{1}{2},k}^{*}\frac{1}{\delta y}\left\{\theta_{i,j,k}^{n+1} - \theta_{i,j-1,k}^{n+1}\right\}\right\} \\
& + \frac{\delta t}{\delta z}\left\{\left(\varepsilon_s\kappa_s\right)_{i,j,k+\frac{1}{2}}^{*}\frac{1}{\delta z}\left\{\theta_{i,j,k+1}^{n+1} - \theta_{i,j,k}^{n+1}\right\} - \left(\varepsilon_s\kappa_s\right)_{i,j,k-\frac{1}{2}}^{*}\frac{1}{\delta z}\left\{\theta_{i,j,k}^{n+1} - \theta_{i,j,k-1}^{n+1}\right\}\right\} \\
& - \delta t 3\beta_{i,j,k}^{n}\theta_{i,j,k}^{n+1} - \delta t\left(\frac{\gamma_k}{\theta}\right)_{i,j,k}^{*}\theta_{i,j,k}^{n+1}
\end{aligned}
\tag{2.17}
$$

In this equation the superscript * indicates that a term is computed based upon the most recent information, which complies with the $(n+1)^{\text{th}}$ time level when all iterative loops have converged. Further the convective transport and the viscous generation of fluctuating kinetic energy have been collected in the explicit term D^*. The iterative solution procedure for the granular energy equations continuous until the convergence criteria

$$
\theta_{i,j,k}^{n+1} - \theta_{i,j,k}^{*} < eps_{\theta}\cdot\theta_{i,j,k}^{n+1} \tag{2.18}
$$

are simultaneously satisfied for all cells within the computational domain. For a typical value of $eps_{\theta} = 10^{-6}$ this takes only a couple of iterations per time step.

3.2. Solution procedure of the finite difference equations

The numerical solution of the discretised model equations evolves through a sequence of computational cycles, or time steps, each of duration δt. For each computational cycle the advanced $(n+1)$-level values at time $t + \delta t$ of all key variables have to be calculated through the entire computational domain. This calculation requires the old n-level values at time t, which are known from either the previous computational cycle or the specified initial conditions. Then each computational cycle consists of two distinct phases:

1. calculation of the explicit terms A^n, B^n and C^n in the momentum equations for all interior cells,
2. implicit determination of the pressure, volume fraction and granular temperature distributions throughout the computational domain with an iterative procedure.

The implicit phase consists of several steps. The first step in involves the calculation of the mass residuals $(D_g)_{i,j,k}$ and $(D_s)_{i,j,k}$ from the continuity equations, for all interior cells:

$$\begin{aligned}(D_g)^*_{i,j,k} = &\left(\varepsilon_g\rho_g\right)^*_{i,j,k} - \left(\varepsilon_g\rho_g\right)^n_{i,j,k} + \frac{\delta t}{\delta x}\left\{\left\langle\varepsilon_g\rho_g u_{g,x}\right\rangle^*_{i+\frac{1}{2},j,k} - \left\langle\varepsilon_g\rho_g u_{g,x}\right\rangle^*_{i-\frac{1}{2},j,k}\right\} \\ &+ \frac{\delta t}{\delta y}\left\{\left\langle\varepsilon_g\rho_g u_{g,y}\right\rangle^*_{i,j+\frac{1}{2},k} - \left\langle\varepsilon_g\rho_g u_{g,y}\right\rangle^*_{i,j-\frac{1}{2},k}\right\} + \frac{\delta t}{\delta z}\left\{\left\langle\varepsilon_g\rho_g u_{g,z}\right\rangle^*_{i,j,k+\frac{1}{2}} - \left\langle\varepsilon_g\rho_g u_{g,z}\right\rangle^*_{i,j,k-\frac{1}{2}}\right\}\end{aligned} \tag{2.19}$$

$$\begin{aligned}(D_s)^*_{i,j,k} = &\left(\varepsilon_s\rho_s\right)^*_{i,j,k} - \left(\varepsilon_s\rho_s\right)^n_{i,j,k} + \frac{\delta t}{\delta x}\left\{\left\langle\varepsilon_s\rho_s u_{s,x}\right\rangle^*_{i+\frac{1}{2},j,k} - \left\langle\varepsilon_s\rho_s u_{s,x}\right\rangle^*_{i-\frac{1}{2},j,k}\right\} \\ &+ \frac{\delta t}{\delta y}\left\{\left\langle\varepsilon_s\rho_s u_{s,y}\right\rangle^*_{i,j+\frac{1}{2},k} - \left\langle\varepsilon_s\rho_s u_{s,y}\right\rangle^*_{i,j-\frac{1}{2},k}\right\} + \frac{\delta t}{\delta z}\left\{\left\langle\varepsilon_s\rho_s u_{s,z}\right\rangle^*_{i,j,k+\frac{1}{2}} - \left\langle\varepsilon_s\rho_s u_{s,z}\right\rangle^*_{i,j,k-\frac{1}{2}}\right\}\end{aligned} \tag{2.20}$$

If the convergence criteria

$$(D_g)^*_{i,j,k} < eps_g \cdot (\varepsilon_g\rho_g)^*_{i,j,k} \tag{2.21}$$

$$(D_s)^*_{i,j,k} < eps_s \cdot (\varepsilon_s\rho_s)^*_{i,j,k} \tag{2.22}$$

are not satisfied for all computational cells (typically $eps_g = eps_s = 10^{-6}$), a whole field pressure correction is calculated, satisfying:

$$\begin{aligned}&(J_g)^n_{i-1,j,k}(\delta P_g)_{i-1,j,k} + (J_g)^n_{i+1,j,k}(\delta P_g)_{i+1,j,k} + (J_g)^n_{i,j-1,k}(\delta P_g)_{i,j-1,k} + (J_g)^n_{i,j+1,k}(\delta P_g)_{i,j+1,k} \\ &+ (J_g)^n_{i,j,k-1}(\delta P_g)_{i,j,k-1} + (J_g)^n_{i,j,k+1}(\delta P_g)_{i,j,k+1} + (J_g)^n_{i,j,k}(\delta P_g)_{i,j,k} = -(D_g)^*_{i,j,k}\end{aligned} \tag{2.23}$$

where J^n_g represents the Jacobi matrix for the gas phase. This matrix contains the derivatives of the defects D_g with respect to the gas phase pressure, for which explicit expressions can be obtained from the continuity equation for the gas phase in combination with the momentum equations. To save computational effort the elements of the Jacobi matrix are evaluated at the old time level. The banded matrix problem corresponding to equation 2.23 is solved using a standard ICCG sparse matrix technique. Once new pressures have been obtained, the corresponding new gas phase densities are calculated.

So far the new solution procedure has been exactly the same as the SIMPLE procedure that is usually applied for the solution of the 'classic' two-fluid models with constant property closure equations. In the next step however, the older procedures continue with the computation of new velocities from the coupled momentum equations, where after new volume fractions are obtained from the solids phase mass balances. Only then the new solids pressures are determined, which regularly leads to excessive compaction and extremely high particle pressures in areas where the particle packing densities are close to random close packing. Therefore the new solution procedure computes the particle volume fractions, taking the compressibility of the solids phase more directly into account. Similar to the pressure correction for the gas phase, a whole field particle volume fraction correction is computed, satisfying:

$$\begin{aligned}(J_s)^n_{i-1,j,k}(\delta\varepsilon_s)_{i-1,j,k} + (J_s)^n_{i+1,j,k}(\delta\varepsilon_s)_{i+1,j,k} + (J_s)^n_{i,j-1,k}(\delta\varepsilon_s)_{i,j-1,k} + (J_s)^n_{i,j+1,k}(\delta\varepsilon_s)_{i,j+1,k} \\ + (J_s)^n_{i,j,k-1}(\delta\varepsilon_s)_{i,j,k-1} + (J_s)^n_{i,j,k+1}(\delta\varepsilon_s)_{i,j,k+1} + (J_s)^n_{i,j,k}(\delta\varepsilon_s)_{i,j,k} = -(D_s)^*_{i,j,k}\end{aligned} \tag{2.24}$$

In this equation J^n_s is the Jacobi matrix for the solids phase, which contains the derivatives of the mass residuals for the particulate phase to the solids volume fraction. Explicit expressions for the elements of the Jacobi matrix can be obtained from the continuity for the solids phase and the momentum equations. For example, for the central element the following expression is obtained from the solids phase continuity equation, in which the convective terms are evaluated with central finite difference expressions:

$$\begin{aligned}(J^n_s)_{i,j,k} = \frac{\partial(D_s)^*_{i,j,k}}{\partial(\varepsilon_s)^*_{i,j,k}} = (\rho_s)^*_{i,j,k} + \frac{\delta t}{\delta x}\left\{\frac{\partial\left(\varepsilon_s\rho_s u_{s,x}\right)^*_{i+\frac{1}{2},j,k}}{\partial(\varepsilon_s)^*_{i,j,k}} - \frac{\partial\left(\varepsilon_s\rho_s u_{s,x}\right)^*_{i-\frac{1}{2},j,k}}{\partial(\varepsilon_s)^*_{i,j,k}}\right\} \\ + \frac{\delta t}{\delta y}\left\{\frac{\partial\left(\varepsilon_s\rho_s u_{s,y}\right)^*_{i,j+\frac{1}{2},k}}{\partial(\varepsilon_s)^*_{i,j,k}} - \frac{\partial\left(\varepsilon_s\rho_s u_{s,y}\right)^*_{i,j-\frac{1}{2},k}}{\partial(\varepsilon_s)^*_{i,j,k}}\right\} + \frac{\delta t}{\delta z}\left\{\frac{\partial\left(\varepsilon_s\rho_s u_{s,z}\right)^*_{i,j,k+\frac{1}{2}}}{\partial(\varepsilon_s)^*_{i,j,k}} - \frac{\partial\left(\varepsilon_s\rho_s u_{s,z}\right)^*_{i,j,k-\frac{1}{2}}}{\partial(\varepsilon_s)^*_{i,j,k}}\right\}\end{aligned} \tag{2.25}$$

The derivatives of the mass fluxes to the solids volume fractions can subsequently be obtained from the solids phase momentum equations. From equation 2.14, the discretised *x*-momentum equation, the derivatives of the mass fluxes in the *x*-direction can easily be obtained, e.g.:

$$\frac{\partial\left(\varepsilon_s \rho_s u_{s,x}\right)^*_{i+\frac{1}{2},j,k}}{\partial\left(\varepsilon_s\right)^*_{i,j,k}} = -\frac{1}{2}\frac{\delta t}{\delta x}\left\{\left(P_g\right)^*_{i+1,j,k} - \left(P_g\right)^*_{i,j,k}\right\} + \frac{\delta t}{\delta x}\left(\frac{\partial P_s}{\partial \varepsilon_s}\right)^*_{i,j,k} + \delta t \beta^n_{i+\frac{1}{2},j,k} \frac{\partial\left(u_{g,x} - u_{s,x}\right)^*_{i+\frac{1}{2},j,k}}{\partial\left(\varepsilon_s\right)^*_{i,j,k}} \tag{2.26}$$

The second term on the right hand side of this equation shows that the compressibility of the solids phase is taken directly into account in the estimation of the new particle volume fractions. Further the expression for the derivatives of the velocities to the solids pressure can be obtained by combination with the *x*-momentum equation for the gas phase, which taking the derivative to the solids volume fraction results in:

$$\frac{\partial\left(\varepsilon_g \rho_g u_{g,x}\right)^*_{i+\frac{1}{2},j,k}}{\partial\left(\varepsilon_s\right)^*_{i,j,k}} = \frac{1}{2}\frac{\delta t}{\delta x}\left\{\left(P_g\right)^*_{i+1,j,k} - \left(P_g\right)^*_{i,j,k}\right\} - \delta t \beta^n_{i+\frac{1}{2},j,k} \frac{\partial\left(u_{g,x} - u_{s,x}\right)^*_{i+\frac{1}{2},j,k}}{\partial\left(\varepsilon_s\right)^*_{i,j,k}} \tag{2.27}$$

Together with equation 2.24 this equation forms a set of equations from which explicit expressions for the derivatives of the velocities can readily be obtained. Expressions for the *y*- and *z*-direction and for the other elements of the Jacobi matrix are obtained in a similar manner.

After the new solids volume fractions have been obtained from equation 2.24, new particle pressures are calculated where after new velocities can obtained from the coupled momentum equations. Next, new granular temperatures are calculated from the granular energy equations by an iterative procedure described in the previous section. Finally the new mass residuals $(D_g)_{i,j,k}$ and $(D_s)_{i,j,k}$ are computed and the convergence criteria are checked again.

Though this new algorithm still requires some time step refinement for computations with highly inelastic particles, the computations presented in this chapter could all be carried out with acceptable time steps of 10^{-5} s or larger. An alternative numerical method that is also based on the compressibility of the dispersed particulate phase is presented by Laux (1998). In this so-called compressible disperse phase method the shear stresses in the momentum equations are implicitly taken into account, which further enhances the stability of the code in the quasi-static state near minimum fluidisation, especially when frictional shear is taken into account. In theory the stability of the numerical solution method can be further enhanced by fully implicit dicretisation and simultaneous solution of all governing equations. This latter is however not expected to results in faster solution of the two-fluid model equations, since the numerical efforts per time step increase.

4. Effect of coefficient of restitution on bed dynamics

4.1. Simulation conditions

To study the influence of the coefficient of restitution on the hydrodynamics of a mono-disperse powder in a dense gas-fluidised bed, a number of two-dimensional two-fluid simulations with various values for the coefficient of restitution have been performed. The obtained results will be compared to experimental results obtained in a pseudo two-dimensional setup. The experimental conditions and simulation settings are specified in table 2.2.

The collision properties of the particles used in the experiment were obtained from detailed impact measurements performed by the Impact Research Group of the Open University at Milton Keynes, where an accurate technique to measure collision parameters has been developed (Kharaz et al., 1999). The measured collision parameters are presented in table 2.3. A detailed discussion on their physical meaning can be found in chapter 3 (paragraph 2.2), where the three-parameter collision model from which they originate is discussed.

Table 2.2. Experimental conditions and simulation settings for two-fluid simulations.

Height of experimental setup	70.0	cm	Freeboard pressure	101325.0 Pa
Width of experimental setup	15.0	cm	Temperature	293 K
Depth of experimental setup	1.50	cm	Gas phase shear viscosity, μ_g	1.810^{-5} Pas
			Gas phase bulk viscosity, λ_g	0.0 Pas
Initial bed height	15.0	cm		
Fluidisation velocity	1.38	m/s	Particle diameter, d_p	1.50 mm
Horizontal grid size, δx	5.0	mm	Particle density, ρ_s	2523 kg/m^3
Vertical grid size, δz	5.0	mm	Particle shape factor, ϕ_s	1
Number of cells in horizontal direction	30		Minimum fluidisation velocity, U_{mf}	0.92 m/s
Number of cells in vertical direction	90		Minimum fluidisation porosity, ε_{mf}	0.417

Table 2.3. Particle collision properties (measured by Gorham and Kharaz, 1999).

	Particle-particle collisions	*Particle-wall collisions*
Coefficient of normal restitution	$e_n = 0.97 \pm 0.01$	$e_{n,wall} = 0.97 \pm 0.01$
Coefficient of friction	$\mu = 0.15 \pm 0.015$	$\mu_{wall} = 0.10 \pm 0.01$
Coefficient of tangential restitution	$\beta_0 = 0.33 \pm 0.05$	$\beta_{0,wall} = 0.33 \pm 0.05$

All simulations have been performed with non-slip boundary conditions for the gas phase, whereas the partial slip boundary conditions that are applied to the particulate phase are given by (Sinclair and Jackson, 1989):

$$(\bar{\bar{I}} - \bar{n}\bar{n}) \cdot \varepsilon_s \bar{\bar{\tau}}_s \cdot \bar{n} = \frac{\alpha_{wall} \pi \varepsilon_s \rho_s g_0 \sqrt{\theta}}{2\sqrt{3}\varepsilon_0} \bar{u}_s \tag{33}$$

$$\varepsilon_s \bar{q}_s \cdot \bar{n} = -\bar{u}_s \cdot \varepsilon_s \bar{\bar{\tau}}_s \cdot \bar{n} + \frac{\sqrt{3}\pi (1 - e_{n,wall}^2) \varepsilon_s \rho_s g_0 \sqrt{\theta}}{4\varepsilon_0} \theta \tag{34}$$

Thus, particle-wall interactions are described by the coefficient of restitution ($e_{n,wall}$) and a specularity coefficient (α_{wall}). For the first coefficient the measured value for the coefficient of normal restitution is applied, whereas the specularity coefficient is set to zero (impact of perfect sphere on flat wall), since it can not directly be related to the measured coefficients of friction and tangential restitution (Jenkins, 1992).

In all simulations the minimum fluidisation condition was used as initial condition, where after the gas inflow velocity was stepwise set to 1.5 U_{mf}. Small perturbations were applied to the initial particle volume fraction and the gas inflow velocity at the bottom, to improve resemblance with experimental conditions and avoid unrealistic start up behaviour due to perfect symmetry of the numerical solution. Grid refinement was studied, but the grid size did not have a significant influence on the obtained results.

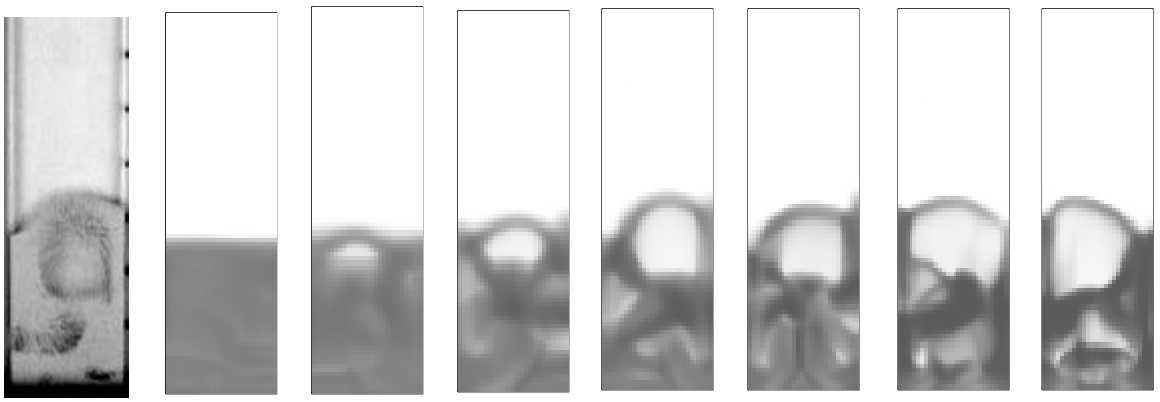

Figure 2.3. Snapshot of an experiment and simulations at the moment of bubble eruption at the bed surface for various values of the coefficient of restitution.

4.2. Simulation results

Figure 2.3 shows some snapshots of the experiment and simulations for various values of the coefficient of restitution at the moment of bubble eruption at the bed surface. It can be seen from this figure that as collisions become less ideal (and more energy is dissipated due to inelastic collisions) particles become closer packed in the densest regions of the bed, resulting in sharper porosity contours and larger bubbles. In simulations with ideal particles bubble formation did not appear for fluidisation velocities below 3 U_{mf}.

To gain more insight into the influence of the coefficient of restitution on bed dynamics, a detailed study of the contribution all sources and sinks of fluctuating kinetic energy in the pseudo-thermal energy equation has been performed. Therefore the bed and time averaged contributions of all sources and sinks in the fluctuating kinetic energy equation have been calculated. The average contribution of particle pressure is for example obtained from:

$$< P_s \bar{\bar{I}} : \nabla \bar{u}_s >= \frac{1}{t_{max} - t_{min}} \frac{1}{nx \cdot nz} \int_{t_{min}}^{t_{max}} \sum_{i=1}^{nx} \sum_{k=1}^{nz} \left(P_s \nabla \cdot \bar{u}_s \right)_{i,k} dt \qquad (2.28)$$

For the calculation of these averages the initial 2 seconds of the simulations where not taken into account (t_{min} = 2 s) in order to avoid start-up effects from influencing the results, whereas the simulations were run for 20 seconds (t_{max} = 20 s). The average production of fluctuating kinetic energy due to particle pressure and viscous shear and dissipation due to inelastic collisions and gas-particle drag are shown in figure 2.4. The contribution due to net conduction to the system walls was so small that it has not been taken into account in this figure.

Besides the contributions of the sources and sinks in the granular temperature equation, the weighted averages of the particle phase state variables, granular temperature and particle pressure, and the rheologic properties have also been calculated to gain some feeling for their dependence on the coefficient of restitution. The average granular temperature for example has been obtained from:

$$< \theta >= \frac{1}{t_{max} - t_{min}} \frac{1}{\sum_{i=1}^{nx} \sum_{k=1}^{nz} (\varepsilon_s)_{i,k}} \int_{t_{min}}^{t_{max}} \sum_{i=1}^{nx} \sum_{k=1}^{nz} (\varepsilon_s)_{i,k} \theta_{i,k} dt \qquad (2.29)$$

The results are presented in figures 2.5 and 2.6.

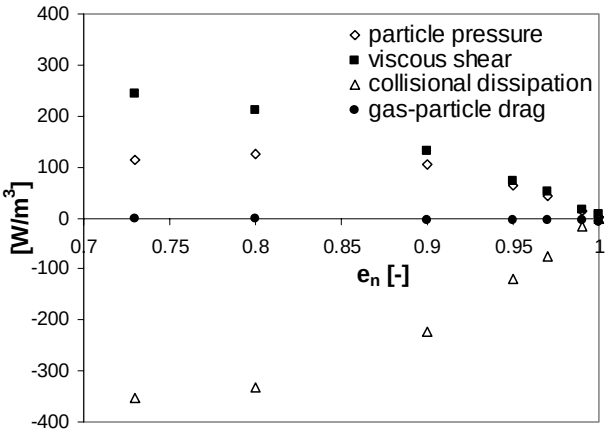

Figure 2.4. Average contribution of sources and sinks in the pseudo-thermal energy equation as a function of the coefficient of restitution.

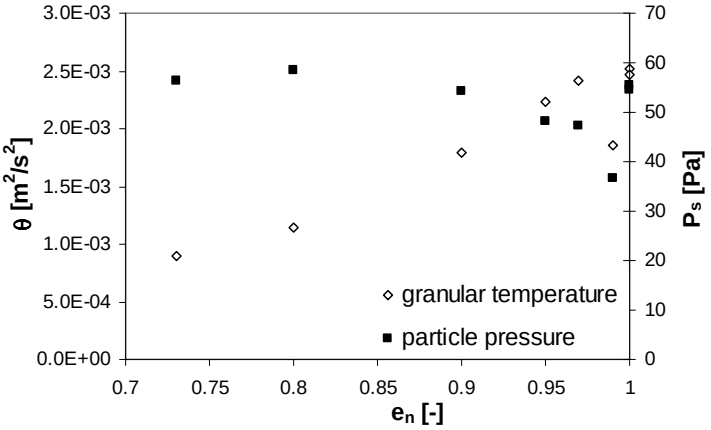

Figure 2.5. Average state variables for the particulate phase as a function of the coefficient of restitution.

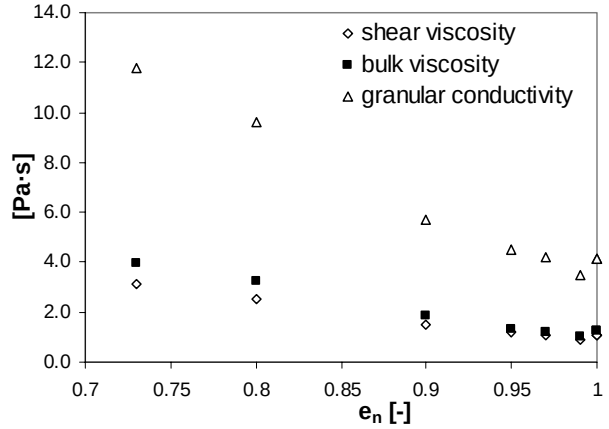

Figure. 2.6. Average solids viscosity and conductivity as a function of the coefficient of restitution.

It can be seen from figure 2.4 that as the coefficient of restitution decreases and particle interactions become less ideal, more fluctuating kinetic energy is generated by particle pressure and viscous shear. This energy is almost completely dissipated by deformation of particles upon inelastic collision, while dissipation by gas-particle drag hardly contributes.

Figure 2.5 shows that the granular temperature decreases as particle interactions become less ideal, even though figure 2.4. indicates that the energy production rates increase. The particle pressure remains relatively constant within the investigated range of the coefficient of restitution. From figure 2.6 it can be concluded that the fluidised particle mixture becomes more viscous if the coefficient of restitution decreases. Further the average shear viscosity is in good agreement with measured values of 0.1-2.6 Pas (Schügerl et al., 1961; Stewart, 1968; Grace, 1970).

To show the effect of the coefficient of restitution on bed dynamics the computed instantaneous pressure drop over the bed is presented in figure 2.7 for three simulations. It can be seen that the intensity of the pressure fluctuations strongly depends on the coefficient of restitution. The more energy is dissipated in non-ideal particle collisions the stronger the pressure drop fluctuations are (i.e. more vigorous bubbling is observed).

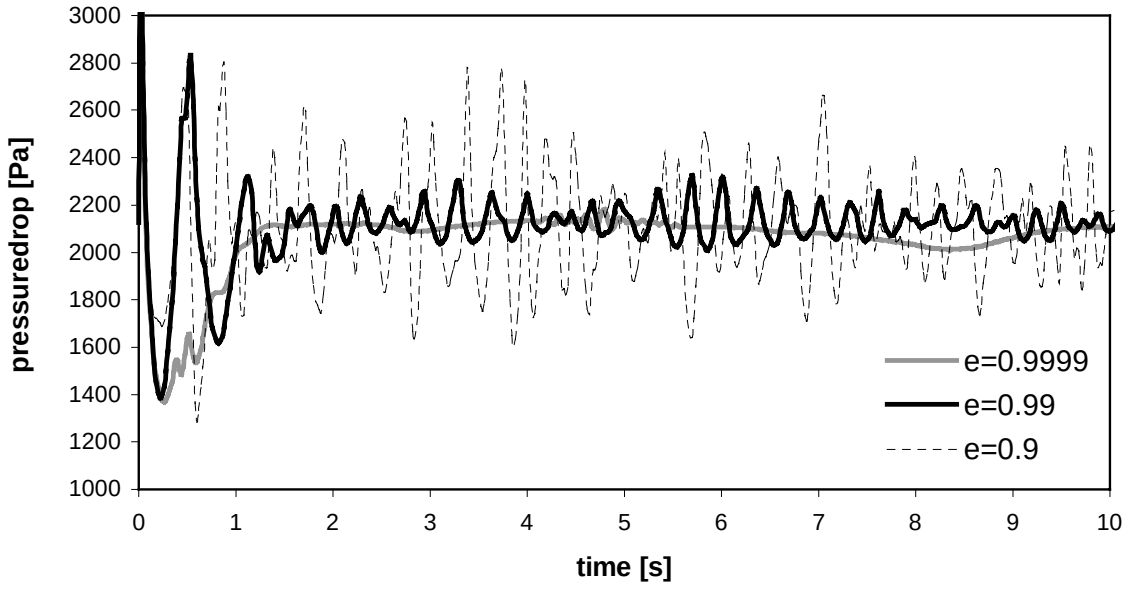

Figure 2.7. Pressure drop fluctuations over the bed for various values of the coefficient of restitution.

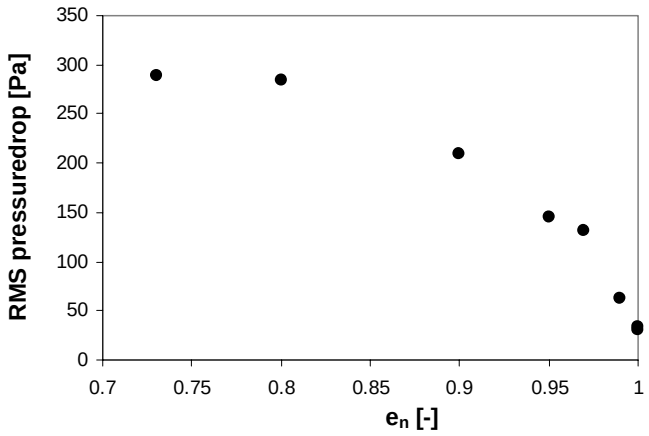

Figure 2.8. Root Mean Square (RMS) of the pressure drop fluctuations over the bed as a function of coefficient of restitution.

Figure 2.8 shows the root mean square of the pressure fluctuations as a function of the coefficient of restitution (the initial 2 seconds of the simulations were again not taken into account). From this figure it can be seen that the intensity of pressure fluctuations decreases gradually when the coefficient of restitution approaches 1 and the model does not show any extreme sensitivity with respect to the coefficient of restitution.

Finally it can be observed from figure 2.3 that the snapshot taken from the simulation with coefficient of normal restitution equal to the measured value of 0.97 does not show the best resemblance with the experimental bubble pattern. From video recordings of the experiment and animations of the simulations it can be observed that the resemblance between experiment and simulations is the best for e_n =0.9. This difference between the experimental results and the simulations can be explained from the fact that the total energy dissipation during a collision results from inelastic deformation as well as from frictional slip (Johnson, 1985). Hence the kinetic theory model underestimates the total amount of energy dissipated in particle collisions. However, it was demonstrated in this chapter that correct prediction of the amount of energy dissipated in collisions is of prime importance in order to obtain the correct bed dynamics from fundamental hydrodynamic models. Therefore more attention will be paid to this topic in the next two chapters.

Discussion and conclusions

It is demonstrated that hydrodynamics of dense gas-fluidised beds strongly depend on the amount of energy dissipated in particle-particle encounters. Due to the tendency of inelastic particles to contract in high-density clusters and the strong non-linear dependence of the particle pressure on the solids volume fraction, the numerical stability of classical multi-phase versions of the SIMPLE algorithm is adversely affected. Therefore a modified SIMPLE algorithm that takes the compressibility of the suspended particulate phase more directly into account has been presented.

A strong increase in bubble formation and consequent pressure drop fluctuations is observed when the amount of energy dissipated in collisions increases. These results are consistent with results obtained from more detailed discrete particle simulations by Hoomans et al. (1996, 1998a). Since bubbles dominate the hydrodynamic behaviour of dense gas-fluidised beds it is concluded that, in order to obtain realistic fluidised bed dynamics from fundamental hydrodynamic models, it is of prime importance to correctly take the effect of energy dissipation due to non-ideal particle interactions into account. Further, there is a great need for experiments with well-defined experimental systems to validate these fundamental hydrodynamic models. These experiments should be carried out in beds with a well-defined geometry and accurately controlled gas inflow conditions. Besides the particle density, size and shape, also all particle collision parameters should be accurately known.

Chapter 3.

Comparison and validation of a 3D hard-sphere discrete particle model and a two-fluid continuum model

Abstract

A critical comparison of a hard-sphere discrete particle model, the two-fluid model presented in chapter 2 and experiments performed in a pseudo two-dimensional gas-fluidised bed is made. Bubble patterns, time-averaged particle distributions and bed expansion dynamics measured with a non-intrusive digital image analysis technique are compared to simulation results obtained at three different fluidisation velocities. For both models the simulated flow fields and granular temperature profiles are compared. The effects of grid refinement, particle-wall interaction, long-term particle contacts, particle rotation and gas-particle drag are studied. The mechanical energy balance for the suspended particles is introduced and the energy household for both models is compared.

The most critical comparison between experiments and model results is given by analysis of the bed expansion dynamics. Though both models predict the right fluidisation regime and trends in bubble sizes and bed expansion, the predicted bed expansion dynamics differ significantly from the experimental results. Alternative gas-particle drag models result in significantly different bed dynamics, but the gap between model and experimental results can not be closed.

In comparison with the experimental results the discrete particle model gives superior resemblance. The main difference between both models is caused by the neglect of particle rotation in the kinetic theory closure equations embedded in the two-fluid model. Energy balance analysis demonstrates that over 80% of the total energy is dissipated by sliding friction. Introduction of an effective restitution coefficient that incorporates the additional dissipation due to frictional interactions significantly improves the agreement between both models.

This chapter is based on the paper:

Goldschmidt M.J.V., Beetstra R., Kuipers J.A.M., 2001, Hydrodynamic modelling of dense gas-fluidised beds: Comparison of 3D discrete particle and continuum models, submitted to *Powder Technol.*

1. Introduction

Thanks to the enormous increase in computer power and algorithm development fundamental hydrodynamic modelling of multi-phase reactors has recently come within reach. In the last decade significant research efforts have been made to develop detailed micro balance models to study the complex hydrodynamics of gas-fluidised beds (Gidaspow, 1994; Simonin, 1996; Enwald et al., 1996; Kuipers and van Swaaij, 1998; Goldschmidt et al., 2000). Broadly speaking two different types of hydrodynamic models can be distinguished, Eulerian (continuum) models and Lagrangian (discrete element) models. Both consider the gas phase as a continuum. The flow fields at sub-particle level are not resolved and empirical equations are applied for fluid-particle drag. Owing to the continuum description of the particulate suspension, Eulerian models require additional closure laws to describe particle-particle and/or particle-wall interactions. In most recent continuum models constitutive relations according to the kinetic theory of granular flow are incorporated. This theory is basically an extension of the classical kinetic theory of gases (Chapman and Cowling, 1970) to dense particulate flows, that takes non-ideal particle-particle collisions and gas-particle drag into account. Discrete particle models on the other hand do not require additional closure equations for the suspended particulate phase since they compute the motion of every individual particle, taking collisions and external forces acting on the particles directly into account. However, the number of particles that these models can handle (i.e. typically less than 10^6) is orders of magnitude lower than that encountered in most (industrial) fluidised beds. Therefore continuum models constitute a more natural choice for hydrodynamic modelling of engineering scale systems, whereas discrete particle models can be applied as a valuable research tool to verify and further develop closure laws for these continuum models.

Since discrete element models describe particulate motion in more detail, it is expected that these models show closer resemblance with experimental results. However, a direct comparison between both types of models and experiments has not been made so far. This is mainly because of the large number of particles that is required to justify the application of the continuum approach on one hand and the limited number of particles that can be handled by discrete element models on the other hand. Further complications arise from the fact that a rigorous comparison can only be made if the discrete element model accounts for the full three-dimensional motion of the particles, since two-dimensional modelling of the collision dynamics is too restrictive (Hoomans, 2000a). This strongly increases the required number of particles and consequently computational

demands. Then there is still the lack of detailed experimental data that has to be coped with. As discussed in chapter 2, both types of fundamental models have revealed a great sensitivity of the overall bed dynamics to the particle collision parameters. Despite the fact that a number of research groups are capable of measuring collision parameters (Foerster et al., 1994; Bernasconi et al., 1997; Labous et al., 1997; Kharaz et al., 1999), they are unfortunately scarcely reported for fluidisation experiments in the literature.

To overcome the lack of suitable experimental data, experiments with relatively large glass beads, for which the collision parameters were accurately measured, were performed in a laboratory scale fluidised bed. A digital image analysis technique was developed to non-intrusively study the bed dynamics of mono-disperse and binary systems. The experimental technique and the obtained data are discussed in more detail in chapter 6.

This chapter focuses on the comparison between experimental results and simulations. Experiments performed with approximately 24750 glass beads at three different fluidisation velocities are compared to simulation results obtained with a hard-sphere discrete particle model and a two-fluid continuum model with closures according to the kinetic theory of granular flow. The differences between both models will be discussed and a particle phase energy analysis will be presented for both types of model. In the next chapter the more detailed discrete particle model is applied to check the validity of several important assumptions that are made during the derivation of the closure equations according to the kinetic theory of granular flow.

2. Hard-sphere discrete particle model

As far as discrete particle models are concerned a distinction can be made between soft-sphere and hard-sphere models. In soft-sphere models (Tsuji et al., 1993) the particles are assumed to undergo deformation during their contact where the contact forces are calculated from a simple mechanical analogy involving a spring, a dash pot and a slider. These models are also referred to as time driven models since all particles are moved over a certain period of time where after the collision dynamics are computed from the particle overlaps. In case a particle is in contact with several other particles the resulting contact force follows from the addition of binary contributions.

In the hard-sphere models (Hoomans, 1996) rigid particles are assumed to interact through binary, quasi-instantaneous collisions. Particle collision dynamics are described

by collision laws, which account for energy dissipation due to non-ideal particle interaction by means of the empirical coefficients of normal and tangential restitution and the coefficient of friction. Hard-sphere models are also referred to as event driven models since a sequence of collisions is processed in which all particles are moved until the next collision occurs. Hoomans (2000a) has compared the results of a soft-sphere model to those of the hard sphere model and found that, provided that the spring stiffness was high enough, the differences in bed dynamics between the two types of model were very small. In this thesis the hard-sphere model developed by Hoomans (1996, 2000a) is applied.

2.1. Gas phase hydrodynamics

In accordance with the two-fluid model the gas phase hydrodynamics is calculated from the volume-averaged Navier-Stokes equations:

$$\frac{\partial}{\partial t}(\varepsilon_f \rho_f) + \nabla \cdot (\varepsilon_f \rho_f \bar{u}_f) = 0 \tag{3.1}$$

$$\frac{\partial}{\partial t}(\varepsilon_f \rho_f \bar{u}_f) + \nabla \cdot (\varepsilon_f \rho_f \bar{u}_f \bar{u}_f) = -\varepsilon_f \nabla p_f - \nabla \cdot (\varepsilon_f \bar{\bar{\tau}}_f) - \bar{S}_p + \varepsilon_f \rho_f \bar{g} \tag{3.2}$$

The motion of every individual particle in the system between collisions is calculated from the Newtonian equation of motion:

$$m_p \frac{d\bar{v}_p}{dt} = -V_p \nabla p_f + \frac{V_p \beta}{1-\varepsilon_f}(\bar{u}_f - \bar{v}_p) + m_p \bar{g} \tag{3.3}$$

The same external forces as in the two-fluid model (equations 2.6 and 2.7) are acting. In the dense regime (ε_f < 0.80) the inter-phase momentum transfer coefficient is obtained from the well-know Ergun equation (Ergun, 1952):

$$\beta = 150 \frac{(1-\varepsilon_f)^2}{\varepsilon_f} \frac{\mu_f}{(\phi_s d_p)^2} + 1.75(1-\varepsilon_f) \frac{\rho_f}{\phi_s d_p} |\bar{u}_f - \bar{u}_s| \tag{3.4}$$

In more dilute regimes (ε_f > 0.80) the inter-phase momentum transfer coefficient derived from the correlation of Wen and Yu (1966) is applied:

$$\beta = \frac{3}{4} C_d (1-\varepsilon_f) \frac{\rho_f}{\phi_s d_p} \left|\bar{u}_f - \bar{u}_s\right| \varepsilon_f^{-1.65} \tag{3.5}$$

The reaction force to the drag force exerted on a particle per unit volume is included in the momentum conservation equation for the gas phase via the source term $\bar{S}_p$:

$$\bar{S}_p = \frac{1}{V} \int \sum_{k=0}^{Npart} \frac{V_{p,k}\beta}{1-\varepsilon_f} (\bar{u}_f - \bar{v}_{p,k}) \delta(\bar{r} - \bar{r}_{p,k}) \, dV \tag{3.6}$$

The δ-function ensures that the reaction force acts as a point force at the position of the particle in the system.

2.2. Collision dynamics

In the hard sphere model a sequence of binary collisions is processed one collision at a time. In the collision model it is assumed that collisions are quasi-instantaneous where contact occurs at a point and the interaction forces are impulsive. For a binary collision between two rigid spheres *a* and *b* the relative velocity at the contact point is defined as:

$$\bar{v}_{ab} = (\bar{v}_a - \bar{v}_b) - (R_a \bar{\omega}_a + R_b \bar{\omega}_b) \times \bar{n} \tag{3.7}$$

The normal and tangential unit vectors that define the collision coordinate system are given by (velocities prior to collision are indicated by subscript $_0$):

$$\bar{n} = \frac{\bar{r}_a - \bar{r}_b}{\left|\bar{r}_a - \bar{r}_b\right|} \tag{3.8}$$

$$\bar{t} = \frac{\bar{v}_{ab,0} - \bar{n}(\bar{v}_{ab,0} \cdot \bar{n})}{\left|\bar{v}_{ab,0} - \bar{n}(\bar{v}_{ab,0} \cdot \bar{n})\right|} \tag{3.9}$$

For a binary collision of two rigid spheres *a* and *b* the following equations can be derived by applying Newton's laws:

$$m_a(\bar{v}_a - \bar{v}_{a,0}) = -m_b(\bar{v}_b - \bar{v}_{b,0}) = \bar{J} \tag{3.10}$$

$$\frac{I_a}{R_a}(\bar{\omega}_a - \bar{\omega}_{a,0}) = \frac{I_b}{R_b}(\bar{\omega}_b - \bar{\omega}_{b,0}) = \bar{J} \times \bar{n} \tag{3.11}$$

These can be rearranged using $(\bar{n}\times\bar{J})\times\bar{n} = \bar{J} - \bar{n}(\bar{J}\cdot\bar{n})$ and equation 3.7 to obtain:

$$\bar{v}_{ab} - \bar{v}_{ab,0} = B_1\bar{J} - (B_1 - B_2)\bar{n}(\bar{J}\cdot\bar{n}) \tag{3.12}$$

where the coefficients B_1 and B_2 for rigid spheres ($I = \frac{2}{5}m_p R^2$) are given by:

$$B_1 = \frac{7}{2}\left(\frac{1}{m_a} + \frac{1}{m_b}\right) \tag{3.13}$$

$$B_2 = \frac{1}{m_a} + \frac{1}{m_b} \tag{3.14}$$

At this point constitutive relations are required that account for energy dissipation due to non-ideal particle interaction. Therefore a three-parameter model that is nowadays widely applied in hard-sphere discrete particle simulations (Walton, 1993; Lun and Bent, 1994) is used. This model gives a reasonably accurate description of experiments performed with real macroscopic spheres by Maw et al. (1981), Foerster et al. (1994) and Gorham and Kharaz (1999). The first collision parameter that enters the model is the coefficient of normal restitution ($0 \le e_n \le 1$):

$$\bar{v}_{ab}\cdot\bar{n} = -e_n(\bar{v}_{ab,0}\cdot\bar{n}) \tag{3.15}$$

Combining this definition with equation 3.12 leads to the following expression for the normal component of the impulse vector:

$$J_n = -(1+e_n)\frac{\bar{v}_{ab,0}\cdot\bar{n}}{B_2} \tag{3.16}$$

The amount of energy dissipated in the collision due to non-ideal normal restitution is given by the following integral over the duration of the collision:

$$E_{n,rest} = \int \bar{v}_{ab}\cdot\bar{n}\, dJ_n = \frac{(\bar{v}_{ab,0}\cdot\bar{n})^2}{2B_2}(1-e_n^2) \tag{3.17}$$

The second and the third collision parameter that enter the model are the coefficient of friction ($\mu \ge 0$) and the coefficient of tangential restitution ($0 \le \beta_0 \le 1$) defined by:

$$\left|\bar{J}\times\bar{n}\right| = -\mu(\bar{J}\cdot\bar{n}) \tag{3.18}$$

$$\bar{v}_{ab}\cdot\bar{t} = -\beta_0(\bar{v}_{ab,0}\cdot\bar{t}) \tag{3.19}$$

These two collision parameters describe the tangential component of the impact, for which two types of collisions can be distinguished that are called sticking and sliding. If the tangential component of the impact velocity is sufficiently high gross sliding occurs during the whole duration of the impact and the collision is of the sliding type. In sticking collisions, after an initial sliding phase, the relative tangential velocity between the two colliding particles becomes zero during the impact, where after inversion of the relative tangential velocity takes place. The criterion to determine the type of collision is:

$$\mu < \frac{(1+\beta_0)\bar{v}_{ab.0}\cdot\bar{t}}{J_n B_1} \quad \text{sliding collision} \tag{3.20}$$

$$\mu \geq \frac{(1+\beta_0)\bar{v}_{ab.0}\cdot\bar{t}}{J_n B_1} \quad \text{sticking collision} \tag{3.21}$$

For each type of collision the tangential impulse is given by:

$$J_{t,sliding} = -\mu J_n \tag{3.22}$$

$$J_{t,sticking} = -(1+\beta_0)\frac{\bar{v}_{ab,0}\cdot\bar{t}}{B_1} \tag{3.23}$$

The amount of energy dissipated by the tangential component of the collision is given by:

$$E_{t,sliding} = \int \bar{v}_{ab}\cdot\bar{t}\, dJ_{t,sliding} = \mu J_n(\bar{v}_{ab,0}\cdot\bar{t} - \frac{1}{2}\mu B_1 J_n) \tag{3.24}$$

$$E_{t,sticking} = \int \bar{v}_{ab}\cdot\bar{t}\, dJ_{t,sticking} = \frac{(\bar{v}_{ab,0}\cdot\bar{t})^2}{2B_1}(1-\beta_0^2) \tag{3.25}$$

The total impulse vector is then simply obtained by addition of J_t and J_n and the post-collision velocities can now be calculated from equations 3.10 and 3.11.

3. Comparison of CFD models and experimental results

3.1. Experimental conditions

The experiments have been carried out in a laboratory scale pseudo two-dimensional gas-fluidised bed, constructed of glass. To obtain homogeneous gas inflow and suppress pressure drop fluctuations at the bottom of the bed, a 3 mm thick stainless steel porous plate with 10 micron pores is used as gas distributor. The inlet flow rate is accurately controlled by mass flow controllers and rapidly switching magnetic valves. To prevent the build up of static electricity the humidity of the inlet air is maintained at 60-70% by addition of steam. A coarse grid is mounted on the top of the bed to prevent the particles from accidentally leaving the system. The pressure drop over this grid is negligible and the freeboard pressure is atmospheric.

The collision parameters for particle-particle and particle-wall collisions were obtained from detailed impact measurements performed by the Impact Research Group of the Open University at Milton Keynes, where an accurate technique to measure collision parameters has been developed (Kharaz et al., 1999). The measured particle collision parameters that were assumed to be independent of impact angle and velocity are summarised in table 3.1, together with further experimental details on bed dimensions and particle properties.

Table 3.1. Experimental system.

Bed dimensions:		*Particle properties:*	
width	150 mm	Diameter	2.49 ± 0.02 mm
depth	15 mm	Density	2526 ± 6 kg/m^3
height	700 mm	Shape factor	~ 1
		Minimum fluidisation velocity	1.25 ± 0.01 m/s
Number of particles	~ 24750		
Initial bed height	15 cm		

Particle collision properties(Gorham and Kharaz, 1999):

	Particle-particle collisions	*Particle-wall collisions*
coefficient of normal restitution	e_n = 0.97 ± 0.01	$e_{n,wall}$ = 0.97 ± 0.01
coefficient of friction	μ = 0.10 ± 0.01	μ_{wall} = 0.09 ± 0.01
coefficient of tangential restitution	β_0 = 0.33 ± 0.05	$\beta_{0,wall}$ = 0.33 ± 0.05

Initially the bed was filled up to 15 cm with approximately 24750 glass beads. Experiments have been carried out at 1.25, 1.50 and 2.00 times the minimum fluidisation velocity. The bed behaviour was recorded with a 3-CCD digital video camera at a frequency of 25 Hz. The digital image analysis technique reported in chapter 6 has been applied to measure bubble patterns and bed expansion dynamics that are used to validate the CFD simulations in this chapter. Though the bed was only 6 particle diameters in depth, smooth fluidisation behaviour was observed at all operating conditions. Visual observation of the lowest 13 mm of the bed close to the gas distributor was obstructed by a flange, which has been applied to mount the bed onto the distributor.

3.2. Simulation conditions

Since the simulated system is a flat fluidised bed the motion of the gas in the depth direction is neglected and the gas phase hydrodynamics are only resolved in 2D. The numerical methods that are applied to solve the gas-phase flow field are taken exactly the same for both models. A finite difference technique, employing a staggered grid to improve numerical stability, is used to solve the gas phase conservation equations. The simulations are carried out on a 1 cm x 1 cm grid of 15 x 45 cells. To reduce numerical diffusion the second order accurate Barton scheme (Centrella and Wilson, 1984; Hawley et al., 1984) is applied to resolve the convective fluxes in all conservation equations. For the gas phase a prescribed influx condition is applied at the bottom, no-slip boundary conditions are applied at the side walls and a prescribed pressure condition is applied at the top of the bed.

In the discrete particle model the motion of all particles is resolved in full 3D. Particle-particle and particle-wall collisions are described with the collision parameters specified in table 3.1. In the continuum model the 3D motion of the particles is taken into account in the derivation of the KTGF closure equations, but the conservation equations themselves are only resolved in 2D. The effect of non-ideal particle-particle collisions is taken into account in the KTGF by the coefficient of normal restitution. The partial slip boundary conditions that are applied to the particulate phase are given by (Sinclair and Jackson, 1989):

$$(\bar{\bar{I}} - \bar{n}\bar{n}) \cdot \varepsilon_s \bar{\bar{\tau}}_s \cdot \bar{n} = \frac{\alpha_{wall} \pi \varepsilon_s \rho_s g_0 \sqrt{\theta}}{2\sqrt{3}\varepsilon_0} \bar{u}_s \tag{3.26}$$

$$\varepsilon_s \bar{q}_s \cdot \bar{n} = -\bar{u}_s \cdot \varepsilon_s \bar{\bar{\tau}}_s \cdot \bar{n} + \frac{\sqrt{3}\pi(1-e_{n,wall}^2)\varepsilon_s \rho_s g_0 \sqrt{\theta}}{4\varepsilon_0} \theta \tag{3.27}$$

So particle-wall interactions are described by the coefficient of restitution for particle-wall collisions ($e_{n,wall}$) and the specularity coefficient of the wall (α_{wall}). The specularity coefficient is set to 0 (impact of perfect sphere on flat wall), since it cannot be directly related to the measured coefficients of friction and tangential restitution (Jenkins, 1992).

In all simulations the minimum fluidisation condition is used as initial condition, where after the gas inlet velocity is stepwise set to the required fluidisation velocity. In the two-fluid simulations small perturbations have been applied to the initial particle volume fraction and the gas inflow velocity at the bottom, to improve resemblance with experimental conditions and avoid unrealistic start-up behaviour due to perfect symmetry of the obtained numerical solution.

3.3. Comparison of bubble patterns

Figure 3.1 shows images taken from the experiments and simulations obtained from both CFD models at the moment of bubble eruption at the bed surface. It can be seen from this figure that just as in the experiments both models predict slugging fluidisation. Larger bubbles and higher bed expansion are observed as the fluidisation velocity increases. For all fluidisation conditions images taken from the discrete particle simulation show the best agreement with pictures taken from the experiments. As can be observed from figure 3.1 and could even better be seen from animations that were made of all simulations, the discrete particle model is better capable of capturing complex structures that are observed in experiments, such as initialisation of small bubbles near the bottom of the bed and strings of particles within larger bubbles.

3.4. Comparison of time-average flow patterns

It is tempting to conclude from images such as shown in figure 3.1 that the discrete particle model shows better agreement with the experiments than the continuum model, especially since the discrete representation of all particles makes the results look more realistic. But, apart from being able to capture the bubble pattern, CFD models should also be able to predict the correct bed dynamics and time-average bed behaviour. Therefore the bed expansion dynamics and time-average particle volume fractions were measured using the digital image analysis method presented in chapter 6.

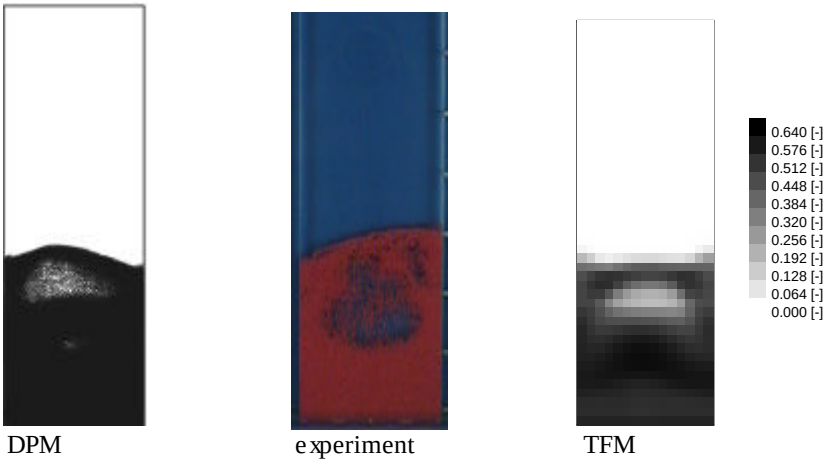

DPM experiment TFM

a) Snapshots taken at 1.25 U_{mf}.

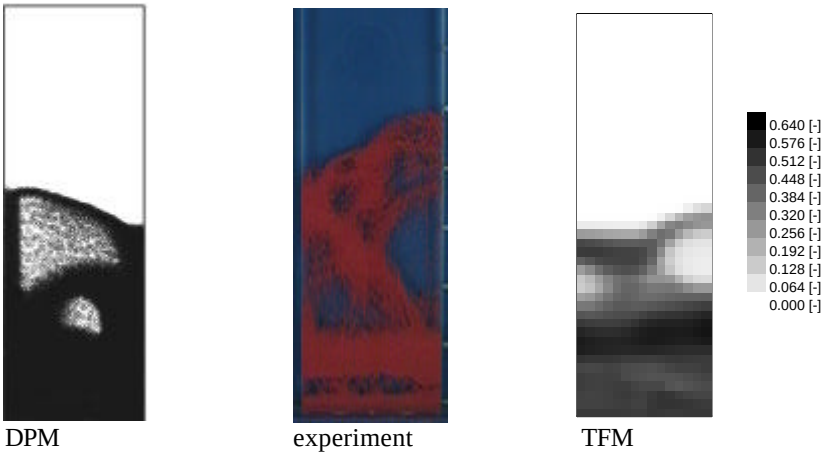

DPM experiment TFM

b) Snapshots taken at 1.50 U_{mf}.

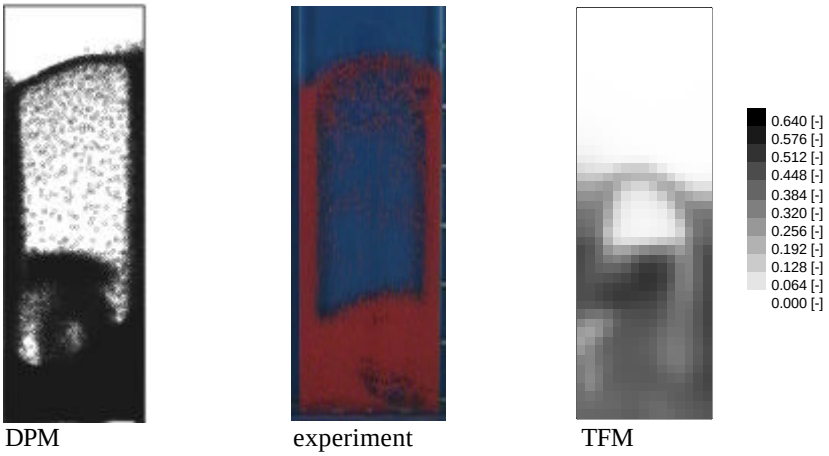

DPM experiment TFM

c) Snapshots taken at 2.00 U_{mf}.

Figure 3.1. Snapshots taken from experiments and CFD simulations with the Discrete Particle Model and the Two-Fluid Model at the moment of bubble eruption.

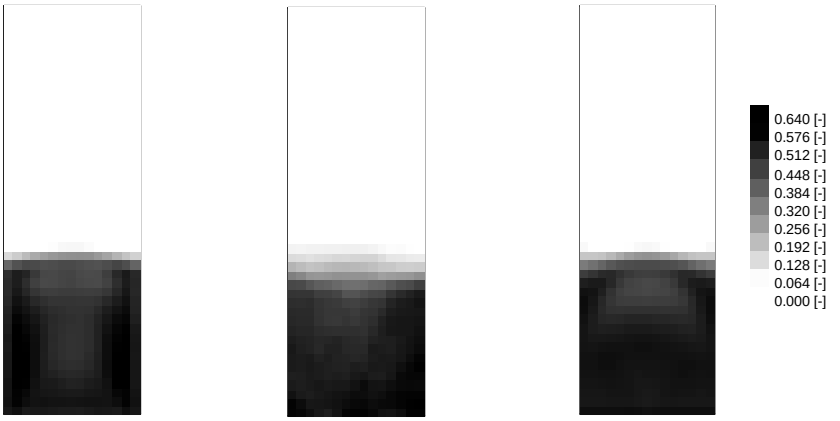

DPM experiment TFM

a) Time average particle volume fractions at 1.25 U_{mf}.

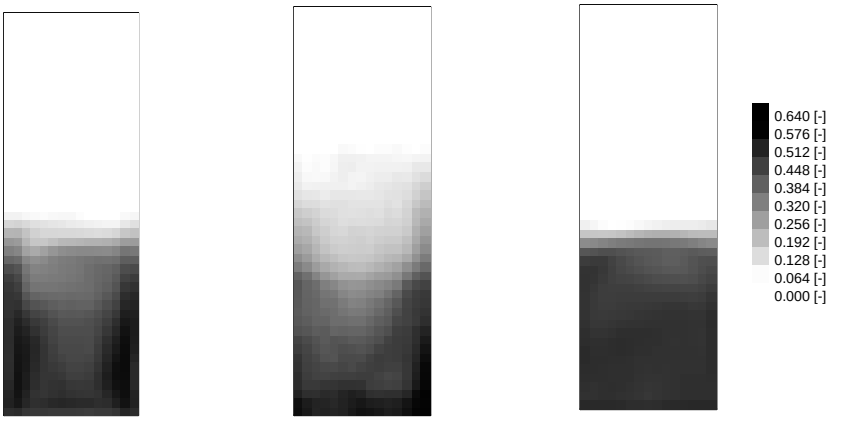

DPM experiment TFM

b) Time average particle volume fractions at 1.50 U_{mf}.

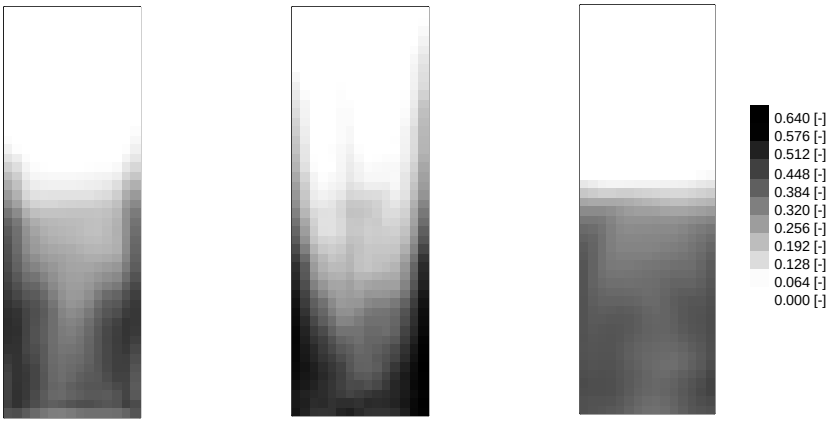

DPM experiment TFM

c) Time average particle volume fractions at 2.00 U_{mf}.

Figure 3.2. Comparison of measured time average (t = 5-10 s) particle volume fractions to results of CFD simulations with the Discrete Particle Model and the Two-Fluid Model.

The time-average particle concentration patterns that have been obtained from averaging the measured particle volume fractions are presented in figure 3.2. Though the measurements were performed for several minutes a relatively short averaging period of 5 seconds was applied. This was done so to obtain a fairer comparison with the averages obtained from the simulations that were only run for 10 seconds. As can be seen from figure 3.2 the measured average particle concentration patterns are reasonably symmetric and comparison to other averages that were taken for different averaging periods confirmed that they are representative. The experimental results in figure 3.2 show that especially at higher fluidisation velocities the particle fractions are the highest near the system walls. This is due to the fact that bubbles in the dense bottom of the bed mostly pass through the centre of the bed and at the moment of eruption particles are ejected into the freeboard.

Figure 3.2 also shows time-average particle volume fractions resulting from simulations with both CFD models. For the discrete particle simulations the solids volume fraction for each computational cell *k* was calculated from the number of particles in that cell using:

$$\varepsilon_{s,k} = \frac{N_{part,k}}{V_{cell,k}} \frac{\pi d_p^3}{6} \tag{3.28}$$

Figure 3.2 confirms that the discrete particle model shows better agreement with the experiments. This is especially clear at 1.50 U_{mf} and 2.00 U_{mf}, where the time-average particle volume fraction profiles obtained from the discrete particle model reflect the experimentally observed higher volume fractions near the walls, while the profiles obtained from the continuum model are much more homogeneous. The homogeneity of the time-averages obtained from the two-fluid model is a result of the lack of small bubbles near the bottom of the bed and the rise of bubbles along the side walls as well as through the core of the bed. It can further be concluded from figure 3.2 that the bed expansion observed in the experiments at 1.50 U_{mf} and 2.00 U_{mf} is somewhat higher than both models predict.

A comparison between the predicted particle phase velocities is presented in figure 3.3. The presented velocities are obtained from the models by volume fraction weighted averaging of the particle phase velocity field:

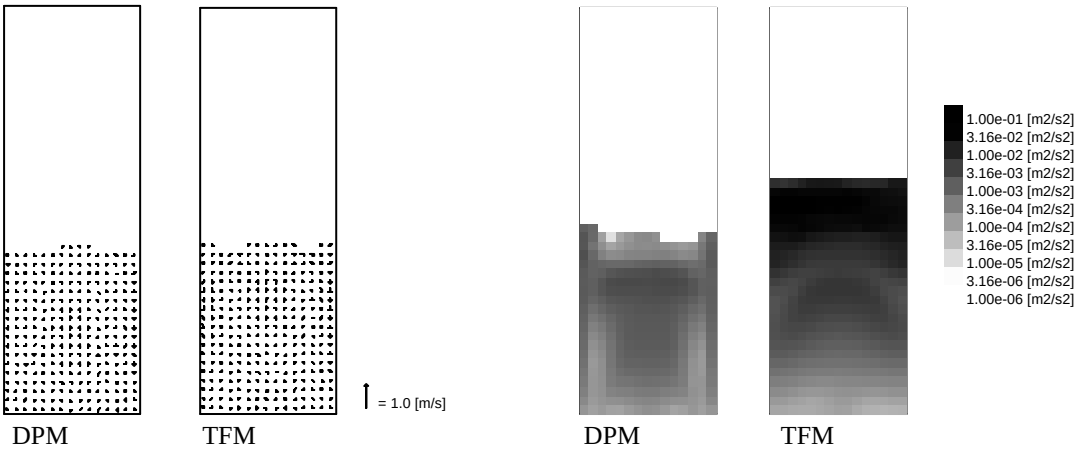

a) Time average particle phase velocity and granular temperature at 1.25 U_{mf}.

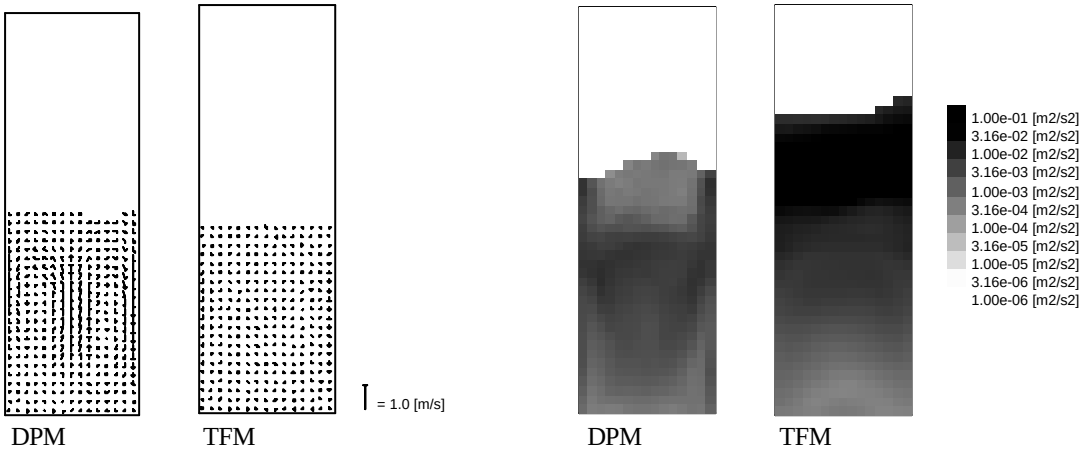

b) Time average particle phase velocity and granular temperature at 1.50 U_{mf}.

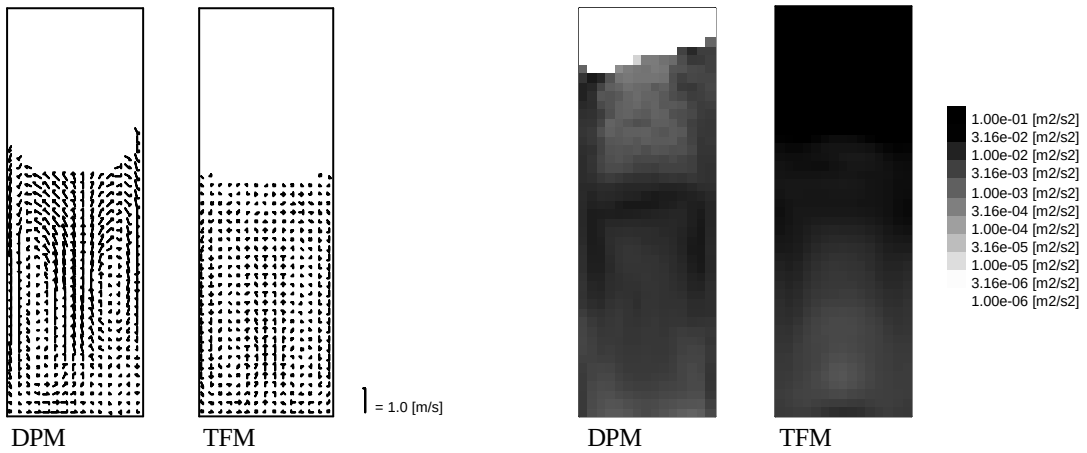

c) Time average particle phase velocity and granular temperature at 2.00 U_{mf}.

Figure 3.3. Comparison between time average (t = 5-10 s) particle velocities and granular temperatures obtained from CFD simulations.

$$< \bar{u}_{s,k} >_t = \frac{1}{< \varepsilon_{p,k} >_t} \int_{t_{min}}^{t_{max}} \varepsilon_{p,k} \bar{u}_{s,k} \, dt \tag{3.29}$$

For the discrete particle model the particle phase velocity for each cell is obtained from averaging the velocities of all particles in that cell according to:

$$\bar{u}_{s,k} = < \bar{v}_p >_k = \frac{\sum_i^{N_{part,k}} \bar{v}_i}{N_{part,k}} \tag{3.30}$$

The same time-average particle flow profile with upward flow through the centre of the column and downward flow near the system walls is obtained for all simulations. It becomes clear from this figure that though both models predict the same time-average particle circulation pattern, the flow obtained by the discrete particle model is much stronger than that obtained by the two-fluid model.

Beside the ensemble averaged particle velocities figure 3.3 also shows the time-averaged fluctuating velocity (granular temperature) profiles for both models. From the discrete particle simulations the granular temperature in each cell is computed from the following equation:

$$\theta_k = \frac{1}{3} \frac{\sum_i^{N_{partk}} (\bar{v}_i - < \bar{v}_p >_k)^2}{N_{part,k}} \tag{3.31}$$

Just as the velocity profiles the presented granular temperature profiles are volume fraction weighted time-averages obtained as:

$$< \theta_k >_t = \frac{1}{< \varepsilon_{s,k} >_t} \int_{t_{min}}^{t_{max}} \varepsilon_{s,k} \theta_k \, dt \tag{3.32}$$

Comparison between the granular temperature profiles and the particle volume fraction profiles presented in figure 3.2 shows that both models predict lower granular temperatures in areas where the particle volume fraction is high and visa versa. Further it can be seen that the continuum model predicts high granular temperatures in the splash zone of the bed, which are not observed in the discrete particle simulation. However, the number of particles on which the computation of the granular temperature in this region from the discrete particle model is based, is too small to obtain a statistically meaningful average. The grey intensities of the figures at different fluidisation velocities indicate that

both models predict an increase in particle velocity fluctuations as the fluidisation velocity increases. A quantitative comparison of the granular temperatures predicted by both models as a function of the fluidisation velocity is given in figure 3.4. In that figure the time-averaged granular temperatures that are obtained from volume fraction weighted averaging over the whole system are presented. This temperature is calculated by:

$$< \theta >_{t,bed} = \frac{1}{t_{\max} - t_{\min}} \int_{t_{\min}}^{t_{\max}} \frac{\sum_{k}^{Ncell} \varepsilon_{p,k} \theta_k}{\sum_{k}^{Ncell} \varepsilon_{p,k}} dt \tag{3.33}$$

The error bars in the figure indicate the fluctuations of this granular temperature, computed from the Root Mean Square (RMS) of the fluctuations of bed average granular temperature:

$$RMS < \theta >_{t,bed} = \sqrt{\frac{1}{t_{\max} - t_{\min}} \int_{t_{\min}}^{t_{\max}} (< \theta >_{bed} - < \theta >_{t,bed})^2 \, dt} \tag{3.34}$$

The conclusion that can be drawn from figure 3.4 is that the granular temperatures that are predicted by both models are of the same order of magnitude. Further it is interesting to notice that both models predict the same dependence of the granular temperature on the fluidisation velocity. These observations confirm that the kinetic theory of granular flow gives meaningful estimates for the fluctuating particle velocity, which is a key variable in the closure equations.

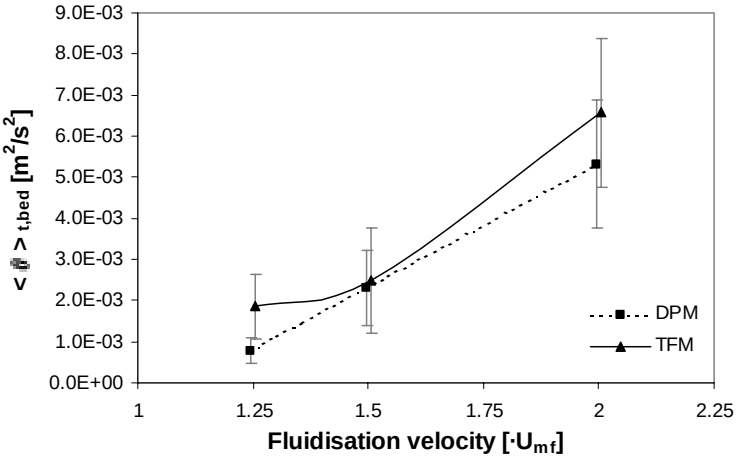

Figure 3.4. Average granular temperature versus fluidisation velocity (RMS indicated by error bars).

3.5. Comparison of bed expansion dynamics

To characterise the bed expansion dynamics the average particle height in all experiments and simulations was computed from:

$$< h_p >_{bed} = \frac{\sum_{i}^{Npart} h_i}{N_{part}} = \frac{\sum_{k}^{Ncells} \varepsilon_{s,k} h_k}{\sum_{k}^{N_{cells}} \varepsilon_{s,k}} \tag{3.35}$$

An example of the bed expansion dynamics that was obtained at 1.50 U_{mf} is presented in figure 3.5. To quantify the bed expansion dynamics the time-average particle height, the intensity of the particle height fluctuations and the dominant fluctuation frequency have been determined. For this analysis the experimental signals obtained from t_{min} = 5 s to t_{max} = 60 s were analysed. These signals were sampled at a frequency of 25 Hz and a standard Fourier analysis technique was applied to determine the dominant bed expansion frequency. All experiments were performed in triplo and their results where within 5 % of the presented average values. The simulated bed expansion signals were sampled at a much higher frequency of at least 1000 Hz. To prevent start up effects from influencing the results only the signals obtained from t_{min} = 5 s to t_{max} = 10 s were analysed. Therefore the accuracy of the bed expansion frequency is somewhat less than for the experiments (about 10%). An overview of the performed bed expansion analyses is presented in table 3.2.

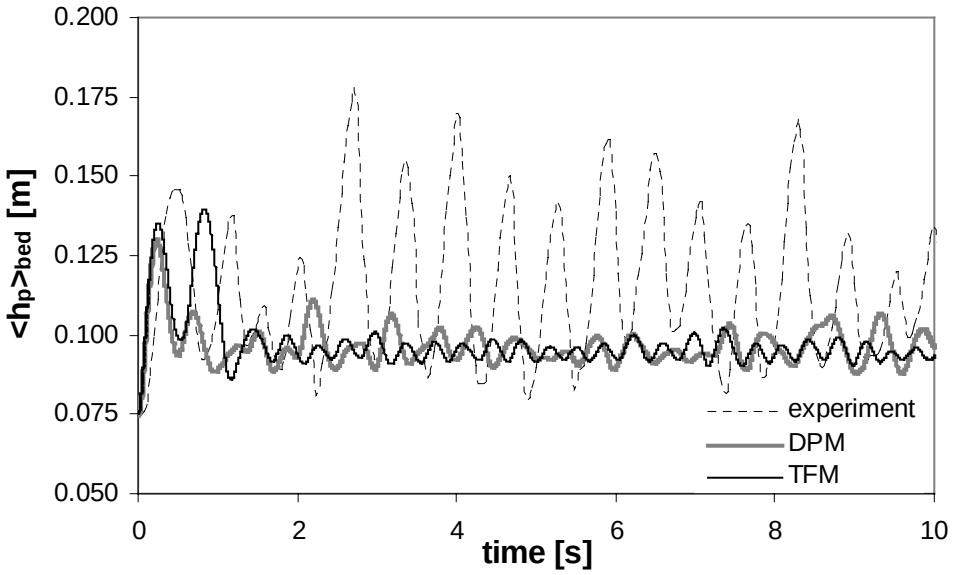

Figure 3.5. Comparison of measured and simulated average particle heights at 1.50 U_{mf}.

Table 3.2. Overview of experimental and simulated bed expansion dynamics.

	fluidisation velocity	**$\langle h \rangle_t$ [m]**	**RMS $\langle h \rangle$ [m]**	**Expansion freq. [Hz]**	**remarks**
experiment	1.25 U_{mf}	0.092	0.0098	1.6	
experiment	1.50 U_{mf}	0.114	0.0226	1.6	
experiment	2.00 U_{mf}	0.135	0.0323	1.4	
DPM	1.25 U_{mf}	0.085	0.0016	3.2	
DPM	1.50 U_{mf}	0.097	0.0052	2.0	
DPM	2.00 U_{mf}	0.120	0.0074	2.0	
TFM	1.25 U_{mf}	0.085	0.0020	3.0	
TFM	1.50 U_{mf}	0.095	0.0026	2.8	
TFM	2.00 U_{mf}	0.118	0.0039	2.4	
Grid refinement					
TFM	1.50 U_{mf}	0.096	0.0030	2.6	fine grid
TFM	2.00 U_{mf}	0.120	0.0060	2.1	fine grid
Wall effects					
DPM	1.50 U_{mf}	0.095	0.0042	2.3	ideal front and back wall
TFM	1.50 U_{mf}	0.095	0.0023	2.8	3D, fine grid
DPM	1.50 U_{mf}	0.095	0.0048	2.8	all walls ideal
TFM	1.50 U_{mf}	0.095	0.0020	3.2	all walls ideal
Effect of rotation					
DPM	1.50 U_{mf}	0.093	0.0030	3.0	no rotation
Effect of contact friction					
TFM	1.50 U_{mf}	0.095	0.0025	2.8	frictional viscosity
Effect of drag model					
TFM	1.92 m/s	0.088	0.0035	3.3	drag Foscolo et al.
TFM	1.92 m/s	0.094	0.0031	3.2	drag Garside and Al-Dibouni
Effective restitution coefficient					
TFM	1.25 U_{mf}	0.085	0.0020	2.4	
TFM	1.50 U_{mf}	0.096	0.0040	2.2	
TFM	2.00 U_{mf}	0.117	0.0062	1.8	

The first thing to notice from figure 3.5 and table 3.2 is that both models predict too low average particle heights and particle height fluctuations have a too low intensity. Also the frequency of the particle height fluctuations is too high. Of both models the discrete particle model again seems to give the best resemblance with the experiments. The models predict about the same average bed expansion, but at 1.50 U_{mf} and 2.00 U_{mf}, as a result of the formation of larger bubbles, the discrete particle model predicts stronger fluctuations at a lower frequency.

3.5.1. Effect of grid refinement

The comparison is actually somewhat flawed, since the grid that was applied for both models might have been too coarse for the continuum model to fully capture the bed dynamics. Especially the prediction of steep particle concentration gradients around bubbles and strings of particles might have been hindered. Therefore the two-fluid simulations at 1.50 U_{mf} and 2.00 U_{mf} were repeated on a refined grid of 30 x 90 cells. At first sight these simulations did not show significantly different results at any of the studied fluidisation velocities. Bubble contours were better resolved but bubble sizes and bed heights observed from images and animations did not improve significantly. The time-average particle volume fraction pattern did not show a significantly increase of the particle fraction near the wall and particle velocities were still lower than those observed in the discrete particle simulation. However, the results of the bed expansion analysis that are presented in table 3.2 show a clear improvement of both the bed expansion frequency and the intensity of the bed height fluctuations, especially at 2.00 U_{mf}. So even though grid refinement hardly changed the instantaneous flow structure and time-averaged flow patterns, the predicted bed dynamics improved significantly. Further grid refinements were carried out but did not show significant improvements.

3.5.2. Wall effects

Since the experiments were carried out in a pseudo two-dimensional bed particle-wall interactions may have had a significant influence on the observed bed dynamics. In the discrete particle simulations particle-wall interactions with all system walls have been described with the experimentally obtained collision parameters. In the continuum simulations on the contrary, the front and the back wall have not been taken into account since the conservation equations were only resolved in 2D. To study the influence that those walls might have had on the simulation results and the experiments, a discrete particle simulation with ideal (e_n = 1, μ = 0, β_0 = 0) front and back walls and a full 3D two-fluid simulation with partial slip wall conditions for all walls have been carried out. An interesting earlier study on this subject was performed by Kawaguchi et al. (1998).

Significant changes regarding the earlier reported bubble patterns and time-averaged flow fields are not observed in either of the simulations. The results for the bed dynamics are summarised in table 3.2. Comparison of the results of the discrete particle simulations with ideal and non-ideal particle-wall interactions shows that there is hardly any effect of the walls on the average particle height and the intensity of the particle height fluctuations. Only the bed expansion frequency increases somewhat. The results of the

two-fluid simulation can best be compared to those of the fine grid simulation, since the 3D simulation was carried out on a 30 x 90 x 3 grid with 0.5 mm spacing. Though the intensity of the bed expansion fluctuations seems to have decreased a little and the frequency increased a bit the differences between the 2D and 3D two-fluid simulations are not significant. To get a better grip on the influence of wall effects simulations in which all particle-wall interactions were assumed to be ideal were performed. These simulations confirmed the influences that the bed expansion frequency rises when there is less particle wall interaction, whereas all other bed characteristics remain essentially unchanged.

3.5.3. Long-term and multi-particle contacts

The first thing that is noticed from table 3.2 is that both models predicted too low average particle heights, particle height fluctuations are too frequent and have a too low intensity. Visual observation of the experiments made clear that these differences were mainly caused by the formation of densely packed regions. In these regions hardly any vibration of particles could be observed. The bed seemed locally defluidised. Densely packed clusters that were formed by particle compression (mostly) at the bottom of the bed were accelerated towards the top. Break up of these clusters took a while which caused large quantities of particles to be lifted. This led to intense fluctuations of the observed particle heights. Though the lack of one degree of freedom in the pseudo 2D experimental setup will have enhanced the formation of defluidised areas, it is believed that this phenomenon will also occur in systems with a greater depth.

In the simulations bed expansion as intense as observed in the experiments only occurred at the start up (see figure 3.5). At that moment the bed was in a randomly packed dense state and animations show that the whole bed content was accelerated, just as in the experiments. So both CFD models are capable of predicting large bed expansion, but the required formation of densely packed bed regions does not occur in either. The best explanation for this is that the kinetic theory model and the discrete particle model both assume that collisions are binary and quasi-instantaneous. Both models neglect long-term and multi-particle contacts and only kinetic and collisional contributions to the viscosity of the particulate suspension are accounted for. However, in regions with high particle volume fractions, the dominant stress generation mechanism is more likely due to long-term and multi-particle contacts. In long term contacts far more energy will be dissipated which leads to a self enhancing mechanism for the formation of extremely dense regions, since particles with hardly any energy left cannot get out of these regions.

The incorporation of long-term particle contacts into a hard sphere discrete particle model is a cumbersome task since this model cannot handle particle overlap that will eventually occur if a lot of particles are together for longer periods of time (because of numerical inaccuracies). Therefore a soft-sphere or hybrid discrete particle approach will be a more appropriate choice to model multi-particle and long-term frictional contacts. For the incorporation of frictional viscosity into continuum models Laux (1998) tested several models from the field of soil mechanics. It was demonstrated that it is worthwhile to include such a frictional stress model to improve the description of phenomena such as heap formation. The frictional viscosity model that gave the best results is given by:

$$\mu_{s,fric} = \frac{6\sin\phi_I}{9-\sin^2\phi_I}\frac{|I_{II}|}{2\sqrt{3|II_D|}} \tag{3.36}$$

where ϕ_I is the internal angle of friction (45° in this work), I_{II} is the first invariant of the particle pressure stress tensor and II_D is the second invariant of the deviator of the rate-of-strain tensor:

$$I_{II} = 3(\lambda_s \nabla\cdot\bar{u}_s - \frac{P_s}{\varepsilon_s}) \tag{3.37}$$

$$II_D = -\frac{1}{2}\bar{\bar{D}}_{ij} : \bar{\bar{D}}_{ij} = -\frac{1}{2}\left(\frac{1}{2}\left((\nabla\bar{u}_s)+(\nabla\bar{u}_s)^T\right)-\frac{1}{3}\nabla\cdot\bar{u}_s\bar{\bar{I}}\right):\left(\frac{1}{2}\left((\nabla\bar{u}_s)+(\nabla\bar{u}_s)^T\right)-\frac{1}{3}\nabla\cdot\bar{u}_s\bar{\bar{I}}\right) \tag{3.38}$$

To study the effect of frictional viscosity on the predicted bed dynamics, this stress model was implemented into the two-fluid model. The model assumes that long-term particle contacts only contribute to the stress tensor above a certain particle volume fraction ε_{lim} (0.5 in this work). The effective hydrodynamic viscosity is then given by the maximum of the viscosity obtained from the kinetic theory model and the frictional viscosity model:

$$\mu_{s,eff} = \begin{cases} max\left|\mu_{s,KTGF},\mu_{s,fric}\right| & \varepsilon_s \geq \varepsilon_{lim} \\ \mu_{s,KTGF} & \varepsilon_s < \varepsilon_{lim} \end{cases} \tag{3.39}$$

To guarantee numerical stability and reasonable convergence rates the viscosity is limited to μ_{lim} ($1\cdot10^{5}$ Pas in this work):

$$\mu_s = min\left|\mu_{s,eff},\mu_{lim}\right|. \tag{3.40}$$

Two fluid simulations with this frictional viscosity model were performed at 1.5 U_{mf}. As can be seen from the results presented in table 3.2 the incorporated model did not affect the simulated bed dynamics at all. Simulations on a refined grid and simulations with alternative gas-particle drag models were performed to verify this result, but also there no changes were observed. It is therefore concluded that the presented frictional viscosity model is not capable of explaining the observed phenomena in the pseudo two-dimensional experimental setup.

Recently Zhang and Rauenzahn (1997, 2000) employed the ensemble averaging technique developed by Zhang and Prosperetti (1994, 1997) to examine the effects of finite particle interaction time and multi-particle contacts in dense granular systems. Their visco-elastic model showed good agreement with the results of the kinetic theory of granular flows at relatively low particle concentrations, while at volume fractions approaching random loose packing ($\varepsilon_s \approx 0.52$) a transition in rheologic behaviour occurred. When the particle volume fraction was greater than 0.3, shear band formation was observed at high shear rates. The particles were divided into layers sliding against each other. Inside each layer little relative particle motion was observed. This anisotropic behaviour was caused by rotation of lines connecting the centres of the particles during their contact, which is not included in the kinetic theory of granular flow. In order to determine coefficients in the constitutive model, direct numerical simulations with a soft-sphere molecular dynamics model had to be performed. Since this visco-elastic model seems to describe the behaviour that was observed in the experiments very well, it should be worthwhile to implement it into 'next generation' continuum models for dense and slow granular flows. Hereby soft-sphere discrete particle models can be a useful tool to calibrate the required coefficients.

3.5.4. Particle rotation

Apart from the different ways of representing the particulate suspension and particle-wall interactions, another main difference between the simulations with both CFD models regards particle rotation. Rotation is taken into account in the discrete particle simulations but not in the continuum simulations. To study the effect of particle rotation on the simulated bed dynamics a discrete particle simulation was carried out in which the coefficients of friction and tangential restitution were set to zero. This prevents the transformation of translational motion into particle rotation upon collision and rotational energy losses become zero.

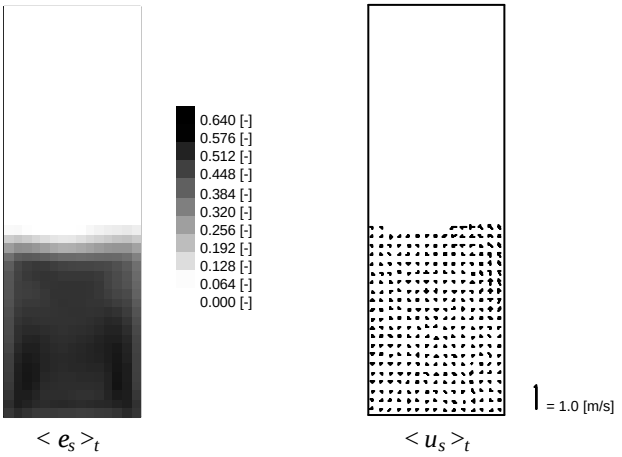

Figure 3.6. Time averages from DPM simulations at 1.5 U_{mf} without particle rotation.

The results of the discrete particle simulation without rotation showed a clear change in bed dynamics. Snapshots taken from the simulation showed that smaller bubbles were formed. These resulted into more frequent and less intense bed dynamics (see table 3.2). The time-average particle volume fraction and velocity patterns are shown in figure 3.6. Comparison with the patterns shown in figures 3.2 and 3.3 makes clear that the time-average particle volume fraction has become more homogeneous and time-average particle velocities decreased. This is because about as many small bubbles rise through the core of the bed as rise along the walls. Apparently the absence of rotation and subsequent energy losses in the two-fluid model is the main reason for the observed differences between both models.

3.5.5. Drag model

Particle fluidisation and fluidised bed expansion are caused by drag exerted by the interstitial gas on the particulate phase. Though most hydrodynamic models nowadays apply the drag model based on the equations of Ergun (1952) and Wen and Yu (1966), there is no general consensus about the modelling of gas-particle drag. An overview of drag models that have been applied can be found in Enwald et al. (1996). To study the influence of the applied drag model on the presented results the two drag models that predict the most and the least gas-particle drag have been implemented in the two-fluid model. The drag model by Foscolo et al. (1983) that predicts the lowest drag force for the studied system is given by:

$$\beta = \left(\frac{17.3}{\mathrm{Re}_p} + 0.336 \right) \varepsilon_f^{-1.8} \, (1-\varepsilon_f) \frac{\rho_f}{d_p} \left| \overline{u}_f - \overline{u}_s \right| \tag{3.41}$$

where

$$\mathrm{Re}_p = \frac{\varepsilon_f \rho_f \left| \overline{u}_f - \overline{u}_s \right| d_p}{\eta_f} \tag{3.42}$$

The highest gas-particle drag is predicted by the equation of Garside and Al-Dibouni (1977) that is given by the following set of equations:

$$\beta = \frac{3}{4} \frac{1}{R_t^2} \left(0.63 + 4.8 \sqrt{\frac{\varepsilon_f R_t}{\mathrm{Re}_k}} \right)^2 \varepsilon_f (1-\varepsilon_f) \frac{\rho_f}{d_p} \left| \overline{u}_f - \overline{u}_s \right| \tag{3.43}$$

$$R_t = 0.5 \left(C_1 - 0.06 \frac{\mathrm{Re}_p}{\varepsilon_f} + \left(\left(0.06 \frac{\mathrm{Re}_p}{\varepsilon_f} \right)^2 + 0.12 \frac{\mathrm{Re}_p}{\varepsilon_f} \left(2C_2 - C_1 \right) + C_1^2 \right)^{0.5} \right) \tag{3.44}$$

with:

$$C_1 = \varepsilon_f^{4.14} \tag{3.45}$$

$$C_2 = \begin{cases} 0.8\varepsilon_f^{1.28} & \varepsilon_f \le 0.85 \\ \varepsilon_f^{2.65} & \varepsilon_f > 0.85 \end{cases} \tag{3.46}$$

A comparison between the three drag models for the studied system is presented in figure 3.7. The drag model by Foscolo et al. (1983) predicts about the same minimum fluidisation velocity as the Ergun equation. These two drag models show good agreement with the experimentally observed minimum fluidisation velocity, whereas predictions of the minimum fluidisation velocity based on the drag model by Garside and Al-Dibouni (1977) is far too low.

Simulations to study the effect of the different drag models were performed at 1.92 m/s (= 1.5 U_{mf} based on Ergun equation). Results of the bed expansion analysis are shown in table 3.2. The average particle height predicted by the model of Foscolo et al. (1983) was somewhat lower than the predictions resulting from the base case. The average particle height obtained using the model of Garside and Al-Dibouni (1977) was not higher as expected, but the bed height fluctuations were stronger and more frequent. No significant differences in bubble size could be observed and the time-average profile for the drag

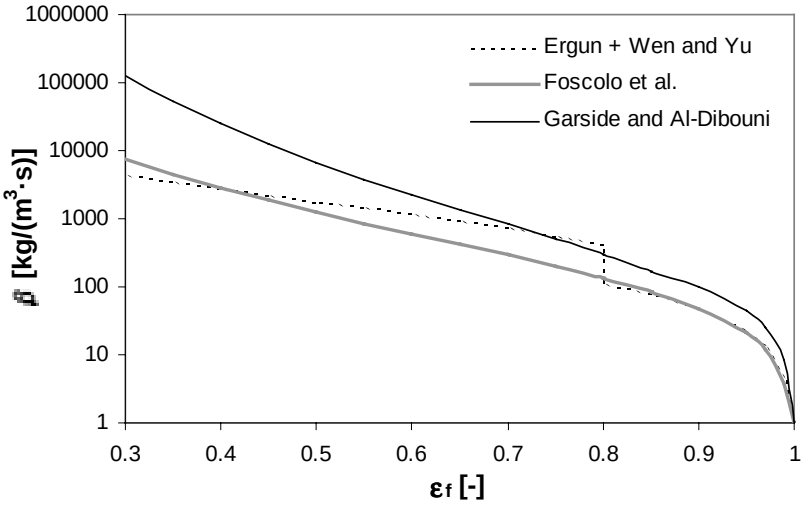

Figure 3.7. Comparison of the applied drag models at superficial slip-velocity 1.92 m/s.

model by Garside and Al-Dibouni (1977) looked exactly like that presented for the base case simulations with the two-fluid model in figure 3.2b. More surprisingly the bed height fluctuations obtained with the drag model by Foscolo et al. (1983) were also stronger than in the base case. From animations of the simulations it could be observed that the packing density in dense areas was higher, which caused acceleration of larger quantities of particles by bigger bubbles passing preferentially through the centre of the bed. The time-average particle volume fraction profile looked like that for the two-fluid model at 1.25 U_{mf} presented in figure 3.2a.

So there are clear differences between the results obtained with the different drag models, but a decision which model is the best cannot be made. Though the bubble sizes and the intensity of the bed expansion are in favour of the model by Foscolo et al. (1983), the average particle height and bed expansion frequency are not. The simulations with the alternative drag models show much larger differences with the experiments than they show with each other. Therefore it is concluded that the search for the most appropriate drag model is important, but it does not have the highest priority. It is further worth noticing that the presented drag models are only applicable if the distribution of particles within a computational cell can be assumed to be homogeneous. Modifications are required to account for structures that are smaller than a computational cell. In that case the effective drag force will be lower, which makes the application of the drag model by Foscolo et al. (1983) most appealing.

4. Particle phase energy analysis of CFD models

It was concluded in the previous section that most of the observed differences between the results of both models could be attributed to the neglect of particle rotation by the continuum model. Dissipation of rotational energy that is supplied by translational motion of particles during collisions contributes to more energy dissipation. When more energy is dissipated in collisions less kinetic energy will be left afterwards for the particles to move apart and stronger cluster formation will occur. In a bubbling fluidised bed as a result of particle clustering bubbles are formed. These bubbles will grow larger if more energy is dissipated, which explains why the bubble intensity is less when rotation is neglected.

From the above argument it can be concluded that the total amount of kinetic energy that is dissipated in collisions plays a dominant role in the process of structure formation in dense fluidised beds. Since kinetic energy has to be supplied by the gas phase the external forces acting on the particles also have to be considered. Therefore the energy balance for the suspended particulate phase was derived and studied for both CFD models.

4.1. Mechanical energy balance for discrete particle model

The total mechanical energy of rigid particles can be split into potential energy (E_{pot}), kinetic energy (E_{kin}) and rotational energy (E_{rot}) as in the total mechanical energy balance derived by Hoomans (2000a). Here, to maintain maximum comparability with the energy balance that will be presented for the continuum model, the kinetic energy of an ensemble of particles has been split into a contribution due to convection of the ensemble as a whole (E_{conv}) and a contribution due to random motion of particles within the ensemble (E_{gran}). So the total amount of energy of the particles in the system is given by:

$$E_{tot} = E_{pot} + E_{conv} + E_{gran} + E_{rot} \tag{3.47}$$

This amount of energy is continuously changed by the forces acting on the particles and energy dissipation due to non-ideal collisions. The amount of work performed by the drag force acting on an ensemble of particles in a computational cell during a time period *dt*, can be computed by integration of the drag force along the trajectories of the particles:

$$W_{drag,k} = \frac{1}{dt} \sum_{i}^{Npart,k} \int_{t}^{t+dt} \frac{V_{p,i}\beta}{1-\varepsilon_f} (\overline{u}_f - \overline{v}_i) \cdot \overline{v}_i \, dt \tag{3.48}$$

An expression for the work performed by the far field pressure gradient can be derived in the same manner. The total amount of energy dissipation by normal restitution, sticking or sliding can be computed by summation over all collisions that occur during a time period *dt* (N_{coll}). For example the amount of energy dissipated by normal restitution is given by:

$$W_{rest} = -\frac{1}{dt}\sum_{Ncoll}\frac{(\bar{v}_{ab,0}\cdot\bar{n})^2}{2B_2}(1-e^2) \tag{3.49}$$

So the mechanical energy balance for the particulate phase that is obtained for the discrete particle model is given by:

$$\frac{d}{dt}\left(E_{pot}+E_{conv}+E_{gran}+E_{rot}\right)=W_{drag}+W_{press}+W_{rest}+W_{sticking}+W_{sliding} \tag{3.50}$$

Expressions for all terms in this equation can be found in table 3.3.

4.2. Mechanical energy balance for continuum model

In this section the particle phase mechanical energy balance for the two-fluid continuum model is derived from the particle phase momentum balance and the granular temperature equation (a derivation from the well-known Boltzmann integral-differential equation is given by Gidaspow (1994)). Taking the dot product of the momentum equation and the particle velocity results in:

$$\frac{D}{Dt}(\frac{1}{2}\varepsilon_s\rho_s u_s^2)-\varepsilon_s\rho_s\bar{u}_s\cdot\bar{g}=-\varepsilon_s\bar{u}_s\cdot\nabla p_f-\bar{u}_s\cdot\nabla\cdot(\varepsilon_s\bar{\bar{\tau}}_s)-\bar{u}_s\cdot\nabla p_s+\bar{u}_s\cdot\beta(\bar{u}_f-\bar{u}_s) \tag{3.51}$$

This equation expresses the change of kinetic energy and potential energy for an ensemble of particles per unit volume per unit time as a result of the forces acting on this ensemble. The change of the amount of kinetic energy contributed due to random motion of the particle within the ensemble is given by the granular temperature equation, which can be slightly rewritten to get:

$$\frac{D}{Dt}(\frac{3}{2}\varepsilon_s\rho_s\theta)=-p_s\nabla\cdot\bar{u}_s-(\varepsilon_s\bar{\bar{\tau}}_s):\nabla\bar{u}_s+\nabla\cdot(\varepsilon_s\kappa_s\nabla\theta)-3\beta\theta-\gamma \tag{3.52}$$

Table 3.3. Terms in particle phase energy balances.

	Discrete particle model	**Continuum model**
E_{kin}	$\sum_{i}^{Npart} \frac{1}{2} m_i \bar{v}_i^{-2}$	-
E_{conv}	$\sum_{k}^{Ncell} N_{part,k} \frac{1}{2} m_p < \bar{v}_p >_k^2$	$\sum_{k}^{Ncell} \frac{1}{2} \varepsilon_{s,k} \rho_s u_{s,k}^2 V_{cell,k}$
E_{gran}	$\sum_{k}^{Ncell} N_{part,k} \frac{3}{2} m_p \theta_k$	$\sum_{k}^{Ncell} \frac{3}{2} \varepsilon_{s,k} \rho_s \theta_k V_{cell,k}$
E_{pot}	$\sum_{i}^{Npart} m_i g_z h_i$	$\sum_{k}^{Ncell} \varepsilon_{s,k} \rho_s g_z h_k V_{cell,k}$
E_{rot}	$\sum_{i}^{Npart} \frac{1}{2} I \bar{\omega}_i^{-2}$	-
W_{rest}	$-\frac{1}{dt} \sum_{Ncoll} \frac{(\bar{v}_{ab,0} \cdot \bar{n})^2}{2B_2} (1 - e_n^2)$	$-\sum_{k}^{Ncell} \gamma_k V_{cell,k}$
$W_{sticking}$	$-\frac{1}{dt} \sum_{Ncoll} \frac{(\bar{v}_{ab,0} \cdot \bar{t})^2}{2B_1} \left(1 - \beta_0^2\right)$	-
$W_{sliding}$	$-\frac{1}{dt} \sum_{Ncoll} \mu J_n (\bar{v}_{ab,0} \cdot \bar{t} - \frac{1}{2} \mu B_1 J_n)$	-
W_{drag}	$\frac{1}{dt} \sum_{k}^{Ncell} \sum_{i}^{Npart,k} \int_{t}^{t+dt} \frac{V_{p,i} \beta}{1 - \varepsilon_f} (\bar{u}_f - \bar{v}_i) \cdot \bar{v}_i dt$	$\sum_{k}^{Ncell} \beta_k \left(\bar{u}_{f,k} - \bar{u}_{s,k}\right) \cdot \bar{u}_{s,k} V_{cell,k}$
$W_{drag,gran}$	-	$-\sum_{k}^{Ncell} 3 \beta_k \theta_k V_{cell,k}$
W_{press}	$-\frac{1}{dt} \sum_{k}^{Ncell} \sum_{i}^{Npart,k} \int_{t}^{t+dt} V_{p,i} \nabla p_f \cdot \bar{v}_i dt$	$-\sum_{k}^{Ncell} \varepsilon_{s,k} \nabla p_{f,k} \cdot \bar{u}_{s,k} V_{cell,k}$

The total mechanical energy balance can then be obtained from addition of equations 3.51 and 3.52. Before deriving this equation the expressions for the work performed by the particle pressure and shear in equation 3.51 are split in two terms each. The new terms in the resulting expression represent the real work done by the external forces on the particulate ensemble and the conversion of kinetic energy from ensemble averaged convection to granular temperature:

$$\frac{D}{Dt}(\frac{1}{2}\varepsilon_s\rho_s u_s^2)-\varepsilon_s\rho_s\bar{u}_s\cdot\bar{g}=-\varepsilon_s\bar{u}_s\cdot\nabla p_f-\nabla\cdot(\varepsilon_s\bar{\bar{\tau}}_s\cdot\bar{u}_s)+(\varepsilon_s\bar{\bar{\tau}}):\nabla\bar{u}_s \\ -\nabla\cdot p_s\bar{u}_s+p_s\nabla\cdot\bar{u}_s+\bar{u}_s\cdot\beta(\bar{u}_f-\bar{u}_s) \tag{3.53}$$

The balance for the change of the total mechanical energy of an ensemble of particles per unit volume per unit time is then given by:

$$\frac{D}{Dt}(\frac{1}{2}\varepsilon_s\rho_s\bar{u}_s^2)+\frac{D}{Dt}(\frac{3}{2}\varepsilon_s\rho_s\theta)-\varepsilon_s\rho_s\bar{u}_s\cdot\bar{g}= \\ -\varepsilon_s\bar{u}_s\cdot\nabla p_f-\nabla\cdot(\varepsilon_s\bar{\bar{\tau}}_s\cdot\bar{u}_s)-\nabla\cdot p_s\bar{u}_s+\bar{u}_s\cdot\beta(\bar{u}_f-\bar{u}_s)-\nabla\cdot(\varepsilon_s q_s)-3\beta\theta-\gamma \tag{3.54}$$

The macroscopic mechanical energy balance for all the particles in the fluidised bed can be obtained from this equation by summation over all computational cells. This results in:

$$\frac{\partial}{\partial t}\left(E_{conv}+E_{gran}+E_{pot}\right)=V_{cell,k}\times \\ \sum_k^{Ncell}\left(-\varepsilon_s\bar{u}_s\cdot\nabla p_f-\nabla\cdot(\varepsilon_s\bar{\bar{\tau}}_s\cdot\bar{u}_s)-\nabla\cdot p_s\bar{u}_s+\bar{u}_s\cdot\beta(\bar{u}_f-\bar{u}_s)-\nabla\cdot(\varepsilon_s q_s)-3\beta\theta-\gamma\right) \tag{3.55}$$

For a system with non-moving walls that do not dissipate any energy this equation can be further simplified to obtain:

$$\frac{\partial}{\partial t}\left(E_{conv}+E_{gran}+E_{pot}\right)=W_{press}+W_{drag}+W_{drag,gran}+W_{rest} \tag{3.56}$$

The expressions for all terms in this equation are given in table 3.3. When comparing equation 3.56 to equation 3.50 it seems that there is an extra contribution of work done by drag, but it can easily be proofed that the sum of the two drag contributions in equation 3.56 equals the work performed by drag in equation 3.50.

Rather than solving the complete granular temperature balance some researchers (e.g. Syamlal et al., 1993; Boemer et al., 1995; van Wachem et al., 1999) assume that granular temperature is generated and dissipated locally, because the generation and dissipation terms dominate this balance in dense flows. In this so-called local equilibrium approach accumulation, convection and diffusion of granular energy are neglected and clearly the total mechanical energy balance is not satisfied. To guarantee satisfaction of this balance for the suspended particulate phase, it might even be better to design new numerical algorithms, that solve equation 3.55 in stead of the granular temperature equation or perform a check on its fulfilment.

4.3. Comparison of CFD models

An example of an energy analysis that was performed for the discrete particle simulation at 1.50 U_{mf} is given in figure 3.8. It can be observed from this figure that the energy levels continuously change as a result of dissipation and the forces acting on the particles. To compare these results for different simulation types and conditions they were time-averaged over the last 5 seconds of the simulation. The absolute energy levels and amounts of work performed and dissipated are summarised in table 3.4. This table also reports the relative contribution of all the terms from which they originate.

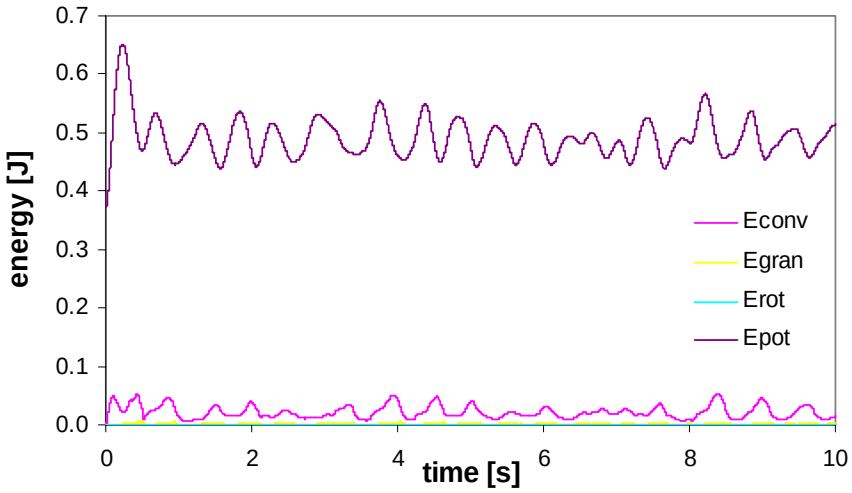

a) Energy levels versus time.

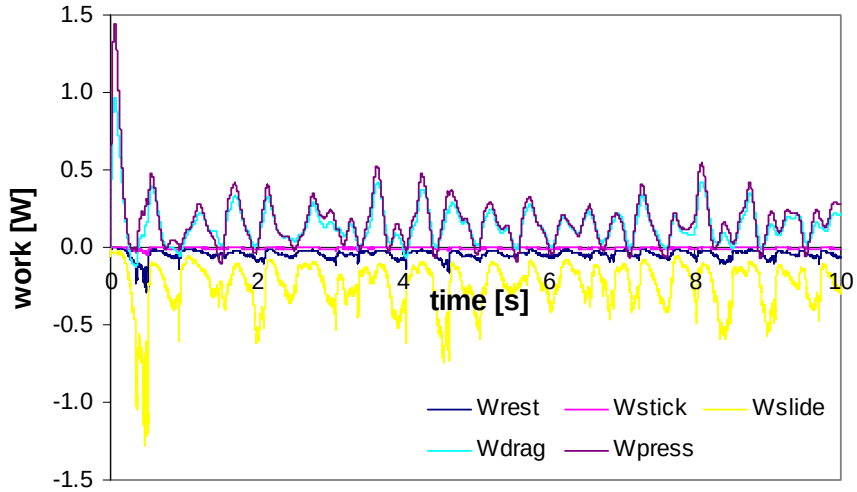

b) Work versus time.

Figure 3.8. Energy analysis for DPM simulation at 1.5 U_{mf}.

Table 3.4. Time averaged result of energy balance analysis (t = 5-10 s).

	fluidisation velocity	E_{tot} [J]	E_{pot} / E_{tot}	E_{gran} / E_{tot}-E_{pot}	E_{conv} / E_{tot}-E_{pot}	E_{rot} / E_{tot}-E_{pot}	W_{gas} [W]	W_{press} / W_{gas}	W_{drag} / W_{gas}	$W_{drag,gran}$ / W_{gas}	W_{dis} [W]	W_{rest} / W_{dis}	W_{stick} / W_{dis}	W_{slide} / W_{dis}	remarks
DPM	1.25 U_{mf}	0.431	99%	13%	85%	2%	0.099	55%	45%	-	-0.097	16%	2%	82%	
DPM	1.50 U_{mf}	0.507	96%	8%	91%	1%	0.284	53%	47%	-	-0.281	15%	2%	82%	
DPM	2.00 U_{mf}	0.660	91%	7%	92%	1%	0.584	49%	51%	-	-0.572	16%	2%	82%	
TFM	1.25 U_{mf}	0.430	99%	28%	72%	-	0.056	72%	33%	-6%	-0.057	100%	-	-	
TFM	1.50 U_{mf}	0.484	98%	25%	75%	-	0.060	70%	38%	-8%	-0.059	100%	-	-	
TFM	2.00 U_{mf}	0.619	95%	17%	83%	-	0.142	37%	72%	-9%	-0.105	100%	-	-	
Grid refinement															
TFM	1.50 U_{mf}	0.489	98%	26%	74%	-	0.078	65%	42%	-7%	-0.078	100%	-	-	fine grid
TFM	2.00 U_{mf}	0.638	95%	19%	81%	-	0.164	49%	60%	-9%	-0.145	100%	-	-	fine grid
Wall effects															
DPM	1.50 U_{mf}	0.496	96%	8%	91%	1%	0.169	51%	49%	-	-0.248	15%	2%	82%	ideal front and back wall
TFM	1.50 U_{mf}	0.485	98%	20%	80%	-	0.063	64%	44%	-7%	-0.053	100%	-	-	3D, fine grid
DPM	1.50 U_{mf}	0.499	95%	8%	92%	1%	0.190	54%	46%	-	-0.188	20%	3%	77%	all walls ideal
TFM	1.50 U_{mf}	0.481	99%	28%	72%	-	0.047	69%	40%	-9%	-0.049	100%	-	-	all walls ideal
Effect of rotation															
DPM	1.50 U_{mf}	0.477	98%	30%	70%	-	0.092	59%	41%	-	-0.082	100%	-	-	no rotation
Effect of drag model															
TFM	1.92 m/s	0.454	98%	27%	73%	-	0.166	63%	40%	-3%	-0.147	100%	-	-	drag Foscolo et al.
TFM	1.92 m/s	0.482	98%	26%	74%	-	0.110	63%	42%	-6%	-0.104	100%	-	-	drag Garside and Al-Dibouni
Effective restitution coefficient															
TFM	1.25 U_{mf}	0.439	97%	7%	93%	-	0.162	45%	56%	-1%	-0.150	21 %			
TFM	1.50 U_{mf}	0.503	96%	6%	94%	-	0.248	47%	54%	-1%	-0.218	21 %			
TFM	2.00 U_{mf}	0.636	92%	5%	95%	-	0.428	58%	44%	-1%	-0.321	21 %			

4.3.1. Energy levels

From the basic simulations that were performed with both models to compare to the experiments, it can be concluded that the total energy accumulation predicted by both models at all operating conditions is about the same. Clearly for this specific system most energy is present as potential energy and the amount of rotational energy is negligible at all operating conditions. Further the part of the total kinetic energy that is contained in fluctuating granular motion is much higher in the continuum simulations than in the discrete particle simulations. This is consistent with earlier observations that the average granular temperature levels were about the same for both models (see figure 3.4) while particle phase convection was much stronger in the discrete particle simulations (see figure 3.3). But the results of the energy analysis much clearer put forward that a comparison of granular temperatures only makes sense if the total convective kinetic energy of the particles is also taken into account.

The absolute energy levels and the distribution between kinetic, potential and rotational energy are hardly influenced by grid refinement, wall effects and the choice of the drag model. Only in the 3D two-fluid simulation a somewhat lower fluctuating kinetic energy level is observed due to the increased energy dissipation by the walls. The results for the discrete particle simulation without rotation on the other hand show a clear increase in fluctuating kinetic energy whereas the total kinetic energy decreases as a result of the formation of smaller bubbles. This improves the agreement between the models significantly and the energy analysis confirm that the main difference between the two CFD models is caused by absence of rotation in the two-fluid model.

4.3.2. Work performed by the gas phase

In both models the total work performed by the interstitial gas phase increases as the fluidisation velocity increases, but at all velocities the performed work is much higher in the discrete particle simulations than in the continuum simulations. In all discrete particle simulations, accept the one in which rotation is neglected, about 50% of the total work performed by the gas phase originates from the far field pressure gradient and the other 50% by the drag force. In general the contribution of the far field pressure gradient was higher in the two-fluid simulations. This can be explained when it is considered that bubbles act as a short cut with low flow resistance for the upward flowing gas phase. The formation of smaller bubbles in the two-fluid simulations thus results in a higher pressure drop over the bed, which leads to a larger contribution of the far field pressure gradient.

The amount of work performed by the gas phase in the two-fluid simulations seems to be strongly affected by grid refinement, wall effects and the choice of the drag model. As a result of grid refinement the amount of work performed by the gas phase increased significantly. Further, as one would expect, more work has to be performed by the gas phase if particle wall interactions become less ideal and more energy is lost in particle wall collisions. Further both alternative drag models show a significant increase in the total amount of work performed by the gas phase.

4.3.3. Energy dissipated in collisions

Total clarity about the influence of particle rotation on the bed dynamics of the simulated system is obtained when the contribution to the total energy dissipation by normal restitution, sticking and sliding is examined. Even though the rotational energy is low, over 80% of the total energy is dissipated due to sliding friction.

It can also be noted from table 3.4 that the dissipated amount of energy does not always exactly equal the amount of work performed by the gas phase. This is caused by accumulation during the time integration interval and disregard of energy leakage to the walls in the energy analysis for the continuum model.

4.3.4. Correction of energy dissipation for the effect of rotation

In principle particle rotation can be incorporated in the two-fluid model by addition of an extra conservation equation for fluctuating spin (Jenkins and Richman, 1985; Lun and Savage 1987). However, since the most important influence of particle rotation on the observed bed dynamics seems to be the additional energy dissipation, a simpler approach in which only the energy dissipation term in the granular temperature balance is modified seems promising. A simple kinetic theory for rapid flow of identical, slightly frictional, nearly elastic spheres (such as glass beads) that is based on the collision model presented in paragraph 2.2., is derived by Zhang and Jenkins (Zhang, 1993; Jenkins and Zhang, 2000). Because the coefficient of friction is assumed to be small, the structure of the resulting theory is essentially the same as that for frictionless spheres. In fact, the only modification that needs to be made is the introduction of an effective coefficient of restitution that incorporates the additional dissipation due to frictional interactions. The effective coefficient of restitution that was derived for simple shearing flow is given by:

$$e_{eff} = e_n - \frac{1}{2}a_1 + \frac{1}{2}\frac{a_2 b_1}{b_2} \tag{3.57}$$

The only equations that need to be modified are the expressions for the dissipation terms in the granular temperature equation and the partial slip boundary condition:

$$\gamma = 3(1+e_n)(1-e_{eff})\varepsilon_s^2 \rho_s g_0 \theta \left[\frac{4}{d_p}\sqrt{\frac{\theta}{\pi}} - (\nabla \cdot \bar{u}_s) \right] \tag{3.58}$$

$$\varepsilon_s \bar{q}_s \cdot \bar{n} = -\bar{u}_s \cdot \varepsilon_s \bar{\bar{\tau}}_s \cdot \bar{n} + \frac{\sqrt{3}\pi(1+e_{n,wall})(1-e_{wall,eff})\varepsilon_s \rho_s g_0 \sqrt{\theta}}{4\varepsilon_0}\theta \tag{3.59}$$

The coefficients a_1, a_2, b_1 and b_2 are defined as (Jenkins and Zhang, 2000):

$$a_1 = \frac{\mu}{\mu_0}\left[\pi\mu_0 (1 - \frac{2}{\pi}\arctan\mu_0) + \frac{2\mu_0^2}{1+\mu_0^2}(1 - 2\frac{\mu}{\mu_0}) \right] \tag{3.60}$$

$$a_2 = 5\frac{\mu}{\mu_0}\left[\frac{\pi}{2}\mu_0 (1 - \frac{2}{\pi}\arctan\mu_0) - \frac{\mu_0^4}{(1+\mu_0^2)^2} \right] \tag{3.61}$$

$$b_1 = \left(\frac{\mu}{\mu_0}\right)^2 \frac{\mu_0^2}{1+\mu_0^2} \tag{3.62}$$

$$b_2 = \frac{\mu}{2\mu_0}\left[\frac{\pi}{2}\mu_0 (1 - \frac{2}{\pi}\arctan\mu_0) + \frac{\mu_0^2}{1+\mu_0^2} \right] \tag{3.63}$$

In the above equations μ_0 is the tangent of the critical angle Φ_0 between the normal and the tangential component of the impact velocity at which the transition from sticking to sliding collision takes place:

$$\mu_0 = \tan\Phi_0 = \frac{7}{2}\frac{\mu(1+e_n)}{(1+\beta_0)} \tag{3.64}$$

When the impact angle is larger than the critical angle Φ_0 a sliding collision occurs. The relation between the effective restitution coefficient and the coefficients of friction and tangential restitution is presented in figure 3.9. It can be seen that the effective restitution

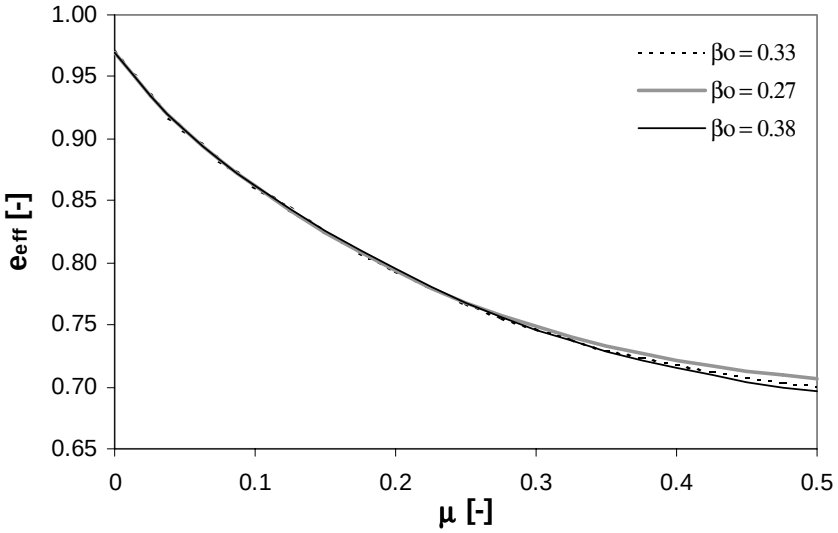

Figure 3.9. Effective coefficient of restitution versus the coefficient of restitution for e_n = 0.97 and three different values for the coefficient of tangential restitution.

coefficient is much more sensitive to the coefficient of friction than to the coefficient of tangential restitution, since most energy is dissipated in sliding collisions. The effective coefficient of restitution that is obtained for particle-particle interactions based on the particle properties specified in table 3.1 is 0.86. For particle-wall collisions an effective restitution coefficient of 0.87 is found.

Simulations that were carried out with the new energy dissipation model show much better agreement with the results of the discrete particle model as can be seen from tables 3.2 and 3.4. Larger bubbles are formed and consequently the intensity of the bed height fluctuations increases while the bed expansion frequency decreases. The energy levels and especially the distribution of the particle phase kinetic energy between fluctuating granular motion and convection show much better agreement with the discrete particle simulations. Also energy production and dissipation rates agree better. So the introduction of an effective restitution coefficient that incorporates the additional energy dissipation due to frictional interactions in the two-fluid model significantly improves the results of the continuum model.

Discussion and conclusions

A comparison of a hard-sphere discrete particle model, a two-fluid model with kinetic theory closure equations and experiments in a pseudo two-dimensional gas-fluidised bed has been made. The discrete particle simulations were performed with a 3D hard-sphere model and the experiments were carried out with particles with well know collision parameters, which enabled a critical comparison of the results. Bubble patterns, time-averaged particle distributions and bed expansion dynamics measured with a non-intrusive digital image analysis technique were compared to simulation results at three different fluidisation velocities.

In all comparisons with experimental results the discrete particle model gave closer resemblance. It was better capable of capturing complex structures such as initialisation of small bubbles near the bottom of the bed and strings of particles within larger bubbles. Time-averaged particle volume fractions obtained with the discrete particle model reflected the experimental results better and bed expansion analyses gave better results as well. The difference between both CFD models was mainly caused by neglect of particle rotation in the kinetic theory closure equations applied by the two-fluid model. Energy balance analysis demonstrated that over 80% of the total energy dissipation was caused by sliding friction. Introduction of an effective restitution coefficient that incorporated the additional energy dissipation due to frictional interactions significantly improved the agreement between both models.

Energy balance analysis proved to be a sensitive tool to study the effect of particle-wall interaction and gas-particle drag on fluidised bed dynamics. The mechanical energy balance combines the total energy of the suspended particles with the energy supplying forces and energy dissipating mechanisms that dominate the dynamics of gas-fluidised beds. It is therefore believed that this balance should play an important role in the continuing search for scale up rules for granular flows in general and more specifically for (dense) gas-fluidised beds.

For both CFD models the simulated flow fields and granular temperature profiles were compared. The results indicated that the kinetic theory of granular flow gave meaningful estimates for the particle phase fluctuating velocity, which is one of the key parameters in the closure equations. However, the results of energy analysis clearly put forward that a

comparison of granular temperatures only makes sense if the total convective kinetic energy of the particles is also taken into account.

The most critical comparison between experiments and modelling results was given by analysis of the bed expansion dynamics. Though both models predicted the right fluidisation regime and trends in bubble sizes and bed expansion, the predicted bed expansion dynamics differed significantly from the experimental results. Alternative gas-particle drag models resulted in significantly different bed dynamics, but the gap between modelling and the experimental results could not be closed. Visual observation of the experiments made clear that the differences were mainly caused by the formation of densely packed regions in which no particle vibration was observed. Formation of such areas did not occur in the simulations and it was concluded that long-term particle contacts and multi-particle interactions most likely caused the gap with the experiments. Hard-sphere discrete particle models cannot account for these contacts and they are neglected in the derivation of the closures for the continuum model according to the kinetic theory of granular flow. A simple frictional viscosity model from the field of soil mechanics could not improve the simulated bed dynamics.

Chapter 4.

Comparison of the kinetic theory of granular flow with 3D hard-sphere discrete particle simulations

Abstract

A novel technique to sample particle velocity distributions and collision characteristics from dynamic discrete particle simulations of intrinsically unsteady, non-homogeneous systems, such as encountered in dense gas-fluidised beds, is presented. The results are compared to the isotropic Maxwellian particle velocity distribution and the impact velocity distribution that constitute the zeroth-order Enskog approximation for the kinetic theory of granular flow. Excellent agreement with the kinetic theory is obtained for elastic particles. The individual particle velocity distribution function is isotropic and Maxwellian. A good fit of the collision velocity distribution and frequency is obtained, using the radial distribution function proposed by Carnahan and Starling (1969). However, for inelastic and rough particles an anisotropic Maxwellian velocity distribution is obtained. It is concluded that the formation of dense particle clusters disturbs spatial homogeneity and results in collisional anisotropy. Analysis of the impact velocity shows that, in dense gas-fluidised beds, not all impact angles are of equal likelihood. The observed anisotropy becomes more pronounced with increasing degree of inelasticity of the particles.

This chapter is based on the paper:

Goldschmidt M.J.V., Beetstra R., Kuipers J.A.M., 2001, Hydrodynamic modelling of dense gas-fluidised beds: Comparison of the kinetic theory of granular flow with 3D hard-sphere discrete particle simulations, submitted to *Chem. Eng. Sci.*

1. Introduction

Owing to the continuum description of the particulate suspension, Eulerian models require additional closure laws to describe particle-particle and/or particle-wall interactions. In most recent continuum models constitutive relations according to the kinetic theory of granular flow are incorporated. This theory is basically an extension of the classical kinetic theory of dense gases (Chapman and Cowling, 1970) to particulate flows, that takes non-ideal particle-particle collisions and gas-particle drag into account. Discrete particle models on the contrary do not require additional closure equations for the suspended particulate phase, since they compute the motion of every individual particle, taking collisions and external forces acting on the particles directly into account. However, the number of particles that these models can handle (i.e. typically less than 10^6) is orders of magnitude lower than that encountered in most (industrial) fluidised beds. Therefore continuum models constitute a more natural choice for hydrodynamic modelling of engineering scale systems, whereas discrete particle models can be applied as a valuable research tool to verify and further develop closure laws for these continuum models.

In the previous chapter a critical comparison is made of a 3D hard-sphere discrete particle model, a two-fluid model with kinetic theory closures and experiments performed in a pseudo two-dimensional gas-fluidised bed at three different operating conditions. In all comparisons of simulated bubble patterns, time averaged particle distributions and bed expansion dynamics, the discrete particle model showed superior resemblance with experimental results. Therefore the 3D hard-sphere discrete particle model will be applied in this chapter to assess the validity of several key assumptions made during the derivation of the closures according to the kinetic theory of granular flow.

Most kinetic theory closures that are nowadays applied in 'state-of-the-art' continuum models for gas-fluidised beds have been derived for smooth, rigid, nearly elastic, spherical particles. However, in many practical systems rough, inelastic particles are encountered, which makes application of the theory questionable. Therefore the effect of particle roughness (rotation) and coefficient of restitution on particle velocity distribution, collision velocity distribution and collision frequency in 3D hard-sphere discrete particle simulations are investigated. Also the implicitly assumed isotropy of the particle velocity distribution seems questionable for dense gas-fluidised beds for two reasons:

(1) The net action of all external forces in vertical direction will disturb isotropy of the particle velocity distribution, if particles are significantly accelerated between successive collisions,
(2) It seems unlikely that in dense particle clusters all impact angles are of equal likelihood, which causes collisional anisotropy that leads to anisotropic particle velocity distributions.
Therefore special attention will be paid to isotropy of the particle velocity distribution in this chapter.

2. Kinetic theory of granular flow

In most recent continuum models (e.g. Gidaspow, 1994; Balzer et al., 1995; Nieuwland et al., 1996; Mathiesen et al., 2000) constitutive equations according to the kinetic theory of granular flow are incorporated. This theory describes the dependence of the rheologic properties of the fluidised particles on local particle concentration and the fluctuating motion of the particles owing to particle-particle collisions. In the kinetic theory of granular flow the actual particle velocity ($\overline{c}$) is decomposed in a local mean solids velocity ($\overline{u}_s$) and a random fluctuating velocity ($\overline{C}$) according to:

$$\overline{c} = \overline{u}_s + \overline{C} \tag{4.1}$$

Associated with the random motion of the particles, analogous to the definition of the temperature of a gas in the classical kinetic theory for dense gases (Chapman and Cowling, 1970), the granular temperature θ for an ensemble of particles is defined as:

$$\theta \equiv \frac{1}{3} < \overline{C} \cdot \overline{C} > \tag{4.2}$$

where the brackets denote ensemble averaging. The variation of the particle velocity fluctuations is described with a separate conservation equation, the so-called granular temperature equation:

$$\frac{3}{2}\left[\frac{\partial}{\partial t}(\varepsilon_s \rho_s \theta) + \nabla \cdot (\varepsilon_s \rho_s \theta \ \overline{u}_s)\right] = -(p_s \overline{\overline{I}} + \varepsilon_s \overline{\overline{\tau}}_s) : \nabla \overline{u}_s - \nabla \cdot (\varepsilon_s q_s) + \beta(< \overline{C}_g \cdot \overline{C} > -3\theta) - \gamma \tag{4.3}$$

This equation brings forward the two conceptual extensions of the kinetic theory of granular flow with regard to the classical kinetic theory for dense gases. The first difference is the possible dissipation of fluctuating kinetic energy in a granular medium due to inelastic particle collisions, represented by the last term on the right hand side of equation 4.3. Furthermore, energy can be dissipated due to frictional interaction with the surrounding gas phase, which is taken into account by the second last term in equation 4.3. For the derivation of the granular temperature equation and the subsequent constitutive equations the interested reader is referred to the books by Chapman and Cowling (1970) and Gidaspow (1994) and the papers by Jenkins and Savage (1983), Ding and Gidaspow (1990) and Nieuwland et al. (1996). This chapter will be focussed on the validity of several key assumptions that support the framework of the kinetic theory of granular flow.

2.1. Velocity distribution and pair distribution function

The kinetic theory of granular flow is a statistical mechanical theory that describes the mean and fluctuating motion of particles within a continuous granular medium. The theory is based on the assumption that the velocity distribution $f(\bar{c},\bar{r},t)$ of individual particles, among a large number $nd\bar{r}$ of particles within an ensemble of volume $d\bar{r}$, can be represented by the distribution of their velocity-points $\bar{c}$ in the velocity space. The number of particles per unit volume and the ensemble average of a particle quantity ϕ are respectively given by:

$$n = \int f(\bar{c},\bar{r},t)\, d\bar{c} \tag{4.4}$$

$$< \phi >= \frac{1}{n} \int \phi\ f(\bar{c},\bar{r},t)\, d\bar{c} \tag{4.5}$$

The kinetic theory of granular flow accounts for two different transport mechanisms of particle properties. On the one hand particles can transport a property by carrying it during free flight between collisions (kinetic transport), on the other hand particle quantities can be transferred during collision. The kinetic transport mechanisms is dominant in dilute systems where the mean free path between collisions is relatively long (e.g. dilute riser flow), whereas the collisional transport mechanism dominates in dense systems where the particles are close together and the collision frequency is much higher (e.g. dense gas-fluidised beds). Modelling these transport mechanisms results in the well-known Boltzmann integral-differential equation, which describes the rates of change of

the velocity distribution function f of particles moving under influence of an external force $\bar{F}$:

$$\frac{Df}{Dt} + \bar{C} \cdot \nabla f + \frac{\partial}{\partial \bar{C}} \cdot (\bar{F} f) - \frac{D\bar{u}_s}{Dt} \cdot \frac{\partial f}{\partial \bar{C}} - \frac{\partial f}{\partial \bar{C}} \bar{C} : \nabla \bar{u}_s = \frac{\partial_e f}{\partial t} \tag{4.6}$$

The left-hand side in this equation originates from the kinetic transport mechanism and the right-hand side emerges from collisional interactions. In the derivation of most kinetic theories the external forces (i.e. friction with the gas phase, far field pressure gradient and gravity) are assumed to be velocity independent. The collisional transport mechanism is described using a pair distribution function $f_{12}(\bar{c}_1, \bar{r}_1, \bar{c}_2, \bar{r}_2, t)$ that represents the probability of finding a pair of particles at time t in volumes $d\bar{r}_1$ and $d\bar{r}_2$ centred at $\bar{r}_1$ and $\bar{r}_2$ having velocities between $\bar{c}_1$ and $\bar{c}_1 + d\bar{c}_1$ and $\bar{c}_2$ and $\bar{c}_2 + d\bar{c}_2$ respectively. Just as the classical kinetic theory the kinetic theory of granular flow assumes 'molecular' chaos. This implies that all particles are homogeneously distributed within an ensemble (no structure formation), that the particle velocity distribution for all particles is isotropic and that the velocities of two particles involved in a collision are not correlated. Then, following Enskog (Chapman and Cowling, 1970), the pair distribution function can be approximated by the product of two single-particle velocity distribution functions and the radial distribution function g_0, that corrects the probability of a collision for the effect of the volume occupied by the particles:

$$f_{12}(\bar{c}_1, \bar{r}_1 - d_p \bar{k}, \bar{c}_2, \bar{r}_2, t) = g_0(\bar{r}_1 - \frac{1}{2} d_p \bar{k})\, f(\bar{c}_1, \bar{r}_1 - d_p \bar{k}, t)\, f(\bar{c}_2, \bar{r}_2, t) \tag{4.7}$$

Using the Enskog approximation, the Boltzmann equation can be solved to obtain the velocity distribution function f, which is required to model the kinetic transport mechanism. The velocity distribution function can be obtained from the Boltzmann equation using Grad's method of moments (Grad, 1949, 1963) or Enskog's method of solution (Chapman and Cowling, 1970), which supposes that the solution is expressible in the form of an infinite series:

$$f = f^{(0)} + f^{(1)} + f^{(2)} + \ldots \tag{4.8}$$

The zeroth-order solution to the velocity distribution function is the well-known Maxwell velocity distribution function, which describes the steady-state equilibrium condition without action of any external forces:

$$f^{(0)} = \frac{n}{(2\pi\theta)^{3/2}} e^{\frac{-C^2}{2\theta}} \tag{4.9}$$

The first-order solution to the velocity distribution function is written as a first-order perturbation to the Maxwellian state:

$$f^{(1)} = f^{(0)}(1+\Phi^{(1)}) \tag{4.10}$$

where

$$\Phi^{(1)} = -\frac{1}{ng_0}\left\{(1+\frac{12}{5}\varepsilon_s g_0)A(C)\overline{C}\cdot\nabla\ln\theta + (1+\frac{8}{5}\varepsilon_s g_0)\frac{B(C)}{\theta}\overline{\overline{C}\overline{C}}:\nabla\overline{u}_s\right\} \tag{4.11}$$

In chapter 5, Chapman and Cowling (1970) and Nieuwland (1995) it is shown in more detail how to derive the first-order perturbation function $\Phi^{(1)}$. The complexity of higher-order terms increases rapidly, which makes a quick convergence of the series a necessity.

2.2. Isotropy

In this paragraph it will be shown how a Maxwellian velocity distribution can be obtained from a simple argument. Often, researchers working on particulate systems implicitly use this well-known argument (Maxwell, 1866), when they state that in first approximation the individual particle velocity distribution is Maxwellian. The basis of the argument is formed by the assumption that the velocities of the particles in the ensemble are isotropically distributed around a local mean velocity, as in the case of 'molecular' chaos. It is assumed that the three velocity components of a particle are independent of each other, and so

$$f(C_x,C_y,C_z)dC_x dC_y dC_z = f(C_x)f(C_y)f(C_z)dC_x dC_y dC_z \tag{4.12}$$

Further the probability of a particle having a particular range of velocity components is assumed to be independent of its direction of flight. So the velocity distribution function depends on the speed, but not on the individual components:

$$f(C)dC = f(C_x)f(C_y)f(C_z)dC_x dC_y dC_z \tag{4.13}$$

Since $C^2 = C_x^2 + C_y^2 + C_z^2$ only an exponential function can satisfy a relation of this kind, consequently:

$$f(C_x) = Ae^{\pm BC_x^2} \tag{4.14}$$

On physical grounds the probability of extremely high velocities must be very small, so the negative sign must be taken in the exponent. Further the particle fluctuating velocity has to be in the range $-\infty < C_x < \infty$ and the total probability of the *x*-component being in that range is 1, so the constant A can be determined:

$$\int_{-\infty}^{\infty} f(C_x)dC_x = A\int_{-\infty}^{\infty} e^{-BC_x^2}\,dC_x = A\left(\frac{\pi}{B}\right)^{1/2} = 1 \tag{4.15}$$

Therefore:

$$f(C_x) = \left(\frac{B}{\pi}\right)^{1/2} e^{-BC_x^2} \tag{4.16}$$

The constant B can be determined by calculating the mean value of C_x^2:

$$< C_x^2 >= \int_{-\infty}^{\infty} C_x^2\, f(C_x)\, dC_x = \left(\frac{B}{\pi}\right)^{1/2} \int_{-\infty}^{\infty} C_x^2 e^{-BC_x^2} dC_x = \frac{1}{2B} \tag{4.17}$$

Now by introduction of the granular temperature in the *x*-direction:

$$\theta_x \equiv < C_x C_x > \tag{4.18}$$

the normalised particle velocity distribution in the *x*-direction becomes a well-known Gaussian distribution around the ensemble mean velocity u_x with standard deviation θ_x:

$$f_x(C_x) = \frac{1}{(2\pi\theta_x)^{1/2}} e^{\frac{-C_x^2}{2\theta_x}} \tag{4.19}$$

Then the velocity distribution of the particles irrespective of the direction of motion can also be derived as:

$$f(C)dC = \frac{1}{(2\pi\theta_x)^{1/2}}\frac{1}{(2\pi\theta_y)^{1/2}}\frac{1}{(2\pi\theta_z)^{1/2}} e^{-\left(\frac{C_x^2}{2\theta_x}+\frac{C_y^2}{2\theta_y}+\frac{C_z^2}{2\theta_z}\right)} dC_x dC_y dC_z \tag{4.20}$$

When isotropy is assumed $\theta_x = \theta_y = \theta_z$, and using $\theta = (\theta_x + \theta_y + \theta_z)/3$ and $dC_x dC_y dC_z = 4\pi C^2 dC$, the normalised Maxwellian particle velocity distribution is obtained:

$$f(C) = 4\pi C^2 \frac{1}{(2\pi\theta)^{3/2}} e^{\frac{-C^2}{2\theta}} \tag{4.21}$$

From this argument it becomes clear that if a (particle) velocity distribution is presumed to be isotropic and Gaussian in each direction, a Maxwellian distribution is obtained. The argument clearly brings forward the consequences of the assumption of 'molecular' chaos that is made in the derivation of the kinetic theory of granular flow. It also shows that inequalities of the granular temperatures sampled in several directions lead to an anisotropic triaxial Gaussian velocity distribution.

2.3. Impact velocity distribution and frequency

Two important results of the kinetic theory of granular flow are the impact velocity distribution and the particle-particle collision frequency. They are a direct consequence of the assumptions that are made regarding the particle velocity distribution function f and the pair distribution function f_{12}. Together with the coefficient of restitution they determine the amount of momentum that is exchanged and dissipated in collisions between particles in an ensemble per unit time. So the impact velocity and frequency are key variables determining the collisional contribution to the rheologic parameters, such as the particle pressure and viscosity, of a continuous particulate suspension and the amount of energy that is dissipated in non-ideal collisions.

Within the kinetic theory of granular flow the distribution of collisions with impact velocity c_{12} is obtained by integration of the pair distribution f_{12} function over the volume of the collision cylinder and all possible impact angles. Assuming that all impact angles are of the same likelihood the zeroth-order approximation of the impact velocity distribution is represented by (see Chapman and Cowling (1970) for derivation):

$$f_{12}^{(0)} = n^2 d_p^2 g_0 (2\pi)^{1/2} \left(\frac{1}{2\theta}\right)^{3/2} e^{\frac{-c_{12}^2}{4\theta}} c_{12}^3 \tag{4.22}$$

The collision frequency per unit volume can be found by integration over all possible impact velocities c_{12}:

$$N_{12}^{(0)} = \int_0^\infty f_{12}^{(0)} \quad dc_{12} = 4n^2 d_p^2 g_0 \sqrt{\pi\theta} \tag{4.23}$$

One should realise that, since equation 4.23 counts each collision between a pair of particles twice over, the number of collisions between pairs of molecules per unit volume is given by $N_{12}^{(0)} / 2$. On the other hand the average number of collisions of any particle is $N_{12}^{(0)} / n$, since each collision affects two particles at once. Division of the collision velocity distribution by $N_{12}^{(0)}$ leads to the dimensionless collision velocity distribution:

$$f_{12}^{(0)}(c_{12}) = \frac{c_{12}^3}{8\theta^2} e^{\frac{-c_{12}^2}{4\theta}} \tag{4.24}$$

Another interesting quantity that can be calculated is the average impact velocity. It is given by:

$$< c_{12} >_{Maxwell} = \frac{1}{N_{12}^{(0)}} \int_0^\infty c_{12} f_{12}^{(0)} \quad dc_{12} = \frac{3}{2}\sqrt{\pi\theta} \tag{4.25}$$

2.4. Radial distribution function

As shown in the previous paragraph the radial distribution function is a key parameter in the particle collision frequency and therefore its choice should receive thorough attention. In molecular dynamics simulations the radial distribution function is often applied to characterise the structure of atomic fluids. In the kinetic theory of granular flow the radial distribution function is applied to correct the probability of a collision for the effect of the volume occupied by the particles, so only its value at the point of contact is of interest. Further, because only slightly inelastic collisions are considered, it is assumed that collisional anisotropy is of little importance, which means that the radial distribution

function only depends on the local particle volume fraction. Therefore the radial distribution at the point of particle contact $g_0(\overline{r_1} - d_p\overline{k}/2)$ is mostly given as $g_0(\varepsilon_s)$ in literature regarding gas-fluidised bed continuum modelling.

Anisotropic radial distribution functions have, to the authors' knowledge, never been applied in continuum simulations for dense gas-fluidised beds. However, if mechanical energy is dissipated in a collision the post-collision velocities of the particles involved are positively correlated. This is one of the reasons why particle clusters, in which all impact angles are most likely not of equal likelihood, are formed in dense granular flows. Anisotropy will also be introduced if particles are significantly accelerated by external forces or subjected to a mean shear field. In early work on the kinetic theory of granular flow a radial distribution function that accounts for anisotropic distribution of collisions due to exposure of the particle ensemble to a mean shear field was introduced by Savage and Jeffrey (1981). Their arguments were adopted by Jenkins and Savage (1983) who argued that the anisotropic radial distribution function should, except from the solids concentration and the particle positions, also depend upon the granular temperature at the point of contact and the mean field velocity at the positions of the particles. Based on an argument of dimensional consistency Jenkins and Savage (1983) proposed:

$$g(\overline{r_1},\overline{r_2}) = g_0(\varepsilon_s)\left[1 - \frac{\alpha d_p \overline{k}\;\;\overline{k} : \nabla \overline{u}_s}{\sqrt{\pi\theta}}\right] \tag{4.26}$$

Here α is an arbitrary function of the solids fraction (and other dimensionless quantities) that remained to be specified. In their early work Savage and Jeffrey (1981), Jenkins and Savage (1983) and Lun et al. (1984) applied the radial distribution function proposed for dense rigid spherical gases by Carnahan and Starling (1969):

$$g_0(\varepsilon_s) = \frac{2 - \varepsilon_s}{2\left(1 - \varepsilon_s\right)^3} \tag{4.27}$$

This expression is in almost exact agreement with molecular dynamics calculations for particle volume fractions up to about 0.55, but above this it predicts values that are too low. To obtain better agreement for high volume fractions and prevent particle volume fractions higher than the theoretical maximum packing density for uniform spheres, $\varepsilon_s^{max} = \pi/3\sqrt{2} = 0.7405$, Savage (1988) used a simple expression for the radial

distribution in his later work. This expression is implicit in the work of Bagnold (1954) and was given later by Ogawa et al. (1980):

$$g_0(\varepsilon_s) = \left[1 - \left(\frac{\varepsilon_s}{\varepsilon_s^{\max}}\right)^{1/3}\right]^{-1} \tag{4.28}$$

Interestingly, Savage (1988) noticed that predictions for stresses were closer to experimental results, for what are probably realistic values of the coefficient of restitution, if the maximum packing density for randomly packed spheres ($\varepsilon_s^{\max} \approx 0.64$) was applied. Ding and Gidaspow (1990) suggested modifying equation 4.28 to get a better match with the data of Alder and Wrainwright (1960):

$$g_0(\varepsilon_s) = \frac{3}{5}\left[1 - \left(\frac{\varepsilon_s}{\varepsilon_s^{\max}}\right)^{1/3}\right]^{-1} \tag{4.29}$$

However, this radial distribution function does not approach 1 for dilute systems. To the authors' knowledge the best fit of the data by Alder and Wrainwright (1960) is presented by Ma and Ahmadi (1986):

$$g_0(\varepsilon_s) = 1 + 4\varepsilon_s \frac{1 + 2.5000\varepsilon_s + 4.5904\varepsilon_s^2 + 4.515439\varepsilon_s^3}{\left[1 - (\frac{\varepsilon_s}{\varepsilon_s^{\max}})^3\right]^{0.67802}} \tag{4.30}$$

with $\varepsilon_s^{max} = 0.64356$.

The main advantage of discrete particle models over continuum models is that they do not make assumptions regarding the structure of the particulate suspension, distribution of the impact angle and possible correlation between the velocities of colliding particles. Therefore hard-sphere discrete particle models can be applied to identify which radial distribution function could best be applied in continuum simulations, as will be demonstrated in this chapter.

2.5. Coefficient of restitution

The single parameter collision model applied in the kinetic theory of granular flow is based upon the velocity difference $\overline{c}_{12}$ between centres of mass of the particles 1 and 2 involved in the collision:

$$\overline{c}_{12} = \overline{c}_1 - \overline{c}_2 \tag{4.31}$$

Since the theory assumes the particles to be smooth, particle velocity changes in the tangential impact direction are neglected. The coefficient of normal restitution e_n is applied to describe the relation between impact and rebound velocities. The relation between the particle velocities before and after collision (indicated by superscript ') according to the kinetic theory of granular flow is given by:

$$\overline{c}'_{12} = \overline{c}'_{12,n} + \overline{c}'_{12,t} = -e_n \overline{c}_{12,n} + \overline{c}_{12,t} \tag{4.32}$$

However, to give a reasonably accurate description of experiments performed with real macroscopic spheres by Maw et al. (1981), Foerster et al. (1994) and Gorham and Kharaz (1999) a three-parameter collision model, based on the actual impact velocity at the point of contact of particles 1 and 2, is required. For a binary collision between two rigid spheres the impact velocity at the point of contact is defined as:

$$\overline{v}_{12,0} = (\overline{c}_1 - \overline{c}_2) - (R_1\overline{\omega}_1 + R_2\overline{\omega}_2)\cdot\overline{t} \tag{4.33}$$

The normal and tangential unit vectors that define the collision co-ordinate system in are given by (the subscript $_0$ refers to the velocity before impact):

$$\overline{n} = \frac{\overline{r}_1 - \overline{r}_2}{\left|\overline{r}_1 - \overline{r}_2\right|} \tag{4.34}$$

$$\overline{t} = \frac{\overline{v}_{12,0} - \overline{n}(\overline{v}_{12,0}\cdot\overline{n})}{\left|\overline{v}_{12,0} - \overline{n}(\overline{v}_{12,0}\cdot\overline{n})\right|} \tag{4.35}$$

The particle rebound velocities according to this collision model can be calculated from:

$$m_1(\overline{v}_1 - \overline{v}_{1,0}) = -m_2(\overline{v}_2 - \overline{v}_{2,0}) = \overline{J} \tag{4.36}$$

$$\frac{2}{5} m_1 R_1 (\bar{\omega}_1 - \bar{\omega}_{1,0}) = \frac{2}{5} m_2 R_2 (\bar{\omega}_2 - \bar{\omega}_{2,0}) = \bar{J} \cdot \bar{t} \tag{4.37}$$

To calculate the impulse J, passed from particle 1 to particle 2, constitutive relations that account for energy dissipation due to non-ideal particle interaction are required. Based on three collision parameters, the coefficient of normal restitution ($0 \leq e_n \leq 1$), the coefficient of friction ($\mu \geq 0$) and the coefficient of tangential restitution ($0 \leq \beta_0 \leq 1$) the constitutive relations are given by:

$$\bar{J} \cdot \bar{n} = -(1 + e_n) \frac{m_1 m_2}{m_1 + m_2} (\bar{v}_{ab,0} \cdot \bar{n}) \tag{4.38}$$

$$(\bar{J} \cdot \bar{t})_{sliding} = -\mu (\bar{J} \cdot \bar{n}) \tag{4.39}$$

$$(\bar{J} \cdot \bar{t})_{sticking} = -(1 + \beta_0) \frac{2}{7} \frac{m_1 m_2}{m_1 + m_2} (\bar{v}_{ab,0} \cdot \bar{t}) \tag{4.40}$$

As in the single parameter collision model applied in the kinetic theory of granular flow, the coefficient of normal restitution describes the normal component of the impulse. The tangential component is described by equation 4.39 in the case of sliding collision and by the equation 4.40 in the case of sticking collision. The criterion to determine which type of impact occurs is based on comparison of the angle of impact Φ between the normal and the tangential component of the impact velocity at the point of contact:

$$\Phi = \arctan \frac{\bar{v}_{ab,0} \cdot \bar{t}}{\bar{v}_{ab,0} \cdot \bar{n}} \tag{4.41}$$

and the critical impact angle Φ_0 defined by:

$$\Phi_0 = \arctan \left(\frac{7}{2} \frac{\mu (1 + e_n)}{1 + \beta_0} \right) \tag{4.42}$$

When the impact angle is larger than the critical angle Φ_0 a sliding collision occurs, otherwise the collision is of the sticking type.

In chapter 3 it is demonstrated that neglecting particle roughness in discrete particle simulations results in totally different gas-fluidised bed dynamics. The most important

influence of particle rotation on the observed bed dynamics seemed to be due to additional energy dissipation. For the studied system, less than 20% of the total energy losses could be assigned to normal restitution, whereas over 80% of the kinetic energy losses were due to sliding friction. Therefore a simple single parameter collision model that takes energy dissipation due to rotation into account is discussed in appendix A. In this model the coefficient of restitution e is defined according to:

$$\vec{c}'_{12} = -e\,\vec{c}_{12} \tag{4.43}$$

The main advantage of such a collision model is that a simple expression for the total amount of energy lost per unit volume per unit time, which can be applied in continuum models, is obtained. However, as shown in appendix A, derivation of an expression that relates the measured collision parameters e_n, μ and β_0 to the coefficient of restitution e, requires information on the correlation between the translational and rotational particle velocities at the point of contact. A statistical mechanical theory that gives this correlation is, to the author's knowledge, not available at this point. However, the three-parameter collision model is nowadays widely applied in hard-sphere discrete particle models (Walton, 1993; Lun and Bent, 1994; Hoomans, 2000a). It will be shown in this chapter how simulations with such models can be applied to estimate the coefficient of restitution e, for a specific set of collision parameters and operation conditions.

3. Simulation conditions

The simulations are carried out with the 3D hard-sphere discrete particle model presented in chapter 3, that was originally developed by Hoomans (2000a). The model solves the Newtonian equations of motion for each individual particle and the Navier-Stokes equations for interpenetrating continua are applied for the gas-phase hydrodynamics. Both two-way coupling between gas and particles and particle-particle and particle-wall collisions are accounted for (i.e. four-way coupling). Collisions are described by hard-sphere collision laws, that taken energy dissipation due to non-ideal particle interactions into account by means of the empirical coefficients of normal restitution (e_n) and tangential restitution (β_0) and the coefficient of friction (μ). For a more detailed description of the model and the numerical solution technique the interested reader is referred to Hoomans et al. (1996), Hoomans (2000a) and chapter 3 of this thesis.

The studied pseudo two-dimensional system contains 24750 particles. It is the same system as applied in chapter 3 for the comparison and validation of the 3D hard-sphere

Table 4.1. Simulation conditions.

Bed dimensions:		*Particle properties:*	
Width (x-direction)	150 mm	Diameter	2.50 mm
Height (y-direction)	450 mm	Density	2526 kg/m^3
Depth (z-direction)	15 mm	Shape factor	1
		Minimum fluidisation velocity	1.28 m/s
Number of particles	24750		
Initial bed height	~ 15 cm		

Particle-particle collision parameters:

Case I	Case II	Case III	Case IV	Case V
$e_n = 1$	$e_n = 0.97$	$e_n = 0.97$	$e_n = 0.90$	$e_n = 0.90$
$\mu = 0$	$\mu = 0$	$\mu = 0.10$	$\mu = 0$	$\mu = 0.10$
$\beta_0 = 0$	$\beta_0 = 0$	$\beta_0 = 0.33$	$\beta_0 = 0$	$\beta_0 = 0.33$

discrete particle model and the two-fluid continuum model with kinetic theory closures presented in chapter 2. All system dimensions and particle properties are specified in table 4.1. Since the simulated system is a flat fluidised bed the motion of the gas in the depth direction is neglected and the gas phase hydrodynamics are resolved in 2D. A finite difference technique is used to solve the gas phase conservation equations that are computed on a 1 cm x 1 cm x 1.5 cm grid of 15 x 45 x 1 cells. To reduce numerical diffusion the second order accurate Barton scheme (Centrella and Wilson, 1984; Hawley et al., 1984) is applied to resolve the convective fluxes in the Navier-Stokes equations. For the gas phase a prescribed influx condition is applied at the bottom, free-slip boundary conditions are applied at the side walls and a prescribed pressure condition is applied at the top of the bed. In all simulations the minimum fluidisation condition is used as initial condition, where after the homogeneous gas inflow at the bottom is stepwise set to 1.5 U_{mf}. To prevent start-up effects from influencing the sampling results, all analyses are started after 5 seconds.

Fundamental hydrodynamic models have revealed a great sensitivity of the overall gas-fluidised bed dynamics to particle collision parameters (Hoomans et al., 1996; Goldschmidt et al., 2001a). Therefore, simulations are carried out with five different sets of collision parameters to study how the assumptions that constitute the framework of the kinetic theory of granular flow are affected. To prevent wall friction from influencing the

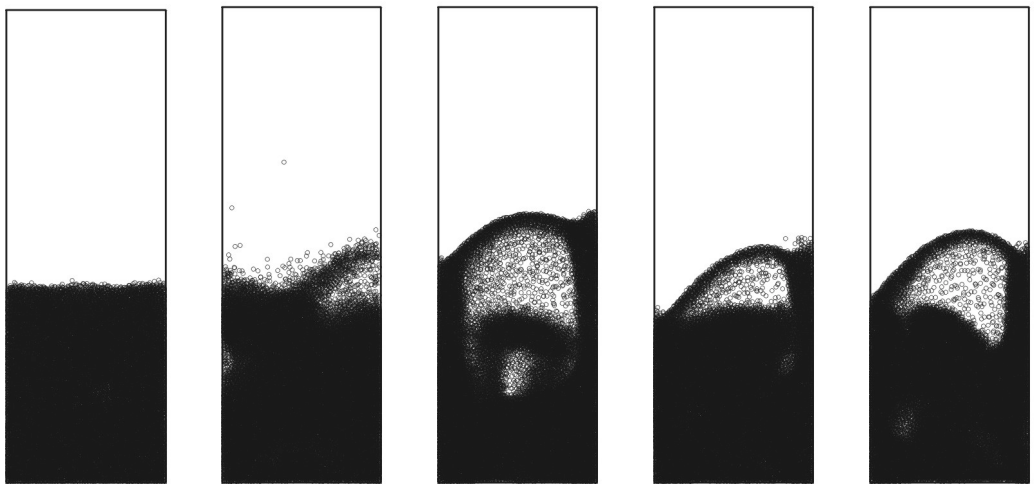

Figure 4.1. Snapshots of the simulations taken at the moment of bubble eruption.

results fully elastic, frictionless (ideal) particle-wall collision have been applied. Some snapshots of the simulations taken at the moment of bubble eruption are shown in figure 4.1. In case I particle-particle collisions are ideal and a nearly homogeneously expanded bed without bubbles is observed. In case II the coefficient of normal restitution is slightly non-ideal and a smoothly bubbling bed is obtained. In cases I, II and IV the particles do not rotate since particle-particle contacts are frictionless. The impact parameters applied in case III were measured for 2.5 mm spherical glass beads by Gorham and Kharaz (1999). For rough particles kinetic energy is transformed into rotation and subsequently more energy is dissipated in collisions. This explains why the bed dynamics observed for cases III and V are most vigorous and the largest bubbles are observed in those cases.

4. Sampling of individual particle velocity distribution functions

In this paragraph the method that is used to sample the particle velocity distribution functions $f_x(C_x)$, $f_y(C_y)$, $f_z(C_z)$ and f(C) from the dynamic discrete particle simulations will be discussed. The sampled velocity distributions will be compared to the normalised Gaussian and Maxwellian velocity distributions and isotropy will be studied.

To obtain a representative velocity distribution from a discrete particle simulation the averaging ensemble should contain a large number of particles. In principle the number of particles in the bed (24750) might be high enough and the velocity distribution of the

whole bed content could be taken as averaging ensemble. However, sampling of the velocity distributions is complicated by the intrinsically unsteady, non-homogeneous behaviour of gas-fluidised beds, that results in a continuously changing flow pattern within the bed. The particle velocity distribution is also a function of the granular temperature that varies with both time and position in the bed. So variations in flow pattern and granular temperature will interfere with sampling if the instantaneous velocity distribution in the whole bed or a time average of the particles at a fixed position in the bed is taken as averaging ensemble.

To remove the influence of the flow pattern and the variation of the granular temperature with position a grid is applied that splits the bed content into smaller particle ensembles. For these ensembles the local granular temperature is computed after every time step that is taken to compute the gas phase flow field. To obtain ensembles of a sufficiently large number of particles, as implied in the kinetic theory of granular flow, it is assumed that the particle velocity distribution mainly depends on the granular temperature. Therefore the observed granular temperature range is split into a discrete number of classes and particle ensembles obtained from t_{min} till t_{max} with granular temperatures within the range of the same granular temperature class are merged.

4.1. Details of the sampling procedure

To determine the particle velocity distributions an analysis grid of 15 x 45 x 1 cells (coarse grid) or 30 x 90 x 1 cells (fine grid) is projected on the simulated system. The cells of the coarse grid typically contain 80-110 particles, whereas the average number of particles per cell for the fine grid reduces to about 25. The granular temperatures of the ensemble in each grid cell k are calculated according to:

$$\theta_{k,x} = \frac{\sum_{i}^{N_{partk}} \overline{C}_{k,x}^{2}}{N_{part,k}} = \frac{\sum_{i}^{N_{partk}} (\overline{c}_{i,x} - \overline{u}_{s,k,x})^{2}}{N_{part,k}}, \quad \theta_{k,y} = \ldots \quad , \quad \theta_{k,z} = \ldots \tag{4.44}$$

and

$$\theta_{k} = \frac{1}{3} \frac{\sum_{i}^{N_{partk}} \overline{C}_{i}^{2}}{N_{part,k}} = \frac{1}{3} \frac{\sum_{i}^{N_{partk}} (\overline{c}_{i} - \overline{u}_{s,k})^{2}}{N_{part,k}} \tag{4.45}$$

whereby

$$\overline{u}_{s,k} = \frac{\sum_{i}^{N_{partk}} \overline{c}_i}{N_{part,k}}, \quad \overline{u}_{s,k,x} = \frac{\sum_{i}^{N_{partk}} \overline{c}_{i,x}}{N_{part,k}}, \quad \overline{u}_{s,k,y} = ..., \quad \overline{u}_{s,k,z} = ... \tag{4.46}$$

The granular temperatures that are observed in the simulations lie in the range from $1·10^{-5}$ up to $1·10^{-1}$ m^2/s^2. This range is split into 16 discrete classes of size $\Delta^{10}\log\theta = 0.25$. So the first class runs from $\theta = 1·10^{-5}$ till $1.78·10^{-5}$ m^2/s^2, the second from $\theta = 1.78·10^{-5}$ till $3.16·10^{-5}$ m^2/s^2, etc. To obtain the particle velocity distribution within each granular temperature class the particle velocity range is also split into 25 discrete classes of width Δv $(=0.25\sqrt{\theta})$. For the sampling of the velocity distributions in each direction (e.g. $f_x(C_x)$) the first class contains all particles with fluctuating velocities below the minimum $(C_x < -2.875\sqrt{\theta_x})$ and the last class all particles with fluctuating velocities above the maximum $(C_x > 2.875\sqrt{\theta_x})$. For the sampling of the complete velocity distribution $f(C)$ the first class starts at zero and the last class contains all particles with fluctuating velocities above $6\sqrt{\theta}$.

The velocity distribution analyses are performed from t_{min} (= 5 s) onwards. After each time step Δt (=10^{-4} s) the granular temperatures of the particle ensembles within each cell are calculated. Based on these granular temperatures the local particle ensembles are added to the larger ensembles characterised by granular temperature classes. Within the larger ensembles, based on their individual velocities, all particles are added to a specific velocity class. The simulation is then proceeded for another time step and velocity analysis is continued until t_{max} (= 10 s) is reached.

This analysis procedure guarantees that the particle velocity distributions obtained for the dominant granular temperature classes are based upon at least 10^8 individual particle velocities. Correlation between particle velocities within a single grid cell at time t and time $t+\Delta t$ is reduced by convection and collisions. At a typical ensemble average particle speed of 1 m/s the particles within an ensemble of 1 x 1 x 1.5 cm will be refreshed every 10^{-2} seconds by convection, whereas the average particle collides over 1000 times per second in the performed simulations.

4.2. Sampled particle velocity distributions

Some typical particle velocity distributions obtained from sampling on the coarse grid are shown in figure 4.2. For comparison the normalised Gaussian and Maxwellian velocity

distributions are shown. For elastic particles (case I) the differences between the Gaussian distribution and the velocity distribution in each direction are too small to be noticeable and the total particle velocity distribution is nearly Maxwellian. For particles with realistic collision parameters (case III) the sampled velocity distributions show a slight deviation from the Gaussian and Maxwellian distributions, but the resemblance is still very good. To quantify the differences between the sampled velocity distributions and Maxwellian distributions for ensembles with the same granular temperature, the ensemble average velocities were calculated by numerical integration and compared to the Maxwellian prediction given by:

$$< C >_{Maxwell} = \frac{1}{n}\int_0^{\infty} C f^{(0)} dC = \sqrt{\frac{8\theta}{\pi}} \tag{4.47}$$

The comparison shows that the deviation is smaller than 5% in the dominant granular temperature classes that contain over 99% of all particles. Deviations are found in the highest and lowest granular temperature classes, where the particle velocity distributions are typically based on less than 10^6 individual particle velocities.

Figure 4.3 shows the velocity distributions sampled from case III in the highest granular temperature class that runs from 5.6210^{-2} up to 1.0010^{-1} m^2/s^2. Such high granular temperature are mostly observed in dilute areas ($\varepsilon_s < 0.25$) that are found at bubble edges and in the splash-zone. Velocity sampling in these zones where (groups of) particles clash into each other leads to high temperatures, which explains the two peaks in the particle velocity distribution in the *y*-direction. The velocity distribution in the *z*-direction at high granular temperature has probably been influenced by wall effects, since the mean free path is of the same order of magnitude as the depth of the bed. An estimate of the mean free path is given by:

$$\ell_{Maxwell} = < C > \frac{n}{N_{12}} = \frac{1}{\pi\sqrt{2}\, n d_p^2 g_0} = \frac{1}{6\sqrt{2} g_0}\frac{d_p}{\varepsilon_s} \tag{4.48}$$

This equation shows no direct dependence of the mean free path on the granular temperature. However, in rapid granular flows high granular temperatures are mostly observed in areas with low particle volume fractions, which explains an indirect dependence of the mean free path on the granular temperature. Applying any of the given expressions for the radial distribution function g_0 (equations 4.27-4.30) it can easily be

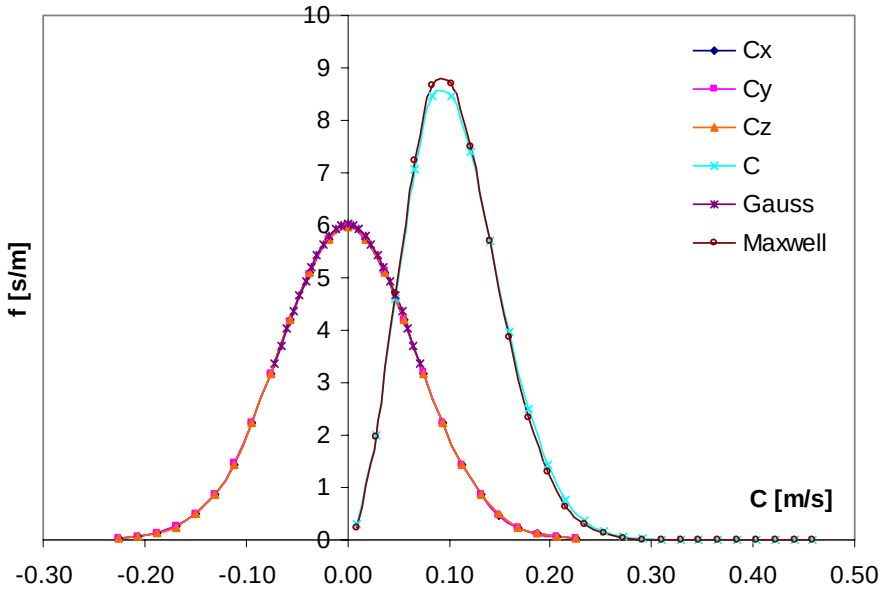

a) Case I: Velocity distributions sampled in the range $3.16\text{10}^{-3} < \theta_{(x,y,z)} < 5.62\text{10}^{-3}$ m^2/s^2 compared to the Gaussian and Maxwellian distributions for $\theta_{(x,y,z)} = 4.39\text{10}^{-3}$ m^2/s^2.

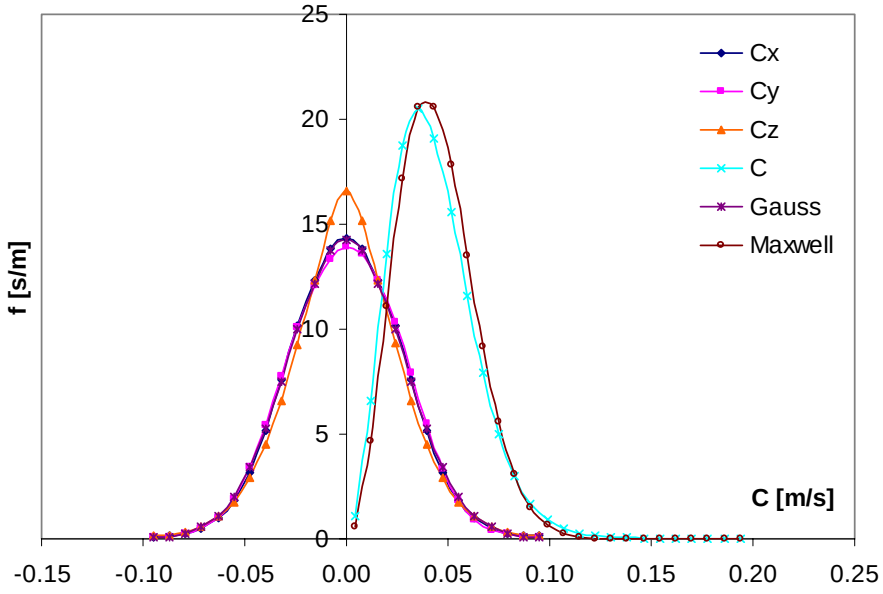

b) Case III: Velocity distributions sampled in the range $5.62\text{10}^{-4} < \theta_{(x,y,z)} < 1.00\text{10}^{-3}$ m^2/s^2 compared to the Gaussian and Maxwellian distributions for $\theta_{(x,y,z)} = 7.81\text{10}^{-4}$ m^2/s^2.

Figure 4.2. Normalised particle velocity distribution functions $f_x(C_x)$, $f_y(C_y)$, $f_z(C_z)$ and $f(C)$ sampled on the coarse grid ($\theta_{(x,y,z)} = \theta$ for $f(C)$, $\theta_{(x,y,z)} = \theta_x$ for $f_x(C_x)$, etc.).

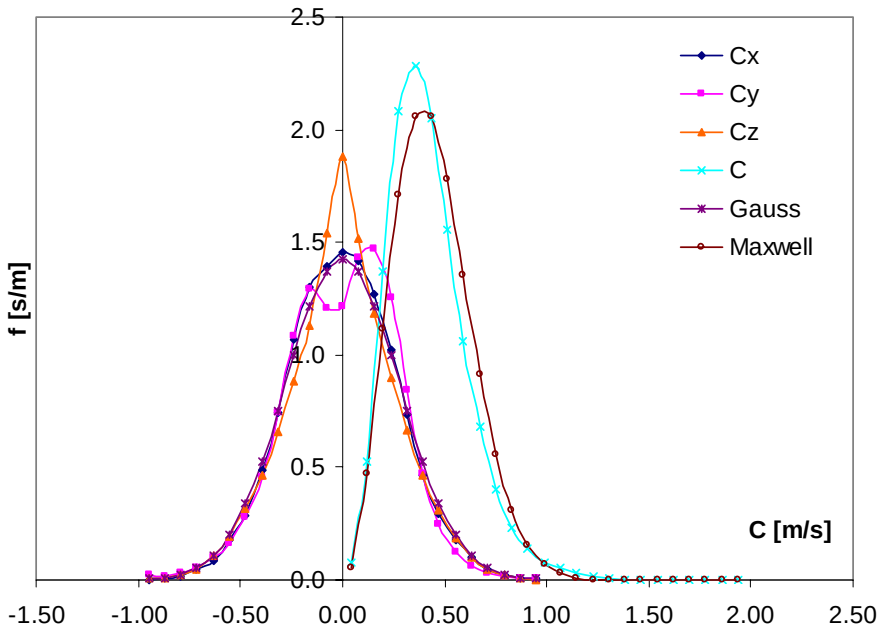

Figure 4.3. Normalised velocity distribution functions sampled for case III on the coarse grid in the range $5.62 10^{-2} < \theta_{(x,y,z)} < 1.00 10^{-1}$ m^2/s^2 compared to the Gaussian and Maxwellian velocity distributions for $\theta_{(x,y,z)} = 7.81 10^{-2}$ m^2/s^2.

shown that the mean free path is already 10 times smaller than the depth of the bed for a particle volume fractions of 0.15. Since over 99.9% of all particles is found in areas with particle volume fractions above 0.15 it can reasonably be assumed that the depth of the bed is chosen deep enough compared to the mean free path, so it does not interfere with the sampled velocity distributions.

To reduce the influence of solids velocity gradients and volume fraction gradients within the sampling ensembles the fine grid is applied for all further analyses in this work. Figure 4.4 shows some particle velocity distributions that are sampled for cases III and V using the fine grid. Comparing figures 4.2b and 4.4a makes clear that grid refinement improves the agreement between the sampled velocity distributions and Gaussian and Maxwellian distributions which indicates that the fluctuating particle motion is not homogeneous and isotropic at subgrid scale. Figure 4.4b shows that even in case V, the simulation with the most inelastic particles, the velocity distributions sampled on the fine grid do no deviate significantly from Gaussian and Maxwellian distributions. The obtained deviations of the average fluctuating velocities from Maxwellian predictions are summarised in table 4.2. In the presented averages the deviations obtained in each

granular temperature class are weighted with the percentage of particles in that class according to:

$$<\phi>_{\theta}=\frac{\sum_{i}\phi(\theta_i)N_{part}(\theta_i)}{\sum_{i}N_{part}(\theta_i)} \tag{4.49}$$

From the presented figures and the data in table 4.2 it can be concluded that, even for inelastic particles, the fluctuating particle motion in the performed hard-sphere discrete particle simulations can be closely approximated by a Maxwellian velocity distribution, that is uniquely defined by the local granular temperature.

4.3. Anisotropy

Though the particle velocity distributions in all directions are Gaussian, within most cells of the analysis grid significant differences are observed between the granular temperatures calculated for different directions. To quantify this anisotropy the ratios of the granular temperatures in each direction to the granular temperature based on the total particle velocity are calculated. For this purpose the granular temperatures are averaged over all cells in the computational domain and the simulation time according to:

$$<<\phi>>=\frac{1}{t_{\max}-t_{\min}}\int_{t_{\min}}^{t_{\max}}\frac{\sum_{k}^{N_{cell}}\varepsilon_{s,k}\phi_k}{\sum_{k}^{N_{cell}}\varepsilon_{s,k}}dt \tag{4.50}$$

The results are presented in table 4.2. It can be seen that the sampled particle velocity distribution is completely isotropic for elastic particles, but the more inelastic the particle collisions become the stronger the anisotropy becomes. The largest particle velocity

Table 4.2. Results of individual particle velocity distribution analyses on fine grid.

	$<\frac{<C>-<C>_{Maxwell}}{<C>_{Maxwell}}>_{\theta}$	$\frac{<<\theta_x>>}{<<\theta>>}$	$\frac{<<\theta_y>>}{<<\theta>>}$	$\frac{<<\theta_z>>}{<<\theta>>}$
Case I	-1.15 %	1.00	1.00	1.00
Case II	-1.59 %	0.99	1.04	0.96
Case III	-2.45 %	0.98	1.24	0.78
Case IV	-2.01 %	0.98	1.15	0.86
Case V	-2.74 %	0.99	1.32	0.69

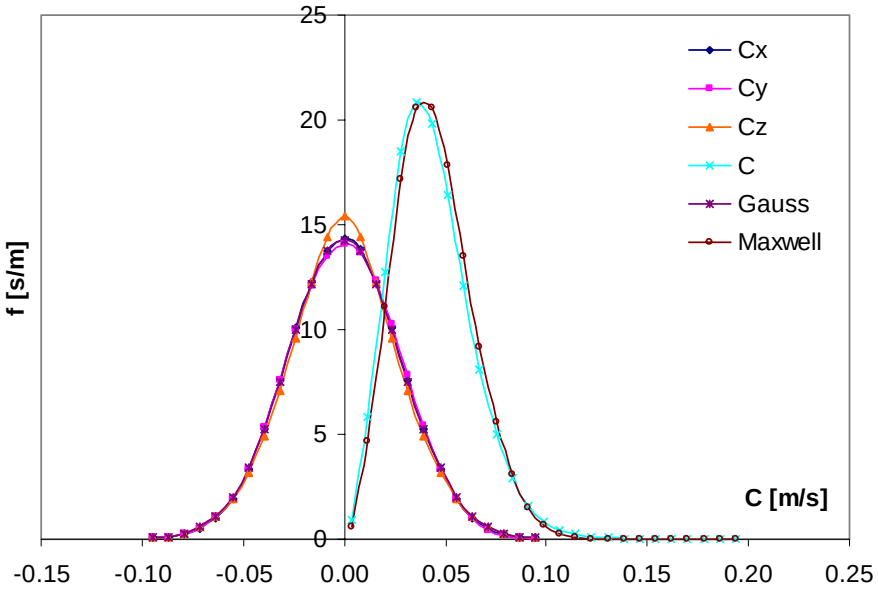

a) Case III

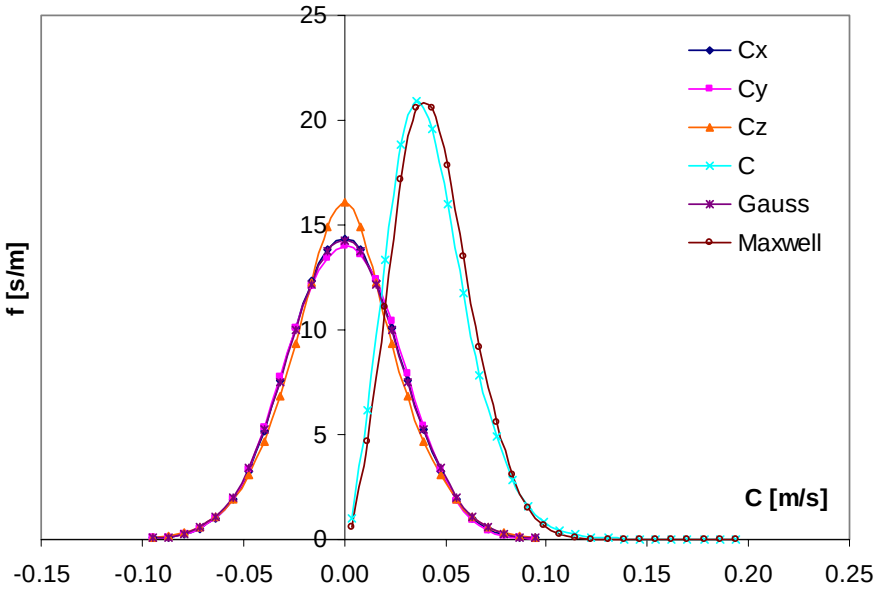

b) Case V

Figure 4.4. Normalised particle velocity distribution functions $f_x(C_x)$, $f_y(C_y)$, $f_z(C_z)$ and $f(C)$ sampled on the fine grid in the range $5.6210^{-4} < \theta_{(x,y,z)} < 1.0010^{-3}$ m^2/s^2 compared to the Gaussian and Maxwellian velocity distributions for $\theta_{(x,y,z)} = 7.8110^{-3}$ m^2/s^2.

fluctuations are observed in the *y*-direction, in which the system is driven, whereas the fluctuations in the narrow *z*-direction are the smallest.

Apparently, in the elastic case, the particle-particle collision frequency is high enough (>1000 Hz) to prevent anisotropy due to acceleration of the particles by the external forces between successive collisions. However, for inelastic particles, the formation of particle clusters disturbs the spatial homogeneity and not all impact angles are of same likelihood (collisional anisotropy), which results in the observed anisotropy in the sampled particle velocity distribution functions. The differences between the observed temperatures in the *x*-direction and the *z*-direction are caused by the narrowness of the *z*-direction. Not because the depth of the bed is too small compared to the mean free path of the particles, but because the narrowness prevents the formation of large-scale convective patterns in the *z*-direction, which dampens the vorticity of the flow pattern and the resulting granular temperature in that direction.

5. Sampling of particle-particle collision characteristics

To sample particle-particle collision characteristics the fine analysis grid as described in paragraph 4.1 is applied. The collision analysis is performed from t_{min} (=5 s) onwards. Before each hydrodynamic time step Δt (10^{-4} s) the local granular temperature and particle volume fraction are calculated for each grid cell. Then the sequence of collisions that occur during that time step is processed. The collision characteristics of each collision are calculated and categorised by the granular temperatures and particle volume fractions of the cells in which the centres of mass of the particles are positioned. The total number of collisions in each category and the number of grid cells with a certain combination of granular temperature and particle volume fraction are logged. The analysis is continued till t_{max} (=10 s) is reached. The same 16 granular temperature classes as for the sampling of the individual particle velocity distribution are used. The velocity domain is split into 24 classes of width Δc_{12} ($=0.375\sqrt{\theta}$) and a last class of impact velocities above $9\sqrt{\theta}$. The particle volume fraction domain that runs from 0 up to $\pi/3\sqrt{2}$ is split into 25 discrete classes of width $\Delta\varepsilon_s$ (= 0.03).

Regarding the particle volume fraction calculation a special remark needs to be made. Since the system is only 6 particle diameters in depth and particle-particle collisions can not occur in the first half diameter from the wall, all particle-particle collisions in a cell effectively take place in 5/6 of the total cell volume. Because the particle collision

frequency depends on the local particle density and the particle volume fraction in the centre of the cell differs from that near the wall, the particle volume fraction calculated for the analysis is based upon the volume in the centre of the cell where particle-particle collisions actually take place (= 5/6 V_{cell}). Apart from the front and the back walls other walls also cause the same kind of complications. Therefore collision information that is obtained in the first layer of cells near the left, right, bottom and top wall is excluded from the analysis.

5.1. Impact velocity distribution and coefficient of restitution

Some typical dimensionless impact velocity distributions are shown in figure 4.5. For comparison the zeroth-order approximation from the kinetic theory of granular flow (equation 4.24) that would have been obtained for an isotropic Maxwellian velocity distribution is also shown. It can be seen that the deviation of the impact velocity distribution from the zeroth-order kinetic theory of granular flow approximation is small for nearly elastic particles and increases the more inelastic the particles get. The most noticeable change is the shift of the maximum of the normalised impact velocity distribution towards a lower velocity, whereas the longer tail of the distribution at high velocities is less noticeable. In the previous paragraph it is concluded that the individual particle velocity distribution is nearly Maxwellian in all cases, so the deviation of the shape of the impact velocity distribution function must be associated with the observed anisotropy.

The deviation of the average sampled impact velocity from the average based on an isotropic Maxwellian distribution is listed in table 4.3. It can be seen that the more inelastic the particles are the more the amount of momentum transferred per collision is overestimated (because of the increasing anisotropy). Though the differences are significant the agreement with the theory is still reasonable when it is realised that

Table 4.3. Results of collision velocity analyses obtained on fine grid.

	$< \frac{< c_{12} > - < c_{12} >_{Maxwell}}{< c_{12} >_{Maxwell}} >_\theta$	$\frac{< \bar{c}_{12} \cdot \bar{n} >_\theta}{< \bar{c}_{12} \cdot \bar{t} >_\theta}$	$< e >_\theta$	N_{coll}
Case I	0.74 %	1.00	1.000	62044969
Case II	-0.76 %	0.97	0.985	63851746
Case III	-15.8 %	0.73	0.941	135609478
Case IV	-8.47 %	0.83	0.958	81532697
Case V	-24.1 %	0.55	0.934	167124382

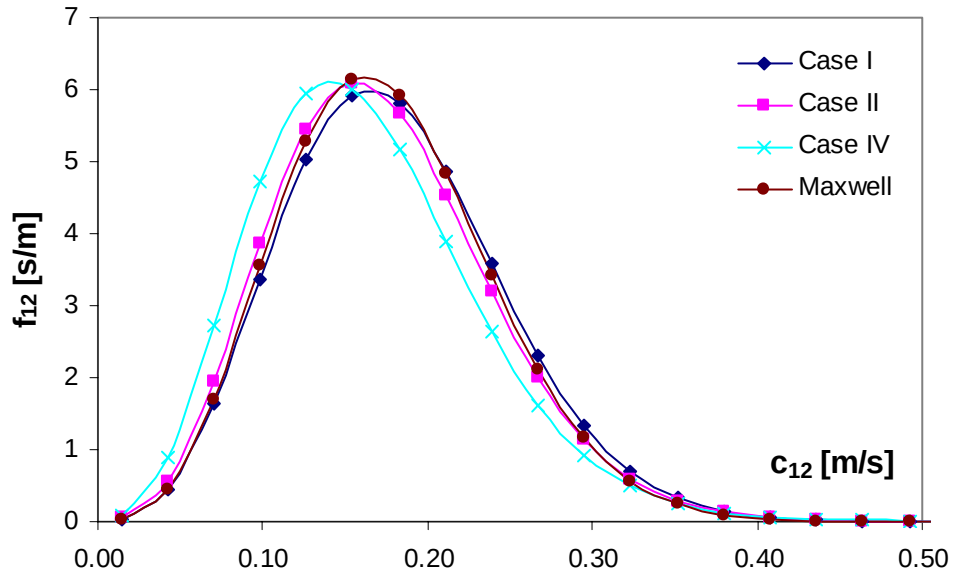

a) Impact velocity distributions sampled in the range $3.16 \cdot 10^{-3} < \theta < 5.62 \cdot 10^{-3}$ m^2/s^2 compared to the zeroth-order approximation from the KTGF for $\theta = 4.39 \cdot 10^{-3}$ m^2/s^2.

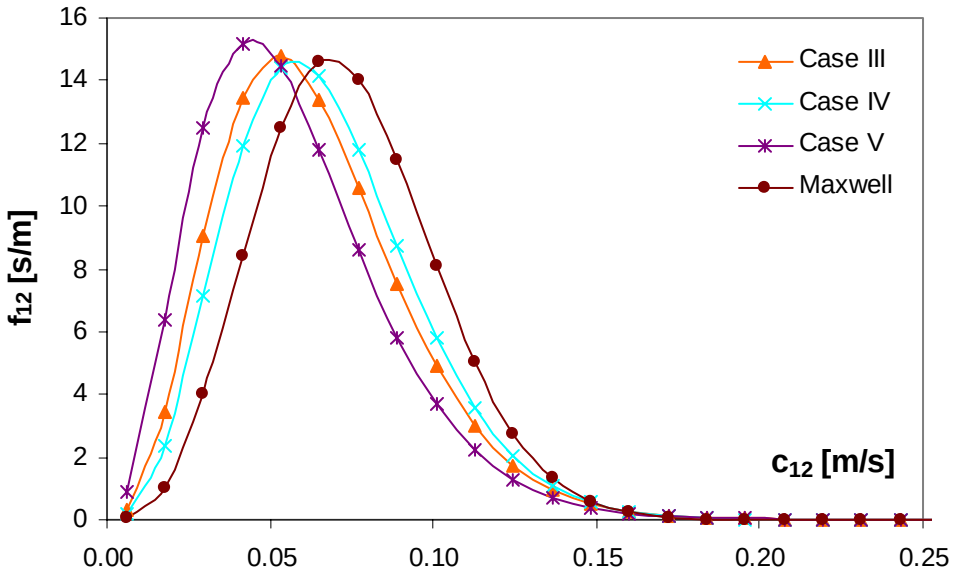

b) Impact velocity distributions sampled in the range $5.62 \cdot 10^{-4} < \theta < 1.00 \cdot 10^{-3}$ m^2/s^2 compared to the zeroth-order approximation from the KTGF for $\theta = 7.81 \cdot 10^{-4}$ m^2/s^2.

Figure 4.5. Normalised impact velocity distributions $f_{12}(c_{12})$ sampled on the fine grid.

deviations of -15.2% and +13.1% are obtained in case the zeroth-order approximation is calculated for the minimum or the maximum temperature in all temperature classes, in stead of for the average temperature.

To characterise collisional anisotropy the centre of mass impact velocity is split into a normal and tangential component that are logged separately. The tangential direction differs from that applied in the three parameter collision model (equation 4.35) by neglect of rotation that is not taken into account in the centre of mass velocities. Therefore the tangential direction can change during an impact due to rotation and has to be recalculated after the collision to calculate the centre of mass rebound velocity. Some typical impact and rebound velocity distributions are shown in figure 4.6. The second column of table 4.3 shows the ratios between the averaged normal and the tangential component of the centre of mass impact velocity that where obtained for all studied cases. If all impact angles would be of equal likelihood and the amount of analysed collisions would be large enough this ratio should equal 1. Table 4.3 shows that collisional isotropy is obtained for elastic particles, but the more inelastic particles get the more glancing particle-particle impacts become. The third column in the table shows the mean coefficient of restitution that was calculated from the ratio of rebound and impact velocities according to:

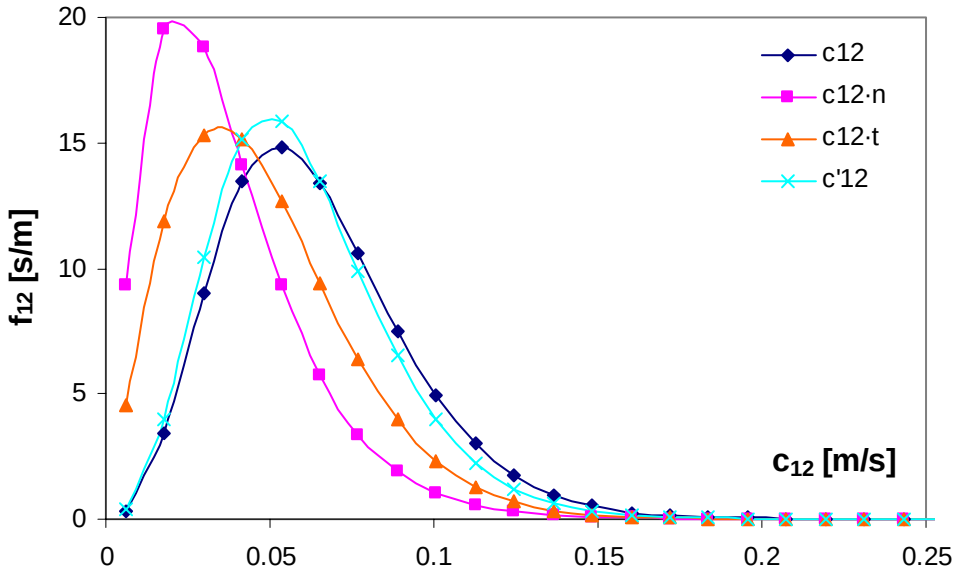

Figure 4.6. Normalised impact and rebound velocity distributions sampled from case III in the range $5.6210^{-4} < \theta < 1.0010^{-3}$ m^2/s^2.

$$< e >_{\theta} = < \frac{< c'_{12} >}{< c_{12} >} >_{\theta} \qquad (4.51)$$

If all impact angles would be of equal likelihood this mean coefficient of restitution would equal $(1+e_n)/2$ for smooth particles, since velocities in the tangential impact direction are not affected during a collision. Analysis of the results for the coefficient of restitution confirms that collisional anisotropy is negligible for slightly inelastic particles (cases I and II) and becomes more pronounced the more inelastic the particles get (case IV: $0.958 > (1+e_n)/2$). As discussed in paragraph 2.5, the relation between the three measurable collision parameters e_n, μ and β_0 for rough particles and the coefficient of restitution e is not a straightforward one. Derivation of an analytical correlation might be possible for simple limiting cases (Jenkins, 1992), but will be extremely complicated when collisional anisotropy has to be accounted for. Therefore, for a specific set of collision parameters at a specific fluidisation velocity, the described statistical analysis method can be a useful tool to obtain a coefficient of restitution that can be applied to characterise the amount of energy dissipated in collisions in continuum models, from detailed hard-sphere simulations. To obtain a more generally applicable relation between the three measurable collisions parameters and the coefficient of restitution many more simulations are required, since the strength of the anisotropy depends on collisions parameters as well as fluidisation conditions.

Though equation 4.24 suggests that the normalised collision velocity distribution is independent of the particle volume fraction, such dependence was observed for the sampled impact velocity distributions. However, since the simulations are performed at a relatively low fluidisation velocity the amount of collisions that occurs at particle volume fractions below 0.4 is limited and more data is required to perform a rigorous analysis. Therefore the data obtained for all particle volume fractions at a specific granular temperature was merged and the influence of the particle volume fraction has to be subject of future research.

5.2. Collision frequency and radial distribution function

The total number of collisions upon which the collision analyses are based is given in the last column of table 4.3. It can be seen that the collision frequency increases as particles collide more inelastic. Since, at a constant energy supply rate, the granular temperature decreases as more fluctuating kinetic energy is dissipated in collisions, the increase of the collision frequency is most likely caused by gathering of particles in denser areas. To gain more insight in the influence of the particle volume fraction and the granular

temperature on the particle-particle collision frequency, the total number of cells and the number of collisions in each specific granular temperature and particle volume class are logged during the analysis period. The results that were obtained from analysis of cases I and III are shown in figure 4.7. This figure shows that the range of particle volume fractions and granular temperatures observed for inelastic particles is much wider than for elastic particles, which is consistent with the observed increasing heterogeneity described in paragraph 3. Figure 4.7 also confirms that the average granular temperature decreases and particles gather at higher densities as collisions become less elastic. Further it illustrates that, though areas with low particle volume fractions do exist, the number of collisions in those areas is relatively low.

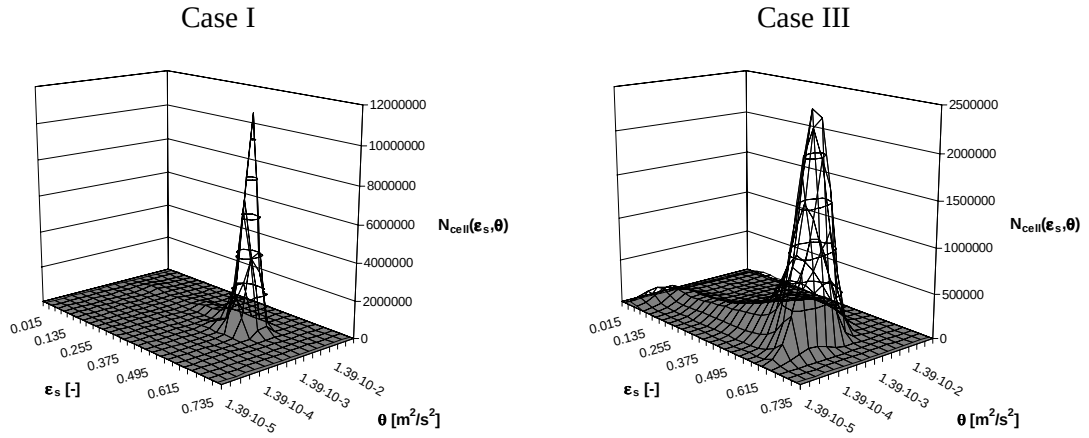

a) Number of grid cells with specific granular temperature and particle volume fraction.

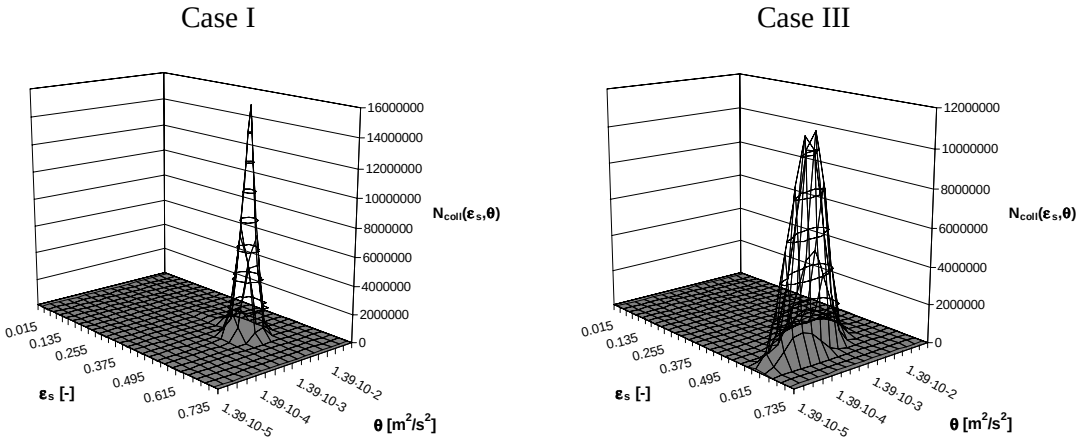

b) Number of collisions in cells with specific granular temperature and particle volume fraction.

Figure 4.7. Distributions sampled from t = 5-10 s.

Since the volume in which the collisions take place and the computational time step are known, the collision frequency per unit volume for each simulated case can be calculated from:

$$\frac{1}{2}N_{12} = \frac{N_{coll}(\varepsilon_s,\theta)}{N_{cell}(\varepsilon_s,\theta)\cdot\frac{5}{6}V_{cell}\cdot\Delta t} \tag{4.52}$$

The value for the radial distribution function that is required to obtain such a collision frequency, can be obtained from rewriting equation 4.23:

$$g_o = N_{12}\cdot\frac{\left(\pi d_p^3\right)^2}{4\left(6\varepsilon_s\right)^2 d_p^2\sqrt{\pi\theta}} \tag{4.53}$$

In the derivation of equation 4.23 it is assumed that the individual particle velocity distribution function is an isotropic Maxwellian distribution. In the performed discrete particle simulations of dense gas-fluidised beds, the individual particle velocity distribution is nearly Maxwellian, but it becomes more anisotropic the more inelastic the particles are. Also the shape of the impact velocity distribution function changes for inelastic particles. Clearly more research is required to fully understand how anistropy affects the kinetic theory of granular flow. However, since anisotropy is not accounted for in the kinetic theory of granular flow closure model that is currently applied for continuum modelling of gas-fluidised beds, it is interesting to know which values for the radial distribution function are obtained from equation 4.53, assuming the velocity distribution is isotropic. Figure 4.8 shows the values of the radial distribution function that are obtained for case I and case III at different granular temperatures applying equation 4.53. Only results based upon more than 10^6 collisions are presented. In the calculation of the radial distribution function in a specific granular temperature and particle volume fraction class, the average granular temperature and particle volume fraction of that class are substituted in equation 4.53. Therefore the results obtained in the limits of the observed granular temperature and porosity range can be somewhat less accurate, since the data points are probably not equally distributed within the sampling classes.

From figure 4.8a it can be seen that the values for the radial distribution function obtained for elastic particles show excellent agreement with the radial distribution function given by Carnahan and Starling (1969). All alternative expressions for the radial distribution

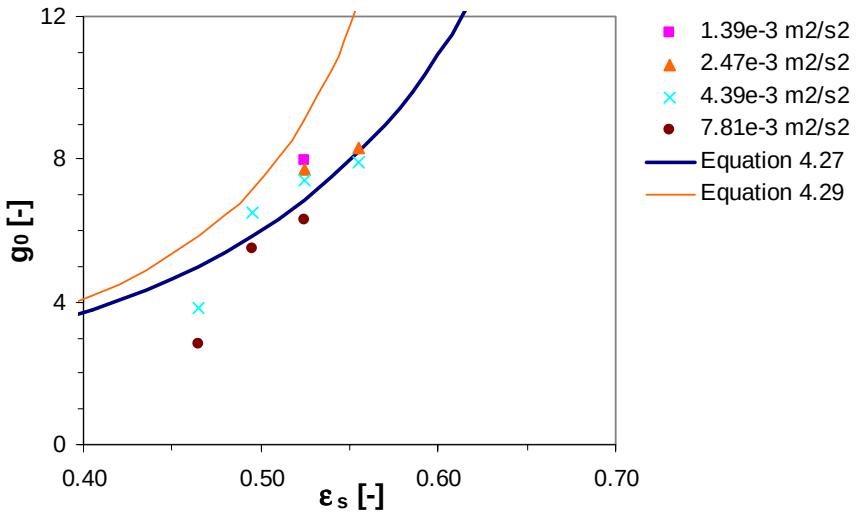

a) Values for radial distribution function sampled from case I at various granular temperatures compared to the radial distribution functions of Carnahan and Starling (1969) and Ding and Gidaspow (1990).

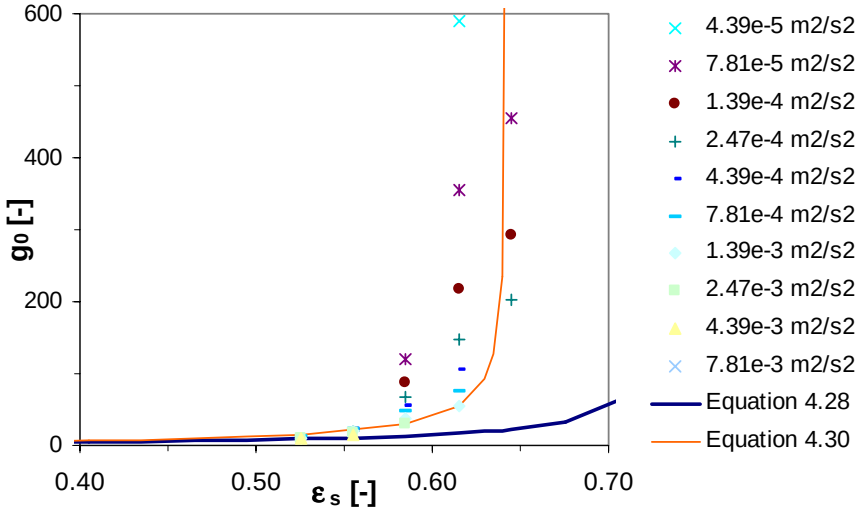

b) Values for radial distribution function sampled from case III at various granular temperatures compared to the radial distribution functions given by Ogawa et al.(1980) and Ma and Ahmadi (1986).

Figure 4.8. Radial distribution function sampled from discrete particle simulations.

function presented in paragraph 2.4 predict higher values for the radial distribution function. To illustrate this, the second best alternative, the radial distribution function given by Ding and Gidaspow (1990), is also shown in figure 4.8a. Though the results

obtained for elastic particles do seem slightly temperature dependent, the dependence is negligible compared to that observed for inelastic particles, as shown in figure 4.8b. The only expression for the radial distribution function that predicts temperature dependence is the anisotropic radial distribution function given by Jenkins and Savage (1983), that can not easily be evaluated at this point. For comparison the radial distribution functions given by Ogawa et al. (1980) and Ma and Ahmadi (1986) are shown in figure 4.8b. It can be seen that the results show larger deviations from the presented relations the lower the granular temperature becomes. Attempts were undertaken to fit the presented results on (amongst others) a function of the following type:

$$g_{fit} = g_0(1+\frac{\alpha\varepsilon_s^a}{\theta^b}) \tag{4.54}$$

However, for non of the presented expressions for g_0, a reasonable fit with constant a,b and α could be obtained. To gain more insight into the effect of anisotropy on the collisional behaviour of gas-fluidised particles, it seems worthwhile to extend the presented sampling method with sampling of the local vorticity of the particulate phase flowfield, which has to be subject of future research.

Discussion and conclusions

It was demonstrated in this chapter that discrete particle models are an excellent tool to provide detailed information about the basic particle flow characteristics, which are (extremely) difficult if not impossible to obtain from experiments. A novel sampling technique to obtain particle velocity distributions and collision characteristics from dynamic discrete particle simulations of intrinsically unsteady, non-homogeneous granular flows of inelastic particles, such as dense gas-fluidised beds, was presented. The results obtained for elastic particles showed excellent agreement with the kinetic theory of granular flow. The individual particle velocity function was an isotropic Maxwellian and a good fit of the sampled collision velocity distribution and frequency can be obtained, using the radial distribution function proposed by Carnahan and Starling (1969). However, for highly inelastic and rough particles an anisotropic Maxwellian particle velocity distribution was observed. The formation of dense particle clusters, that gets stronger the more inelastic the particles are, seemed to disturb spatial homogeneity and resulted in collisional anisotropy. Analysis of the normal and tangential component of the impact velocity showed that, in dense gas-fluidised beds, not all impact angles are of equal likelihood. It was further shown how a value for the coefficient of restitution

defined by equation 4.43, that describes the reduction of the centre of mass velocity in collisions of rough particles, can be obtained from discrete particle simulations if the measurable collision parameters are known.

A significant amount of work on anisotropic particle velocity distributions and the deviations that anisotropy causes from the kinetic theory of granular flow, has been performed by Simonin and co-workers (e.g. Simonin, 1991; He and Simonin, 1993; Simonin et al., 1995; Boelle et al., 1995; Février and Simonin, 1998). They observed anisotropy of the particle fluctuating motion for dilute particle suspensions in homogeneous turbulent gas shear flows and concluded that anisotropy was introduced by the drag force exerted by the gas phase. The anisotropy of the particle stress tensors was found to increase with the production of fluctuating motion due to the mean shear. A continuum modelling approach for turbulent gas-solid flows was presented and the results were compared to the statistics of particles tracked in turbulent flows generated by large eddy simulation (LES). Their model gave a satisfactory description of the mechanisms leading to the anisotropy of the particle fluctuating motion. The accuracy of the model predictions was directly related to the modelling of the fluid-particle velocity correlation, which could be calibrated with discrete particle simulations. Further it was noticed that the inter-particle collision influence leads to a return to isotropy for higher particle densities, where gas phase turbulence also has a negligible effect on the particulate motion. In conclusion the studies by Simonin and co-workers have shown the need of modifying the kinetic theory of granular flow in order to take into account the gas phase influence for systems of moderate and low particle density. However in their work anisotropy introduced by clustering of inelastic particles at high particle densities was never identified.

Increasingly anisotropic flow behaviour for decreasing coefficients of restitution was observed in computer simulations of homogeneous shear flows of granular media (Campbell and Gong, 1986; Walton and Braun, 1986a, 1986b; Lun and Bent, 1994). It was noticed that at high solids fractions, above about 0.5, the layering effects of particles, the formation of high-density microstructures and increase in correlation of particle velocities were the major causes of abrupt changes in flow properties. Interestingly, most particles in the presented simulations are located in such high-density areas, and cluster formation dominates the hydrodynamic behaviour of dense gas-fluidised bed reactors. To describe the observed normal stress differences Jenkins and Richman developed kinetic theory expressions for steady, homogeneous shearing granular flows, based on an anisotropic Maxwellian particle velocity distribution (Jenkins and Richman, 1988;

Richman, 1989). To the authors' knowledge this theory has never been extended to inhomogeneous, dynamic systems, such as dense gas-fluidised beds, but its applicability seems an interesting topic for future research.

To identify the anisotropy of the individual particle velocity distribution function, the ratios of the time-averaged granular temperatures were calculated for the whole bed. However, in retrospect, it seems more meaningful to relate anisotropy within an ensemble to the local direction of the mean shear field. Extension of the analysis method to include sampling of the local vorticity seems required to gain more insight into the effect of the particle collision parameters on the particle velocity distribution function. In that respect it also seems worthwhile to separately log the distribution of the impact angle for each temperature and particle volume fraction class. In this manner the presented sampling technique will be a useful tool to verify the applicability of continuum theories that were developed for specific (steady) flow problems or other areas of application. The sampling results can also contribute to new insight and directions for further theory development and be used to calibrate theories that seem to predict the correct trends. Since anisotropy seems to be related to the local particle volume fraction, future research might explain why a dependence of the normalised collision velocity distribution on the particle volume fraction was observed in this work. It might also reveal what shape of the radial distribution function is required to fit the observed dependence of the collision frequency on particle volume fraction, granular temperature and collision parameters.

However, one should keep in mind the limitations of the hard sphere discrete particle model. Just as the kinetic theory of granular flow it assumes that collisions are binary and instantaneous. This makes the model an appropriate tool to verify kinetic theory expressions, but not such a realistic representation of highly inelastic particulate systems. In such systems multi-particle and long term contacts will occur at high particle densities. A further limitation for the future applicability of hard-sphere models seems to be given by the significant increase in computation times that is required to model non-spherical particles, since accurate detection of the collision point requires much more computational effort. Therefore, soft-sphere or hybrid discrete particle models seem to have some advantageous properties, although the interaction between the particles and the surrounding fluid in those models is also limited to friction with the mean fluid phase flow field. Though more and more detailed descriptions of the particle collisions and the gas phase flow field might result in better discrete particle models, the presented sampling technique (or refinements of it based on new insights) will be a helpful tool to validate and calibrate constitutive theories for application in continuum models.

Appendix 4A. A single parameter collision model for rough particles

A simple single parameter collision model that accounts for the effect of rotation on the center of mass rebound velocity is briefly discussed. In this model the coefficient of restitution e is defined in such a way that relation between the particle velocities before and after collision is given by:

$$\overline{c}'_{12} = -e\,\overline{c}_{12} \tag{A4.1}$$

The main advantage of such a collision model would be that the total amount of kinetic energy lost in a collision, which is required to derive the collisional energy dissipation term in the granular temperature balance (equation 4.3), is simply given by:

$$\Delta E = -\frac{1}{2}\frac{m_1 m_2}{m_2 + m_1}(1-e^2)c_{12}^2 = -\frac{1}{4}m(1-e^2)c_{12}^2 \tag{A4.2}$$

The effective amount of kinetic energy dissipated in rough particle collisions per unit time and volume according to the kinetic theory of granular flow is then obtained from:

$$\gamma_{eff} = \iiint \frac{1}{4}m(1-e^2)c_{12}^2(\overline{k}\cdot\overline{c}_{12,0})\,f_{12}\,d\overline{k}\,d\overline{c}_1\,d\overline{c}_2 \tag{A4.3}$$

Which after evaluation of the integrals (assuming collisional isotropy) results in:

$$\gamma_{eff} = 6(1-e^2)\varepsilon_s^2\rho_s g_0\theta\left[\frac{4}{d_p}\sqrt{\frac{\theta}{\pi}} - (\nabla\cdot\overline{u}_s)\right] = 2\frac{(1-e^2)}{(1-e_n^2)}\gamma \tag{A4.4}$$

To find the relation between the restitution coefficient e defined by equation A4.1 and the measurable collision parameters e_n, μ and β_0 the impact velocity has to be split into a normal and a tangential component. The separate restitution coefficients for each direction are defined by:

$$\overline{c}'_{12,n} = -e_n\,\overline{c}_{12,n} \tag{A4.5}$$

$$\overline{c}'_{12,t} = e_t\,\overline{c}_{12,t} \tag{A4.6}$$

The coefficient of normal restitution in equation A4.5 is the same as the measured coefficient of normal restitution e_n, since rotation does not contribute to the impact

velocity in the normal direction of the impact. On the contrary, the relation between the coefficient of tangential restitution e_t and the measured collision parameters is less clear, especially since for rotating particles the tangential impact direction in this one parameter model might differ from the tangential direction in the three parameter collision model (equation 4.35). For sticking collisions e_t should be related to β_0 and for sliding collisions it should be related to e_n and μ. For rigid spherical particles, the relation between the pre- and post-collision velocities is given by:

$$\overline{c}'_{12} = \overline{c}_{12} + \overline{J}\,\frac{m_1 + m_2}{m_1 m_2} \tag{A4.7}$$

So for the tangential coefficient of restitution it can be found that:

$$e_t = \frac{\overline{c}'_{12,t}}{\overline{c}_{12,t}} = 1 + \frac{\overline{J}_t}{\overline{c}_{12,t}}\,\frac{m_1 + m_2}{m_1 m_2} \tag{A4.8}$$

Then, applying the expressions for the tangential impulse (equations 4.39 and 4.40) results in (v_{12} is the collision velocity at the point of contact defined by equation 4.33):

$$e_{t,sliding} = 1 - \mu(1 + e_n)\,\frac{\overline{v}_{12,0} \cdot \overline{n}}{\overline{c}_{12,t}} \tag{A4.9}$$

$$e_{t,sticking} = 1 - (1 + \beta_0)\,\frac{2}{7}\,\frac{\overline{v}_{12,0} \cdot \overline{t}}{\overline{c}_{12,t}} \tag{A4.10}$$

For particles that initially do not rotate (as assumed in the KTGF) the tangential direction defined in both models is the same and $v_{12,0} = c_{12}$, so relations A4.9 and A4.10 simplify to:

$$e_{t,sliding} = 1 - \mu(1 + e_n)\cot\Phi \tag{A4.11}$$

$$e_{t,sticking} = 1 - \frac{2}{7}(1 + \beta_0) \tag{A4.12}$$

A graphical representation of the so defined tangential restitution coefficient versus the impact angle for the measured collision parameters applied in case III, is given in figure A4.1. This figure also presents the normal restitution coefficient e_n and the restitution coefficient $e(\Phi)$ defined by:

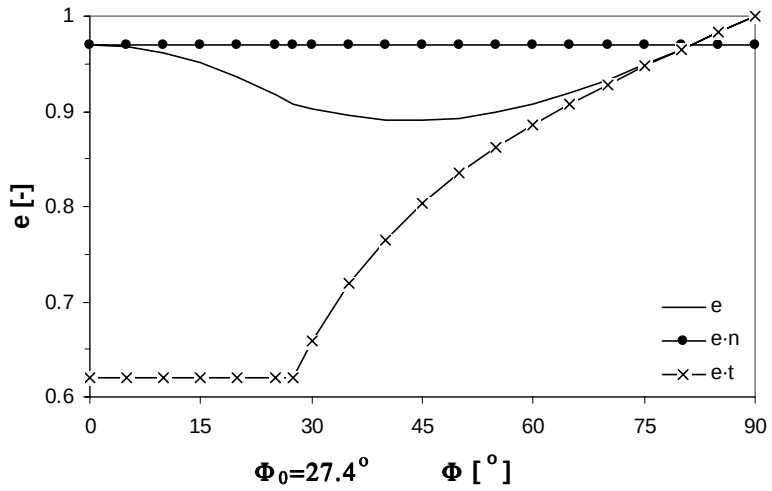

Figure A4.1. Variation of the restitution coefficients with impact angle for e_n = 0.97, μ = 0.10 and β = 0.33.

$$e(\Phi) = \sqrt{e_n^2 \cos^2 \Phi + e_t^2 \sin^2 \Phi} \tag{A4.13}$$

An effective mean value of the restitution coefficient e can then be obtained by integration over all possible collision angles, assuming all impact angles to be of equal likelihood (molecular chaos):

$$e = \frac{2}{\pi} \int_0^{\pi/2} e(\Phi) d\Phi \tag{A4.14}$$

For the measured set of collision parameters used in case III, e = 0.93 is obtained from numerical integration of equation A4.14.

However, the assumption that particles do not rotate before collision can only hold if particle rotation generated in each collision is dissipated immediately by friction with the gas phase, before the particles that were involved in the collision collide again with other particles. This might be reasonable for dilute particle suspensions, but not for dense suspensions as studied in this work. In a dense granular suspension not all rotation will be damped and thus less kinetic energy will be lost, resulting in higher post collision velocities. So equation A4.14 represents the minimum coefficient of restitution that is obtained in the case that all rotation is damped by friction with the gas phase, while a realistic value for the restitution coefficient e will be higher. Further analysis of the relation between the measured collision parameters e_n, μ and β_0 and the coefficient of

restitution e requires information on the correlation between the translational and rotational particle velocities. A generally applicable statistical mechanical theory that gives this correlation is, to the author's knowledge, not available at this point. However, as demonstrated in this chapter, discrete particle models can be applied to obtain an estimate of e, for a specific set of collision parameters and operation conditions.

A comparison between the fluidised bed dynamics obtained from hard-sphere discrete particle simulations, two-fluid simulations with the standard collision model en with the two alternative energy dissipation models proposed in this appendix and chapter 3 of this thesis is made in table A4.1. The comparison is made in terms of bed expansion dynamics and energy balance analyses explained in chapter 3. It can be concluded from this table that both two-fluid simulations with an effective coefficient of restitution, which takes the effect of energy dissipation due to friction into account, show much better agreement with the discrete particle simulation than the standard two-fluid model, on all aspects of the analysis.

Table A4.1. Comparison of dynamics for discrete particle simulations and two-fluid simulations at 1.5 U_{mf} (DPM = Discrete Particle Model, TFM = Two Fluid Model, $e_{eff,Zhang}$ = effective coefficient of restitution from equation 3.57 using equation 3.58, $e_{eff,DPM}$ = effective restitution coefficient from DPM simulations using equation A4.4).

	DPM	**TFM (e_n=0.97)**	**TFM ($e_{eff,Zhang}$=0.86)**	**TFM ($e_{eff,DPM}$=0.941)**
expansion dynamics				
$\langle h \rangle_t$ [m]	0.097	0.095	0.096	0.096
RMS <h> [m]	0.0052	0.0026	0.0040	0.0037
frequency [Hz]	2.0	2.8	2.2	2.4
energy balance				
E_{tot} [J]	0.507	0.484	0.503	0.501
$E_{pot/tot}$	96%	98%	96%	96%
E_{gran}/E_{tot}-E_{pot}	8%	25%	6%	7%
E_{conv}/E_{tot}-E_{pot}	91%	75%	94%	93%
E_{rot}/E_{tot}-E_{pot}	1%	-	-	-
W_{gas} [W]	0.284	0.060	0.248	0.202
W_{press}/W_{gas}	53%	70%	47%	51%
W_{drag}/W_{gas}	47%	38%	54%	50%
$W_{drag,gran}/W_{gas}$	-	-8%	-1%	-2%
W_{dis} [W]	-0.281	-0.059	-0.218	-0.208

Chapter 5.

Multi-fluid continuum modelling of dense gas-fluidised beds: derivation of kinetic theory closure relations

Abstract

To model fluidisation and segregation dynamics of particulate mixtures in engineering scale gas-fluidised beds, multi-fluid continuum models need to be developed. Goldschmidt et al. (2001b) demonstrated that a multi-fluid model with existing kinetic theory closure relations predicts far too fast segregation in comparison to non-intrusive digital image analysis measurements. Therefore the derivation of a novel set of kinetic theory closure relations and a multi-fluid model in which they are incorporated are presented in this chapter. The main difference between the new kinetic theory closure model and the existing model derived by Manger (1996) and Mathiesen (1997) is that segregation is no longer possible in the first (equilibrium) approximation to the particle velocity distribution, but is introduced as a higher order (non-equilibrium) effect. The new theory seems to give a more realistic physical picture for dense particulate systems such as gas-fluidised beds in which the collision frequency is very high. It is therefore expected that the new model will predict more realistic segregation rates, though this remains to be proven.

1. Introduction

In many industrial dense gas-fluidised bed processes, e.g. gas-phase polymerisation and fluidised bed spray granulation, mixtures of particles with different physical properties are encountered. When particles differ in size and/or density, segregation may occur. Segregation is most marked at low gas velocities when there is appreciable particle density difference. Even a strongly segregating system, however, can be fairly well mixed if the gas velocity is increased sufficiently, although it can be difficult to remove the last traces of segregation. Bubbles have been indicated as the vehicle for both mixing and segregation (Rowe and Nienow, 1976). Rising bubbles carry a mixture of particles to the top of the bed and disturb the packing state of the bed so that segregation of larger or heavier particles may occur. Accurate prediction of segregation is required to improve the design, operation and scale-up of gas-fluidised bed processes. Up till now little is known about the rate at which segregation occurs and in what areas of the fluidised bed it (preferentially) takes place. However, for the design of particle growth processes such as fluidised bed spray granulation, in which large particle size and density differences occur and accurate tuning of growth rate and segregation dynamics is required to control product quality, it is of great importance to understand the rate and spatial distribution of segregation.

In the last decade considerable progress has been made in the area of fundamental hydrodynamic modelling of gas-fluidised suspensions. The hydrodynamic behaviour of mono-disperse dense gas-fluidised beds can nowadays be modelled with discrete particle models and two-fluid continuum models, as discussed in previous chapters. Hoomans et al. (1998c, 2000b) demonstrated the ability of discrete particle models to predict segregation in dense gas-fluidised beds. They observed a strong influence of the particle-particle collision parameters on bubble dynamics and consequent segregation rates. To model segregation in engineering scale gas-fluidised beds, multi-fluid continuum models need to be developed. For particulate systems this type of model has been pioneered by Syamlal (1985). Multi-fluid models divide the particle mixture into a discrete number of classes for which different physical properties may be specified. The conservation equations employed are a generalisation of the Navier-Stokes equations for interpenetrating continua. Owing to the continuum representation of the particle mixture, multi-fluid continuum models require additional closure laws to describe the rheology of the particulate suspension. Since accurate modelling of bubble dynamics is of crucial importance to capture segregation dynamics and bubble behaviour strongly depends on

the amount of energy dissipated in collisions, the closure laws should correctly account for the effect of energy dissipation due to non-ideal particle-particle encounters. As discussed in previous chapters, closure laws derived from the kinetic theory of granular flow have significantly improved the description of the rheology of mono-disperse gas-fluidised beds. Therefore, a multi-fluid model with a novel set of closures derived by extension of the kinetic theory to dense granular mixtures is presented in this chapter.

Several authors have worked on the derivation of constitutive relations for binary and multi-component mixtures based on the kinetic theory of granular flow. Most work is based upon the derivations presented by Tham and Gubbins (1971) and Lopez de Haro et al. (1983) for multi-component dense gas mixtures. Tham and Gubbins (1971) used the standard Enskog theory, whereas Lopez de Haro et al. (1983) applied the revised Enskog theory by Van Beijeren and Ernst (1973) to warrant consistency with irreversible thermodynamics. A first attempt to extend the theory to dense granular mixtures was presented by Jenkins and Mancini (1987) for a binary particle mixture. They assumed the particle velocities to be Maxwellian distributed for both particle species, but around a *different* mean velocity and with a *different* granular temperature for each species. A few years later Jenkins and Mancini, (1989) presented a more exact theory following the Chapman-Enskog solution procedure (Chapman and Cowling, 1970). According to this procedure the first approximation to the particle velocity distribution for each species should indeed satisfy a Maxwellian distribution, but the mean velocity and granular temperature in the first (equilibrium) approximation should be *the same* for all species. They derived analytical expressions for the rheologic properties of a binary mixture of nearly elastic spheres in the lowest order Enskog approximation and analysed the mixture viscosity and particle pressure of a binary mixture of hard spheres in a steady, homogeneous shear flow. The work of Jenkins and Mancini was (partly) extended to the second order Enskog approximation by Arnarson and Willits (1998), who applied the kinetic theory to study segregation of a binary mixture of nearly elastic spheres in steady, fully developed flow. The theoretical foundation of the Enskog theory for dense multi-component mixtures of slightly inelastic spheres is given by Zamankhan (1995). Using a generalised Grad moment method (Grad, 1949) constitutive equations up to first order in the gradients are derived. The effects of particle granular temperature perturbations are not considered in this work, hence the component temperatures are equal to the mixture temperature. The theory is applied to study the rheology of binary mixtures of granular materials undergoing steady shearing flow.

In earlier publications (Goldschmidt et al., 2001a, 2001b) the multi-fluid model derived by Manger (1996) and Mathiesen (1997) was applied. This model assumes the particle velocities to be Maxwellian distributed around *different* mean velocities and with *different* granular temperatures for all particle species, which appears to be inconsistent with the first (equilibrium) approximation obtained from the Chapman-Enskog solution procedure. It is now believed that this assumption in the theory might (to a large extent) have caused the far too high segregation rates predicted by the continuum model (see Goldschmidt et al. 2001a, 2001b). Therefore, a novel set of closure relations for multi-component mixtures of slightly inelastic granular materials, derived according to the Chapman-Enskog solution procedure and accurate to the third order Enskog approximation is presented. The derivation outlined in this chapter is based upon the work of Lopez de Haro et al. (1983) and Jenkins and Mancini (1989). For full details of the derivation the interested reader is referred to Goldschmidt and Van Sint Annaland (2001).

2. Kinetic theory of multi-component mixtures

The kinetic theory of granular flow of multi-component mixtures is a statistical mechanical framework that describes the mean and fluctuating motion of particles of all species (1..NP) within a continuous granular medium. The theory is based on the assumption that the velocity distribution $f_n(\overline{c}_n,\overline{r},t)$ of individual particles of species *n*, among a large number $n_n d\overline{r}$ of particles within an ensemble of volume $d\overline{r}$, can be represented by the distribution of their velocity points $\overline{c}_n$ in the velocity space. The number of particles of species *n* per unit volume and the ensemble average of a particle quantity ϕ_n are respectively given by:

$$n_n = \int f_n(\overline{c}_n,\overline{r},t)\,d\overline{c}_n \tag{5.1}$$

$$<\phi_n> = \frac{1}{n_n} \int \phi_n f_n(\overline{c}_n,\overline{r},t)\,d\overline{c}_n \tag{5.2}$$

For example, the mean velocity $\overline{u}_n$ of species *n* is $<\overline{c}_n>$. In terms of it, the mass average mixture velocity $\overline{u}_s$ is given by:

$$\overline{u}_s = \frac{1}{\varepsilon_s \rho_s} \sum_{n=1}^{NP} \varepsilon_n \rho_n \overline{u}_n \tag{5.3}$$

Furthermore the particle number density, the total solids volume fraction and the mixture density are given by:

$$n_s = \sum_{n=1}^{NP} n_n \tag{5.4}$$

$$\varepsilon_s = \sum_{n=1}^{NP} \varepsilon_n \tag{5.5}$$

$$\rho_s = \frac{1}{\varepsilon_s} \sum_{n=1}^{NP} \varepsilon_n \rho_n \tag{5.6}$$

Similar to mono-disperse systems, the actual particle velocity $\overline{c}_n$ is decomposed in the local mean solids velocity $\overline{u}_s$ and the peculiar velocity $\overline{C}_n$:

$$\overline{c}_n = \overline{u}_s + \overline{C}_n \tag{5.7}$$

Associated with the random motion of the particles the granular temperature and the diffusion velocity of species *n* are defined as:

$$\theta_n = \frac{1}{3} m_n < C_n^2 > \tag{5.8}$$

$$\overline{v}_n = < \overline{C}_n > = \overline{u}_n - \overline{u}_s \tag{5.9}$$

from which the mixture granular temperature is obtained by:

$$\theta_s = \frac{1}{n_s} \sum_{n=1}^{NP} n_n \theta_n \tag{5.10}$$

whereas the diffusion velocities satisfy the relation:

$$\sum_{n=1}^{NP} \varepsilon_n \rho_n \overline{v}_v = 0 \tag{5.11}$$

The kinetic theory accounts for two different transport mechanisms of particle properties. On the one hand particles can transport a property by carrying it during free flight between collisions (kinetic transport), on the other hand particle quantities can be

transferred during a collision. Modelling these transport mechanisms for a particulate mixture results in a set of coupled integral-differential equations of the same form as the well-known Boltzmann integral-differential equation for mono-disperse systems. The rate of change of the velocity distribution function f_n of particles of species n, moving under influence of an external force F_n and colliding with particles of all species present in the mixture, is given by:

$$\frac{\partial f_n}{\partial t} + \overline{c}_n \cdot \frac{\partial f_n}{\partial \overline{r}} + \frac{\partial}{\partial \overline{c}_n} \cdot \left(\frac{\overline{F}_n}{m_n} f_n \right) = \sum_p \iint_{\overline{c}_{12_{np}} \cdot \overline{k} > 0} \left[f_{np}^{(2)}(\overline{c}_{1_n}', \overline{r}, \overline{c}_{2_p}', \overline{r} - \sigma_{np}\overline{k}, t) - f_{np}^{(2)}(\overline{c}_{1_n}, \overline{r}, \overline{c}_{2_p}, \overline{r} + \sigma_{np}\overline{k}, t) \right] \sigma_{np}^2 (\overline{c}_{12_{np}} \cdot \overline{k}) d\overline{k} d\overline{c}_{2_p} \tag{5.12}$$

In this *generalised Boltzmann equation* for particulate mixtures $\sigma_{np} = (\sigma_n + \sigma_p)/2$ is the inter-particle distance, $\overline{c}_{12_{np}} = \overline{c}_{1_n} - \overline{c}_{2_p}$ the impact velocity between particle 1 of species n and particle 2 of species p and $\overline{k}$ the unit vector directed from the centre of particle 1 to the centre of particle 2. Furthermore $\overline{c}_{1_n}'$ and $\overline{c}_{2_p}'$ denote the particle velocities evaluated after collision, which can be related to the velocities prior to collision according to:

$$\overline{c}_{1_n}' = \overline{c}_{1_n} - M_{pn}(1 + e_{np})(\overline{c}_{12_{np}} \cdot \overline{k})\overline{k} \tag{5.13}$$

$$\overline{c}_{2_p}' = \overline{c}_{2_p} + M_{np}(1 + e_{np})(\overline{c}_{12_{np}} \cdot \overline{k})\overline{k} \tag{5.14}$$

where the reduced mass is given by $M_{np} = m_n / (m_n + m_p)$ and e_{np} is the coefficient of normal restitution for a collision between particles of species n and p. This coefficient is the only collision parameter accounted for in the kinetic theory of granular flow, and is defined by the following relation between the impact and rebound velocity:

$$\overline{c}_{12_{np}}' \cdot \overline{k} = -e_{np}(\overline{c}_{12_{np}} \cdot \overline{k}) \tag{5.15}$$

The pair distribution function $f_{np}^{(2)}(\overline{c}_{1_n}, \overline{r}_1, \overline{c}_{2_p}, \overline{r}_2, t)$ is defined in such a way that the product $f_{np}^{(2)}(\overline{c}_{1_n}, \overline{r}_1, \overline{c}_{2_p}, \overline{r}_2, t) d\overline{c}_{1_n} d\overline{r}_1 d\overline{c}_{2_p} d\overline{r}_2$ represents the probability of finding a pair of particles at time t in volumes $d\overline{r}_1$ and $d\overline{r}_2$ centred at $\overline{r}_1$ and $\overline{r}_2$ having velocities between $\overline{c}_{1_n}$ and $\overline{c}_{1_n} + d\overline{c}_{1_n}$ and $\overline{c}_{2_p}$ and $\overline{c}_{2_p} + d\overline{c}_{2_p}$ respectively.

2.1. Conservation equations

The ensemble average transport equation for particle property ϕ_n can be obtained by multiplying equation 5.12 with $\phi_n d\overline{c}_n$ and integrating over the entire velocity space, which yields:

$$\int \phi_n \frac{\partial f_n^c}{\partial t} d\overline{c}_n + \int \phi_n \overline{c}_n \cdot \frac{\partial f_n^c}{\partial \overline{r}} d\overline{c}_n + \int \phi_n \frac{\partial}{\partial \overline{c}_n} \cdot \left(\frac{\overline{F}_n}{m_n} f_n^c \right) d\overline{c}_n = \sum_{p=1}^{NP} n_n \Delta_p \phi_n \tag{5.16}$$

in which $n_n \Delta_p \phi_n$ represents the rate of change of property ϕ_n of species n due to collisions with particles of species p. Applying the chain rule to the kinetic transport integrals on the left hand side and expanding the expressions $n_n \Delta_p \phi_n$ into Taylor series, the *Maxwell transport equation* for a property ϕ_n of particle species n is obtained:

$$\begin{aligned} &\frac{\partial < n_n \phi_n >}{\partial t} + \frac{\partial}{\partial \overline{r}} \cdot < n_n \phi_n \overline{c}_n > = \\ &\quad n_n < \frac{\partial \phi_n}{\partial t} > + < n_n \overline{c}_n \cdot \frac{\partial \phi_n}{\partial \overline{r}} > + < \frac{n_n \overline{F}_n}{m_n} \cdot \frac{\partial \phi_n}{\partial \overline{c}_n} > + \sum_{p=1}^{NP} \left[\chi_{np}(\phi_n) - \frac{\partial}{\partial \overline{r}} \cdot \theta_{np}(\phi_n) \right] \end{aligned} \tag{5.17}$$

In this equation the collisional contribution has been decomposed into a collisional source (containing all even powers of the spatial derivatives),

$$\begin{aligned} \chi_{np}(\phi_n) = \sigma_{np}^2 \iiint_{\overline{c}_{12_{np}} \cdot \overline{k} > 0} (\phi'_{1_n} - \phi_{1_n}) \left[1 + \sum_{m=1} \frac{1}{(2m)!} \left(\frac{1}{2} \sigma_{np} \overline{k} \cdot \frac{\partial}{\partial \overline{r}} \right)^{2m} \right] \\ f_{np}^{(2)}(\overline{c}_{1_n}, \overline{r} - \frac{1}{2} \sigma_{np} \overline{k}, \overline{c}_{2_p}, \overline{r} + \frac{1}{2} \sigma_{np} \overline{k}, t) (\overline{c}_{12_{np}} \cdot \overline{k}) d\overline{k} d\overline{c}_{1_n} d\overline{c}_{2_p} \end{aligned} \tag{5.18}$$

and a collisional flux (containing all odd powers of the spatial derivatives):

$$\begin{aligned} \theta_{np}(\phi_n) = -\frac{1}{2} \sigma_{np}^3 \iiint_{\overline{c}_{12_{np}} \cdot \overline{k} > 0} (\phi'_{1_n} - \phi_{1_n}) \left[1 + \sum_{m=1} \frac{1}{(2m+1)!} \left(\frac{1}{2} \sigma_{np} \overline{k} \cdot \frac{\partial}{\partial \overline{r}} \right)^{2m} \right] \\ f_{np}^{(2)}(\overline{c}_{1_n}, \overline{r} - \frac{1}{2} \sigma_{np} \overline{k}, \overline{c}_{2_p}, \overline{r} + \frac{1}{2} \sigma_{np} \overline{k}, t) (\overline{c}_{12_{np}} \cdot \overline{k}) \overline{k} d\overline{k} d\overline{c}_{1_n} d\overline{c}_{2_p} \end{aligned} \tag{5.19}$$

In the current order of approximation only terms up to the first order in the spatial derivatives are retained.

The *continuity equation for species n* can be obtained from the Maxwell transport equation (equation 5.17) by substituting $\phi_n = m_n$, which results in:

$$\frac{\partial(\varepsilon_n \rho_n)}{\partial t} + \nabla \cdot \left[\overline{J}_n + \varepsilon_n \rho_n \overline{u}_s \right] = 0 \tag{5.20}$$

where the diffusion flux of species *n* is defined by:

$$\overline{J}_n = \varepsilon_n \rho_n < \overline{C}_n > \tag{5.21}$$

Substituting equation 5.9 it can readily be shown that the continuity equation can also be simplified to:

$$\frac{\partial(\varepsilon_n \rho_n)}{\partial t} + \nabla \cdot (\varepsilon_n \rho_n \overline{u}_n) = 0 \tag{5.22}$$

By summing all individual continuity equations the *mixture continuity equation* is obtained:

$$\frac{\partial(\varepsilon_s \rho_s)}{\partial t} + \nabla \cdot (\varepsilon_s \rho_s \overline{u}_s) = 0 \tag{5.23}$$

The *momentum equation for species n* can be derived by substituting $m_n \overline{c}_n$ in the Maxwell transport equation (equation 5.17):

$$\begin{aligned} \frac{\partial(\varepsilon_n \rho_n \overline{u}_n)}{\partial t} + \nabla \cdot (\varepsilon_n \rho_n \overline{u}_n \overline{u}_n) = {} & \nabla \cdot (\varepsilon_n \rho_n (\overline{u}_n - \overline{u}_s) \overline{u}_n) - \nabla \cdot (\varepsilon_n \rho_n (\overline{u}_n - \overline{u}_s) \overline{u}_s) \\ & - \nabla P_n^s - \nabla \cdot \overline{\overline{\tau}}_n - \varepsilon_n \nabla P_g + \beta_{ng} (\overline{u}_g - \overline{u}_n) + \sum_{p=1, p \neq n}^{NP} \overline{\beta}_{np} + \varepsilon_n \rho_n \overline{g} \end{aligned} \tag{5.24}$$

whereby the following definitions have been introduced for the transport properties:

$$\overline{\overline{P}}_n^k = n_n m_n < \overline{C}_n \overline{C}_n > \tag{5.25}$$

$$\overline{\overline{P}}_n^c = \sum_{p=1}^{NP} \overline{\overline{P}}_{np}^c = \sum_{p=1}^{NP} \theta_{np} (m_n \overline{c}_n) \tag{5.26}$$

$$\bar{\bar{P}}_n = \bar{\bar{P}}_n^k + \bar{\bar{P}}_n^c = P_n^s \bar{\bar{I}} + \bar{\bar{\tau}}_n \tag{5.27}$$

$$\bar{\beta}_{np} = \chi_{np}(m_n \bar{c}_n) \tag{5.28}$$

Moreover, specifically for gas-fluidised beds, gravity, buoyancy and drag exerted by the gas phase have been taken into account as the external forces acting on the particles:

$$\frac{\bar{F}_n}{m_n} = \bar{g} - \frac{1}{\rho_n}\nabla P_g + \frac{\beta_{ng}}{n_n m_n}(\bar{c}_g - \bar{c}_n) \tag{5.29}$$

Since momentum is conserved in collisions, the momentum source $\bar{\beta}_{np}$ arises only for collisions between unlike pairs. Upon summation of the individual momentum balances this term vanishes and the *mixture momentum balance* can be derived as:

$$\frac{\partial(\varepsilon_s \rho_s \bar{u}_s)}{\partial t} + \nabla\cdot(\varepsilon_s \rho_s \bar{u}_s \bar{u}_s) = -\nabla P_s^s - \nabla\cdot\bar{\bar{\tau}}_s - \varepsilon_s \nabla P_g + \sum_{n=1}^{NP} \beta_{ng}(\bar{u}_g - \bar{u}_n) + \varepsilon_s \rho_s \bar{g} \tag{5.30}$$

where the particle pressure and the stress tensor for the mixture have been defined as:

$$P_s^s = \sum_{n=1}^{NP} P_n^s \tag{5.31}$$

$$\bar{\bar{\tau}}_s = \sum_{n=1}^{NP} \bar{\bar{\tau}}_n = -\left\{\left(\lambda_s - \frac{2}{3}\mu_s\right)(\nabla\cdot\bar{u}_s)\bar{\bar{I}} + \mu_s\left((\nabla\bar{u}_s) + (\nabla\bar{u}_s)^T\right)\right\} \tag{5.32}$$

The *granular temperature balance for species n* (the fluctuating kinetic energy balance) is obtained from the Maxwell transport equation (equation 5.17) by substitution of $\frac{1}{2} m_n c_n^2$ for the property ϕ_n. This results in:

$$\frac{3}{2}\left\{\frac{\partial(n_n\theta_n)}{\partial t} + \nabla\cdot(n_n\theta_n\bar{u}_s)\right\} = -(P_n^s\bar{\bar{I}} + \bar{\bar{\tau}}_n) : \nabla\bar{u}_s - \nabla\cdot\bar{q}_n + \beta_{ng} < \bar{C}_g\cdot\bar{C}_n > -3\frac{\beta_{ng}}{m_n}\theta_n - \gamma_n \tag{5.33}$$

Introducing the following definitions:

$$\bar{q}_n^k = \frac{1}{2} n_n m_n < C_n^2 \bar{C}_n > \tag{5.34}$$

$$\overline{q}_n^c = \sum_{n=1}^{NP} \overline{q}_{np}^c = \sum_{n=1}^{NP} \theta_{np} (\frac{1}{2} m_n C_n^2) \tag{5.35}$$

$$\overline{q}_n = \overline{q}_n^k + \overline{q}_n^c \tag{5.36}$$

$$\gamma_n = -\sum_{p=1}^{NP} \gamma_{np} = -\sum_{p=1}^{NP} \chi_{np} (\frac{1}{2} m_n c_n^2) \tag{5.37}$$

For dense gas fluidised beds the contribution of the term $\beta_{ng} < \overline{C}_g \cdot \overline{C}_n >$, representing the exchange of fluctuating energy between the fluctuating velocity component of the gas phase and the fluctuating particle velocity, can be neglected since gas-phase turbulence at length scales much larger than the particle diameter is fully dampened by the dense suspension of particles with relatively high momentum inertia. The *mixture granular temperature equation* is obtained by summing over all particle species:

$$\frac{3}{2}\left\{\frac{\partial(n_s\theta_s)}{\partial t} + \nabla\cdot(n_s\theta_s\overline{u}_s)\right\} = -(P_s^s\overline{\overline{I}} + \overline{\overline{\tau}}_s) : \nabla\overline{u}_s - \nabla\cdot\overline{q}_s + \sum_{n=1}^{NP}\beta_{ng} < \overline{C}_g \cdot \overline{C}_n > - \sum_{n=1}^{NP} 3\frac{\beta_{ng}}{m_n}\theta_n - \gamma_s \tag{5.38}$$

where the following definitions were applied:

$$\overline{q}_s = \sum_{n=1}^{NP} \overline{q}_n \tag{5.39}$$

$$\gamma_s = \sum_{n=1}^{NP} \gamma_n \tag{5.40}$$

For evaluating the transport coefficients defined in this paragraph explicit functions for the individual particle velocity distribution function f_n and the pair distribution function $f_{np}^{(2)}$ are required.

2.2. Velocity distribution and pair distribution function

In order to determine the collisional terms appearing in the balance laws, the pair distribution functions at contact $f_{np}^{(2)}(\overline{c}_{1_n}, \overline{r} - \frac{1}{2}\sigma_{np}\overline{k}, \overline{c}_{2_p}, \overline{r} + \frac{1}{2}\sigma_{np}\overline{k}, t)$ are needed. Following Enskog, assuming binary interactions and 'molecular' chaos, the pair distribution function can be approximated by the product of two single-particle velocity distribution functions and the radial distribution function $g_{np}(\overline{r} - \frac{1}{2}\sigma_{np}\overline{k}, \overline{r} + \frac{1}{2}\sigma_{np}\overline{k}, t)$, that

corrects the probability of a collision for the effect of the volume occupied by the particles:

$$f_{np}^{(2)}(\bar{c}_{1_n}, \bar{r} - \frac{1}{2}\sigma_{np}\bar{k}, \bar{c}_{2_p}, \bar{r} + \frac{1}{2}\sigma_{np}\bar{k}, t) = g_{np}(\bar{r} - \frac{1}{2}\sigma_{np}\bar{k}, \bar{r} + \frac{1}{2}\sigma_{np}\bar{k}, t)\, f_n(\bar{c}_{1_n}, \bar{r} - \frac{1}{2}\sigma_{np}\bar{k}, t)\, f_p(\bar{c}_{2_p}, \bar{r} + \frac{1}{2}\sigma_{np}\bar{k}, t) \tag{5.41}$$

The only time dependency of the radial distribution function is through the change of the particle concentration. To avoid conflicts with irreversible thermodynamics that arise for multi-size particle mixtures when the radial distribution function is evaluated at any specific point on the line joining the midpoints of the two particles at contact, Van Beijeren and Ernst (1973) proposed the so-called revised Enskog theory. According to the revised Enskog theory the radial distribution function in equation 5.41 has to be taken as a non-local functional of the particle density field. Therefore, gradients of the chemical potentials of all species *n* appear in the revised Enskog theory where the gradient of the radial distribution function appears in the standard Enskog theory. The revised Enskog theory was also employed by Lopez de Haro et al. (1983) and Jenkins and Mancini (1989), whose results have been used to derive detailed expressions for the particle velocity distribution functions for multi-component mixtures of inelastic spheres.

In order to obtain an expression for the particle velocity distribution function for particles of species *n* the generalised Boltzmann equation (equation 5.12) has to be solved. Here the Chapman-Enskog solution method of successive approximation (Chapman and Cowling, 1970) is applied:

$$f_n = f_n^{(0)} + f_n^{(1)} + f_n^{(2)} + \ldots \tag{5.42}$$

In this work terms up to the second approximation $f_n^{(1)}$ are taken into account. The first approximation to the velocity distribution function is the velocity distribution of a non-dissipative system at equilibrium. The effects of energy dissipation and spatial gradients are taken into account in the second approximation by the coefficients of normal restitution e_{np} and a perturbation function $\Phi_n^{(1)}$. It is assumed that higher order gradients are small so the contribution of higher approximations to the velocity distribution can be neglected. Then the particle velocity distribution function up to the second approximation of the Chapman-Enskog solution procedure (up to first order in gradients) is given by:

$$f_n = f_n^{(0)} + f_n^{(1)} = f_n^{(0)}(1 + \Phi_n^{(1)}) \tag{5.43}$$

2.2.1. First approximation $f_n^{(0)}$

In first approximation the particulate suspension is assumed to be at equilibrium. It is assumed that the system is in steady state, that the particles that are uniformly suspended so that there are no spatial gradients, that the particles are not subjected to external forces and that no energy is dissipated in collisions. Then, following Chapman and Cowling (1970), it can be shown that the first approximation to the particle velocity distribution should satisfy a *Maxwellian velocity distribution* given by:

$$f_n^{(0)} = n_n \left(\frac{m_n}{2\pi\theta_s} \right)^{\frac{3}{2}} e^{-\frac{m_n(\bar{c}_n - \bar{u}_s)^2}{2\theta_s}} \tag{5.44}$$

Since the velocity distribution functions for all particle species are coupled by collisional interactions, the Chapman-Enskog solution procedure *requires* that the particle velocities for all particle species are distributed around *the same mean velocity* (the mixture velocity) with *the same granular temperature* (the mixture temperature). So for the first approximations to the diffusion flux and granular temperature of all species *n* we have:

$$\bar{J}_n^{(0)} = 0 \tag{5.45}$$

$$\theta_n^{(0)} = \theta_s \tag{5.46}$$

Substituting the first approximation to the velocity distribution in the conservation equations for the mixture the *Euler equations* for a multi-component mixture of fluidised hard-spheres are obtained:

$$\frac{\partial_0 n_n}{\partial t} + \nabla \cdot (n_n \bar{u}_s) = 0 \tag{5.47}$$

$$\frac{\partial_0 \bar{u}_s}{\partial t} + \bar{u}_s \cdot \nabla \bar{u}_s = -\frac{1}{\varepsilon_s \rho_s} \nabla P_s^{s(0)} - \frac{1}{\rho_s} \nabla P_g + \frac{1}{\varepsilon_s \rho_s} \sum_{n=1}^{NP} \beta_{n0} (\bar{u}_g - \bar{u}_s) + \bar{g} \tag{5.48}$$

$$\frac{\partial_0 \theta_s}{\partial t} + \bar{u}_s \cdot \nabla \theta_s = -\frac{2}{3n_s} \left(P_s^{s(0)} \nabla \cdot \bar{u}_s - \sum_{n=1}^{NP} \beta_{ng} < \bar{C}_g \cdot \bar{C}_n > + \sum_{n=1}^{NP} \frac{3\beta_{ng}}{m_n} \theta_s \right) \tag{5.49}$$

At this order the mixture pressure is given by:

$$P_s^{s(0)} = \theta_s \left(n_s + \frac{2\pi}{3} \sum_{n=1}^{NP} \sum_{p=1}^{NP} n_n n_p \sigma_{np}^3 g_{np} \right) \tag{5.50}$$

Furthermore $\bar{\bar{\tau}}_s^{(0)}$, $\bar{\beta}_{np}^{(0)}$, $\bar{q}_s^{(0)}$ and $\gamma_s^{(0)}$ are equal to zero. At this point it should be mentioned that, in order to avoid inconsistencies in the second approximation which will be discussed in the next paragraph, all coefficients of restitution have to be taken equal to 1 in the first approximation of the closure equations. As a result the coefficients of restitution do not appear in the particle pressure (equation 5.50) and the energy dissipation term ($\gamma_s^{(0)}$) equals zero.

2.2.2. Second approximation $f_n^{(1)}$

The second approximation of the particle velocity distribution function can be obtained by substitution of equation 5.43 in the generalised Boltzmann equation (equation 5.12). Its derivation is one of the more tedious parts of the theory and a detailed discussion can be found in Goldschmidt and Van Sint Annaland (2001). Considering the dependency of the external forces on the peculiar particle velocity as a higher order effect (ignoring the last two terms in equation 5.49), the second approximation to the Boltzmann equation reduces to the following partial differential-integral equation for $\Phi_n^{(1)}$:

$$\begin{aligned}\sum_{p=1}^{NP} n_n n_p g_{np} I_{np}(\Phi_n^{(1)} + \Phi_p^{(1)}) = &- f_n^{(0)} \times \\ &\left\{ \left(1 + \frac{8\pi}{5} \sum_{p=1}^{NP} n_p \sigma_{np}^3 M_{np} M_{pn} g_{np} \right) \left(\bar{\square}_{1_n}^2 - \frac{5}{2} \right) \bar{C}_{1_n} \cdot \nabla \ln \theta_s \right. \\ &+ \left(1 + \frac{8\pi}{15} \sum_{p=1}^{NP} n_p \sigma_{np}^3 M_{pn} g_{np} \right) 2 \bar{\square}_{1_n}^{o} \bar{\square}_{1_n} : \nabla \bar{u}_s \\ &\left. + \frac{2}{3} \left(1 + \frac{4\pi}{3} \sum_{p=1}^{NP} n_p \sigma_{np}^3 M_{pn} g_{np} - \frac{P_s^{s(0)}}{n_s \theta_s} \right) \left(\bar{\square}_{1_n}^2 - \frac{3}{2} \right) \nabla \cdot \bar{u}_s + \frac{n_s}{n_n} \bar{C}_{1_n} \cdot \bar{d}_n \right\}\end{aligned} \tag{5.51}$$

In this equation the collision integral is defined as:

$$I_{np}(F) = \frac{1}{n_n n_p} \iint_{\bar{c}_{12_{np}} \cdot \bar{k} > 0} f_{1_n}^{(0)} f_{2_p}^{(0)} (F - F') \sigma_{np}^2 (\bar{c}_{12_{np}} \cdot \bar{k}) d\bar{k} d\bar{c}_{2_p} \tag{5.52}$$

and the dimensionless peculiar velocity is given by:

$$\bar{\square}_n = \sqrt{\frac{m_n}{2\theta_s}} \bar{C}_n \tag{5.53}$$

Further, applying the revised Enskog theory, the diffusion force is given by:

$$\begin{aligned}\overline{d}_n = &-\frac{\varepsilon_n \rho_n}{\varepsilon_s \rho_s n_s \theta_s}\left[\nabla P_s^{s(0)} + \sum_{p=1}^{NP}\left(\varepsilon_n \rho_n \frac{\overline{\overline{F}}_{\overline{u},n}}{m_n} - \varepsilon_p \rho_p \frac{\overline{\overline{F}}_{\overline{u},p}^{(0)}}{m_p}\right)\right] \\ &+ \frac{n_n}{n_s}\sum_{p=1}^{NP}\left[\delta_{np} + \frac{4\pi}{3} M_{np} n_p \sigma_{np}^3 g_{np}\right]\nabla \ln \theta_s + \frac{n_n}{n_s \theta_s}\sum_{p=1}^{NP}\left(\frac{\partial \mu_n}{\partial n_p}\right)_{T, n_{k\neq p}} \nabla n_p\end{aligned} \tag{5.54}$$

in which μ_n is the chemical potential for species *n*. It should be marked that the diffusion forces are not independent, but have to satisfy the relation:

$$\sum_{n=1}^{NP} \overline{d}_n = 0 \tag{5.55}$$

to obtain a consistent set of closure relations. Therefore, in the expression for the external forces exerted upon species *n* that have been obtained from the first approximation, $\overline{u}_n^{(0)}$ (formally equal to $\overline{u}_s$) is replaced by $\overline{u}_n$ to guarantee that the external forces in equation 5.54 cancel upon summation over all species. This substitution is legitimate since the velocity dependence of the external forces is also regarded as a higher order effect on the velocity distribution function. Thus, the following external forces have been substituted for a gas-fluidised particulate suspension:

$$\frac{\overline{\overline{F}}_{\overline{u},n}^{(0)}}{m_n} \approx \frac{\overline{\overline{F}}_{\overline{u},n}}{m_n} = \left\{\overline{g} - \frac{1}{\rho_n}\nabla P_g + \frac{\beta_{ng}}{n_n m_n}(\overline{u}_g - \overline{u}_n)\right\} \tag{5.56}$$

All other terms in equation 5.54 cancel against each other upon summation over all species, because of the basic thermodynamic relations between particle pressure, granular temperature, chemical potential and radial distribution function resulting from the same equation of state (see appendix 5A and the book of Reed and Gubbins, 1973).

Comparison of equation 5.51 to expression obtained by Jenkins and Mancini (1989) for binary mixtures (their expression 28):

$$\sum_{p=1}^{2} n_n n_p g_{np} I_{np}(\Phi_n^{(1)} + \Phi_p^{(1)}) + O(1-e_{np}) = -f_n^{(0)} \times$$
$$\left\{\left(1+\frac{8\pi}{5}\sum_{p=1}^{2} n_p \sigma_{np}^3 M_{np} M_{pn} g_{np}\right)\left(\square_{1_n}^{2} - \frac{5}{2}\right)\overline{C}_{1_n} \cdot \nabla \ln \theta_s\right.$$
$$+\left(1+\frac{8\pi}{15}\sum_{p=1}^{2} n_p \sigma_{np}^3 M_{pn} g_{np}\right) 2\overline{\square}_{1_n}^{o} \overline{\square}_{1_n} : \nabla \overline{u}_s \qquad (5.57)$$
$$+\frac{2}{3}\left(1+\frac{4\pi}{3}\sum_{p=1}^{2} n_p \sigma_{np}^3 M_{pn} g_{np} - \frac{P_s^{s(0)}}{n_s \theta_s}\right)\left(\square_{1_n}^{2} - \frac{3}{2}\right)\nabla \cdot \overline{u}_s$$
$$\left.+\frac{n_s}{n_n}\overline{C}_{1_n} \cdot \overline{d}_n - \frac{2}{3 n_s \theta_s}\left(\square_{1_n}^{2} - \frac{3}{2}\right)\gamma^{(0)}\right\}$$

shows that Jenkins and Mancini retrieved two additional terms. However, the first extra term, $O(1-e_{np})$, according to Jenkins and Mancini (1989) may be ignored in the second approximation, because it is of a higher order in gradients. The second extra term, the last term in equation 5.57 containing $\gamma_s^{(0)}$, regards the effect of energy dissipation on the particle velocity distribution function of species *n*. In the theory derived by Jenkins and Mancini (1989) this term is effectively equal to zero, because they only regard the lowest order Enskog approximation. However, when higher order Enskog approximations are applied, incorporation of the energy dissipation term leads to an inconsistent set of equations for the coefficients in the Sonine polynomials related to it (see Goldschmidt and Van Sint Annaland (2001) for details). Annarson and Willets (1998) extended the revised Enskog theory developed by Jenkins and Mancini (1989) to second order Enskog approximation, but (remarkably) did not take the effect of energy dissipation on the particle velocity distribution into account. It should further be noticed that the energy dissipation term also appears in the derivation of the granular kinetic theory for a single constituent, in which it (to the author's knowledge) has always been ignored.

To avoid the mentioned inconsistency, the coefficients of restitution in all expressions derived from the first approximation have been set equal to 1, which limits the applicability of the theory to slightly inelastic particles. At various points in their derivation Jenkins and Mancini (1989) must also have made this approximation. This can be concluded from the omission of an additional factor $(1+e_{np})/2$, which would have appeared in front of every g_{np} in the right hand side of expression 5.57 and in their expression 26 for the particle pressure. This factor would eventually give rise to an inconsistency between the chemical potential (derived from equilibrium thermodynamics

for a hard sphere gas) and all other thermodynamic properties in the expressions for the diffusion force acting on species *n* (equation 5.54). With the additional factor $(1+e_{np})/2$ the diffusion forces would not have summed to zero (condition 5.55) for granular materials with coefficients of restitution smaller than 1, and the theory would become inconsistent. The relations presented in this chapter are therefore regarded as the current 'state of the art' of kinetic theory closures for multi-component granular media, developed within the framework of the Chapman-Enskog solution strategy.

Since the right-hand side of equation 5.51 is linear in $\Phi_n^{(1)}$ and the left-hand side linear in the gradients of macroscopic quantities of different tensorial character, $\Phi_n^{(1)}$ will be of the form (see Lopez de Haro et al. (1983) and Goldschmidt and Van Sint Annaland (2001) for details):

$$\Phi_n^{(1)} = -\frac{1}{n_s} A_n(\square_n)\bar{C}_n \cdot \nabla \ln \theta_s - \frac{1}{n_s} B_n(\square_n)\overset{0}{\bar{C}}_n\bar{C}_n : \nabla \bar{u}_s - \frac{1}{n_s}\sum_i D_n^{(i)}(\square_n)\bar{C}_n \cdot \bar{d}_i + \frac{1}{n_s} H_n(\square_n)\nabla \cdot \bar{u}_s \tag{5.58}$$

In this equation A_n, B_n, $D_n^{(i)}$ and H_n are functions of C_n, which are expanded in a set of orthonormal functions, the Sonine polynomials, to obtain the following definite expressions:

$$A_n(\square_n) = -\frac{m_n}{2\theta_s}\sum_{r=0}^{N-1} a_r^{(n)} S_{3/2}^{(r)}(\square_n^2) \tag{5.59a}$$

$$B_n(\square_n) = \frac{m_n}{2\theta_s}\sum_{r=0}^{N-1} b_r^{(n)} S_{5/2}^{(r)}(\square_n^2) \tag{5.59b}$$

$$H_n(\square_n) = \sum_{r=0}^{N-1} h_r^{(n)} S_{1/2}^{(r)}(\square_n^2) \tag{5.59c}$$

$$D_n^{(i)}(\square_n) = \frac{m_n}{2\theta_s}\sum_{r=0}^{N-1} d_{n,r}^{(i)} S_{3/2}^{(r)}(\square_n^2) \tag{5.59d}$$

In the *N*-th Enskog approximation the first *N* Sonine polynomials of each expansion are taken into account, so that *r* runs from 0 to *N*-1. The Enskog solution procedure requires that the higher order terms in the expansion for f_n (equation 5.42) do not contribute to the local number densities n_n, the mixture velocity $\bar{u}_s$ and the mixture granular temperature θ_s, which implies the following conditions:

$$\sum_{n=1}^{NP} \frac{\varepsilon_n \rho_n}{\varepsilon_s \rho_s} a_0^{(n)} = 0 \tag{5.60a}$$

$$h_0^{(n)} = 0 \tag{5.60b}$$

$$\sum_{n=1}^{NP} \frac{n_n}{n_s} h_1^{(n)} = 0 \tag{5.60c}$$

$$\sum_{n=1}^{NP} \frac{\varepsilon_n \rho_n}{\varepsilon_s \rho_s} d_{n,r}^{(l)} = 0 \qquad (l = 1, 2, .., \text{NP}) \tag{5.60d}$$

Following Lopez de Haro et al. (1983) the equations for $a_r^{(n)}$ are obtained:

$$\sum_{p=1}^{NP} \sum_{r=0}^{N-1} \Lambda_{np}^{qr} a_r^{(p)} = \frac{4}{5} \frac{n_n}{n_s} K_n \delta_{q1} \qquad (n = 1, 2, .., \text{NP};\ q = 0, 1, .., \text{N-1}) \tag{5.61}$$

in which $\delta_{\alpha\beta}$ is the Kronecker delta which equals 1 for α = β and 0 for all other α and β. For dense granular materials K_n and Λ_{np}^{qr} are given by:

$$K_n = 1 + \frac{8\pi}{5} \sum_{p=1}^{NP} n_p \sigma_{np}^3 M_{np} M_{pn} g_{np} \tag{5.62}$$

$$\Lambda_{np}^{qr} = g_{np} \frac{8}{75} \frac{\sqrt{m_n m_p}}{\theta_s} \left\{ \delta_{np} \sum_{l=1}^{NP} \frac{n_n n_l}{n_s^2} \left[S_{3/2}^{(q)}(\square_n^2)\bar{\square}_n, S_{3/2}^{(r)}(\square_n^2)\bar{\square}_n \right]'_{nl} + \frac{n_n n_p}{n_s^2} \left[S_{3/2}^{(q)}(\square_n^2)\bar{\square}_n, S_{3/2}^{(r)}(\square_n^2)\bar{\square}_n \right]''_{np} \right\} \tag{5.63}$$

and the bracket integrals [F,G]' and [F,G]'' are defined by:

$$[F,G]'_{np} = \int G_n I_{np}(F_n) d\bar{c}_{1_n} = \frac{1}{n_n n_p} \iiint f_{1_n}^{(0)} f_{2_p}^{(0)} G_n (F_n - F_n') \sigma_{np}^2 (\bar{c}_{12_{np}} \cdot \bar{k}) d\bar{k} d\bar{c}_{1_n} d\bar{c}_{2_p} \tag{5.64a}$$

$$[F,G]''_{np} = \int G_n I_{np}(F_p) d\bar{c}_{1_n} = \frac{1}{n_n n_p} \iiint f_{1_n}^{(0)} f_{2_p}^{(0)} G_n (F_p - F_p') \sigma_{np}^2 (\bar{c}_{12_{np}} \cdot \bar{k}) d\bar{k} d\bar{c}_{1_n} d\bar{c}_{2_p} \tag{5.64b}$$

The set of equations (5.61) contains one equation that is a linear combination of NP-1 other equations in the set. Replacing the equation for n = 1 and q = 0 by equation 5.60a results in a well-defined set of equations from which the coefficients $a_r^{(n)}$ can be determined.

Similarly, for $b_r^{(n)}$ the following equations are obtained in *N*-th Enskog approximation:

$$\sum_{p=1}^{NP}\sum_{r=0}^{N-1} H_{np}^{qr} b_r^{(p)} = \frac{2}{\theta_s}\frac{n_n}{n_s} K_n' \delta_{q0} \qquad (n = 1, 2, .., NP;\ q = 0, 1, .., N\text{-}1) \tag{5.65}$$

with

$$K_n' = 1 + \frac{8\pi}{15}\sum_{p=1}^{NP} n_p \sigma_{np}^3 M_{pn} g_{np} \tag{5.66}$$

$$H_{np}^{qr} = g_{np}\frac{2}{5\theta_s}\left[\delta_{np}\sum_{l=1}^{NP}\frac{n_n n_l}{n_s^2}\left[S_{5/2}^{(q)}(\xi_n^2)\bar{\bar{\xi}}_n\bar{\bar{\xi}}_n, S_{5/2}^{(r)}(\xi_n^2)\bar{\bar{\xi}}_n\bar{\bar{\xi}}_n\right]_{nl}' + \frac{n_n n_p}{n_s^2}\left[S_{5/2}^{(q)}(\xi_n^2)\bar{\bar{\xi}}_n\bar{\bar{\xi}}_n, S_{5/2}^{(r)}(\xi_n^2)\bar{\bar{\xi}}_n\bar{\bar{\xi}}_n\right]_{np}''\right] \tag{5.67}$$

The set of equations does not contain any dependent equations, so the coefficients $b_r^{(n)}$ are uniquely defined.

The equations for $h_r^{(n)}$ are:

$$\sum_{p=1}^{NP}\sum_{r=1}^{N-1} \Gamma_{np}^{qr} h_r^{(p)} = \frac{n_n}{n_s} K_n'' \delta_{q1} \qquad (n = 1, 2, .., NP;\ q = 1, .., N\text{-}1) \tag{5.68}$$

with

$$K_n'' = 1 + \frac{4\pi}{3}\sum_{p=1}^{NP} n_p \sigma_{np}^3 M_{pn} g_{np} - \frac{P_s^{s(0)}}{n_s \theta_s} \tag{5.69}$$

$$\Gamma_{np}^{qr} = g_{np}\delta_{np}\sum_{l=1}^{NP}\frac{n_n n_l}{n_s^2}\left[S_{1/2}^{(q)}(\xi_n^2), S_{1/2}^{(r)}(\xi_n^2)\right]_{nl}' + \frac{n_n n_p}{n_s^2}\left[S_{1/2}^{(q)}(\xi_n^2), S_{1/2}^{(r)}(\xi_n^2)\right]_{np}'' \tag{5.70}$$

Note that the indices *r* and *q* in 5.68 only run from 1 to *N*-1 instead of from 0 to *N*-1, to satisfy condition 5.60b. Furthermore, the set of equations (5.68) still contains one dependent equation which is a linear combination of other equations in the set. A well-defined set of equations from which the coefficients $h_r^{(n)}$ can be determined is obtained by replacing the equation for $n = 1$ and $q = 1$ by condition 5.60c.

Finally the equations for $d_{nr}^{(l)}$ read:

$$\sum_{p=1}^{NP}\sum_{r=0}^{N-1}\Delta_{np}^{qr}d_{p,r}^{(l)} = 3\left(\delta_{nl} - \frac{\varepsilon_n\rho_n}{\varepsilon_s\rho_s}\right)\delta_{q0} \qquad (n = 1, 2, .., NP;\ q = 0, 1, .., N\text{-}1;\ l = 1, 2, .., NP) \tag{5.71}$$

with

$$\Delta_{np}^{qr} = g_{np}\frac{\sqrt{m_n m_p}}{\theta_s}\left\{\delta_{np}\sum_{l=1}^{NP}\frac{n_n n_l}{n_s^2}\left[S_{3/2}^{(q)}(\square_n^2)\square_n, S_{3/2}^{(r)}(\square_n^2)\square_n\right]_{nl}' + \frac{n_n n_p}{n_s^2}\left[S_{3/2}^{(q)}(\square_n^2)\square_n, S_{3/2}^{(r)}(\square_n^2)\square_n\right]_{np}''\right\} \tag{5.72}$$

This set of equations (5.71) also contains one dependent equation and the coefficients $d_{nr}^{(l)}$ can be uniquely defined by replacing the equation for $n = 1$ and $q = 0$ by condition 5.60d.

The bracket integrals needed to determine the coefficients $a_r^{(n)}, b_r^{(n)}, d_{nr}^{(l)}$ and $h_r^{(n)}$ to third order Enskog approximation are given in appendix 5B. They have been obtained with little rewriting from the integrals given by Ferziger and Kaper (1972) and Lopez de Haro et al. (1983).

2.2.3. Radial distribution function and chemical potential

To calculate the collisional contributions an explicit expression for the radial distribution function at contact g_{np}, that accounts for the increase in collision frequency due to the volume occupied by the particles themselves, is required. As discussed in the previous section it is important that this radial distribution function matches the expression applied for the chemical potential, i.e. they result from the same equation of state, to fulfil criterion 5.55. Appendix 5A discusses the essential thermodynamic relations that are required to derive a radial distribution function and matching expressions for the chemical potential from some known equation of state for a hard-sphere fluid. An equation of state for a multi-component hard-sphere fluid that diverges near random closest packing is derived in this appendix, applying a simple recipe proposed by Santos et al. (1999). The recipe enables the derivation of the compressibility factor z of a multi-component hard-sphere mixture in terms of the (well-known) compressibility of a single-

component hard-sphere system. The radial distribution function that corresponds to the equation of state proposed by Santos et al. (1999) corresponds to:

$$g_{np}(\varepsilon_s, x_2, ..., x_{NP}, \sigma_1, ..., \sigma_{NP}) = \frac{1}{1-\varepsilon_s} + \left[g_0(\varepsilon_s) - \frac{1}{1-\varepsilon_s} \right] \frac{<\sigma^{(2)}>\sigma_n \sigma_p}{<\sigma^{(3)}>\sigma_{np}} \tag{5.73}$$

where

$$<\sigma^{(n)}> = \sum_{i=1}^{NP} \frac{n_i}{n_s} \sigma_i^n \tag{5.74}$$

It can be seen from equation 5.73 that g_{np} correctly reduces to the radial distribution function g_0 for the single-component system when the number of particle phases *NP* equals 1 and is also consistent when particles of all species have the same size. The general form of the radial distribution function of a mono-disperse hard-sphere fluid is given by:

$$g_0(\varepsilon_s) = \frac{\sum_{n=0} c_n \varepsilon_s^n}{(1-(\varepsilon_s / \varepsilon_s^{max})^a)^b} \tag{5.75}$$

The coefficients in this equation obtained by different authors are presented in table A5.1 in the appendix. Although the best fit of Molecular Dynamics simulation data for mono-disperse systems is obtained by the equation of state given by Ma and Ahmadi (1986), the equation of state derived by Song et al. (1988) is preferred for mathematical reasons explained in appendix 5A. The general expression for the chemical potential of species *n* in a hard-sphere mixture is given by:

$$\mu_n = \theta_s \ln n_n + \theta_s \ln \Lambda_n^3 + \mu_n^{ex} \tag{5.76}$$

in which Λ_n is the equivalent of the De Broglie wavelength for granular materials. For further details on the expression for the excess chemical potential μ_n^{ex} the reader is referred to appendix 5A.

2.3. Constitutive relations

Explicit expressions for the constitutive relations up to first order in gradients can now be obtained from substitution of the velocity distribution function given by equations 5.43, 5.44 and 5.58 in the definitions of the transport coefficients given in paragraph 2.1. For the diffusion flux and the granular temperature substitution of the velocity distribution in relations 5.21 and 5.8 yields:

$$\overline{J}_n^{(1)} = -\frac{\varepsilon_n \rho_n}{2n_s}\left[\sum_{l=1}^{NP} d_{n,0}^{(l)}\overline{d}_l - a_0^{(n)}\nabla \log\theta_s\right] \tag{5.77}$$

$$\theta_n^{(1)} = \theta_s\left(1-\frac{h_1^{(n)}}{n_s}(\nabla\cdot\overline{u}_s)\right) \tag{5.78}$$

So the second approximation, unlike the first approximation, accounts for segregation and temperature differences between particles of different species. From the pressure tensor defined by equations 5.25-5.27, 5.31 and 5.32 expressions for the particle pressure, bulk and shear viscosity are obtained:

$$P_s^{s(1)} = \theta_s\left(n_s + \frac{2\pi}{3}\sum_{n=1}^{NP}\sum_{p=1}^{NP} n_n n_p \sigma_{np}^3 \frac{1+e_{np}}{2} g_{np}\right) \tag{5.79}$$

$$\begin{aligned}\mu_s^{(1)} = {} & \frac{\theta_s}{2n_s}\sum_{n=1}^{NP}\left(1+\frac{8\pi}{15}\sum_{p=1}^{NP} n_p \sigma_{np}^3 M_{pn}\frac{1+e_{np}}{2} g_{np}\right) n_n b_0^{(n)} \\ & + \frac{4}{15}\sqrt{2\pi\theta_s}\sum_{n=1}^{NP}\sum_{p=1}^{NP} n_n n_p \sigma_{np}^4 \sqrt{m_n M_{pn}}\frac{1+e_{np}}{2} g_{np}\end{aligned} \tag{5.80}$$

$$\begin{aligned}\lambda_s^{(1)} = {} & \frac{4\pi}{3}\frac{\theta_s}{n_s}\sum_{n=1}^{NP}\sum_{p=1}^{NP} n_n n_p \sigma_{np}^3 M_{pn}\frac{1+e_{np}}{2} g_{np} h_1^{(n)} \\ & + \frac{4}{9}\sqrt{2\pi\theta_s}\sum_{n=1}^{NP}\sum_{p=1}^{NP} n_n n_p \sigma_{np}^4 \sqrt{m_n M_{pn}}\frac{1+e_{np}}{2} g_{np}\end{aligned} \tag{5.81}$$

A constitutive relation for momentum exchange between particles of different species is obtained by substituting the velocity distribution in equation 5.28. This results in:

$$\overline{\beta}_{np}^{(1)} = \frac{2\pi}{3} n_n n_p \sigma_{np}^3 \frac{1+e_{np}}{2} g_{np} \theta_s \left[\nabla \ln \frac{n_n}{n_p} + \frac{m_p - m_n}{m_n + m_p} \nabla \ln \theta_s \right] \tag{5.82}$$

Finally, evaluation of the granular energy flux and energy dissipation defined by equations 5.34-5.37, 5.39 and 5.40 gives:

$$\begin{aligned} \overline{q}_s^{(1)} = & -\frac{5}{4} \frac{\theta_s}{n_s} \sum_{n=1}^{NP} \left(1 + \frac{24\pi}{15} \sum_{p=1}^{NP} n_p \sigma_{np}^3 M_{np} M_{pn} \frac{1+e_{np}}{2} g_{np} \right) n_n \left(a_1^{(n)} \nabla log\, \theta_s - \sum_l d_{n,1}^{(l)} \overline{d}_l \right) \\ & - \frac{4}{3} \theta_s \sum_{n=1}^{NP} \sum_{p=1}^{NP} \left(\frac{2\pi m_n m_p \theta_s}{m_n + m_p} \right)^{\frac{1}{2}} \frac{n_n n_p}{m_n + m_p} \sigma_{np}^4 \frac{1+e_{np}}{2} g_{np} \nabla log\, \theta_s \\ & + \theta_s \frac{2\pi}{3} \sum_{n=1}^{NP} \sum_{p=1}^{NP} n_p \sigma_{np}^3 (M_{np} - M_{pn}) \frac{1+e_{np}}{2} g_{np} \frac{\overline{J}_n^{(1)}}{m_n} \\ & + \frac{5}{2} \theta_s \sum_{p=1}^{NP} (1 + \frac{2\pi}{3} \sum_{n=1}^{NP} n_n \sigma_{np}^3 \frac{1+e_{np}}{2} g_{np}) \frac{\overline{J}_p^{(1)}}{m_p} \end{aligned} \tag{5.83}$$

$$\gamma_s^{(1)} = \pi \theta_s \sum_{n=1}^{NP} \sum_{p=1}^{NP} n_n n_p \sigma_{np}^3 \frac{m_p}{m_n + m_p} (1 - e_{np}^2) g_{np} \left[\frac{4}{\sigma_{np}} \left(\frac{(m_n + m_p)\theta_s}{2 m_n m_p \pi} \right)^{\frac{1}{2}} - \nabla \cdot \overline{u}_s \right] \tag{5.84}$$

2.4. Collision characteristics

For many particle rate processes the number of collisions, the mean time between successive collisions, the average collision velocity and the collisions velocity distribution are important quantities. For fluidised bed spray granulation e.g., the impact velocity and frequency (amongst others) determine agglomerate breakage and growth rates. The kinetic theory provides a systematic framework to obtain an estimate for these quantities and generate more insight into their dependency on the macroscopic flow characteristics. Therefore several key relations will be given in this paragraph. Besides their importance for practical applications these relations can also be applied to verify the kinetic theory results with more detailed discrete particle models, as shown in the previous chapter.

2.4.1. Number of collisions and collision frequency

An expression for the number of collisions can be obtained from the kinetic theory by evaluating the following integral:

$$N_{np} = \iiint_{\bar{c}_{12_{np}} \cdot \bar{k} > 0} f_{np}^{(2)}(\bar{c}_{12_{np}} \cdot \bar{k})\sigma_{np}^2 d\bar{k} d\bar{c}_{1_n} d\bar{c}_{2_p} \tag{5.85}$$

Up to the second approximation, the *number of collisions per unit volume and time*, between particles of species *n* and *p* is given by:

$$N_{np}^{(1)} = \pi n_n n_p \sigma_{np}^3 g_{np} \left[\frac{4}{\sigma_{np}} \left(\frac{\theta_s}{\pi} \frac{m_n + m_p}{2 m_n m_p} \right)^{\frac{1}{2}} - \frac{2}{3} (\nabla \cdot \bar{u}_s) \right] \tag{5.86}$$

Some care should be taken calculating the number of collisions between pairs of particles of type *n*, per unit volume and time. It is equal to $\frac{1}{2}N_{nn}$ because N_{nn} counts each collision between a pair of particles A, B twice over, once regarding A as particle 1 with velocity c_1 and once as particle 2 with velocity c_2. On the other hand the average number of collisions of any one particle of species *n*, per unit time, with similar particles is N_{nn}/n_n, not $N_{nn}/2n_n$, since each collision affects two particles at once.

The average number of collisions undergone by each particle per unit time is called the *collision frequency*. Thus the frequency for a particle of the first species with like particles is N_{11}/n_1; for collisions with species 2 it is N_{12}/n_1, etc. The frequency of collisions for a particle of species *n* with particles of all kinds is given by:

$$F_n = (N_{n1} + N_{n2} + ...)/n_n = \frac{1}{n_n} \sum_p N_{np} \tag{5.87}$$

2.4.2. Mean fluctuating velocity and mean free path

The *mean fluctuating velocity* for particles of species *n* is given by:

$$< C_n >= \frac{1}{n_n} \int C_n f_n^{(0)} d\bar{C}_n = \left(\frac{8\theta_s}{\pi m_n} \right)^{\frac{1}{2}} \tag{5.88}$$

The *mean free path*, the mean distance travelled by a particle between successive collisions, can now be derived from the collision frequency and the mean fluctuating velocity by:

$$\ell_n = \frac{< C_n >}{F_n} = \frac{n_n}{\sum_p^{NP} N_{np}} \left(\frac{8\theta_s}{\pi m_n} \right)^{\frac{1}{2}} \tag{5.89}$$

2.4.3. Collision velocity distribution and mean impact velocity

The collision velocity distribution can be obtained from the derivation of the number of collisions by carrying out all integrals except the one over the impact velocity. Then the following expression for the normalised *collision velocity distribution* for impacts between particles of species *n* and *p* is obtained:

$$f_{np}^{(1)} = \frac{1}{N_{np}} \sqrt{2\pi} n_n n_p \sigma_{np}^2 g_{np} \left(\frac{1}{\theta_s} \frac{m_n m_p}{m_n + m_p} \right)^{\frac{3}{2}} \times \left(1 - c_{12_{np}} \frac{2}{9} \sigma_{np} \left(\frac{1}{\theta_s} \frac{m_n m_p}{m_n + m_p} \right) \nabla \cdot \overline{u}_s \right) c_{12_{np}}^3 \, e^{-\frac{1}{2\theta_s} \frac{m_n m_p}{m_n + m_p} c_{12_{np}}^2} \tag{5.90}$$

The mean impact velocity is obtained from this distribution by performing the following integration:

$$< c_{12_{np}} >= \int_0^\infty c_{12_{np}} f_{12_{np}} dc_{12_{np}} \tag{5.91}$$

which results in:

$$< c_{12_{np}} >^{(1)} = \frac{1}{N_{np}^{(1)}} n_n n_p \sigma_{np}^3 g_{np} \left(\frac{\pi\theta_s}{m_n} \frac{m_n + m_p}{2m_p} \right)^{\frac{1}{2}} \left(\frac{6}{\sigma_{np}} \left(\frac{(m_n + m_p)\pi\theta_s}{2m_n m_p} \right)^{\frac{1}{2}} - \frac{32}{9} \nabla \cdot \overline{u}_s \right) \tag{5.92}$$

3. Multi-fluid model

In this section we summarise the equations required by a multi-fluid continuum model based on the kinetic theory derivations in the previous paragraphs. Within the multi-fluid model the gas phase and the suspended particle phase are considered as interpenetrating continua. The conservation equations employed can in fact be seen as a generalisation of the Navier-Stokes equations for interacting continua. For the gas phase the same conservation equations as for the two-fluid model described in chapter 2 are employed, whereas the particulate phase is described by the kinetic theory closure model. A summary of the governing equations is presented in table 5.1.

Table 5.1. Governing equations for the multi-fluid model

Gas phase continuity equation

$$\frac{\partial(\varepsilon_g \rho_g)}{\partial t} + \nabla \cdot (\varepsilon_g \rho_g \bar{u}_g) = 0 \tag{5.1.1}$$

Solids phase continuity equations for species n

$$\frac{\partial(\varepsilon_n \rho_n)}{\partial t} + \nabla \cdot \left[\bar{J}_n + \varepsilon_n \rho_n \bar{u}_s \right] = 0 \tag{5.1.2}$$

Gas phase momentum equation

$$\frac{\partial(\varepsilon_g \rho_g \bar{u}_g)}{\partial t} + \nabla \cdot (\varepsilon_g \rho_g \bar{u}_g \bar{u}_g) = -\nabla \cdot (\varepsilon_g \bar{\bar{\tau}}_g) - \varepsilon_g \nabla P_g - \sum_{n=1}^{NP} \beta_{ng} (\bar{u}_g - \bar{u}_n) + \varepsilon_g \rho_g \bar{g} \tag{5.1.3}$$

Solids phase momentum equation

$$\frac{\partial(\varepsilon_s \rho_s \bar{u}_s)}{\partial t} + \nabla \cdot (\varepsilon_s \rho_s \bar{u}_s \bar{u}_s) = -\nabla P_s^s - \nabla \cdot \bar{\bar{\tau}}_s - \varepsilon_s \nabla P_g + \sum_{n=1}^{NP} \beta_{ng} (\bar{u}_g - \bar{u}_n) + \varepsilon_s \rho_s \bar{g} \tag{5.1.4}$$

Granular energy equation

$$\frac{3}{2}\left\{ \frac{\partial(n_s \theta_s)}{\partial t} + \nabla \cdot (n_s \theta_s \bar{u}_s) \right\} = -(P_s^s \bar{\bar{I}} + \bar{\bar{\tau}}_s) : \nabla \bar{u}_s - \nabla \cdot \bar{q}_s - \sum_{n=1}^{NP} 3 \frac{\beta_{ng}}{m_n} \theta_n - \gamma_s \tag{5.1.5}$$

The gas-phase bulk and shear viscosities are assumed to be constant and the density of the gas phase is related to the pressure and the temperature by the ideal gas law. In the dense regime ($\varepsilon_g < 0.80$) the gas-solid momentum transfer coefficient between the gas phase and particle species *n* can be obtained from a generalisation of the well known Ergun equation (Ergun, 1952) to multi-component mixtures as given by Syamlal (1986):

$$\beta_{ng} = 150\,\varepsilon_n \frac{1-\varepsilon_g}{\varepsilon_g}\frac{\mu_g}{(\phi_n d_n)^2} + 1.75\,\varepsilon_n \frac{\rho_g}{\phi_n d_n}\left|\overline{u}_g - \overline{u}_n\right| \tag{5.92}$$

In more dilute regimes ($\varepsilon_g > 0.80$) the inter-phase momentum transfer coefficient can be derived from the correlation by Wen and Yu (1966):

$$\beta_{ng} = \frac{3}{4} C_{d,n}\varepsilon_n \frac{\rho_g}{\phi_n d_n}\left|\overline{u}_g - \overline{u}_n\right|\varepsilon_g^{-1.65} \tag{5.93}$$

where the drag coefficient is given by:

$$C_{d,n} = \begin{cases} \dfrac{24}{Re_n}\left(1 + 0.15\left(Re_n\right)^{0.687}\right) & Re_n < 1000 \\ 0.44 & Re_n > 1000 \end{cases} \tag{5.94}$$

with:

$$Re_n = \frac{\varepsilon_n \rho_g \left|\overline{u}_g - \overline{u}_n\right| d_n}{\mu_g} \tag{5.95}$$

For the solids phase all particle densities are assumed to be constant. It is further assumed that the coefficients of restitution do no depend on the impact velocity. All other constitutive relations required to describe the solids phase rheology specified by the kinetic theory of granular flow are given in paragraph 2.3.

Discussion and conclusions

In this chapter a novel engineering scale multi-fluid model for hydrodynamic modelling of dense multi-component gas-fluidised beds has been presented. The model applies closure equations according to the kinetic theory of granular flow that regards segregation and temperature differences between particles of several species as higher order (non-equilibrium) effects. It is therefore expected that this newly developed model will predict slower (more realistic) segregation rates than the multi-fluid model derived by Manger (1996) and Mathiesen (1997), previously applied by Goldschmidt et al. (2001a, 2001b).

Because of the development of dedicated numerical techniques, the implementation of the previous model applied by Goldschmidt et al. (2001a, 2001b) could handle simulations of several seconds with mixtures of up to 10 components within acceptable runtime and numerical accuracy (on a single SGI R10000 processor!). Since the number of momentum and granular temperature equations that needs to be solved for the solids phase has been reduced from $2NP$ in the previous model to 2 in the new model, it is expected that the new model will run at least as efficient as the previous model, though the numerical effort required to calculate the transport coefficients will increase significantly. Clearly these assumptions need to be proven in the near future.

The sensitive dynamic equilibrium between segregation and mixing has proven to be a severe test case for hydrodynamic models (Goldschmidt et al., 2001b). Since bubbles play a dominant role in segregation and mixing, validation of the model should be focused on the prediction of bubble dynamics, segregation rates and segregation patterns. In chapter 2 it was shown that particle collision parameters have a strong influence on bubble dynamics. Therefore, the energy dissipation term in the multi-component kinetic theory (equation 5.84) will have to be modified to account for the effect of frictional energy losses, as discussed in chapters 3 and 4. Since segregation typically takes place at low gas velocities, incorporation of a contact friction model that takes viscosity and energy dissipation due to long term particle contacts into account, seems necessary to obtain accurate modelling results. Further attention should also be devoted to the effect of the mixture composition on the maximum packing density, which has not been taken into account in the presented model. Finally, as demonstrated in chapter 4, discrete particle models can be applied as a valuable research tool to verify and further improve the presented multi-fluid kinetic theory closure model.

Appendix 5A*: On the thermodynamic relations of a multi-component hard-sphere fluid

In this appendix the key thermodynamic relations for hard-sphere fluids which are relevant within the framework of the kinetic theory of granular flow are presented. The ideal and excess part of the chemical potential are considered for both single and multi-component systems. Where the ideal part can be calculated directly from elementary statistical thermodynamics (see e.g. Reed and Gubbins, 1973) the excess part depends on the details of the particle interactions. It will be demonstrated how the excess chemical potential and the matching radial distribution function can be derived when the excess compressibility z^{ex} is known. An expression for the excess compressibility of a multi-component hard-sphere mixture that diverges at random closed packing is obtained, applying the recipe presented by Santos et al. (1999) and the equation of state for mono-disperse systems derived by Song et al. (1988).

A5.1. General thermodynamic relations (single and multi component)

All thermodynamic properties of any system at given volume, temperature and number of particles (of each component), can be calculated from the Helmholtz free energy $A(V,\theta_s,\{N\})$ where $\{N\}$ stands for N_1, N_2, ..., N_{NP}, the number of particles of each component. The specific relations for particle pressure P_s and the chemical potential μ_n of component n are:

$$P_s = -\left(\frac{\partial A}{\partial V}\right)_{\theta_s,\{N\}} \tag{A5.1}$$

$$\mu_n = \left(\frac{\partial A}{\partial N_n}\right)_{\theta_s,V,\{N\}\neq N_n} \tag{A5.2}$$

It is sometimes more convenient to use the free energy per particle $a = A/N_{part}$, which is an intensive property that only depends on the intensive variables: total particle number density n_s (= N_{part}/V), temperature θ_s and mixture composition x_2, ..., x_{NP}. The relation for the particle pressure then becomes:

* This appendix is based on notes and figures provided by Dr. M.A. van der Hoef

$$\frac{P_s}{n_s^2} = \left(\frac{\partial a}{\partial n_s} \right)_{\theta_s, \{x\}} \tag{A5.3}$$

or in terms of the compressibility $z = \frac{P_s}{n_s \theta_s}$:

$$\frac{z}{n_s} = \left(\frac{\partial \beta a}{\partial n_s} \right)_{\theta_s, \{x\}} \tag{A5.4}$$

with $\beta = 1/\theta_s$ for granular media (substituting $\beta = 1/k_b T$ where k_b is Boltzmann's constant all relations presented in this appendix directly reduce to the thermodynamic relations for a hard sphere gas).

The Helmholtz free energy can thus be obtained from the compressibility by integrating from some state point for which the free energy is known. Such a state point is the ideal gas state ($n_s \to 0$) in which limit $z \to 1$, or $z^{ex} = z - 1$ goes to zero. Since the thermodynamic properties of an ideal gas are completely known, it is useful to consider only the non-ideal (or 'excess') part, which is due to particle interactions. Thus:

$$A = A^{id} + A^{ex} \tag{A5.5}$$

$$z = z^{id} + z^{ex} = 1 + z^{ex} \tag{A5.6}$$

and similar relations for all other properties.

A5.2. Single component systems

A5.2.1. General relations

For a system with only one component the Helmholtz free energy is given by:

$$\beta A^{id} = N_{part} \ln \frac{N_{part}}{V} + N_{part} \ln \Lambda^3 - N_{part} \tag{A5.7}$$

For molecular gases the De Broglie wavelength Λ is defined as a function of temperature, molecular mass, Boltzmann's (k_b) constant and Planck's constant (h) as:

$$\Lambda = \left(\frac{h^2}{2\pi m k_b T} \right)^{1/2} \tag{A5.8}$$

Since the constants and the particle mass only contribute to the offset level for the ideal part of the thermodynamic quantities of interest, they can be gathered in one constant here. Thus, for granular systems:

$$\Lambda = Const \cdot \left(\frac{1}{\theta_s} \right)^{1/2} \tag{A5.9}$$

The ideal part of the chemical potential is then obtained from:

$$\beta\mu^{id} = \left(\frac{\partial \beta A^{id}}{\partial N_{part}} \right)_{\theta_s, V} = \ln n_s + \ln \Lambda^3 \tag{A5.10}$$

The excess chemical potential can be derived by differentiation of the free energy with respect to the number of particles by:

$$\begin{aligned} \beta\mu^{ex} &= \frac{\partial \beta A^{ex}}{\partial N_{part}} = \beta a^{ex} + N_{part} \frac{\partial \beta a^{ex}}{\partial n_s} \frac{\partial n_s}{\partial N_{part}} = \beta a^{ex} + n_s \frac{\partial \beta a^{ex}}{\partial n_s} = \beta a^{ex} + \frac{\beta p^{ex}}{n_s} \\ &= \beta a^{ex} + z^{ex} \end{aligned} \tag{A5.11}$$

So the excess chemical potential of the fluid can be computed as soon as z^{ex} is known, because a^{ex} can be calculated by the following integral:

$$\beta a^{ex} = \int_0^{n_s} \frac{z^{ex}(n_s', \theta_s)}{n_s'} dn_s' \tag{A5.12}$$

Further note that equation A5.11 is consistent with the following definition of the chemical potential in terms of the Gibbs free energy (G):

$$\mu = \frac{G}{N_{part}} = \frac{A + PV}{N_{part}} = a + \frac{P}{n_s} \tag{A5.13}$$

A5.2.2. Application to hard-sphere systems

For hard-sphere systems some explicit expressions for z^{ex} exist in literature. For such systems it is custom to use the packing fraction ε_s instead of the particle number density n_s which are related by:

$$\varepsilon_s = \frac{\pi}{6}\sigma^3 n_s \tag{A5.14}$$

By studying the exact molecular dynamics results for the hard-sphere virial coefficients, Carnahan and Starling (1969) were able to show that these coefficients obeyed a recursive formula. The Carnahan and Starling equation of state, which is in almost exact agreement with molecular dynamics simulations up to packing fractions of about 0.55 is given by:

$$z_{CS}^{ex} = 4\varepsilon_s \frac{2-\varepsilon_s}{2(1-\varepsilon_s)^3} \tag{A5.15}$$

Then the corresponding expression for the free energy required to calculate the chemical potential is obtained by:

$$\beta a_{CS}^{ex} = 4\int_0^{\varepsilon_s} \frac{2-\varepsilon_s'}{2(1-\varepsilon_s')^3} d\varepsilon_s' = \frac{4\varepsilon_s - 3\varepsilon_s^2}{(1-\varepsilon_s)^2} \tag{A5.16}$$

The matching expression for the radial distribution function at contact is for a hard-sphere system directly related to the excess compressibility by:

$$g_0(\varepsilon_s) = \frac{z^{ex}}{4\varepsilon_s} = \frac{2-\varepsilon_s}{2(1-\varepsilon_s)^3} \tag{A5.17}$$

For non-dissipative systems such as gases, where packing fractions above 0.55 are rarely obtained, this equation of state has been applied with great success. However, for granular systems in which energy is dissipated and particles contract at high densities close to the maximum particle packing density, the Carnahan and Starling equation of state can not be applied since it diverges at ε_s=1 instead of at random close packing.

Therefore various equations of state have been proposed in literature that diverge near random close packing, most of which have the following general form:

$$z^{ex}(\varepsilon_s) = 4\varepsilon_s \frac{\sum_{n=0} c_n \varepsilon_s^n}{(1-(\varepsilon_s/\varepsilon_s^{max})^a)^b} \qquad \text{(A5.18)}$$

In table A5.1 the parameters obtained by different authors are summarised, whereas the various equations of state are compared with available simulation data in figure A5.1. It can be seen from this figure that up to packing fractions of 0.50 all equations of state show excellent agreement with the molecular dynamics calculations. Although the Carnahan and Starling equation of state appears to give the closest approximation of the molecular dynamics results in the intermediate range from 0.50 up to 0.57, it fails to predict the exponential rise in the compressibility as random close packing is approached. The best agreement with the molecular dynamics data is obtained by the equation of state proposed by Ma and Ahmadi (1986). The radial distribution function matching any equation of state of the form given in A5.17 can be readily obtained by dividing equation A5.17 by a factor $4\varepsilon_s$, as shown in A5.16 for the Carnahan and Starling equation of state.

Table A5.1. Values for the coefficients in A5.18 for various equations of state (CS: Carnahan and Starling (1969); MA: Ma and Ahmadi (1986); SSM: Song, Stratt and Mason (1988); TC: Tobochnik and Chapin (1988)).

	CS	MA	SSM	TC
ε_s^{max}	1	0.64356	0.6435	0.6875
a	1	3	1	1
b	3	0.67802	0.76	1
c_0	1	1	1	1
c_1	-0.5	2.5	0.32984	0.26134
c_2	0	4.5904	0.088674^{2}	0.059684^{2}
c_3	0	4.515439	0.014724^{3}	0.0059054^{3}
c_4	0	0	0.00053964^{4}	-0.0011914^{4}
c_5	0	0	-0.00035744^{5}	-0.00044554^{5}
c_6	0	0	-0.00057054^{6}	-0.00048184^{6}
c_7	0	0	-0.00012124^{7}	-0.000036364^{7}
c_8	0	0	-0.00011514^{8}	-0.000081824^{8}

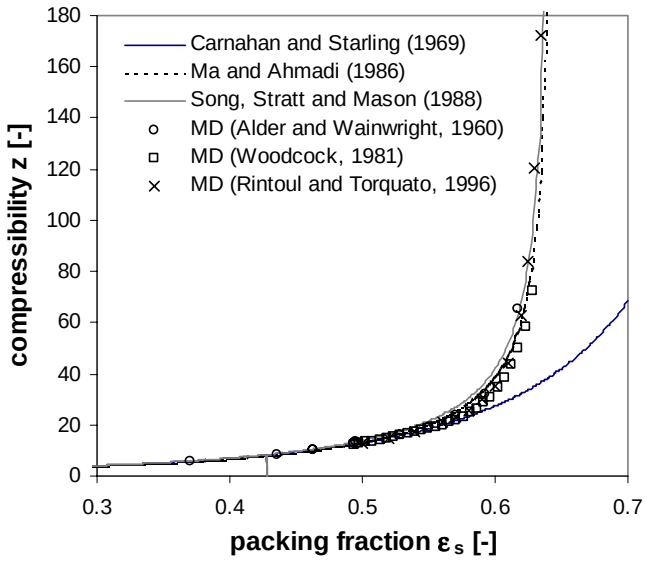

Figure A5.1. Comparison of the various equations of state for hard-spheres with molecular dynamics (MD) data.

The excess free energy matching the equation of state of the form A5.18 is then given by:

$$\beta a^{ex}(\varepsilon_s) = 4\int_0^{\varepsilon_s} \frac{\sum c_n \varepsilon_s'^n}{(1-(\varepsilon_s'/\varepsilon_s^{max})^a)^b} d\varepsilon_s' = 4\varepsilon_s^{max} \sum_{n=0} c_n (\varepsilon_s^{max})^n \int_0^{\varepsilon_s/\varepsilon_s^{max}} \frac{x^n}{(1-x^a)^b} dx \qquad \text{(A5.19)}$$

According to Gradshteyn and Ryzhik (1980), the integral

$$I = \int \frac{x^n}{(1-x^a)^b} dx \qquad \text{(A5.20)}$$

can only be expressed in terms of rational functions if (i) b is an integer, or (ii) $(n+1)/a$ is an integer, or (iii) $b+(n+1)/a$ is an integer. This rules out the Ma and Ahmadi equation of state, whereas the other three equations do fulfil (i) or (ii). For all these equations of state $a = 1$ and the following integral is obtained:

$$I = \int_0^{\varepsilon_s/\varepsilon_s^{max}} \frac{x^n}{(1-x)^b} dx = -\int_1^{1-\varepsilon_s/\varepsilon_s^{max}} \frac{(1-y)^n}{y^b} dy \qquad \text{(A5.21)}$$

Applying the binomial expansion for the nominator gives:

$$I = -\sum_{m=0}^{n}(-1)^m \binom{n}{m} \int_1^{1-\varepsilon_s/\varepsilon_s^{max}} y^{m-b}\,dy = -\sum_{m=0}^{n} \frac{(-1)^m}{m-b+1}\binom{n}{m}\left[\left(1-\frac{\varepsilon_s}{\varepsilon_s^{max}}\right)^{m-b+1} - 1\right] \tag{A5.22}$$

if $b > 1$ (if $b = 1$ there is a term y^{-1} in the integral which yields ln y). So the final expression for the Helmholtz free energy becomes (for $a = 1$):

$$\beta a^{ex} = 4\varepsilon_s^{max}\sum_{n=0} c_n(\varepsilon_s^{max})^n \sum_{m=0}^{n}\frac{(-1)^m}{m-b+1}\binom{n}{m}\left[1-\left(1-\frac{\varepsilon_s}{\varepsilon_s^{max}}\right)^{m-b+1}\right] \tag{A5.23}$$

A check of this relation with the result for the Carnahan and Starling equation of state gives:

$$\begin{aligned}\beta a^{ex} &= 4\sum_{n=0}^{1} c_n \sum_{m=0}^{n}\frac{(-1)^m}{m-2}\binom{n}{m}\left[1-(1-\varepsilon_s)^{m-2}\right] \\ &= -2\left(1-\frac{1}{(1-\varepsilon_s)^2}\right)+\left(1-\frac{1}{(1-\varepsilon_s)^2}\right)-2\left(1-\frac{1}{1-\varepsilon_s}\right) = \frac{1}{(1-\varepsilon_s)^2}+\frac{2}{1-\varepsilon_s}-3\end{aligned} \tag{A5.24}$$

which is indeed equal to A5.16.

A5.3. Multi-component systems

A5.3.1. General relations

For a multi-component system with *NP* species the ideal Helmholtz free energy is given by:

$$\beta A^{id} = \sum_{n=1}^{NP}\beta A_n^{id} \tag{A5.25}$$

where A_n^{id} is the free energy for species *n*:

$$\beta A_n^{id} = N_n\, ln\frac{N_n}{V} + N_n\, ln\,\Lambda_n^3 - N_n \tag{A5.26}$$

and thus

$$\beta A^{id} = \sum_{n=1}^{NP} N_n \, ln \frac{N_n}{V} + \sum_{n=1}^{NP} N_n \, ln \, \Lambda_n^3 - \sum_{n=1}^{NP} N_n \tag{A5.27}$$

From this equation we can determine the ideal part of the chemical potential for species *n* via:

$$\beta \mu_n^{id} = \frac{\partial \beta A^{id}}{\partial N_n} = ln \, n_n + ln \, \Lambda_n^3 \tag{A5.28}$$

The excess chemical potential for species *n* can be calculated by:

$$\beta \mu_n^{ex} = \frac{\partial \beta A^{ex}}{\partial N_n} \tag{A5.29}$$

Thus the excess chemical potential can be calculated as soon as the excess compressibility z^{ex} for the mixture is known, because the excess free energy A^{ex} for mixtures can also be obtained from the compressibility by performing the integration presented in equation A5.12.

A5.3.2. Application to hard-sphere systems

Santos et al. (1999) developed a simple recipe to derive the compressibility of a multi-component mixture of additive hard spheres from the compressibility of a single component system. The equation of state for a multi-component hard-sphere system according to Santos et al. (1999) reads (their equation 12):

$$z^{ex} = f^I z^I + f^{II} z^{II} \tag{A5.30}$$

in which z^1 is the compressibility of a single component system and further:

$$z^{II} = \frac{\varepsilon_s}{1 - \varepsilon_s} \tag{A5.31}$$

$$f^I = \frac{1}{2}(m_1 + m_2) \tag{A5.32}$$

$$f^{II} = 1 + m_1 - 2m_2 \tag{A5.33}$$

with:

$$m_1 = \frac{<\sigma^{(1)}><\sigma^{(2)}>}{<\sigma^{(3)}>} \tag{A5.34}$$

$$m_2 = \frac{<\sigma^{(2)}>^3}{<\sigma^{(3)}>^2} \tag{A5.35}$$

and

$$<\sigma^{(n)}> = \sum_{i=1}^{NP} x_i \sigma_i^n = \sum_{i=1}^{NP} \frac{n_i}{n_s} \sigma_i^n \tag{A5.36}$$

So equation A5.30 correctly yields z^I for a single component system for which m_1 and m_2 both equal 1 so $f^I = 1$ and $f^{II} = 0$. Inserting A5.30 into A5.12 results in:

$$\beta A^{ex} = f^I N_{part} \int_0^{n_s} \frac{z^I(n_s')}{n_s'} dn_s' + f^{II} N_{part} \int_0^{n_s} \frac{z^{II}(n_s')}{n_s'} dn_s' \tag{A5.37}$$

or

$$A^{ex} = f^I A^I + f^{II} A^{II} \tag{A5.38}$$

with A^K ($K = I,II$) the excess free energy determined from the excess compressibility in the normal way:

$$\beta A^K = N_{part} \int_0^{n_s} \frac{z^K(n_s')}{n_s'} dn_s' \tag{A5.39}$$

Then the excess chemical potential for species n can be calculated by:

$$\beta\mu_n^{ex} = \frac{\partial \beta A^{ex}}{\partial N_n} = f^I \frac{\partial \beta A^I}{\partial N_n} + f^{II} \frac{\partial \beta A^{II}}{\partial N_n} + \beta A^I \frac{\partial f^I}{\partial N_n} + \beta A^{II} \frac{\partial f^{II}}{\partial N_n} \tag{A5.40}$$

Evaluation of the derivatives results in:

$$\frac{\partial \beta A^K}{\partial N_n} = \beta a^K + \frac{\sigma_n^3}{<\sigma^{(3)}>} z^K \tag{A5.41}$$

$$\frac{\partial f^K}{\partial N_n} = \frac{\partial (N_{part}^{-1}(N_{part} f^K))}{\partial N_n} = -\frac{1}{N_{part}} f^K + \frac{1}{N_{part}} g^K \tag{A5.42}$$

with

$$g_n^I = \frac{\partial (N_{part} f^I)}{\partial N_n} = \frac{1}{2}\left[m_1 (y_n^{(1)} + y_n^{(2)} - y_n^{(3)}) + m_2 (3y_n^{(2)} - 2y_n^{(3)}) \right] \tag{A5.43}$$

$$g_n^{II} = \frac{\partial (N_{part} f^{II})}{\partial N_n} = 1 + m_1 (y_n^{(1)} + y_n^{(2)} - y_n^{(3)}) - 2m_2 (3y_n^{(2)} - 2y_n^{(3)}) \tag{A5.44}$$

and

$$y_i^{(n)} = \frac{\sigma_i^n}{<\sigma^{(n)}>} \tag{A5.45}$$

Inserting A5.41 - A5.44 in A5.40 gives the final expression for the excess chemical potential of component *n* in a mixture of *NP* species:

$$\beta \mu_n^{ex} = y_n^{(3)} \left[f^I z^I + f^{II} z^{II} \right] + g_n^I \beta a^I + g_n^{II} \beta a^{II} \tag{A5.46}$$

Calculation of the excess chemical potential requires expressions for the Helmholtz free energies a^I and a^{II}, which correspond to the excess compressibilities z^I and z^{II}. The expression for the mono-disperse system (a^I and z^I) are given in the previous section by equations A5.18 and A5.23 for which we might take any set of coefficients from table A5.1. The expression for the Helmholtz free energy corresponding to z^{II} given by A5.31 is obtained by the following integration:

$$\beta a^{II}(\varepsilon_s) = \int_0^{\varepsilon_s} \frac{z^{II}}{\varepsilon_s'} d\varepsilon_s' = -\ln(1-\varepsilon_s) \tag{A5.47}$$

Thus the total chemical potential for species *n* in a multi-component mixture is:

$$\beta \mu_n = \ln n_n + \ln \Lambda_n^3 + \beta \mu_n^{ex} \tag{A5.48}$$

The matching radial distribution function at contact for a multi component system (g_{np}) is given by:

$$\frac{z^{ex}}{4\varepsilon_s} = \sum_{n=1}^{NP}\sum_{p=1}^{NP} x_n x_p \frac{\sigma_{np}^3}{<\sigma^{(3)}>} g_{np} \tag{A5.49}$$

For the equation of state proposed by Santos et al. (1999) this corresponds to (their equation 3):

$$g_{np}(\varepsilon_s, x_2, ..., x_{NP}, \sigma_1, ..., \sigma_{NP}) = \frac{1}{1-\varepsilon_s} + \left[g_0(\varepsilon_s) - \frac{1}{1-\varepsilon_s} \right] \frac{<\sigma^{(2)}>\sigma_n\sigma_p}{<\sigma^{(3)}>\sigma_{np}} \tag{A5.50}$$

with $g_0(\varepsilon_s)$ the radial distribution function corresponding to z^I, i.e. $g_0 = z^I / 4\varepsilon_s$.

It finally needs to be noted that the equation of state for a multi-disperse system does not necessarily have to converge at the same random close packing as a mono-disperse system, because with particles of different sizes the packing can be much closer. This effect has been neglected in the derivation of the chemical potential and the matching radial distribution function in this appendix and the derived expressions are therefore only accurate for mixtures with small particle size differences.

A5.3.3. Comparison with simulation data

The only simulation data available is for binary systems. In figure A5.2 the compressibility computed by the Santos equation of state (equation A5.30) based on the equations of state for mono-disperse systems by Carnahan and Starling (1969) and Song et al. (1988) is compared to simulation data for a binary mixture. For comparison the usual favourite equation of state for multi-component systems by Boublk (1970) and Mansoori et al. (1971) is also shown. This equation of state reads:

$$z_{BMCSL} = \frac{1}{1-\varepsilon_s} + \frac{3\varepsilon_s}{(1-\varepsilon_s)^2}\frac{<\sigma^{(1)}><\sigma^{(2)}>}{<\sigma^{(3)}>} + \frac{\varepsilon_s^2(3-\varepsilon_s)}{(1-\varepsilon_s)^3}\frac{<\sigma^{(2)}>^3}{<\sigma^{(3)}>^2} \tag{A5.51}$$

It can be seen from figure A5.2a that all equations of state give an accurate estimate of the compressibility for packing fractions up to 0.5. Almost exact agreement is obtained between the equation of state by Santos et al. (1999) based on the Carnahan and Starling

equation of state for mono-disperse systems (Carnahan and Starling, 1969) and the equation of state for multi-component systems by Boublík (1970) and Mansoori, Carnahan, Starling and Leland (1971), which demonstrates that the recipe by Santos et al. (1999) leads to accurate results. As for mono-disperse systems these equations of state give an accurate estimate of the simulation data up to packing fractions of about 0.6, but fail to predict the exponential rise in the compressibility that occurs near random close packing. A comparison of the available simulation data for the excess chemical potential of species 1 and 2 in the mixture with predictions by equation A5.48 is given in figure A5.2b. This figure shows the excellent agreement between the simulation data and the developed expressions for the chemical potential. Unfortunately simulation data for mixtures at very high packing density is not available, but based on the superior predictions for mono-disperse systems the equation of state by Santos et al. (1999) in combination with the equation of state by Song et al. (1988) for mono-disperse systems seems the best that is currently available for application in the kinetic theory of granular flow, as presented in this chapter.

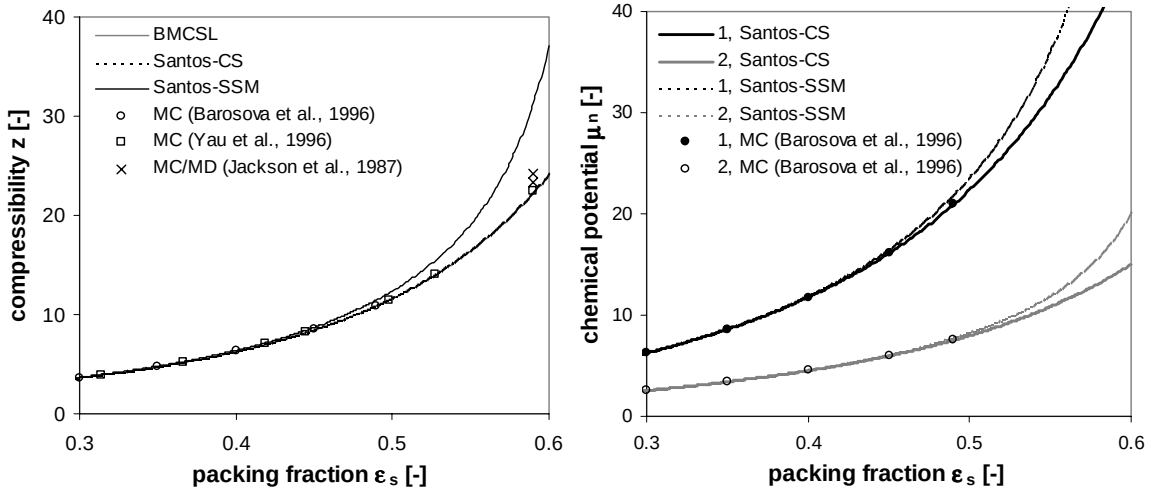

a) Compressibility. **b)** Chemical potential of species 1 and 2.

Figure A5.2. Comparison of various equations of state to available Monte-Carlo (MC) and Molecular Dynamics (MD) simulation data for a binary mixture with $x_1 = x_2 = 0.5$ and $\sigma_2 / \sigma_1 = 0.6$ (BMCSL: Boublík (1970) and Mansoori, Carnahan, Starling and Leland (1971); Santos-CS: equation of state of Santos et al. (1999) based on Carnahan and Starling (1969); Santos-SSM: equation of state of Santos et al. (1999) based on Song, Stratt and Mason(1988)).

Appendix 5B: The bracket integrals

Tables for the bracket integrals $\left[S_{3/2}^{(q)}(\square_n^2)\bar{\square}_n, S_{3/2}^{(r)}(\square_n^2)\bar{\square}_n\right]_{np}'$, $\left[S_{3/2}^{(q)}(\square_n^2)\bar{\square}_n, S_{3/2}^{(r)}(\square_n^2)\bar{\square}_n\right]_{np}''$, $\left[S_{5/2}^{(q)}(\square_n^2)\bar{\square}_n^{o}\bar{\square}_n, S_{5/2}^{(r)}(\square_n^2)\bar{\square}_n^{o}\bar{\square}_n\right]_{np}'$ and $\left[S_{5/2}^{(q)}(\square_n^2)\bar{\square}_n^{o}\bar{\square}_n, S_{5/2}^{(r)}(\square_n^2)\bar{\square}_n^{o}\bar{\square}_n\right]_{np}''$ required to calculate the coefficients $a_r^{(n)}, b_r^{(n)}$ and $d_{nr}^{(l)}$ up to the third Enskog approximation are given by Ferziger and Kaper (1972) in tables 7.3-7.6, based on earlier work by Mason (1957). Lopez de Haro et al. (1983) derived explicit expressions for $\left[S_{1/2}^{(q)}(\square_n^2), S_{1/2}^{(r)}(\square_n^2)\right]_{np}'$ and $\left[S_{1/2}^{(q)}(\square_n^2), S_{1/2}^{(r)}(\square_n^2)\right]_{np}''$, which enable calculation of $h_r^{(n)}$. For completeness these bracket integrals are also given here. The interaction potential $\Omega_{np}^{(q,r)}$ for hard spheres that appears in the integrals is given by:

$$\Omega_{np}^{(q,r)} = \left(\frac{2\pi(m_n+m_p)\theta_s}{m_n m_p}\right)^{\frac{1}{2}} \frac{(r+1)!}{4}\left[1-\left(\frac{1+(-1)^q}{2(q+1)}\right)\right]\sigma_{np}^2 \tag{B5.1}$$

Explicit expressions for the integrals are given in tables B5.1.-B5.3. Since [F,G]'=[G,F]' and [F,G]"=[G,F]" the tables present all terms that are required to obtain the bracket integrals for q, r = 0, 1, 2.

Table B5.1. Bracket integrals required to calculate the coefficients $h_r^{(n)}$.

q	r	$\left[S_{1/2}^{(q)}(\square_n^2), S_{1/2}^{(r)}(\square_n^2)\right]_{np}'$	$\left[S_{1/2}^{(q)}(\square_n^2), S_{1/2}^{(r)}(\square_n^2)\right]_{np}''$
0	0	0	0
0	1	0	0
0	2	0	0
1	1	$16M_nM_p\Omega_{np}^{(1,1)}$	$-16M_nM_p\Omega_{np}^{(1,1)}$
1	2	$M_nM_p^2\left(80\Omega_{np}^{(1,1)}-32\Omega_{np}^{(1,2)}\right)$	$-M_n^2M_p\left(80\Omega_{np}^{(1,1)}-32\Omega_{np}^{(1,2)}\right)$
2	2	$M_nM_p^3\left(64\Omega_{np}^{(1,3)}-384\Omega_{np}^{(1,2)}+560\Omega_{np}^{(1,1)}\right)$ $+64M_n^3M_p\Omega_{np}^{(1,1)}$ $+64M_n^2M_p^2\Omega_{np}^{(2,2)}$ $+M_nM_p\left(M_p-M_n\right)\left(64\Omega_{np}^{(1,2)}-160\Omega_{np}^{(1,1)}\right)$	$-M_n^2M_p^2$ $\left(64\Omega_{np}^{(1,3)}-320\Omega_{np}^{(1,2)}+560\Omega_{np}^{(1,1)}-64\Omega_{np}^{(2,2)}\right)$

Table B5.2. Bracket integrals required to calculate the coefficients $a_r^{(n)}$ and $d_{nr}^{(l)}$.

q	r	$\left[S_{3/2}^{(q)}(\square_n^2)\bar{\square}_n, S_{3/2}^{(r)}(\square_n^2)\bar{\square}_n\right]'_{np}$	$\left[S_{3/2}^{(q)}(\square_n^2)\bar{\square}_n, S_{3/2}^{(r)}(\square_n^2)\bar{\square}_n\right]''_{np}$
0	0	$8M_p\Omega_{np}^{(1,1)}$	$-8M_n^{1/2}M_p^{1/2}\Omega_{np}^{(1,1)}$
0	1	$M_p^2(20\Omega_{np}^{(1,1)}-8\Omega_{np}^{(1,2)})$	$-M_n^{3/2}M_p^{1/2}(20\Omega_{np}^{(1,1)}-8\Omega_{np}^{(1,2)})$
0	2	$M_p^3(35\Omega_{np}^{(1,1)}-28\Omega_{np}^{(1,2)}+4\Omega_{np}^{(1,3)})$	$-M_p^{5/2}M_p^{1/2}(35\Omega_{np}^{(1,1)}-28\Omega_{np}^{(1,2)}+4\Omega_{np}^{(1,3)})$
1	1	$(60M_n^2M_p+50M_p^3)\Omega_{np}^{(1,1)}$ $-40M_p^3\Omega_{np}^{(1,2)}+8M_p^3\Omega_{np}^{(1,3)}$ $+16M_nM_p^2\Omega_{np}^{(2,2)}$	$-M_n^{3/2}M_p^{3/2}$ $(110\Omega_{np}^{(1,1)}-40\Omega_{np}^{(1,2)}+8\Omega_{np}^{(1,3)}-16\Omega_{np}^{(2,2)})$
1	2	$(210M_n^2M_p^2+\frac{175}{2}M_p^4)\Omega_{np}^{(1,1)}$ $-(84M_n^2M_p^2+105M_p^4)\Omega_{np}^{(1,2)}$ $+M_p^4(38\Omega_{np}^{(1,3)}-4\Omega_{np}^{(1,4)})$ $+M_nM_p^3(56\Omega_{np}^{(2,2)}-16\Omega_{np}^{(2,3)})$	$-M_n^{5/2}M_p^{3/2}$ $(\frac{595}{2}\Omega_{np}^{(1,1)}-189\Omega_{np}^{(1,2)}+38\Omega_{np}^{(1,3)}$ $-4\Omega_{np}^{(1,4)}-56\Omega_{np}^{(2,2)}+16\Omega_{np}^{(2,3)})$
2	2	$(175M_n^4M_p+735M_n^2M_p^3+\frac{1225}{8}M_p^5)\Omega_{np}^{(1,1)}$ $-(588M_n^2M_p^3+245M_p^5)\Omega_{np}^{(1,2)}$ $+(108M_n^2M_p^3+133M_p^5)\Omega_{np}^{(1,3)}$ $-M_p^5(28\Omega_{np}^{(1,4)}-2\Omega_{np}^{(1,5)})$ $+(112M_n^3M_p^2+196M_nM_p^4)\Omega_{np}^{(2,2)}$ $-M_nM_p^4(112\Omega_{np}^{(2,3)}-16\Omega_{np}^{(2,4)})$ $+16M_n^2M_p^3\Omega_{np}^{(3,3)}$	$-M_n^{5/2}M_p^{5/2}$ $(\frac{8505}{8}\Omega_{np}^{(1,1)}-833\Omega_{np}^{(1,2)}+241\Omega_{np}^{(1,3)}$ $-28\Omega_{np}^{(1,4)}+2\Omega_{np}^{(1,5)}-308\Omega_{np}^{(2,2)}$ $+112\Omega_{np}^{(2,3)}-16\Omega_{np}^{(2,4)}+16\Omega_{np}^{(3,3)})$

Table B5.3. Bracket integrals required to calculate the coefficients $b_r^{(n)}$.

q	r	$\left[S_{5/2}^{(q)}(\square_n^2)\overline{\square}_n^{\,o}\overline{\square}_n, S_{5/2}^{(r)}(\square_n^2)\overline{\square}_n^{\,o}\overline{\square}_n \right]'_{np}$	$\left[S_{5/2}^{(q)}(\square_n^2)\overline{\square}_n^{\,o}\overline{\square}_n, S_{5/2}^{(r)}(\square_n^2)\overline{\square}_n^{\,o}\overline{\square}_n \right]''_{np}$
0	0	$\frac{80}{3}M_nM_p\Omega_{np}^{(1,1)}+8M_p^2\Omega_{np}^{(2,2)}$	$-\frac{80}{3}M_nM_p\Omega_{np}^{(1,1)}+8M_nM_p\Omega_{np}^{(2,2)}$
0	1	$M_nM_p^2(\frac{280}{3}\Omega_{np}^{(1,1)}-\frac{112}{3}\Omega_{np}^{(1,2)})$ $M_p^3(28\Omega_{np}^{(2,2)}-8\Omega_{np}^{(2,3)})$	$-M_n^2M_p$ $(\frac{280}{3}\Omega_{np}^{(1,1)}-\frac{112}{3}\Omega_{np}^{(1,2)}-28\Omega_{np}^{(2,2)}+8\Omega_{np}^{(2,3)})$
0	2	$M_nM_p^3(210\Omega_{np}^{(1,1)}-168\Omega_{np}^{(1,2)}+24\Omega_{np}^{(1,3)})$ $+M_p^4(63\Omega_{np}^{(2,2)}-36\Omega_{np}^{(2,3)}+4\Omega_{np}^{(2,4)})$	$-M_n^3M_p(210\Omega_{np}^{(1,1)}-168\Omega_{np}^{(1,2)}+24\Omega_{np}^{(1,3)}$ $-63\Omega_{np}^{(2,2)}+36\Omega_{np}^{(2,3)}-4\Omega_{np}^{(2,4)})$
1	1	$(\frac{560}{3}M_n^3M_p+\frac{980}{3}M_nM_p^3)\Omega_{np}^{(1,1)}$ $-M_nM_p^3(\frac{784}{3}\Omega_{np}^{(1,2)}-\frac{128}{3}\Omega_{np}^{(1,3)})$ $+(\frac{308}{3}M_n^2M_p^2+98M_p^4)\Omega_{np}^{(2,2)}$ $-M_p^4(56\Omega_{np}^{(2,3)}-8\Omega_{np}^{(2,4)})+16M_nM_p^3\Omega_{np}^{(3,3)}$	$-M_n^2M_p^2$ $(\frac{1540}{3}\Omega_{np}^{(1,1)}-\frac{784}{3}\Omega_{np}^{(1,2)}+\frac{128}{3}\Omega_{np}^{(1,3)}$ $-\frac{602}{3}\Omega_{np}^{(2,2)}+56\Omega_{np}^{(2,3)}-8\Omega_{np}^{(2,4)}+16\Omega_{np}^{(3,3)})$
1	2	$(840M_n^3M_p^2+735M_nM_p^4)\Omega_{np}^{(1,1)}$ $-(336M_n^3M_p^2+882M_nM_p^4)\Omega_{np}^{(1,2)}$ $+M_nM_p^4(276\Omega_{np}^{(1,3)}-24\Omega_{np}^{(1,4)})$ $+(462M_n^2M_p^3+\frac{441}{2}M_p^5)\Omega_{np}^{(2,2)}$ $-(132M_n^2M_p^3+189M_p^5)\Omega_{np}^{(2,3)}$ $+M_p^5(50\Omega_{np}^{(2,4)}-4\Omega_{np}^{(2,5)})$ $+M_nM_p^4(72\Omega_{np}^{(3,3)}-16\Omega_{np}^{(3,4)})$	$-M_n^3M_p^2$ $(1575\Omega_{np}^{(1,1)}-1218\Omega_{np}^{(1,2)}+276\Omega_{np}^{(1,3)}$ $-24\Omega_{np}^{(1,4)}-\frac{1365}{2}\Omega_{np}^{(2,2)}+321\Omega_{np}^{(2,3)}$ $-50\Omega_{np}^{(2,4)}+4\Omega_{np}^{(2,5)}+72\Omega_{np}^{(3,3)}-16\Omega_{np}^{(3,4)})$
2	2	$(630M_n^5M_p+3780M_n^3M_p^3+\frac{6615}{4}M_nM_p^5)\Omega_{np}^{(1,1)}$ $-(3024M_n^3M_p^3+2646M_nM_p^5)\Omega_{np}^{(1,2)}$ $+(504M_n^3M_p^2+1242M_nM_p^4)\Omega_{np}^{(1,3)}$ $-M_nM_p^5(216\Omega_{np}^{(1,4)}-12\Omega_{np}^{(1,5)})$ $+(567M_n^4M_p^2+2079M_n^2M_p^4+\frac{3969}{8}M_p^6)\Omega_{np}^{(2,2)}$ $-(1188M_n^2M_p^4+567M_p^6)\Omega_{np}^{(2,3)}$ $+(156M_n^2M_p^4+225M_p^6)\Omega_{np}^{(2,4)}$ $-M_p^6(36\Omega_{np}^{(2,5)}-2\Omega_{np}^{(2,6)})$ $+(168M_n^3M_p^3+324M_nM_p^5)\Omega_{np}^{(3,3)}$ $-M_nM_p^5(144\Omega_{np}^{(3,4)}-16\Omega_{np}^{(3,5)})$ $+M_nM_p^416\Omega_{np}^{(4,4)}$	$-M_n^3M_p^3$ $(\frac{24255}{4}\Omega_{np}^{(1,1)}-5670\Omega_{np}^{(1,2)}+1746\Omega_{np}^{(1,3)}$ $-216\Omega_{np}^{(1,4)}+12\Omega_{np}^{(1,5)}-\frac{25137}{8}\Omega_{np}^{(2,2)}$ $+1755\Omega_{np}^{(2,3)}-381\Omega_{np}^{(2,4)}+36\Omega_{np}^{(2,5)}-2\Omega_{np}^{(2,6)}$ $+492\Omega_{np}^{(3,3)}-144\Omega_{np}^{(3,4)}+16\Omega_{np}^{(3,5)}-16\Omega_{np}^{(4,4)})$

Chapter 6.

Digital image analysis measurements of bed expansion and segregation dynamics in dense gas-fluidised beds

Abstract

One of the most crucial steps in the development of fundamental hydrodynamic models is the validation of these models with accurate, detailed experimental data. Therefore a whole-field, non-intrusive digital image analysis technique has been developed which enables measurement of bed expansion and segregation dynamics of coloured particles in dense gas-fluidised beds. The development, calibration and accuracy of the technique are discussed in detail. The image analysis technique traces bubbles and voidage waves accurately, whereas the mixture composition in a fluidised bed could be determined within 10%.

Experiments have been carried out with 1.5 mm and 2.5 mm coloured glass beads, for which particle-particle and particle-wall collision parameters were accurately known. They were performed in pseudo two-dimensional laboratory scale fluidised beds with a simple rectangular geometry and well-defined gas inflow conditions. An extensive set of results obtained with both mono-disperse systems and binary mixtures, suitable for validation of fundamental hydrodynamic models, is presented.

This chapter is based on the papers:

Goldschmidt M.J.V., Kuipers J.A.M., Van Swaaij W.P.M., 2001, Hydrodynamic modelling of dense gas-fluidised beds: validation of a multi-fluid continuum model with non-intrusive digital image analysis measurements, in '*Fluidization X*' edited by Kwauk M., Li J. and Yang W.-C., 405-412

Goldschmidt M.J.V., Link J.M., Mellema S., Kuipers J.A.M., 2001, Digital image analysis measurements of bed expansion and segregation dynamics in dense gas-fluidised beds, submitted to *Powder Technol.*

1. Introduction

In earlier chapters of this thesis, recent progress made in the area of fundamental hydrodynamic modelling of dense gas-fluidised beds has been discussed. Fluidised beds can nowadays be modelled with discrete particle Lagrangian and multi-fluid Eulerian models. Both kinds of model exhibit pronounced sensitivity of dense bed dynamics with respect to particle collision parameters. However, experimental results obtained with particles for which all particle collision parameters are accurately known, as required for quantitative validation of fundamental hydrodynamic models, are not yet available.

In many industrial dense gas-fluidised bed processes, e.g. gas-phase polymerisation and fluidised bed granulation, mixtures of particles with different physical properties are encountered. When particles differ in size and/or density, segregation may occur. Segregation is most marked at low gas velocities when there is appreciable particle density difference. Even a strongly segregating system, however, can be fairly well mixed if the gas velocity is increased sufficiently, although it can be difficult to remove the last traces of segregation. Much has been reported on particle mixing and segregation in dense gas-fluidised beds (Rowe and Nienow, 1976; Hoffmann and Romp, 1991; Wang and Chou, 1995). Bubbles have been indicated as the vehicle for both mixing and segregation. Rising bubbles carry a mixture of particles to the top of the bed and disturb the packing state of the bed so that segregation of larger or heavier particles may occur. Since bubble dynamics and segregation rates are strongly coupled, they should be measured from the same experiment, at the same time and preferably with the same technique.

Up to now most authors only report steady-state axial segregation profiles and hardly any information can be found on the spatial distribution and rate of segregation (Yang and Keairns, 1982; Agarwal et al., 1996; Gilbertson and Eames, 2001). Combined measurements of segregation and bubble dynamics performed with particles with well-known properties (size, shape, density and collision properties) in a bed with a well-defined geometry and gas inflow conditions on short time scales that can currently be handled by fundamental hydrodynamic models are not yet available. However, for thorough validation of these models this kind of information is required.

Most current activity in the development of novel investigative techniques for dense gas-fluidised beds focuses on the use of tomographic methods to provide cross-sectional and three-dimensional images of the multi-phase flow behaviour (Simons, 1995; Chaouki et

al., 1996). The majority of the work focuses on radiation absorption methods (X-ray absorption, γ-ray absorption, positron emission tomography) and electrical capacitance methods. However, major disadvantages of these techniques are the poor spatial resolution and/or long scan times. Further the limited size of the interrogation area, relative high capital investment and radiation hazards do not favour widespread application of these techniques. For the validation of segregation and bubble dynamics in laboratory scale dense gas-fluidised beds, a non-invasive, whole-field technique with reasonable spatial (< 1 cm) and temporal (> 10 Hz) resolution is required. Further this technique should be able to distinguish between particles of different species and be able to perform measurements in systems with particle densities close to random closest packing. Lim and Agarwal (Lim et al., 1990a, 1990b, 1992, 1993; Agarwal et al., 1996) demonstrated these capabilities for digital image analysis techniques in their studies of bubble dynamics, mixing and segregation in pseudo two-dimensional bubbling gas-fluidised beds. When coloured particles are applied in a transparent set-up, different species in particulate mixtures can easily be distinguished by (colour) cameras. However, the main disadvantage of video techniques is that measurements in dense particulate systems are limited to two-dimensional images of the near wall zone. Therefore, to avoid gradients in the third dimension, a pseudo two-dimensional experimental set-up has to be used. Though in such a set-up wall effects will influence particle packing structure, bubble and segregation dynamics, this is not regarded a problem for the validation of fundamental hydrodynamic models. In current three-dimensional versions of Eulerian and Lagrangian hydrodynamic models, wall effects can (easily) be taken into account. However, bubble and segregation dynamics measured in a pseudo two-dimensional system will differ from that in systems with other dimensions (and consequently different dynamics) and they will therefore not directly apply to industrial practice.

Thus, a digital image analyses technique has been developed to study segregation of mixtures of coloured particles in transparent pseudo two-dimensional gas-fluidised beds. The experimental set-up, the outline of the image analysis technique and an elaborated set of experimental results are presented in this chapter. All experiments were carried out with relatively large spherical glass beads, which qualify as Geldart D-type particles, to enable accurate measurement of the collision parameters. The use of relatively large particles and a pseudo two-dimensional fluidised bed is further motivated by the fact that the number of particles in the system will remain within the modelling capacities of discrete particle models. Therefore the measurements can be applied for (critical) comparison of discrete particle and continuum models, as demonstrated in chapter 3.

2. Experimental set-up

2.1. Fluidised bed equipment

An impression of the fluidised bed equipment is given in figure 6.1. Most experiments were carried out in a small 15 cm wide, 70 cm high, 1.5 cm deep pseudo two-dimensional gas-fluidised bed. In such a small laboratory scale fluidised bed, the number of particles is limited and the bed can be operated in single bubble mode for Geldart D-type particles, which allows for accurate determination of the bed expansion dynamics. Further a 57 cm wide, 100 cm high, 1.5 cm deep laboratory scale bed was applied to acquire measurement data with higher numbers of particles, more suitable for the validation of continuum models. Both beds were constructed of glass. Visual observation of the lowest 1.3 cm of the bed close to the gas distributor was obstructed by a flange, which has been applied to mount the bed onto the distributor.

Pressurised air is applied as the fluidisation gas. Accurate control of the inlet gas flow rate is obtained by the application of calibrated mass flow controllers and rapidly responding magnetic valves controlled by a 486 PC. A three millimetre thick porous plate gas distributor with an average pore size of 10 micron is applied to obtain sufficient pressure drop to guarantee homogeneous gas distribution over the whole bottom of the bed. Steam is added to the fluidising air prior to injection to keep the relative humidity within the range of 60% - 70%, which prevents the build up of static electricity and consequent ill behaved fluidisation.

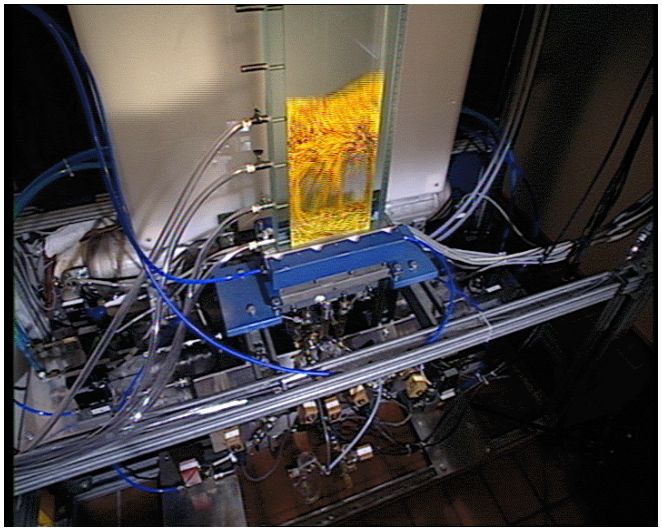

Figure 6.1. Photograph of the small fluidised bed and the experimental rig.

2.2. Image analysis equipment

The experiments were recorded with a 3-CCD interlaced digital video camera (JVC KY-F55B) at a frame rate of 25 frames per second (actually 50 half frames per second since the camera is interlaced). Directly behind the 4-8 mm variable zoom lens, the colour components red, green and blue (RGB) are split by a prism and the colour intensity of each individual component is registered on an array of 576 x 720 picture elements (pixels) by a separate 1/3 inch CCD chip. The light intensity registered on each pixel is proportional to an electric charge which is registered by the camera. The recorded information is bundled in a PAL signal that is transferred to a frame-grabber (DPS PVR-3500). This frame-grabber records the signals supplied by the camera on a hard disk of a Pentium PC which is used to perform the off-line image analysis.

To prevent uncontrolled interference of the camera with 50 Hz strip lights, the set-up is placed in an isolated box. Continuous high intensity uniform illumination of the bed is obtained with six 500 Watt halogen lamps. These lamps are mounted next to the bed and their light is projected on the front of the bed by two diffuse reflectors, made out of aluminium foil. Direct illumination of the lens by the lamps is prevented by a shaft which is placed around it. Further, to prevent direct reflections of the surroundings of the camera into the glass bed, black curtains were mounted next to the camera. A blue background, which provides good contrast with the colours of the particles, is positioned behind the bed to improve bubble detection. A sketch of the configuration of the lights, the bed and the camera is presented in figure 6.2.

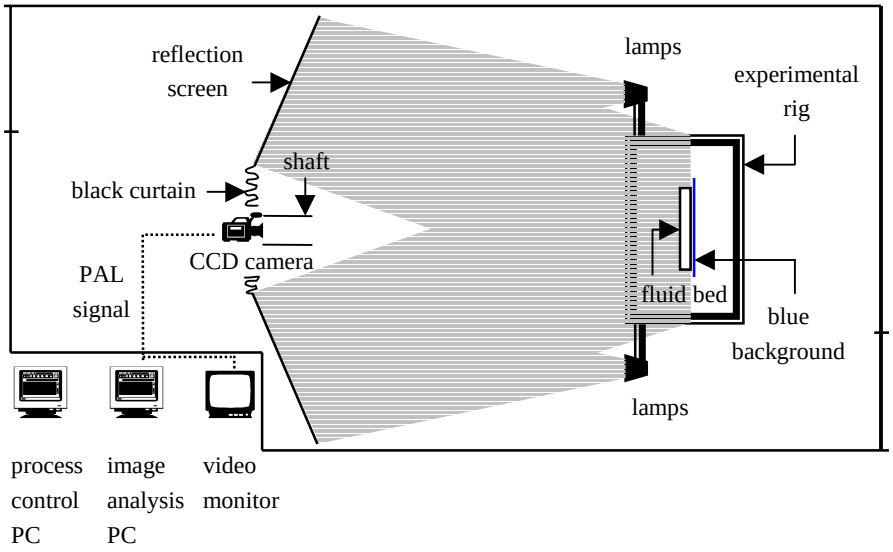

Figure 6.2. Sketch of the configuration of experimental rig, illumination and camera.

2.2.1. Camera settings

To maximise the quality of the recorded images, besides high intensity uniform illumination conditions, diaphragm and shutter time of the camera need to be selected carefully. On the one hand, the shutter time should be as short as possible to prevent blurring caused by motion effects. On the other hand, short shutter times reduce the amount of light registered by the camera and therewith contrast, which should be as high as possible to develop an accurate image analysis method. Though the light intensity in the centre of the image was in principle high enough to apply a shutter time of 1/250 second, the intensity in the corners of the image was not and thus a shutter time of 1/120 second was applied.

Homogeneity of recorded illumination intensity and depth of focus can be optimised with the diaphragm. When the diaphragm is completely opened the light intensity in the centre of the recorded area is higher than in the corners. For a shutter time of 1/120 second, the light intensity in the centre of a white board placed in front of the fluidised bed exceeds the maximum intensity. This causes the pixels in the centre of the CCD chips to overcharge and consequently 'blooming' (spreading of overload to neighbouring pixels) occurs. Closing the diaphragm reduces the maximum light intensity and homogenises the illumination between the centre and the corners of the image. A compromise must be made between light intensity level and homogenisation of the illumination conditions. In this work it was chosen to keep the diaphragm open as far as possible for maximum contrast (which comes down to 60 % opening to prevent blooming), and correct for the difference in local light intensity by application of a correction field for every individual colour with the digital image analysis technique. The illumination intensities for a white board placed in front of the fluidised bed, recorded with these camera settings, are shown in figure 6.3.

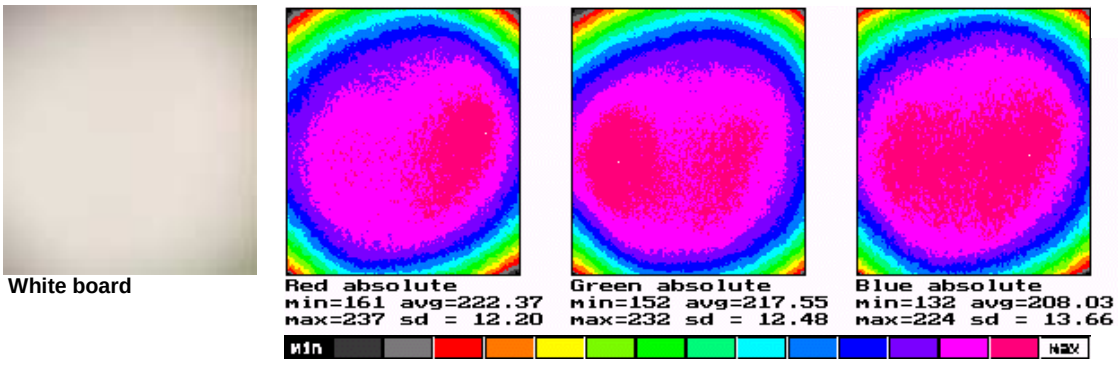

Figure 6.3. Absolute red, green and blue intensity on a scale from 0 to 255 for a white board placed in front of the fluidised bed (shutter time 1/120 s, diaphragm 60% open).

2.2.2. Data compression

The camera has three different kinds of analogue output signals (RGB, Y/C and PAL). The RGB signal transfers colour intensities for all three colours separately, the Y/C signal splits colour and intensity information in two different signals, reducing the required band width by a factor 2/3, whereas the PAL (standard TV) signal combines all colour and intensity information and requires only 1/3 of the bandwidth of the RGB signal. Since the higher quality Betacam/MII and S-video inputs of the frame-grabber were not compatible with the RGB and Y/C signals supplied by the camera, the PAL signal was applied in this work. As a result sharp colour gradients were badly captured and overshoot of green and red intensities occurred at pixel level in areas with sharp gradients. However, the influence of signal quality is hardly visible for the human eye and remained within acceptable limits for the developed digital image analysis technique.

A special AV hard disk was directly connected to a SCSI port on the frame-grabber to guarantee a high data transfer rate (7 Mb per second). Nevertheless, the data storage rate of the hard disk was not high enough to store all data supplied by the camera, which would require a data storage rate of 30 Mb per second. Therefore, the signal was compressed by JPEG compression hardware, available on the frame-grabber. The compression factor for the JPEG hardware was set at a constant value throughout all measurements. The influence of information loss by JPEG compression on the developed digital image analysis technique was studied with snapshots taken of a packed bed. The influence of data loss by compression was found to be negligible for the low level of compression applied in this work.

2.3. Particle characteristics

In this work two different sizes of coloured spherical glass beads have been applied. Since the purpose of the experimental work was to supply experimental data suitable for critical validation of fundamental hydrodynamic models, all particle characteristics were accurately determined. Special attention was paid to the collision properties of the particles which were obtained from detailed impact experiments (Gorham and Kharaz, 1999). These experiments were performed by the Impact Research Group of the Open University at Milton Keynes, where an accurate technique to measure particle collision parameters has been developed (Kharaz et al., 1999). An in-depth discussion on the physical meaning of all three collision parameters can be found in chapter 3 (paragraph 2.2). An overview of the particle properties is given in table 6.1.

Table 6.1. Particle properties.

	Small particles		*Large particles*	
Colour	yellow		red	
Diameter, d_p	1.52 ± 0.04	mm	2.49 ± 0.02	mm
Density, ρ_p	2523 ± 6	kg/m^3	2526 ± 6	kg/m^3
Shape factor, ϕ_p	~ 1	-	~ 1	-
Collision parameters for particle-particle collisions:				
Coefficient of normal restitution, e_n	0.97 ± 0.01	-	0.97 ± 0.01	-
Coefficient of friction, μ	0.15 ± 0.015	-	0.10 ± 0.01	-
Coefficient of tangential restitution, β_0	0.33 ± 0.05	-	0.33 ± 0.05	-
Collision parameters for particle-wall collisions:				
Coefficient of normal restitution, $e_{n,wall}$	0.97 ± 0.01	-	0.97 ± 0.01	-
Coefficient of friction, μ_{wall}	0.10 ± 0.01	-	0.09 ± 0.01	-
Coefficient of tangential restitution, $\beta_{0,wall}$	0.33 ± 0.05	-	0.33 ± 0.05	-

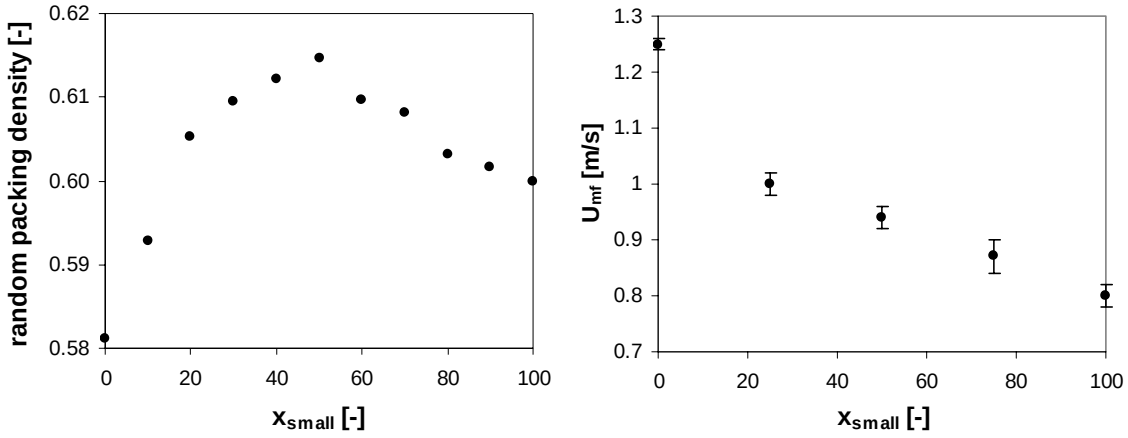

a) Packing fractions. **b)** Minimum fluidisation velocities.

Figure 6.4. Random particle packing fraction and minimum fluidisation velocity for binary mixtures of small and large glass beads at various compositions.

The random packing densities for mixtures possessing different mass fractions small particles (x_{small}), which have been determined from particle packing heights of well-mixed packed beds, are shown in figure 6.4. The maximum random packing density for the mixtures is clearly higher than that for a single component. The figure further shows the minimum fluidisation velocities, determined from pressure drop measurements, for all compositions studied in the experiments. Accurate determination of the minumum fluidisation velocity of mixtures was troubled by hysteresis, caused by segregation.

3. Digital image analysis technique

The main difference between this work and earlier works by Lim and Agarwal (Lim et al. 1990a, 1990b, 1992, 1993, Agarwal et al., 1996) is caused by the application of a colour camera. Whereas the basic principles of bubble detection based on thresholding developed for black and white cameras can readily be applied, more accurate quantitative determination of the local mixture composition is possible by comparison of colour intensities. Comparison of ratios of colour intensities also allows for (better) detection of smaller bubbles and voidage waves that do not span the whole depth of the bed.

The recorded images can be accessed as bitmaps that consist of 576 x 720 picture elements, containing information on the local red, green and blue intensity levels on an integer scale from 0 to 255. The analysis area for the small bed covers about 125 x 445 pixels in the middle of the images, whereas 470 x 628 pixels are analysed for the large bed. Thus, for both situations, pixels are slightly smaller than the smallest particles. The blue background emits (mainly) blue light and red particles emit (mainly) red light. Yellow particles emit both green and red light and the absolute intensity of the red light emitted by the yellow particles is even higher than that emitted by red ones.

In this section some issues regarding the signal quality will be briefly discussed, whereafter the digital image analysis technique developed to detect bubbles and measure particle concentrations is presented. Special attention is thereby paid to calibration and testing of the accuracy of bubble detection and concentration measurement.

3.1. Signal characteristics

For the development of a quantitative digital image analysis technique, the quality and reproducibility of the signal on which the analyses are based have to be examined. Therefore recordings of a white board, placed in front of the fluidised bed, were studied.

First, the time dependence of the absolute and relative intensity of each of the colour components has been studied. On the short time scale of several seconds, random fluctuations (noise) up to 5% of the absolute colour intensity level of an individual pixel were observed for all colour components. The noise level could be reduced to about 1% by averaging the colour intensities for all pixels in an area of 1 square centimetre. Since temperature effects cause a small background charge on CCD chips (this effect is known as 'dark count'), the intensity levels for the white board were registered at regular intervals over a longer period of 5 hours. During this period the camera heated up and the

average absolute red intensity registered for the white board increased about 3%, the green intensity remained almost constant and the blue intensity decreased approximately 5%. For all colour components a reproducible intensity was obtained after the camera had been on-line for 2 hours or more, so this warming-up time was taken into account before recording any of the presented experiments.

Further, as can be seen from figure 6.3, the registered light intensity depends on the position in the image. The highest light intensities are registered for the centre of the white board, whereas the lowest intensities are observed near the corners. This position dependence is mainly caused by the zoom-lens in combination with the wide opening of the diaphragm, though the exact alignment of the lamps will also have played a role. To correct the local light intensities for (accidental) changes in alignment of the lamps and influences of lens and diaphragm opening, a short movie containing 128 images of the white board was recorded before the start of every experiment. From this movie a correction field was then constructed to correct the local variations in light intensities and obtain a 'homogeneously illuminated' image for further analysis.

3.2. Calibration data

To obtain information on the relation between light intensities and mixture composition and be able to determine threshold values for bubble detection, a calibration data set was recorded. Therefore, the small bed was filled up to approximately 36 centimetres with 11 different mixtures of well-know composition. The mixture compositions varied from 0 to 100 % small particles with increments of 10 %. A well-mixed packed bed was obtained by fluidising the particles at high velocity, whereby steam was added to prevent build up of static electricity which preferentially attracted smaller particles to the walls of the bed. Then the gas inflow was suddenly shut off and a snapshot of the obtained packed bed was taken. Next the bed was mixed again and another snapshot was taken. In this manner a large set of images of packed beds of well-known composition was acquired.

The observed relationship between mixture composition and light intensity for all three colour components is shown in figure 6.5a. To construct this figure the recorded images were first corrected for the local light intensity, whereafter the average colour intensity of all pixels in a set of 64 images was calculated. The size of the calibration set was investigated and it was found that a set of 32 images or more was large enough to diminish the effect of the incidental particle positions in one single image on the obtained

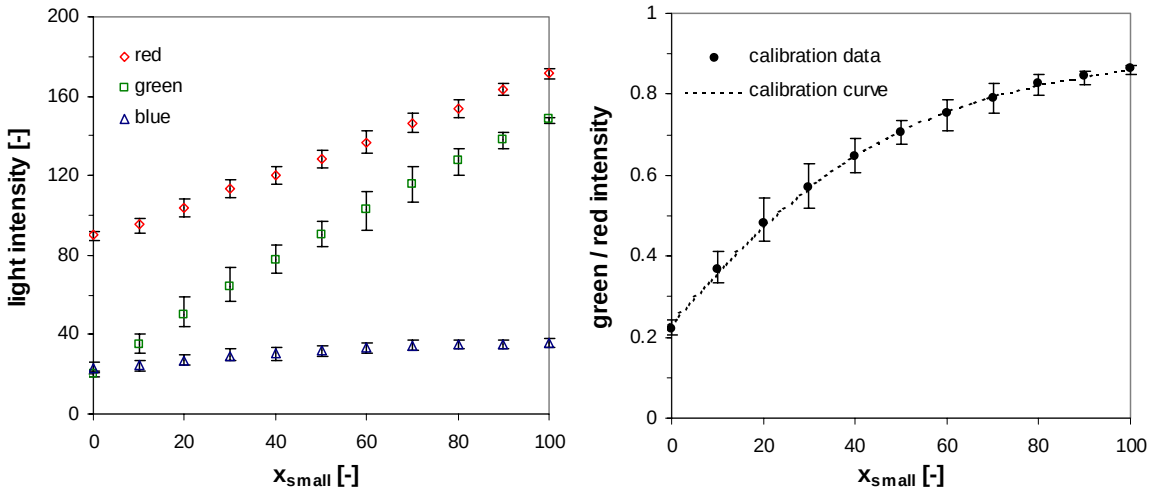

a) Absolute colour intensities. **b)** Ratio of green to red intensity.

Figure 6.5. Light intensities as a function of the mixture composition (error bars indicate the maximum and minimum observed for the 64 images in the calibration set).

average intensities and the standard deviation amongst those intensities. The error bars in figure 6.5 indicate the maximum and minimum colour intensities (averaged over all pixels) found in any one of the images in the calibration set. It can be seen from this figure that there is strong and accurate correlation between the absolute red and green intensity and the mixture composition, whereas the blue intensity has a nearly constant (low) value. In principle the correlation between the absolute red or green intensity and the mixture composition could be used to construct a calibration curve for determination of particle concentrations from measured light intensities. The absolute light intensities however are susceptible to variations in the local illumination intensity which occur in a dynamic fluidised bed situation due to shading near bubbles. Therefore, the ratio between the green and red light intensity shown in figure 6.5b provides a more accurate measure for determination of the mixture composition. Through experiments with various shutter times it was confirmed that this relative light intensity remained constant for various illumination conditions.

3.3. Image analysis procedure

3.3.1. Bubble detection

In the first step of the analysis bubbles are detected at pixel level. Large bubbles that span the whole depth of the pseudo two-dimensional bed could easily be distinguished from

particles by the relatively high blue intensity of the background. However, applying only one threshold value for the relative blue intensity, either bubbles were not detected because the threshold was set to high or too many pixels were incorrectly appointed as bubbles because of compression errors and noise on the measured intensity signals. Therefore a second threshold value was introduced which based on the relatively low red intensity emitted by the blue background. By applying a combination of these two threshold values, large bubbles could accurately be detected.

The red intensity level also plays a key role in the detection of small bubbles that do not span the whole depth of the bed. Small bubbles (mostly voidage waves near the bottom of the bed) are visually observed as shaded areas. To detect small bubbles, first the mixture composition in the surrounding of the pixel was estimated (see next paragraph). Then a threshold which depends on the mixture composition was applied to detect small bubbles based on the absolute red intensity. This intensity for small bubbles turns out to be lower than expected for the estimated mixture composition. Again the exact value of the threshold which is applied is a trade of between recognition of small bubbles and exclusion of too many pixels from the composition analysis because of compression errors and noise. Addition of a second criterion for small bubble detection in this case could not improve the bubble detection method.

To give an impression of the performance of the developed bubble detection method, figure 6.6 demonstrates how a large bubble in the top of the bed and a small voidage wave near the right bottom corner are detected from a segregation experiment.

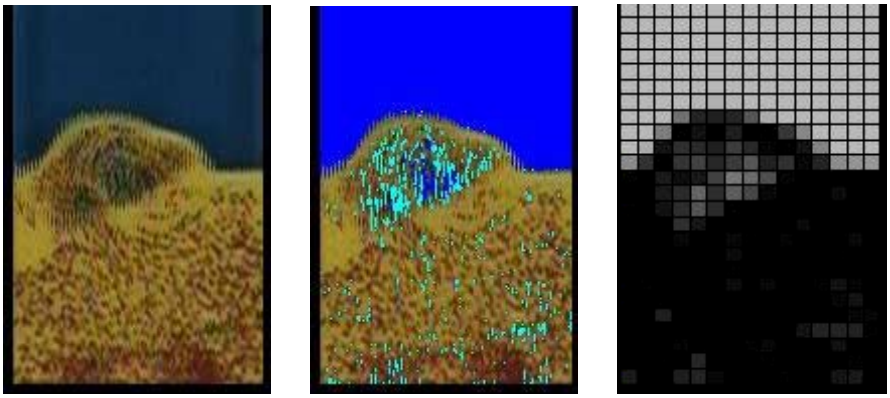

a) Original image. **b)** Bubble detection at pixel level. **c)** Bubble concentration pattern at grid level.

Figure 6.6. Demonstration of bubble detection (the dark blue pixels in figure b are recognised as large bubble whereas light blue ones are detected as small bubbles).

3.3.2. Measurement of mixture composition

In the second step of the image analysis procedure the composition of the particle mixture outside the bubbles is determined. To obtain interrogation areas that contain a sufficient amount of particles to perform concentration measurements, colour intensity information of pixels that are not assigned to bubbles is combined on a 1 cm x 1 cm mesh. The ratio of the green and red light intensity is then used to determine the mixture composition in each element of the mesh (cell). Therefore a calibration curve has been fitted through the recorded calibration data, as shown in figure 6.5b. Using this calibration curve the particle concentrations can be determined at grid level, as demonstrated in figure 6.7.

3.3.3. Accuracy of bubble detection and composition measurement

To test the accuracy of the developed digital image analysis method, images of well-mixed packed beds with a well-know composition were analysed. Ideally the image analysis method should not detect any bubbles at all in these images. However, due to noise and errors introduced by data compression some pixels were recognised as small bubbles. To study the severity of this effect, the total particle mass observed by the digital image analysis technique was calculated from the results of the particle concentration measurements. Figure 6.8a shows the percentage of the total particle mass that is removed because pixels are falsely appointed as bubbles. The error caused by the bubble detection method is about 4% for a mono-disperse system of large (red) particles, whereas for a mono-disperse system of small (yellow) particles it could be reduced to 1.5%. This is because the absolute red intensity level on which the small bubble detection

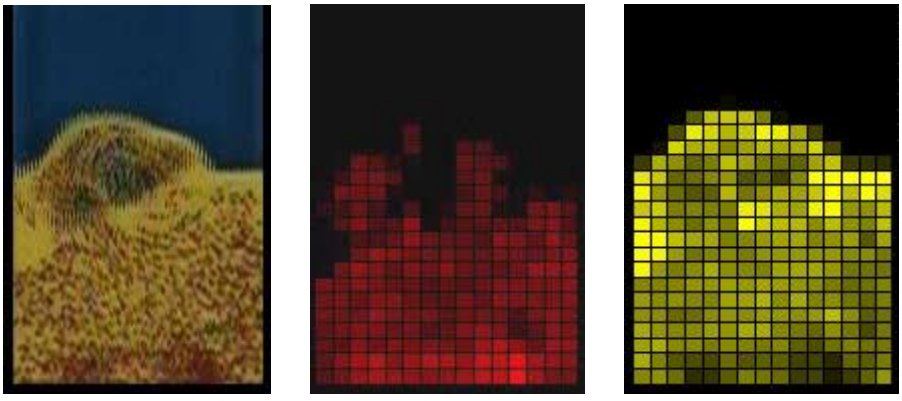

a) Original image. **b)** Concentration large particles. **c)** Concentration small particles.

Figure 6.7. Mixture composition and bubble concentration determined at grid level.

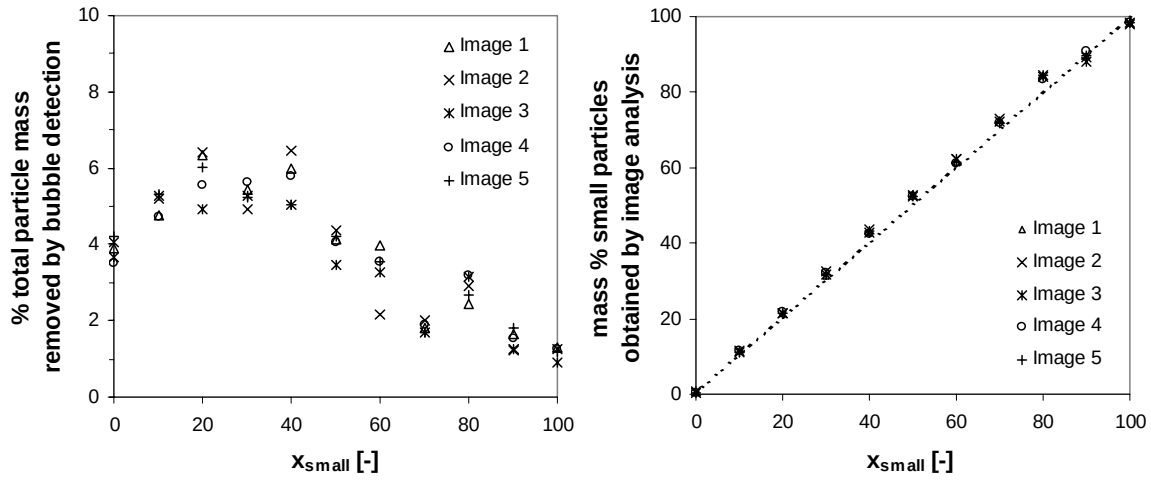

a) Accuracy of bubble detection method. **b)** Accuracy of composition measurement.

Figure 6.8. Accuracy of digital image analysis method tested for images of packed beds with well-known composition.

method is based is lower for the red particles, which leaves less margin for selection of a threshold value. Further it can be seen from figure 6.8a that errors by bubble detection up to 6.5% are made for mixtures containing 20% to 40% small particles. The accuracy of the bubble detection method is somewhat lower for mixtures than for mono-disperse systems, since compression errors are introduced when neighbouring pixels vary a lot in colour intensity.

Figure 6.8b shows the parity plot of the mass percentage small particles that is obtained by digital image analysis, versus the mass percentage that was actually present in the packed bed. The analysed images are the same ones as the ones with which the accuracy of the bubble detection method was tested. As can been seen from the parity plot, the concentration determination method is very accurate and the largest deviation of 4.5% is observed for a mixture containing 80% small particles. Further it can be seen from this figure that the mass percentage of small (yellow) particles is systematically overestimated, which is a result of the preferential removal of red (large) particles by the bubble detection method.

Since, on the contrary to the packed beds applied for calibration, the particles are in motion in a fluidised bed, it was necessary to investigate the influence of particle motion on the accuracy of the composition measurement method. Therefore a rotating disk was constructed which could be filled with a particulate mixture of well-known composition.

Experiments with this disk placed at the position of the fluidised bed and mixtures of various compositions were performed. In these experiments the absolute particle velocity was varied from 0 to 7 m/s. For mono-disperse systems the influence of motion on the registered intensity signals was negligible. For particulate mixtures, blurring removed sharp spatial gradients from the images, which improved the bubble detection method. However, the green/red intensity level also rose as particle velocities increased, which in the worst case caused overprediction of the small particle concentration by 5%. This overprediction is probably due to the more than proportional contribution of the bright yellow colour of the small particles to the blurred image.

Combining the errors due to the effect of motion to the errors observed from the parity plot it can be concluded that the developed image analysis method is capable of determining the mixture composition in a fluidised bed within 10%, whereby the fraction of small particles is systematically overestimated. Further, in the fluidised bed situation, the mean particle packing fraction in dense areas is generally lower than in the packed bed situation due to expansion of the bed. Therefore, even though pixels are falsely removed by the bubble detection method, an increase in the total bed area covered by particles up to 15% for high fluidisation velocities was observed by the image analysis method. Though animations of the image analysis results confirmed that the developed technique traced bubbles and voidage waves quite accurately, the method is not suitable to determine the particle packing fractions in dense areas.

4. Experimental results

Experiments have been carried out with homogeneously fluidised mono-disperse and binary systems of various composition. Initially an accurately weighed amount of particles was poured into the bed. A well-mixed initial condition was obtained by fluidising the particles at a velocity somewhat higher than the minimum fluidisation velocity of the largest particles for several minutes, whereafter the gas inflow was suddenly switched of and the bed collapsed. The mass flow controllers were then set for the required flow conditions and recording of the experiments started just before the gas flow to the bed was switched on again by the rapid switching magnetic valves.

Though a tremendous amount of snapshots has been acquired for a broad range of operating conditions, only few of them will be shown here. In chapter 3 it was discussed how snapshots of particle concentrations can be applied to get an impression of the bed

structure and see how well fundamental hydrodynamic models capture it, but their use in quantitative validation of fundamental hydrodynamic models is very limited. Apart from being able to capture the bed structure it seems more important that fundamental hydrodynamic models are capable of predicting correct bed dynamics and time-average behaviour. Therefore time-average particle concentration profiles have been determined applying the developed digital image analysis technique. Some of these time averages are shown in chapter 3. However, the value of the time-average particle concentration profiles is still limited for critical validation of fundamental hydrodynamic models, when associated flow patterns and granular temperature profiles are not available. It was concluded in chapter 3 that the most critical comparison between digital image analysis experiments and modelling results can be made based upon bed expansion dynamics. For this reason the presentation of the experimental results in this chapter will focus on bed expansion dynamics and segregation rates for binary systems.

4.1. Mono-disperse systems

To characterise the bed expansion dynamics for mono-disperse systems, the average particle height in the fluidised bed was calculated for every recorded image from:

$$< h_p >_{bed} = \frac{\sum_{k}^{Ncells} \varepsilon_{s,k} h_k V_k}{\sum_{k}^{Ncells} \varepsilon_{s,k} V_k} \tag{6.1}$$

In this equation h_k is the height of the centre of cell k above the gas distributor, V_k represents the volume of that cell and $\varepsilon_{s,k}$ is the total particle volume fraction in the cell. Except for the bottom row of cells, representing the area where visual observation is blocked by the flange, the height and volume of all cells was the same. The height of the cells in the bottom row equalled 2.0 cm, since apart from the lowest 1.3 cm of the bed directly blocked by the flange, the flange also caused a dark shade on the lowest 0.7 cm of the visible area of the bed. This causes prediction of too high bubble concentrations in this area due to lack of contrast. Since the best estimate of the particle fraction (and for mixtures also the mixture composition) in the invisible bottom row is made assuming it equals that in the lowest visible row, the extra 0.7 cm have been removed from the analysis to assure the accuracy for the analysis of the lowest visible cells. The total particle fraction in all visible cells has been determined by:

$$\varepsilon_{s,k} = \varepsilon_s^{max} \cdot \frac{A_{solids,k}}{A_{bubbles,k} + A_{solids,k}} \tag{6.2}$$

Here, $A_{solids,k}$ represents the total area of the pixels in cell k that have been identified as particles and $A_{bubbles,k}$ is the total area of the pixels in cell k that have been characterised as bubbles. The factor ε_s^{max} accounts for the maximum loose packing of particles in the particulate areas, which has been set to a constant value of 0.58 for all mixture compositions throughout this work.

An example of the bed expansion dynamics obtained for 1.5 mm glass beads at three different fluidisation velocities is presented in figure 6.9. To quantify such expansion dynamics the time average particle height and the root mean square (RMS) of the particle height fluctuations have been calculated according to:

$$< h_p >_{t,bed} = \frac{1}{t_{\max} - t_{\min}} \int_{t_{\min}}^{t_{\max}} < h_p >_{bed} \, dt \tag{6.3}$$

$$\mathrm{RMS} < h_p >_{bed} = \sqrt{\frac{1}{t_{\max} - t_{\min}} \int_{t_{\min}}^{t_{\max}} (< h_p >_{bed} - < h_p >_{t,bed})^2 \, dt} \tag{6.4}$$

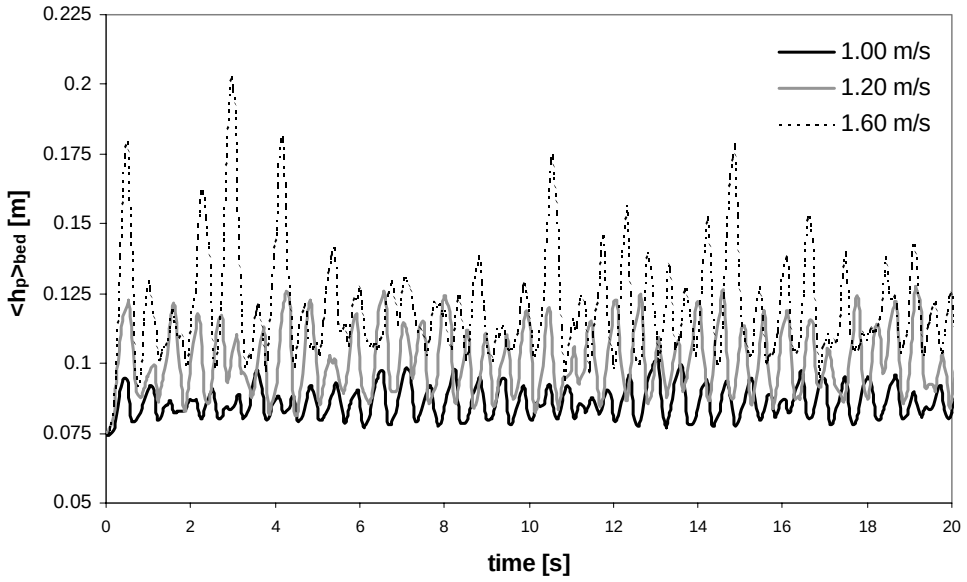

Figure 6.9. Bed expansion dynamics for 1.5 mm glass beads in a 150 x 15 x 700 mm fluidised bed at three different fluidisation velocities.

Table 6.1. Signal analysis results for the signals presented in figure 6.9.

fluidisation velocity [m/s]	$<h_p>_{t,bed}$ [m]	RMS $<h_p>_{bed}$ [m]	f_{bed} [Hz]
1.00	0.0861	0.0056	1.8
1.20	0.1002	0.0116	1.9
1.60	0.1182	0.0168	1.6

To prevent start up effects from influencing the results, the analysis of the signal characteristics was started at t_{min} = 5 s and ended at t_{max} = 60 s. A standard Fourier analysis technique was applied to determine the dominant bed expansion frequency (f_{bed}) for the same period of time. The signal analysis results for the bed expansion dynamics presented in figure 6.9 are shown in table 6.1. These results give a quantitative representation of the increase in average bed height and bed height fluctuations, which can be observed from figure 6.9. Further the results obtained from Fourier analysis shows that the bed expansion frequency is about the same for all three fluidisation velocities. Triple measurements are presented in appendix 6A, table A6.1. They show that the results are very well reproducible. The average particle height differs less than 1% between the three experiments, whereas the root mean square varies 15% at most. For the lowest two fluidisation velocities the bed expansion frequency could be accurately determined within 0.1 Hz, since the bed was operated in a single bubble mode. At the highest fluidisation velocity (2 U_{mf}) several bubbles were tailing each other in the bed and severe slugging occurred. This complicated the determination of one single bed expansion frequency, but the characteristic frequencies all laid within a rather narrow band of 0.2 Hz around the presented frequency.

In the same manner the bed expansion dynamics of an extensive set of experiments with both 1.5 mm and 2.5 mm glass beads, performed in the small and the large bed at 1.25, 1.50 and 2.00 U_{mf}, have been analysed. A complete overview of all experimental results can be found in appendix 6A. In general it was observed that both the average bed height and the intensity of bed height fluctuations increased as the fluidisation velocity increased, whereas the expansion frequency shows a tendency to decrease. From experiments with different initial bed loads in the large bed, it was found that at a fixed fluidisation velocity the bed expansion frequency decreases as the bed load increases. Furthermore, comparison of experiments performed with the 1.5 mm glass beads to experiments performed with 2.5 mm glass beads shows that both bed expansion and bed height fluctuations at 1.25, 1.50 and 2.00 U_{mf} are higher for the larger particles, which is

mainly due to the higher excess gas velocity. Finally, for the same initial bed height, comparison of the results obtained in the small bed to those obtained in the large bed shows that, both average bed expansion and intensity of bed height fluctuations are smaller in the larger bed whilst the bed expansion frequency increases. This can be explained by the lesser degree of slugging observed in the larger bed.

4.2. Binary mixtures

As for mono-disperse systems an extensive set of experiments has been carried out inthe small system with binary particle mixtures. The influences of fluidisation velocity, mixture composition and bed height on bed expansion dynamics and segregation rates have been studied. In this paragraph the method by which the results have been analysed will be discussed and the observed trends are presented. An extensive overview of all experimental results is presented in appendix 6A.

The segregation pattern obtained for a binary mixture containing 50 mass % small particles fluidised at a superficial gas velocity of 1.10 m/s is shown in figure 6.10. This figure shows that within 15 seconds the whole top layer of the bed is occupied by small particles. During the first minute the layer of small particles grows significantly, while two heaps of (defluidised) large particles form near the bottom. Thus, the rate of segregation is reasonably high, which makes the system suitable for validation of fundamental hydrodynamic models. To quantify segregation rate and bed dynamics the average particle height for both species is calculated, as for a mono-disperse system. Taking the mixture composition into account, the average height of the small particles (e.g.) is obtained from:

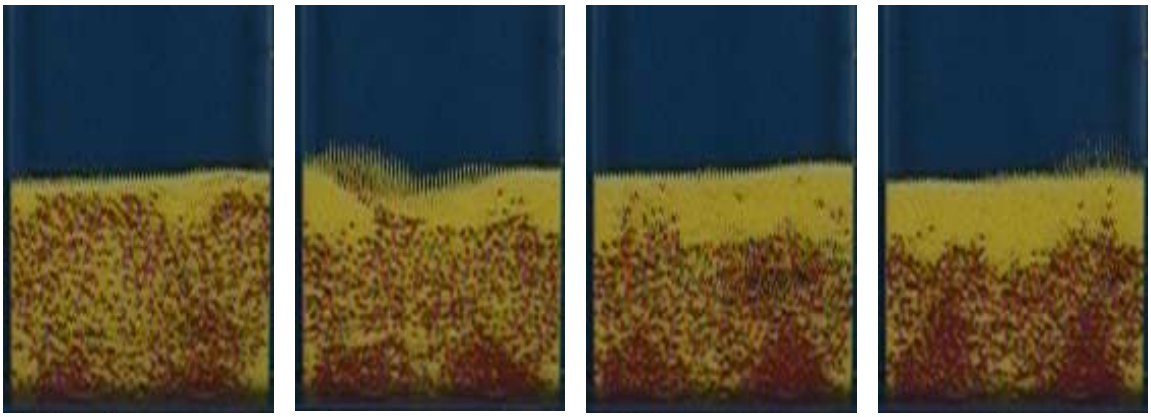

t = 15 s t = 30 s t = 45 s t = 60 s

Figure 6.10. Snapshots of a segregation experiment performed at 1.10 m/s (x_{small} = 0.5).

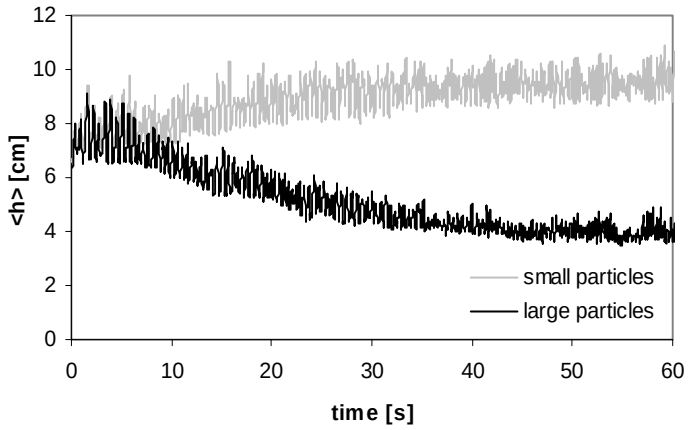

Figure 6.11. Average particle heights during a segregation experiment performed at 1.10 m/s (x_{small} = 0.5), obtained from digital image analysis.

$$< h_{small} >= \frac{\sum_{k}^{Ncells} x_{small}\varepsilon_{s,k}h_k V_k}{\sum_{k}^{Ncells} x_{small}\varepsilon_{s,k}V_k} \tag{6.5}$$

The results of digital image analysis of bed expansion and segregation dynamics are shown in figure 6.11. The trends for the average particle heights show that the rate of segregation is high during the first 40 seconds, whereafter a dynamic equilibrium between mixing and segregation is slowly approached. Further the figure shows that the intensity of the height fluctuations for the small particles stays relatively constant throughout the measurement, whereas the intensity of the fluctuations for the large particles decreases as a result of segregation. Just as for mono disperse systems the intensity of the particle height fluctuations has been quantified by calculation of the root mean square of these fluctuations. Therefore, the average particle height for each species was first fitted as a function of time by a second order polynomial $h^{fit}(t)$, to account for the trends in the bed height. Then, the root mean square for 6 different 10-second periods (0-10 s, 10-20 s, etc.) was calculated from:

$$\mathrm{RMS} < h_{small} >= \sqrt{\frac{1}{t_{\max} - t_{\min}} \int_{t_{\min}}^{t_{\max}} (< h_{small} > - h_{small}^{fit}(t))^2 \, dt} \tag{6.6}$$

The calculated average bed heights and bed height fluctuations are reported in appendix 6A, for quantitative validation of numerical models. In that appendix the characteristic

fluctuation frequencies, obtained from Fourier analysis, are also presented. The results of the frequency analysis were quite accurate for non-segregating systems, whereas for segregating systems they should be regarded as an indication with an accuracy of approximately 0.2-0.5 Hz, depending on the degree of segregation. For strongly segregating systems the peaks actually concentrated around two dominant frequencies, one frequency lower than the presented average for the hardly fluidised bottom zone of the bed and a higher frequency for the shallow bed of mainly smaller particles on top of that.

For comparison of experiments with different mixture compositions and bed heights it is convenient to express the extent of segregation in one single measure,

$$s = \frac{S - 1}{S_{\max} - 1} \tag{6.7}$$

This measure will hereafter be referred to as the *percentage of segregation*, since it equals 0 when the particles are perfectly mixed and 1 when the mixture has completely segregated. The numerator in equation 6.7 contains the ratio of the actual heights of the small and the large particles, which can be seen as the actual degree of segregation:

$$S = \frac{< h_{small} >}{< h_{large} >} \tag{6.8}$$

The denominator in equation 6.7 contains the associated maximum degree of segregation, which can be calculated in terms of the mixture composition (assuming the maximum packing density in the fluidised state for small particle equals that for large particles) from:

$$S_{\max} = \frac{2 - x_{small}}{1 - x_{small}} \tag{6.9}$$

A summary of all segregation experiments in terms of 1.0-second averages of the percentage of segregation is presented in figure 6.12. The data points in the figure represent the averages of double and triple measurements presented in appendix 6A. Except from one set of experiments with 25 mass % small particles at 1.35 m/s (which was apparently on the critical edge of segregation), all experiments were very well reproducible, as can be seen from the figures presented appendix 6A.

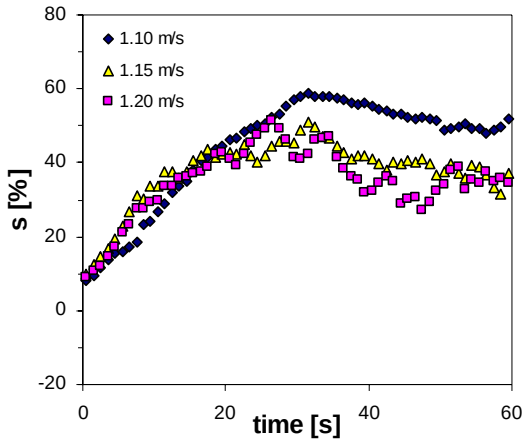

a) x_{small} = 0.50, $h_b \approx$ 7.5 cm.

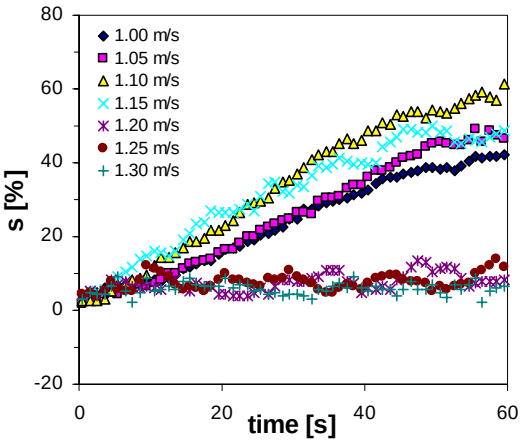

b) x_{small} = 0.50, $h_b \approx$ 15 cm.

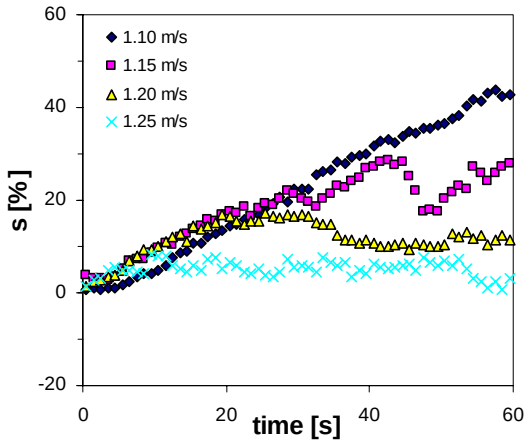

c) x_{small} = 0.50, $h_b \approx$ 22.5 cm.

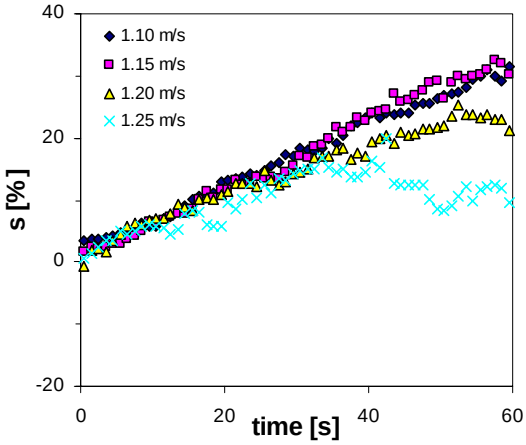

d) x_{small} = 0.50, $h_b \approx$ 30 cm.

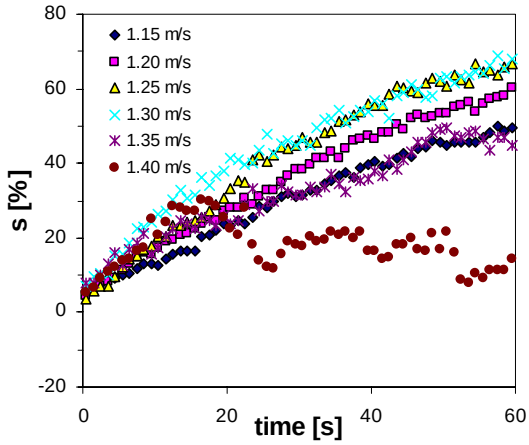

e) x_{small} = 0.25, $h_b \approx$ 15 cm.

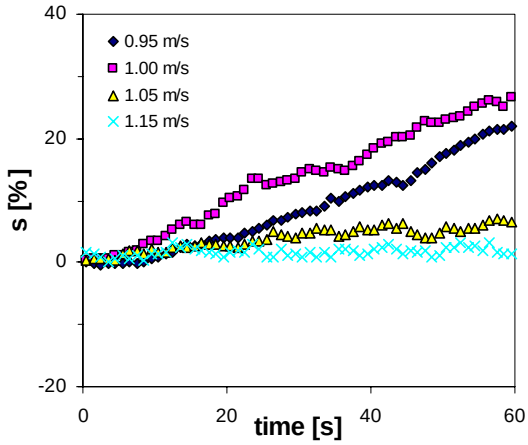

f) x_{small} = 0.75, $h_b \approx$ 15 cm.

Figure 6.12. Overview of segregation rates obtained from digital image analysis.

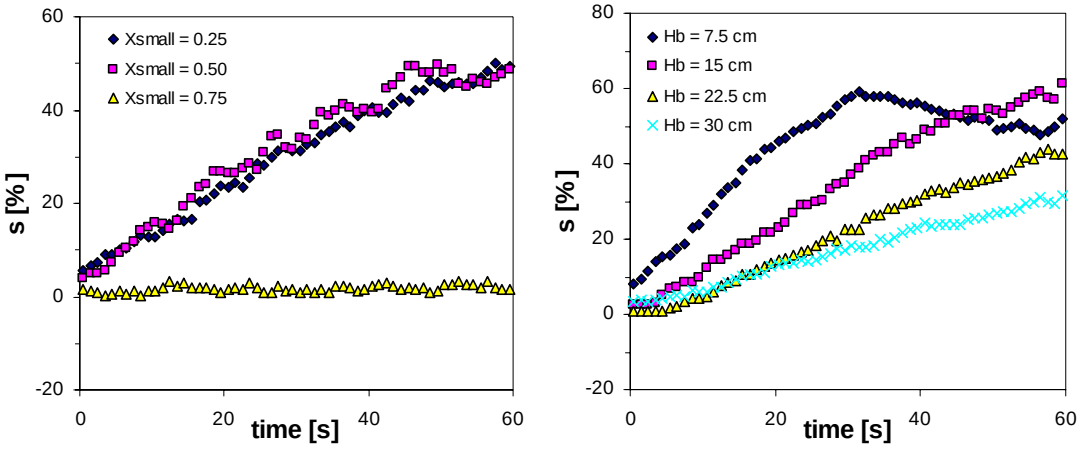

a) Influence of mixture composition on segregation rate at 1.15 m/s.

b) Influence of bed height on segregation rate at 1.10 m/s.

Figure 6.13. Influence of mixture composition and initial bed height on the rate of segregation.

All experimental results shown in figure 6.12 show the same influence of the fluidisation velocity on the rate of segregation (this influence is best seen from figures b and e). At low fluidisation velocities the particles hardly move and segregation is slow. As the fluidisation velocity increases the rate of segregation also increases until a certain critical fluidisation velocity is reached. Above this critical velocity particle mixing by bubbles is so strong that the effects of segregation are hardly noticeable.

The exact value of the critical fluidisation velocity for segregation depends on mixture composition and initial bed height. For the applied mixture of glass beads which only slightly differed in size, segregation was not observed above the minimum fluidisation velocity of the largest particles, except for high beds and mixtures containing mainly large particles. From figures 6.13a it can be seen that at exactly the same fluidisation velocity and bed height, mixtures containing 25 and 50 mass percent small particles do segregate quickly, whereas mixtures containing 75 mass percent small particles do not segregate at all. In general it was observed that a small amount of smaller particles segregates easier from a mixture containing mainly larger particles than a small amount of larger particles does from a mixture containing mainly smaller ones. The influence of the initial bed height on the rate of segregation is shown in figure 6.13b. It can be seen that it takes much longer to reach a certain degree of segregation in a high bed than in a shallow bed, which is due to the longer distance the particles have to move to segregate.

Discussion and Conclusions

A whole field, non-intrusive, digital image analysis technique to study bed dynamics and segregation rates in pseudo two-dimensional dense gas-fluidised beds has been presented. Through the use of a 3-CCD colour camera, besides large bubbles that span the whole depth of the bed, small bubbles and voidage waves could also be detected. The full power of the digital image analysis technique is demonstrated by experiments carried out with binary mixtures of coloured particles, for which the local mixture composition could be determined within 10% accuracy in the entire bed.

The errors in the bubble detection method were mainly caused by the poor quality of the applied PAL signal, whereas information loss by JPEG compression on the frame-grabber played a minor role. The obtained results should be readily useable for critical assessment of fundamental hydrodynamic models, though further improvement is possible by application of a higher quality video signal. Further the quality of the technique can still improve in the near future since, because of the development of hard disks with higher data storage rates and the availability of larger amounts of RAM memory in which complete measurements can be stored, the need for data compression will vanish.

Another source of error was introduced by the construction of the fluidised bed set-up. Due to the flange applied to mount the glass bed on the metal gas-distributor, visual observation of the lowest 1.3 cm of the bed was obstructed. Further, because of the dark shade the flange caused, another 0.7 cm had to be excluded from the analyses to assure accurate extrapolation of the particle concentrations to the invisible zone of the bed near the distributor. The error may be reduced by modification of the construction of the bed, but care should be paid to the homogeneity of aeration and prevention of gas leakages.

An extensive set of quantitative experimental data, suitable for critical validation of fundamental hydrodynamic models, has been presented. The experiments were carried out in a pseudo two-dimensional gas-fluidised bed for which the gas inflow conditions were accurately controlled. Mono-disperse systems and binary mixtures of 1.5 mm and 2.5 mm spherical glass beads have been studied. For these particles all particle properties, including the collision parameters, were accurately known. It was concluded in chapter 3 that the use of snapshots and time average concentration profiles for validation of fundamental hydrodynamic models is limited and therefore only the results for the bed expansion dynamics were presented. Those dynamics were quantified in terms of the

average bed height, the intensity and the frequency of the bed height fluctuations. For the comparison of segregation experiments at different operation conditions a new single parameter measure, the percentage of segregation, was introduced.

The particles applied in this research were Geldart D-type particles, which are hardly applied in real industrial applications. The main reason for selecting this type of particles was that the particle collision parameters could be accurately determined for such large particles. However, as soon as the ongoing development in measurement techniques for particle collision properties enables accurate measurements for smaller particles, experiments should be performed with smaller particles as well. Further more, the experimental work presented in this chapter is limited to mono-disperse and binary systems, whereas the need for accurate experimental data with multi-component mixtures still exists.

Appendix 6A. Overview of experimental results

A6.1. Mono-disperse systems

A6.1.1. Small bed, 1.5 mm glass beads

bed dimensions: 150 x 15 x 700 mm
total particle mass: 494.3 gram
number of particles: ~ 110,870
initial bed height: ~ 15 cm

Table A6.1. Bed expansion dynamics for small glass beads in the small bed (h_b = 15 cm).

fluidisation velocity [m/s]	$<h_p>_{t,bed}$ [m]	RMS $<h_p>_{bed}$ [m]	f_{bed} [Hz]
1.00	0.0857	0.0049	1.8
1.00	0.0861	0.0056	1.8
1.00	0.0856	0.0050	1.9
1.20	0.1007	0.0121	1.8
1.20	0.1009	0.0120	1.8
1.20	0.1002	0.0116	1.9
1.60	0.1175	0.0162	~ 1.9
1.60	0.1182	0.0168	~ 1.6
1.60	0.1184	0.0158	~ 1.5

A6.1.2. Small bed, 2.5 mm glass beads

bed dimensions: 150 x 15 x 700 mm
total particle mass: 494.3 gram
number of particles: ~ 23,920
initial bed height: ~ 15 cm

Table A6.2. Bed expansion dynamics for large glass beads in the small bed (h_b = 15 cm).

fluidisation velocity [m/s]	$<h_p>_{t,bed}$ [m]	RMS $<h_p>_{bed}$ [m]	f_{bed} [Hz]
1.56	0.0918	0.0096	1.6
1.56	0.0916	0.0099	1.65
1.56	0.0915	0.0100	1.65
1.88	0.1143	0.0230	1.6
1.88	0.1141	0.0225	1.55
1.88	0.1136	0.0224	1.6
2.50	0.1326	0.0295	~ 1.5
2.50	0.1359	0.0324	~ 1.4
2.50	0.1378	0.0347	~ 1.4

A6.1.3. Large bed, 1.5 mm glass beads

bed dimensions: 570 x 15 x 1000 mm
total particle mass: 1878.2 gram
number of particles: ~ 421,260
initial bed height: ~ 15 cm

Table A6.3. Bed expansion dynamics for small glass beads in the large bed (h_b = 15 cm).

fluidisation velocity [m/s]	$<h_p>_{t,bed}$ [m]	RMS $<h_p>_{bed}$ [m]	f_{bed} [Hz]
1.00	0.0826	0.0016	2.1
1.00	0.0827	0.0015	2.2
1.20	0.0933	0.0039	2.2
1.20	0.0936	0.0043	2.3
1.60	0.1101	0.0069	1.8
1.60	0.1113	0.0077	1.9

bed dimensions: 570 x 15 x 1000 mm
total particle mass: 6533.2 gram
number of particles: ~ 1,465,300
initial bed height: ~ 50 cm

Table A6.4. Bed expansion dynamics for small glass beads in the large bed (h_b = 50 cm).

fluidisation velocity [m/s]	$<h_p>_{t,bed}$ [m]	RMS $<h_p>_{bed}$ [m]	f_{bed} [Hz]
1.00	0.2775	0.0038	0.9
1.00	0.2787	0.0039	1.0
1.20	0.3119	0.0117	0.9
1.20	0.3111	0.0113	0.9

A6.1.4. Large bed, 2.5 mm glass beads

bed dimensions: 570 x 15 x 1000 mm
total particle mass: 1878.2 gram
number of particles: ~ 90,885
initial bed height: ~ 15 cm

Table A6.5. Bed expansion dynamics for large glass beads in the large bed (h_b = 15 cm).

fluidisation velocity [m/s]	$<h_p>_{t,bed}$ [m]	RMS $<h_p>_{bed}$ [m]	f_{bed} [Hz]
1.56	0.0845	0.0031	2.0
1.56	0.0844	0.0030	2.1
1.88	0.0962	0.0063	2.2
1.88	0.0960	0.0068	2.1

bed dimensions: 570 x 15 x 1000 mm
total particle mass: 6533.2 gram
number of particles: ~ 316,140
initial bed height: ~ 50 cm

Table A6.6. Bed expansion dynamics for large glass beads in the large bed (h_b = 50 cm).

fluidisation velocity [m/s]	$<h_p>_{t,bed}$ [m]	RMS $<h_p>_{bed}$ [m]	f_{bed} [Hz]
1.56	0.2867	0.0072	0.9
1.56	0.2872	0.0070	1.0
1.88	0.3262	0.0218	1.0
1.88	0.3267	0.0211	1.0

A 6.2. Binary mixtures

A 6.2.1. 25 mass % small glass beads

bed dimensions: 150 x 15 x 700 mm
total particle mass: 494.3 gram
number of 1.5 mm glass beads: ~ 27,720
number of 2.5 mm glass beads: ~ 17,940
initial bed height: 15 cm

Table A 6.7. Bed expansion dynamics for a binary mixture (x_{small} = 0.25, h_b = 15 cm).

Fluidisation velocity	**1.15 m/s**		**1.20 m/s**			**1.25 m/s**		
0-10 s								
$<h_{large}>$ [m]	0.0787	0.0820	0.0825	0.0846	0.0839	0.0850	0.0852	0.0844
$<h_{small}>$ [m]	0.0913	0.0901	0.0958	0.0953	0.0953	0.0931	0.0992	0.0993
RMS $<h_{large}>$ [m]	0.0030	0.0046	0.0046	0.0056	0.0053	0.0058	0.0065	0.0056
RMS $<h_{small}>$ [m]	0.0032	0.0047	0.0062	0.0059	0.0063	0.0060	0.0072	0.0069
10-20 s								
$<h_{large}>$ [m]	0.0760	0.0798	0.0789	0.0794	0.0805	0.0793	0.0814	0.0804
$<h_{small}>$ [m]	0.0977	0.0951	0.1037	0.1048	0.1012	0.1024	0.1100	0.1087
RMS $<h_{large}>$ [m]	0.0025	0.0040	0.0041	0.0044	0.0045	0.0037	0.0059	0.0053
RMS $<h_{small}>$ [m]	0.0037	0.0048	0.0062	0.0068	0.0066	0.0053	0.0089	0.0089
20-30 s								
$<h_{large}>$ [m]	0.0728	0.0773	0.0771	0.0763	0.0790	0.0747	0.0755	0.0775
$<h_{small}>$ [m]	0.1048	0.1005	0.1106	0.1124	0.1091	0.1111	0.1180	0.1211
RMS $<h_{large}>$ [m]	0.0021	0.0036	0.0047	0.0044	0.0051	0.0032	0.0041	0.0057
RMS $<h_{small}>$ [m]	0.0039	0.0054	0.0071	0.0080	0.0077	0.0064	0.0083	0.0111
30-40 s								
$<h_{large}>$ [m]	0.0713	0.0745	0.0738	0.0740	0.0754	0.0725	0.0737	0.0741
$<h_{small}>$ [m]	0.1088	0.1062	0.1152	0.1182	0.1176	0.1194	0.1243	0.1239
RMS $<h_{large}>$ [m]	0.0018	0.0028	0.0034	0.0039	0.0044	0.0044	0.0043	0.0044
RMS $<h_{small}>$ [m]	0.0039	0.0057	0.0072	0.0079	0.0085	0.0084	0.0092	0.0087
40-50 s								
$<h_{large}>$ [m]	0.0704	0.0721	0.0717	0.0723	0.0731	0.0693	0.0707	0.0716
$<h_{small}>$ [m]	0.1124	0.1110	0.1211	0.1212	0.1214	0.1232	0.1289	0.1276
RMS $<h_{large}>$ [m]	0.0013	0.0022	0.0033	0.0028	0.0033	0.0030	0.0035	0.0036
RMS $<h_{small}>$ [m]	0.0042	0.0054	0.0076	0.0069	0.0075	0.0069	0.0081	0.0084
50-60 s								
$<h_{large}>$ [m]	0.0692	0.0708	0.0702	0.0706	0.0715	0.0676	0.0697	0.0703
$<h_{small}>$ [m]	0.1143	0.1135	0.1238	0.1237	0.1241	0.1260	0.1302	0.1290
RMS $<h_{large}>$ [m]	0.0010	0.0019	0.0025	0.0026	0.0029	0.0025	0.0029	0.0030
RMS $<h_{small}>$ [m]	0.0039	0.0051	0.0070	0.0070	0.0072	0.0070	0.0079	0.0078

Table A6.7. Continued.

Fluidisation velocity	**1.30 m/s**			**1.35 m/s**		**1.40 m/s**	
0-10 s							
$<h_{large}>$ [m]	0.0884	0.0884	0.0884	0.0929	0.0911	0.0983	0.0956
$<h_{small}>$ [m]	0.1065	0.1050	0.1089	0.1089	0.1093	0.1107	0.1165
RMS $<h_{large}>$ [m]	0.0088	0.0068	0.0084	0.0092	0.0091	0.0122	0.0114
RMS $<h_{small}>$ [m]	0.0100	0.0089	0.0103	0.0113	0.0108	0.0122	0.0139
10-20 s							
$<h_{large}>$ [m]	0.0808	0.0810	0.0810	0.0913	0.0852	0.0924	0.0932
$<h_{small}>$ [m]	0.1170	0.1143	0.1162	0.1097	0.1204	0.1213	0.1309
RMS $<h_{large}>$ [m]	0.0057	0.0056	0.0053	0.0094	0.0071	0.0115	0.0112
RMS $<h_{small}>$ [m]	0.0087	0.0087	0.0093	0.0100	0.0111	0.0144	0.0186
20-30 s							
$<h_{large}>$ [m]	0.0783	0.0795	0.0789	0.0918	0.0797	0.0972	0.0906
$<h_{small}>$ [m]	0.1262	0.1245	0.1219	0.1099	0.1268	0.1115	0.1207
RMS $<h_{large}>$ [m]	0.0065	0.0061	0.0060	0.0092	0.0055	0.0116	0.0096
RMS $<h_{small}>$ [m]	0.0107	0.0120	0.0103	0.0100	0.0098	0.0162	0.0131
30-40 s							
$<h_{large}>$ [m]	0.0747	0.0770	0.0766	0.0915	0.0792	0.0924	0.0946
$<h_{small}>$ [m]	0.1286	0.1281	0.1269	0.1164	0.1298	0.1213	0.1152
RMS $<h_{large}>$ [m]	0.0046	0.0052	0.0051	0.0104	0.0057	0.0102	0.0114
RMS $<h_{small}>$ [m]	0.0089	0.0109	0.0103	0.0127	0.0106	0.0137	0.0140
40-50 s							
$<h_{large}>$ [m]	0.0732	0.0753	0.0737	0.0861	0.0784	0.0970	0.0946
$<h_{small}>$ [m]	0.1324	0.1335	0.1285	0.1253	0.1320	0.1106	0.1252
RMS $<h_{large}>$ [m]	0.0040	0.0054	0.0042	0.0088	0.0072	0.0108	0.0107
RMS $<h_{small}>$ [m]	0.0104	0.0123	0.0083	0.0140	0.0124	0.0123	0.0149
50-60 s							
$<h_{large}>$ [m]	0.0724	0.0735	0.0724	0.0890	0.0738	0.0946	0.0965
$<h_{small}>$ [m]	0.1357	0.1362	0.1353	0.1224	0.1383	0.1106	0.1114
RMS $<h_{large}>$ [m]	0.0040	0.0051	0.0042	0.0102	0.0046	0.0100	0.0115
RMS $<h_{small}>$ [m]	0.0101	0.0121	0.0094	0.0137	0.0100	0.0109	0.0127

Table A6.8. Mean bed expansion frequencies for a binary mixture (x_{small} = 0.25, h_b = 15 cm).

Fluidisation velocity	**1.15 m/s**	**1.20 m/s**	**1.25 m/s**	**1.30 m/s**	**1.35 m/s**	**1.40 m/s**
measurement 1	1.6	1.6	1.7	1.9	1.9	1.9
measurement 2	1.5	1.6	1.8	1.8	2.1	1.9
measurement 3		1.7	1.7	1.9		

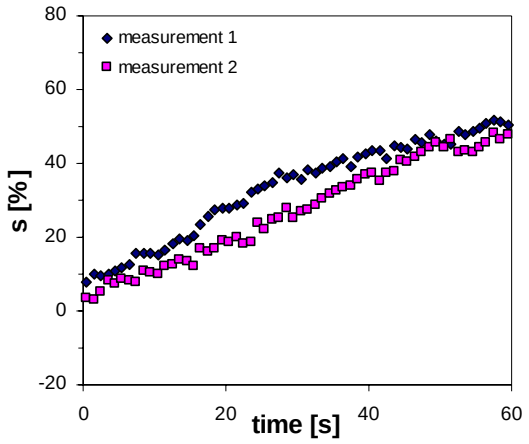

a) 1.15 m/s.

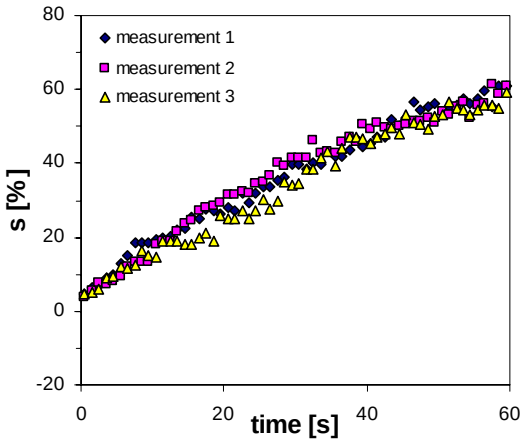

b) 1.20 m/s.

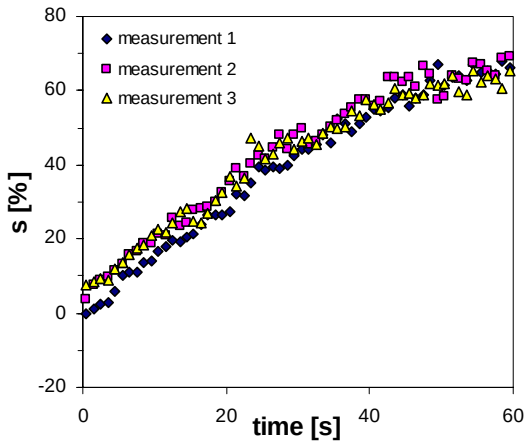

c) 1.25 m/s.

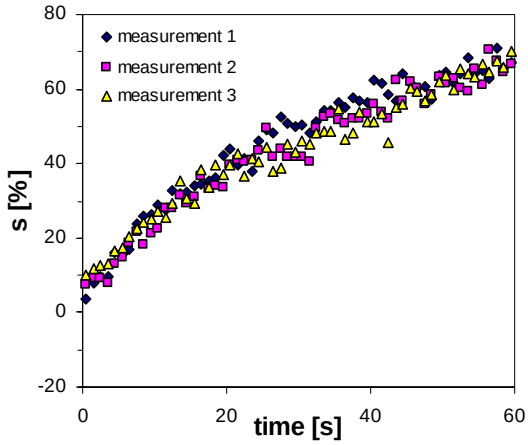

d) 1.30 m/s.

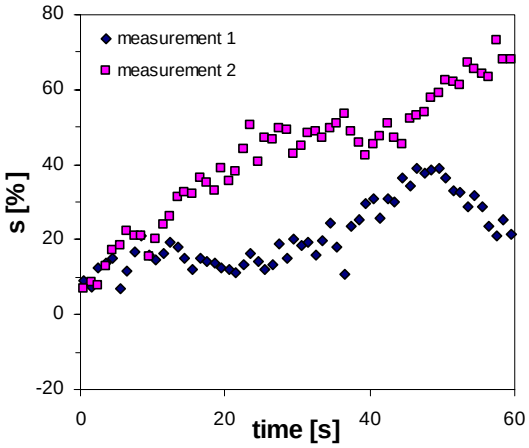

e) 1.35 m/s.

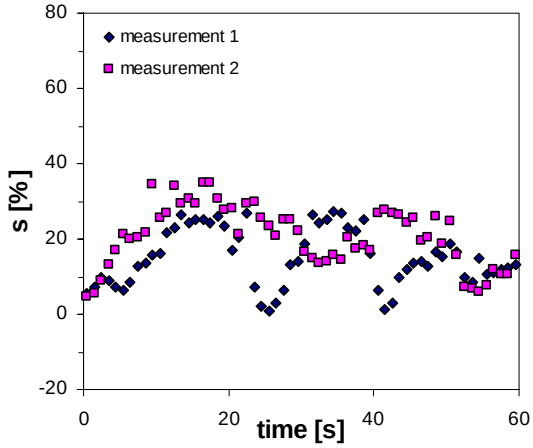

f) 1.40 m/s.

Figure A6.1. Segregation rates for a binary mixture at various fluidisation velocities (x_{small} = 0.25, h_b = 15 cm).

A 6.2.2. 50 mass % small glass beads

bed dimensions: 150 x 15 x 700 mm
total particle mass: 247.1 gram
number of 1.5 mm glass beads: ~ 27,710
number of 2.5 mm glass beads: ~ 5,980
initial bed height: 7.5 cm

Table A6.9. Bed expansion dynamics for a binary mixture (x_{small} = 0.50, h_b = 7.5 cm).

Fluidisation velocity	**1.10 m/s**			**1.15 m/s**			**1.20 m/s**		
0-10 s									
$<h_{large}>$ [m]	0.0377	0.0389	0.0388	0.0389	0.0399	0.0397	0.0398	0.0421	0.0423
$<h_{small}>$ [m]	0.0493	0.0511	0.0511	0.0577	0.0555	0.0557	0.0567	0.0568	0.0575
RMS $<h_{large}>$ [m]	0.0026	0.0033	0.0032	0.0045	0.0044	0.0044	0.0049	0.0048	0.0050
RMS $<h_{small}>$ [m]	0.0026	0.0037	0.0033	0.0057	0.0050	0.0052	0.0054	0.0057	0.0061
10-20 s									
$<h_{large}>$ [m]	0.0313	0.0322	0.0322	0.0319	0.0337	0.0328	0.0343	0.0349	0.0342
$<h_{small}>$ [m]	0.0531	0.0563	0.0556	0.0593	0.0577	0.0585	0.0585	0.0609	0.0600
RMS $<h_{large}>$ [m]	0.0017	0.0022	0.0023	0.0033	0.0030	0.0031	0.0042	0.0034	0.0036
RMS $<h_{small}>$ [m]	0.0024	0.0034	0.0033	0.0038	0.0041	0.0043	0.0049	0.0050	0.0051
20-30 s									
$<h_{large}>$ [m]	0.0277	0.0283	0.0286	0.0302	0.0322	0.0312	0.0321	0.0326	0.0299
$<h_{small}>$ [m]	0.0559	0.0572	0.0577	0.0597	0.0574	0.0577	0.0576	0.0607	0.0611
RMS $<h_{large}>$ [m]	0.0013	0.0014	0.0015	0.0031	0.0031	0.0026	0.0053	0.0031	0.0032
RMS $<h_{small}>$ [m]	0.0023	0.0026	0.0028	0.0039	0.0041	0.0040	0.0040	0.0048	0.0044
30-40 s									
$<h_{large}>$ [m]	0.0270	0.0273	0.0283	0.0327	0.0301	0.0300	0.0386	0.0309	0.0307
$<h_{small}>$ [m]	0.0568	0.0598	0.0606	0.0575	0.0595	0.0594	0.0566	0.0615	0.0603
RMS $<h_{large}>$ [m]	0.0012	0.0019	0.0024	0.0039	0.0037	0.0027	0.0057	0.0032	0.0027
RMS $<h_{small}>$ [m]	0.0021	0.0031	0.0039	0.0041	0.0045	0.0039	0.0048	0.0047	0.0043
40-50 s									
$<h_{large}>$ [m]	0.0266	0.0286	0.0299	0.0308	0.0357	0.0313	0.0411	0.0332	0.0355
$<h_{small}>$ [m]	0.0580	0.0591	0.0576	0.0583	0.0565	0.0592	0.0553	0.0618	0.0596
RMS $<h_{large}>$ [m]	0.0014	0.0029	0.0031	0.0030	0.0051	0.0030	0.0065	0.0049	0.0048
RMS $<h_{small}>$ [m]	0.0025	0.0037	0.0036	0.0037	0.0048	0.0045	0.0049	0.0056	0.0051
50-60 s									
$<h_{large}>$ [m]	0.0262	0.0287	0.0315	0.0288	0.0391	0.0348	0.0382	0.0317	0.0355
$<h_{small}>$ [m]	0.0575	0.0577	0.0555	0.0613	0.0547	0.0579	0.0564	0.0616	0.0606
RMS $<h_{large}>$ [m]	0.0014	0.0030	0.0037	0.0024	0.0059	0.0040	0.0061	0.0040	0.0046
RMS $<h_{small}>$ [m]	0.0024	0.0035	0.0033	0.0039	0.0047	0.0048	0.0050	0.0053	0.0055

Table A6.10. Mean bed expansion frequencies for a binary mixture (x_{small} = 0.50, h_b = 7.5 cm).

Fluidisation velocity	**1.10 m/s**	**1.15 m/s**	**1.20 m/s**
measurement 1	3.4	3.4	3.0
measurement 2	3.4	3.0	3.4
measurement 3	3.1	3.4	3.4

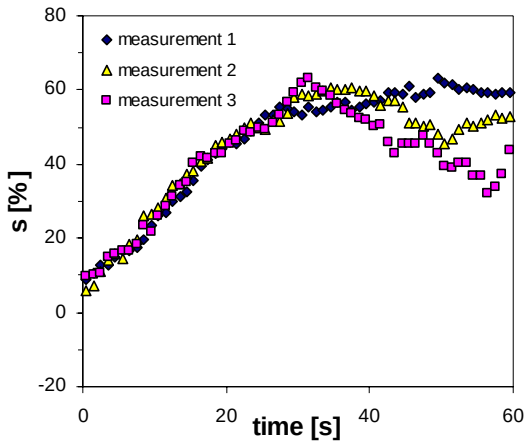

a) 1.10 m/s.

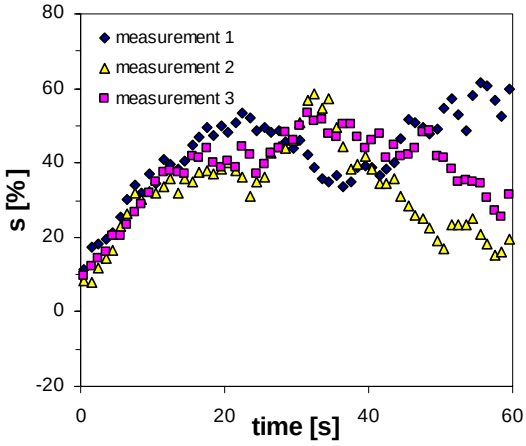

b) 1.15 m/s.

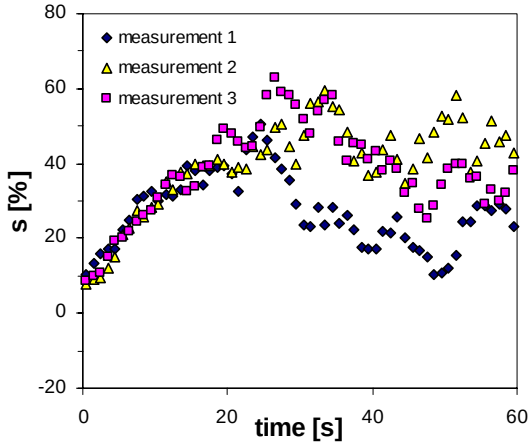

c) 1.20 m/s.

Figure A6.2. Segregation rates for a binary mixture at various fluidisation velocities (x_{small} = 0.50, h_b = 7.5 cm).

bed dimensions:	150 x 15 x 700 mm
total particle mass:	494.3 gram
number of 1.5 mm glass beads:	~ 55430
number of 2.5 mm glass beads:	~ 11960
initial bed height:	15 cm

Table A 6.11. Bed expansion dynamics for a binary mixture (x_{small} = 0.50, h_b = 15 cm).

Fluidisation velocity	**1.00 m/s**		**1.05 m/s**		**1.10 m/s**		
0-10 s							
$\langle h_{large} \rangle$ [m]	0.0755	0.0768	0.0815	0.0790	0.0771	0.0825	0.0813
$\langle h_{small} \rangle$ [m]	0.0844	0.0858	0.0866	0.0886	0.0891	0.0902	0.0885
RMS $\langle h_{large} \rangle$ [m]	0.0029	0.0037	0.0048	0.0039	0.0044	0.0064	0.0061
RMS $\langle h_{small} \rangle$ [m]	0.0029	0.0036	0.0042	0.0038	0.0040	0.0061	0.0058
10-20 s							
$\langle h_{large} \rangle$ [m]	0.0719	0.0733	0.0769	0.0731	0.0694	0.0696	0.0740
$\langle h_{small} \rangle$ [m]	0.0888	0.0891	0.0889	0.0952	0.0945	0.0982	0.0939
RMS $\langle h_{large} \rangle$ [m]	0.0029	0.0038	0.0036	0.0047	0.0026	0.0044	0.0044
RMS $\langle h_{small} \rangle$ [m]	0.0032	0.0042	0.0044	0.0057	0.0041	0.0058	0.0058
20-30 s							
$\langle h_{large} \rangle$ [m]	0.0666	0.0684	0.0704	0.0677	0.0641	0.0601	0.0674
$\langle h_{small} \rangle$ [m]	0.0944	0.0943	0.0947	0.1010	0.0994	0.1046	0.0992
RMS $\langle h_{large} \rangle$ [m]	0.0024	0.0032	0.0032	0.0039	0.0031	0.0039	0.0042
RMS $\langle h_{small} \rangle$ [m]	0.0035	0.0045	0.0046	0.0060	0.0046	0.0058	0.0060
30-40 s							
$\langle h_{large} \rangle$ [m]	0.0617	0.0637	0.0653	0.0631	0.0569	0.0533	0.0610
$\langle h_{small} \rangle$ [m]	0.0999	0.0982	0.1003	0.1054	0.1045	0.1083	0.1034
RMS $\langle h_{large} \rangle$ [m]	0.0021	0.0025	0.0033	0.0036	0.0022	0.0027	0.0028
RMS $\langle h_{small} \rangle$ [m]	0.0038	0.0041	0.0053	0.0064	0.0045	0.0047	0.0052
40-50 s							
$\langle h_{large} \rangle$ [m]	0.0589	0.0592	0.0598	0.0579	0.0534	0.0495	0.0569
$\langle h_{small} \rangle$ [m]	0.1021	0.1020	0.1045	0.1082	0.1072	0.1111	0.1059
RMS $\langle h_{large} \rangle$ [m]	0.0013	0.0019	0.0024	0.0022	0.0015	0.0021	0.0027
RMS $\langle h_{small} \rangle$ [m]	0.0032	0.0044	0.0053	0.0053	0.0040	0.0046	0.0050
50-60 s							
$\langle h_{large} \rangle$ [m]	0.0576	0.0570	0.0573	0.0550	0.0526	0.0486	0.0532
$\langle h_{small} \rangle$ [m]	0.1030	0.1040	0.1064	0.1100	0.1083	0.1123	0.1088
RMS $\langle h_{large} \rangle$ [m]	0.0010	0.0014	0.0018	0.0019	0.0011	0.0027	0.0025
RMS $\langle h_{small} \rangle$ [m]	0.0034	0.0037	0.0045	0.0047	0.0037	0.0050	0.0055

Table A 6.11. Continued.

Fluidisation velocity	**1.15 m/s**			**1.20 m/s**			**1.25 m/s**		
0-10 s									
$<h_{large}>$ [m]	0.0819	0.0816	0.0811	0.0891	0.0880	0.0926	0.0926	0.0913	0.0918
$<h_{small}>$ [m]	0.0928	0.0954	0.0990	0.1033	0.0971	0.1019	0.1034	0.1049	0.1015
RMS $<h_{large}>$ [m]	0.0058	0.0050	0.0072	0.0107	0.0070	0.0109	0.0106	0.0115	0.0100
RMS $<h_{small}>$ [m]	0.0067	0.0065	0.0083	0.0111	0.0078	0.0105	0.0101	0.0118	0.0094
10-20 s									
$<h_{large}>$ [m]	0.0721	0.0762	0.0715	0.0880	0.0897	0.0889	0.0915	0.0906	0.0887
$<h_{small}>$ [m]	0.1000	0.1025	0.1060	0.1007	0.0983	0.1023	0.1029	0.1042	0.1044
RMS $<h_{large}>$ [m]	0.0049	0.0063	0.0056	0.0086	0.0087	0.0101	0.0112	0.0104	0.0110
RMS $<h_{small}>$ [m]	0.0061	0.0079	0.0084	0.0089	0.0087	0.0099	0.0105	0.0102	0.0104
20-30 s									
$<h_{large}>$ [m]	0.0663	0.0678	0.0656	0.0896	0.0904	0.0893	0.0894	0.0878	0.0901
$<h_{small}>$ [m]	0.1039	0.1065	0.1089	0.1005	0.0957	0.1024	0.1031	0.1068	0.1017
RMS $<h_{large}>$ [m]	0.0044	0.0047	0.0051	0.0097	0.0091	0.0093	0.0088	0.0110	0.0099
RMS $<h_{small}>$ [m]	0.0063	0.0070	0.0072	0.0092	0.0085	0.0094	0.0090	0.0108	0.0082
30-40 s									
$<h_{large}>$ [m]	0.0641	0.0616	0.0620	0.0890	0.0864	0.0897	0.0899	0.0918	0.0913
$<h_{small}>$ [m]	0.1090	0.1109	0.1109	0.1051	0.1021	0.1031	0.1018	0.1044	0.1021
RMS $<h_{large}>$ [m]	0.0056	0.0047	0.0054	0.0107	0.0086	0.0109	0.0091	0.0110	0.0111
RMS $<h_{small}>$ [m]	0.0076	0.0077	0.0068	0.0109	0.0086	0.0101	0.0089	0.0104	0.0089
40-50 s									
$<h_{large}>$ [m]	0.0545	0.0587	0.0628	0.0875	0.0863	0.0901	0.0901	0.0923	0.0897
$<h_{small}>$ [m]	0.1128	0.1146	0.1091	0.1023	0.1014	0.1075	0.1043	0.1093	0.1022
RMS $<h_{large}>$ [m]	0.0037	0.0047	0.0057	0.0105	0.0079	0.0126	0.0090	0.0115	0.0109
RMS $<h_{small}>$ [m]	0.0067	0.0080	0.0071	0.0100	0.0074	0.0121	0.0098	0.0125	0.0092
50-60 s									
$<h_{large}>$ [m]	0.0525	0.0606	0.0633	0.0875	0.0894	0.0875	0.0883	0.0902	0.0928
$<h_{small}>$ [m]	0.1151	0.1143	0.1098	0.1046	0.1006	0.1054	0.1081	0.1082	0.1040
RMS $<h_{large}>$ [m]	0.0038	0.0050	0.0053	0.0100	0.0100	0.0100	0.0108	0.0111	0.0115
RMS $<h_{small}>$ [m]	0.0070	0.0076	0.0060	0.0101	0.0091	0.0104	0.0114	0.0118	0.0114

Table A6.12. Mean bed expansion frequencies for a binary mixture (x_{small} = 0.50, h_b = 15 cm).

Fluidisation velocity	**1.00 m/s**	**1.05 m/s**	**1.10 m/s**	**1.15 m/s**	**1.20 m/s**	**1.25 m/s**
measurement 1	1.8	1.85	1.95	2.05	2.05	2.0
measurement 2	1.65	1.8	2.1	2.35	2.0	1.9
measurement 3			1.90	2.15	1.9	2.0

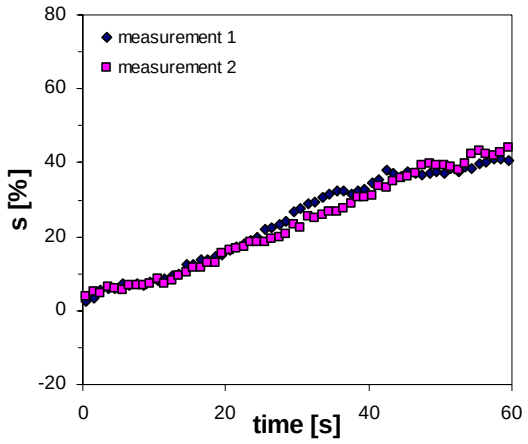

a) 1.00 m/s.

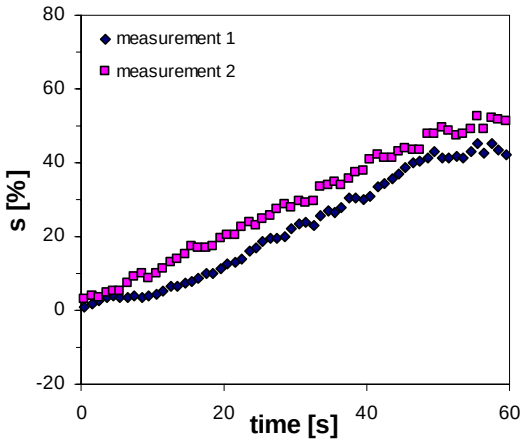

b) 1.05 m/s.

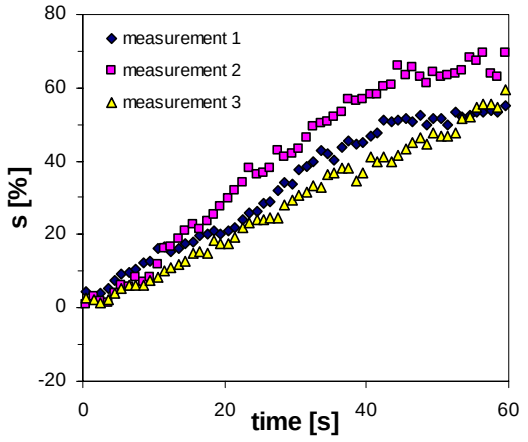

c) 1.10 m/s.

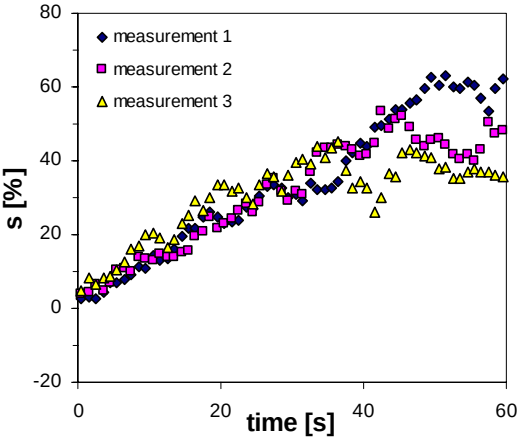

d) 1.15 m/s.

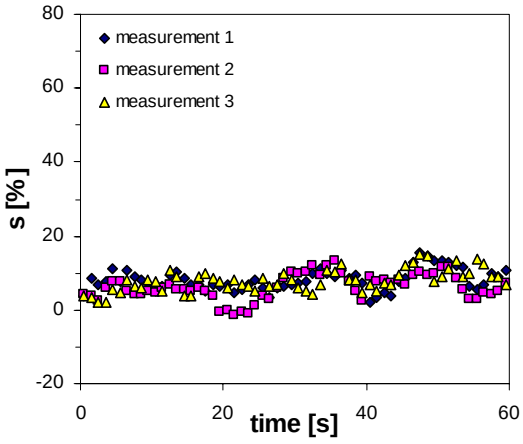

e) 1.20 m/s.

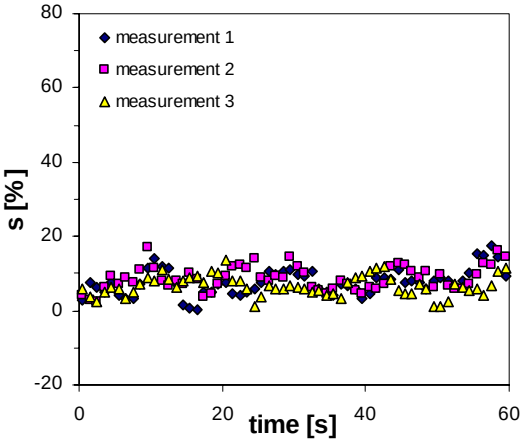

f) 1.25 m/s.

Figure A6.3. Segregation rates for a binary mixture at various fluidisation velocities (x_{small} = 0.50, h_b = 15 cm).

bed dimensions: 150 x 15 x 700 mm
total particle mass: 741.4 gram
number of 1.5 mm glass beads: ~ 83140
number of 2.5 mm glass beads: ~ 17940
initial bed height: 22.5 cm

Table A 6.13. Bed expansion dynamics for a binary mixture (x_{small} = 0.50, h_b = 22.5 cm).

Fluidisation velocity	**1.10 m/s**			**1.15 m/s**		
0-10 s						
$<h_{large}>$ [m]	0.1200	0.1284	0.1236	0.1267	0.1298	0.1272
$<h_{small}>$ [m]	0.1295	0.1277	0.1294	0.1367	0.1435	0.1424
RMS $<h_{large}>$ [m]	0.0067	0.0109	0.0070	0.0096	0.0129	0.0107
RMS $<h_{small}>$ [m]	0.0065	0.0087	0.0074	0.0093	0.0140	0.0117
10-20 s						
$<h_{large}>$ [m]	0.1136	0.1147	0.1153	0.1152	0.1177	0.1172
$<h_{small}>$ [m]	0.1379	0.1351	0.1361	0.1453	0.1500	0.1470
RMS $<h_{large}>$ [m]	0.0066	0.0223	0.0059	0.0082	0.0098	0.0092
RMS $<h_{small}>$ [m]	0.0078	0.0073	0.0073	0.0090	0.0118	0.0109
20-30 s						
$<h_{large}>$ [m]	0.1054	0.1048	0.1065	0.1040	0.1120	0.1124
$<h_{small}>$ [m]	0.1441	0.1426	0.1436	0.1507	0.1514	0.1503
RMS $<h_{large}>$ [m]	0.0060	0.0347	0.0049	0.0091	0.0100	0.0082
RMS $<h_{small}>$ [m]	0.0082	0.0074	0.0074	0.0089	0.0103	0.0103
30-40 s						
$<h_{large}>$ [m]	0.0966	0.0990	0.0964	0.1012	0.1116	0.1072
$<h_{small}>$ [m]	0.1506	0.1471	0.1507	0.1541	0.1521	0.1547
RMS $<h_{large}>$ [m]	0.0059	0.0451	0.0047	0.0093	0.0093	0.0082
RMS $<h_{small}>$ [m]	0.0082	0.0080	0.0078	0.0095	0.0108	0.0116
40-50 s						
$<h_{large}>$ [m]	0.0903	0.0915	0.0911	0.0980	0.1088	0.1070
$<h_{small}>$ [m]	0.1539	0.1505	0.1542	0.1552	0.1541	0.1526
RMS $<h_{large}>$ [m]	0.0040	0.0584	0.0039	0.0093	0.0103	0.0097
RMS $<h_{small}>$ [m]	0.0074	0.0070	0.0071	0.0083	0.0111	0.0099
50-60 s						
$<h_{large}>$ [m]	0.0866	0.0850	0.0869	0.0976	0.1068	0.1063
$<h_{small}>$ [m]	0.1565	0.1548	0.1578	0.1563	0.1530	0.1530
RMS $<h_{large}>$ [m]	0.0037	0.0726	0.0030	0.0089	0.0079	0.0080
RMS $<h_{small}>$ [m]	0.0068	0.0069	0.0065	0.0083	0.0090	0.0106

Table A 6.13. Continued.

Fluidisation velocity	**1.20 m/s**			**1.25 m/s**	
0-10 s					
$<h_{large}>$ [m]	0.1311	0.1354	0.1320	0.1373	0.1387
$<h_{small}>$ [m]	0.1455	0.1490	0.1448	0.1551	0.1452
RMS $<h_{large}>$ [m]	0.0133	0.0140	0.0118	0.0163	0.0179
RMS $<h_{small}>$ [m]	0.0134	0.0142	0.0125	0.0176	0.0176
10-20 s					
$<h_{large}>$ [m]	0.1168	0.1252	0.1217	0.1375	0.1342
$<h_{small}>$ [m]	0.1530	0.1564	0.1496	0.1470	0.1580
RMS $<h_{large}>$ [m]	0.0119	0.0128	0.0113	0.0139	0.0143
RMS $<h_{small}>$ [m]	0.0123	0.0158	0.0114	0.0122	0.0162
20-30 s					
$<h_{large}>$ [m]	0.1125	0.1204	0.1205	0.1387	0.1373
$<h_{small}>$ [m]	0.1539	0.1605	0.1527	0.1441	0.1594
RMS $<h_{large}>$ [m]	0.0127	0.0114	0.0115	0.0124	0.0175
RMS $<h_{small}>$ [m]	0.0104	0.0150	0.0109	0.0108	0.0168
30-40 s					
$<h_{large}>$ [m]	0.1233	0.1185	0.1223	0.1410	0.1356
$<h_{small}>$ [m]	0.1487	0.1586	0.1538	0.1431	0.1629
RMS $<h_{large}>$ [m]	0.0144	0.0119	0.0117	0.0128	0.0190
RMS $<h_{small}>$ [m]	0.0118	0.0130	0.0103	0.0098	0.0187
40-50 s					
$<h_{large}>$ [m]	0.1251	0.1290	0.1254	0.1408	0.1323
$<h_{small}>$ [m]	0.1518	0.1537	0.1511	0.1417	0.1626
RMS $<h_{large}>$ [m]	0.0142	0.0138	0.0128	0.0124	0.0170
RMS $<h_{small}>$ [m]	0.0121	0.0130	0.0125	0.0091	0.0190
50-60 s					
$<h_{large}>$ [m]	0.1203	0.1275	0.1258	0.1414	0.1397
$<h_{small}>$ [m]	0.1565	0.1545	0.1499	0.1427	0.1586
RMS $<h_{large}>$ [m]	0.0141	0.0128	0.0104	0.0133	0.0196
RMS $<h_{small}>$ [m]	0.0138	0.0139	0.0109	0.0104	0.0179

Table A6.14. Mean bed expansion frequencies for a binary mixture (x_{small} = 0.50, h_b = 22.5 cm).

Fluidisation velocity	**1.10 m/s**	**1.15 m/s**	**1.20 m/s**	**1.25 m/s**
measurement 1	1.65	1.55	1.6	1.6
measurement 2	1.65	1.55	1.4	1.4
measurement 3	1.5	1.5	1.7	

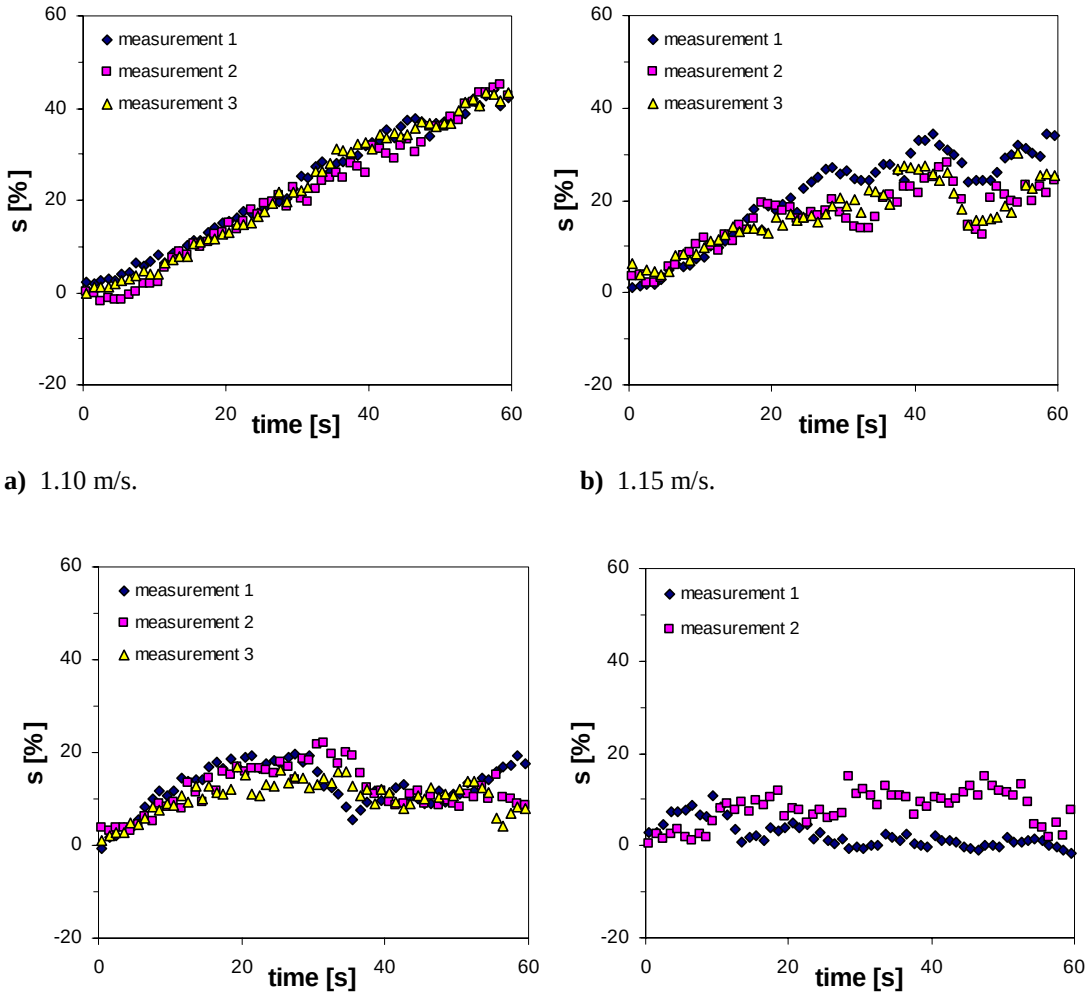

a) 1.10 m/s.

b) 1.15 m/s.

c) 1.20 m/s

d) 1.25 m/s.

Figure A6.4. Segregation rates for a binary mixture at various fluidisation velocities (x_{small} = 0.50, h_b = 22.5 cm).

bed dimensions: 150 x 15 x 700 mm
total particle mass: 988.6 gram
number of 1.5 mm glass beads: ~ 110870
number of 2.5 mm glass beads: ~ 23940
initial bed height: 30 cm

Table A 6.15. Bed expansion dynamics for a binary mixture (x_{small} = 0.50, h_b = 30 cm).

Fluidisation velocity	**1.10 m/s**			**1.15 m/s**		
0-10 s						
$<h_{large}>$ [m]	0.1572	0.1512	0.1568	0.1648	0.1708	0.1735
$<h_{small}>$ [m]	0.1592	0.1768	0.1713	0.1838	0.1830	0.1765
RMS $<h_{large}>$ [m]	0.0088	0.0080	0.0069	0.0117	0.0128	0.0120
RMS $<h_{small}>$ [m]	0.0077	0.0088	0.0072	0.0116	0.0139	0.0108
10-20 s						
$<h_{large}>$ [m]	0.1538	0.1427	0.1515	0.1570	0.1600	0.1623
$<h_{small}>$ [m]	0.1697	0.1825	0.1784	0.1901	0.1897	0.1837
RMS $<h_{large}>$ [m]	0.0069	0.0080	0.0071	0.0121	0.0103	0.0102
RMS $<h_{small}>$ [m]	0.0071	0.0100	0.0088	0.0131	0.0121	0.0105
20-30 s						
$<h_{large}>$ [m]	0.1444	0.1358	0.1438	0.1514	0.1492	0.1556
$<h_{small}>$ [m]	0.1762	0.1892	0.1844	0.1931	0.1963	0.1896
RMS $<h_{large}>$ [m]	0.0053	0.0075	0.0061	0.0129	0.0088	0.0109
RMS $<h_{small}>$ [m]	0.0066	0.0088	0.0086	0.0133	0.0123	0.0104
30-40 s						
$<h_{large}>$ [m]	0.1390	0.1303	0.1361	0.1402	0.1415	0.1488
$<h_{small}>$ [m]	0.1816	0.1945	0.1903	0.2022	0.2056	0.1956
RMS $<h_{large}>$ [m]	0.0048	0.0071	0.0051	0.0103	0.0081	0.0115
RMS $<h_{small}>$ [m]	0.0071	0.0092	0.0086	0.0127	0.0137	0.0122
40-50 s						
$<h_{large}>$ [m]	0.1330	0.1237	0.1316	0.1364	0.1340	0.1364
$<h_{small}>$ [m]	0.1846	0.1985	0.1948	0.2038	0.2118	0.2059
RMS $<h_{large}>$ [m]	0.0032	0.0067	0.0052	0.0109	0.0082	0.0095
RMS $<h_{small}>$ [m]	0.0055	0.0091	0.0096	0.0125	0.0144	0.0121
50-60 s						
$<h_{large}>$ [m]	0.1287	0.1176	0.1269	0.1377	0.1284	0.1296
$<h_{small}>$ [m]	0.1901	0.2027	0.1958	0.2065	0.2144	0.2116
RMS $<h_{large}>$ [m]	0.0058	0.0069	0.0036	0.0116	0.0078	0.0088
RMS $<h_{small}>$ [m]	0.0081	0.0095	0.0076	0.0132	0.0134	0.0127

Table A 6.15. Continued.

Fluidisation velocity	**1.20 m/s**			**1.25 m/s**	
0-10 s					
$<h_{large}>$ [m]	0.1785	0.1798	0.1812	0.1962	0.1930
$<h_{small}>$ [m]	0.1953	0.1936	0.1910	0.2117	0.2061
RMS $<h_{large}>$ [m]	0.0177	0.0164	0.0167	0.0285	0.0259
RMS $<h_{small}>$ [m]	0.0186	0.0183	0.0173	0.0269	0.0250
10-20 s					
$<h_{large}>$ [m]	0.1726	0.1699	0.1648	0.1837	0.1834
$<h_{small}>$ [m]	0.1987	0.1982	0.2007	0.2076	0.2051
RMS $<h_{large}>$ [m]	0.0173	0.0161	0.0160	0.0227	0.0205
RMS $<h_{small}>$ [m]	0.0160	0.0157	0.0161	0.0214	0.0208
20-30 s					
$<h_{large}>$ [m]	0.1641	0.1615	0.1577	0.1739	0.1762
$<h_{small}>$ [m]	0.1965	0.1993	0.2121	0.2121	0.2192
RMS $<h_{large}>$ [m]	0.0140	0.0166	0.0145	0.0173	0.0206
RMS $<h_{small}>$ [m]	0.0135	0.0132	0.0170	0.0188	0.0218
30-40 s					
$<h_{large}>$ [m]	0.1637	0.1535	0.1502	0.1712	0.1743
$<h_{small}>$ [m]	0.2059	0.2005	0.2166	0.2266	0.2209
RMS $<h_{large}>$ [m]	0.0161	0.0143	0.0134	0.0166	0.0193
RMS $<h_{small}>$ [m]	0.0145	0.0126	0.0176	0.0246	0.0236
40-50 s					
$<h_{large}>$ [m]	0.1578	0.1491	0.1472	0.1760	0.1717
$<h_{small}>$ [m]	0.2138	0.2058	0.2201	0.2198	0.2196
RMS $<h_{large}>$ [m]	0.0165	0.0142	0.0131	0.0192	0.0194
RMS $<h_{small}>$ [m]	0.0185	0.0130	0.0204	0.0244	0.0222
50-60 s					
$<h_{large}>$ [m]	0.1574	0.1453	0.1443	0.1855	0.1735
$<h_{small}>$ [m]	0.2137	0.2187	0.2210	0.2184	0.2178
RMS $<h_{large}>$ [m]	0.0183	0.0139	0.0127	0.0259	0.0201
RMS $<h_{small}>$ [m]	0.0194	0.0174	0.0192	0.0269	0.0229

Table A6.16. Mean bed expansion frequencies for a binary mixture (x_{small} = 0.50, h_b = 30 cm).

Fluidisation velocity	**1.10 m/s**	**1.15 m/s**	**1.20 m/s**	**1.25 m/s**
measurement 1	1.1	1.25	1.2	1.1
measurement 2	1.25	1.35	1.35	1.2
measurement 3	1.1	1.35	1.25	

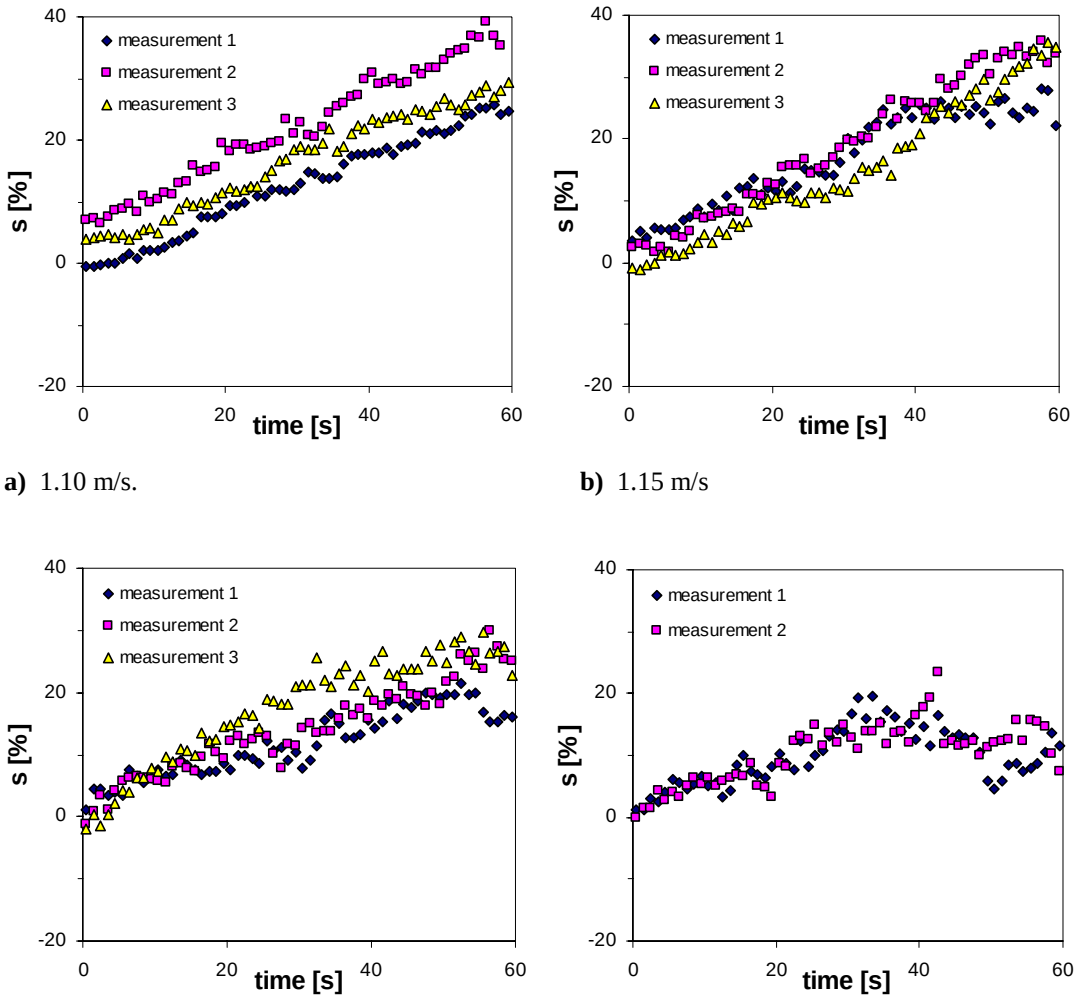

a) 1.10 m/s. **b)** 1.15 m/s

c) 1.20 m/s. **d)** 1.25 m/s.

Figure A6.5. Segregation rates for a binary mixture at various fluidisation velocities (x_{small} = 0.50, h_b = 30 cm).

A 6.2.3. 75 mass % small glass beads

bed dimensions: 150 x 15 x 700 mm
total particle mass: 494.3 gram
number of 1.5 mm glass beads: ~ 83,150
number of 2.5 mm glass beads: ~ 5,980
initial bed height: 15 cm

Table A 6.17. Bed expansion dynamics for a binary mixture (x_{small} = 0.75, h_b = 15 cm).

Fluidisation velocity	**0.95 m/s**			**1.00 m/s**		
0-10 s						
$<h_{large}>$ [m]	0.0818	0.0829	0.0803	0.0838	0.0757	0.0825
$<h_{small}>$ [m]	0.0813	0.0810	0.0821	0.0818	0.0871	0.0860
RMS $<h_{large}>$ [m]	0.0052	0.0051	0.0058	0.0048	0.0062	0.0068
RMS $<h_{small}>$ [m]	0.0031	0.0030	0.0033	0.0024	0.0049	0.0048
10-20 s						
$<h_{large}>$ [m]	0.0754	0.0768	0.0752	0.0749	0.0651	0.0714
$<h_{small}>$ [m]	0.0835	0.0834	0.0844	0.0850	0.0898	0.0881
RMS $<h_{large}>$ [m]	0.0052	0.0049	0.0061	0.0054	0.0055	0.0047
RMS $<h_{small}>$ [m]	0.0036	0.0033	0.0039	0.0035	0.0044	0.0042
20-30 s						
$<h_{large}>$ [m]	0.0722	0.0699	0.0664	0.0628	0.0581	0.0611
$<h_{small}>$ [m]	0.0846	0.0857	0.0857	0.0878	0.0928	0.0917
RMS $<h_{large}>$ [m]	0.0051	0.0047	0.0049	0.0056	0.0053	0.0053
RMS $<h_{small}>$ [m]	0.0040	0.0038	0.0036	0.0036	0.0050	0.0046
30-40 s						
$<h_{large}>$ [m]	0.0642	0.0599	0.0629	0.0608	0.0535	0.0585
$<h_{small}>$ [m]	0.0866	0.0882	0.0864	0.0904	0.0936	0.0934
RMS $<h_{large}>$ [m]	0.0040	0.0045	0.0037	0.0055	0.0048	0.0059
RMS $<h_{small}>$ [m]	0.0039	0.0036	0.0033	0.0050	0.0046	0.0053
40-50 s						
$<h_{large}>$ [m]	0.0555	0.0569	0.0592	0.0519	0.0504	0.0516
$<h_{small}>$ [m]	0.0893	0.0894	0.0881	0.0908	0.0948	0.0953
RMS $<h_{large}>$ [m]	0.0033	0.0033	0.0036	0.0041	0.0045	0.0051
RMS $<h_{small}>$ [m]	0.0034	0.0034	0.0033	0.0041	0.0051	0.0050
50-60 s						
$<h_{large}>$ [m]	0.0471	0.0512	0.0538	0.0467	0.0476	0.0487
$<h_{small}>$ [m]	0.0920	0.0915	0.0892	0.0928	0.0959	0.0963
RMS $<h_{large}>$ [m]	0.0026	0.0026	0.0034	0.0030	0.0043	0.0050
RMS $<h_{small}>$ [m]	0.0027	0.0033	0.0032	0.0042	0.0046	0.0049

Table A 6.17. Continued.

Fluidisation velocity	**1.05 m/s**			**1.15 m/s**	
0-10 s					
$<h_{large}>$ [m]	0.0872	0.0818	0.0845	0.0989	0.0957
$<h_{small}>$ [m]	0.0870	0.0884	0.0894	0.1020	0.0995
RMS $<h_{large}>$ [m]	0.0071	0.0061	0.0071	0.0128	0.0115
RMS $<h_{small}>$ [m]	0.0046	0.0048	0.0060	0.0111	0.0104
10-20 s					
$<h_{large}>$ [m]	0.0863	0.0805	0.0791	0.0955	0.0918
$<h_{small}>$ [m]	0.0883	0.0900	0.0910	0.1009	0.1003
RMS $<h_{large}>$ [m]	0.0093	0.0065	0.0070	0.0128	0.0124
RMS $<h_{small}>$ [m]	0.0057	0.0056	0.0054	0.0092	0.0090
20-30 s					
$<h_{large}>$ [m]	0.0783	0.0833	0.0787	0.0966	0.0934
$<h_{small}>$ [m]	0.0909	0.0902	0.0931	0.1020	0.1002
RMS $<h_{large}>$ [m]	0.0078	0.0080	0.0083	0.0139	0.0126
RMS $<h_{small}>$ [m]	0.0061	0.0055	0.0066	0.0109	0.0098
30-40 s					
$<h_{large}>$ [m]	0.0772	0.0743	0.0791	0.0946	0.0964
$<h_{small}>$ [m]	0.0904	0.0936	0.0923	0.1004	0.1015
RMS $<h_{large}>$ [m]	0.0069	0.0071	0.0067	0.0139	0.0141
RMS $<h_{small}>$ [m]	0.0049	0.0062	0.0058	0.0100	0.0108
40-50 s					
$<h_{large}>$ [m]	0.0793	0.0712	0.0816	0.0971	0.0964
$<h_{small}>$ [m]	0.0911	0.0951	0.0928	0.1031	0.1047
RMS $<h_{large}>$ [m]	0.0075	0.0075	0.0089	0.0148	0.0154
RMS $<h_{small}>$ [m]	0.0055	0.0069	0.0066	0.0111	0.0133
50-60 s					
$<h_{large}>$ [m]	0.0750	0.0731	0.0781	0.0933	0.0954
$<h_{small}>$ [m]	0.0922	0.0948	0.0926	0.1032	0.1026
RMS $<h_{large}>$ [m]	0.0080	0.0086	0.0083	0.0140	0.0125
RMS $<h_{small}>$ [m]	0.0056	0.0074	0.0063	0.0106	0.0099

Table A6.18. Mean bed expansion frequencies for a binary mixture (x_{small} = 0.75, h_b = 15 cm).

Fluidisation velocity	**0.95 m/s**	**1.00 m/s**	**1.05 m/s**	**1.15 m/s**
measurement 1	1.7	1.8	1.95	2.0
measurement 2	1.7	2.1	2.05	1.85
measurement 3	1.7	2.1	1.85	

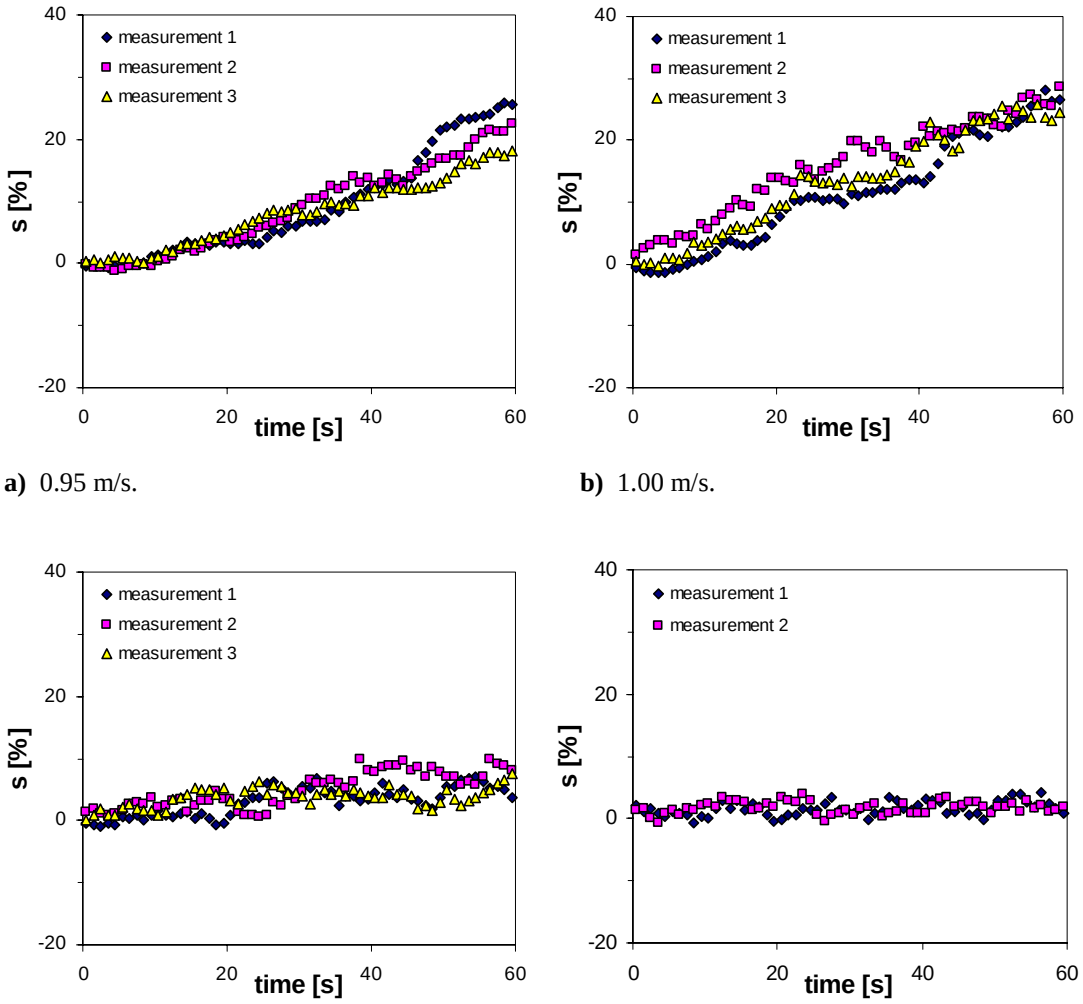

a) 0.95 m/s.

b) 1.00 m/s.

c) 1.05 m/s.

d) 1.15 m/s.

Figure A6.6. Segregation rates for a binary mixture at various fluidisation velocities (x_{small} = 0.75, h_b = 15 cm).

Chapter 7.

Discrete element modelling of fluidised bed spray granulation

Abstract

A novel discrete element spray granulation model that captures the key features of fluidised bed hydrodynamics, liquid-solid contacting and agglomeration is presented. The model computes the motion of every individual particle and droplet in the system, considering the gas phase as a continuum. The hydrodynamic behaviour of a batch granulation process containing 50.000 primary particles is simulated, whereby micro scale processes such as particle-particle collisions, droplet-particle coalescence and agglomeration are directly taken into account by simple closure models. The simulations demonstrate the great potential of the model to predict the influence of several key process conditions such as fluidisation velocity, spray rate and spray pattern on powder product characteristics. In all performed simulations droplet-particle coalescence and agglomeration took place in the freeboard and at the top of the bed throughout the batch runs. Particle growth was dominated by layering, whereas agglomeration of equally sized particles and bed penetration by droplets or wetted particles rarely occurred. Severe size segregation was observed in the simulations. Big granules mainly remained at the bottom of the bed while above the spray nozzle mainly primary particles were detected. Furthermore a low particle concentration was observed in the spray zone, because particles are directed back into the bed as soon as a droplet hits them.

This chapter is based on the paper:

Goldschmidt M.J.V., Weijers G.G.C., Boerefijn R., Kuipers J.A.M., 2001, Discrete element modelling of fluidised bed spray granulation, submitted to *AIChE J.*

Goldschmidt M.J.V., Weijers G.G.C., Boerefijn R., Kuipers J.A.M., 2002, Discrete element modelling of fluidised bed spray granulation, submitted to '*World congress on particle technology 4'*, 21-25 July, Sydney, Australia

1. Introduction

Fluidised bed granulation is an important powder production process with several key advantages compared to other powder production processes, such as spray drying or high-shear granulation. The most characteristic and essential part of spray granulation is the wetting of particles by an atomised liquid feed (solution, suspension or melt) and the induced growth of particles in a gas-fluidised bed. The process is commonly used for the production of granules for agricultural, pharmaceutical and other fine chemical applications, as it provides good control over composition and structural properties of the powder. Further it allows all essential steps of the granulation process to take place in one apparatus. Reviews signifying the interest of this type of granulation process are given by Kristensen and Schaeffer (1987), Banks and Aulton (1991) and Nienow (1995).

Thorough understanding of the mechanisms prevailing in the spray granulation process is a prerequisite for understanding the process and prevailing proper control over the powder properties. Mechanisms of granulation are often distinguished as wetting (or nucleation), progressive growth (agglomeration or layering) by a sequence of many binary collisions, breakage and consolidation. It is virtually impossible to expect that these mechanisms will occur singly or sequentially. Many granulator design and operation parameters, such as mode of operation (continuous or batch), fluidisation velocity, reactor geometry, positioning of internals, type of nozzle, liquid feed rate, operating temperature, etc., etc., will influence these mechanisms and consequently the powder characteristics.

Though fluidised bed spray granulation processes have been studied and operated for decades, no generic models exist, which allow for accurate prediction and understanding of the influences of process design and operating conditions on powder characteristics. A lot of research has been focused on modelling and understanding of the separate mechanisms (e.g. *wetting:* Simons and Fairbrother 2000, Litster et al., 2001; *growth:* Smith and Nienow, 1983; Bińet al., 1985; Ennis et al., 1991; Lian et al., 1998; *breakage:* Bemrose and Bridgwater, 1987; Thornton et al., 1999; *consolidation:* Becher and Schlüder, 1998). To model the agglomeration process in fluid-bed granulators these mechanisms have been integrated into population balance models (Waldie et al., 1987; Hounslow, 1998; Cryer, 1999; Lee and Matsoukas, 2000). These population balances have been used successfully to provide insight into the mechanisms by which particles grow. Using growth kernels representing distinct physical growth mechanisms, very good

fits of population balance models on experimental data have been obtained by Boerefijn et al. (2001), using only one adjustable growth rate constant extracted from experimental data. However, the growth rate constants that were obtained in their work appeared to be highly sensitive to the powder properties, such as shape and porosity. Besides the powder characteristics all parameters regarding essential hydrodynamic processes such as liquid-solid contacting, particle mixing and segregation are also lumped into the single growth rate constant. Therefore, though population balance models may be an appropriate tool to gain more insight into experimental observations, such models (on their own) can not be applied for the a-priori design and scale-up of fluid bed granulation processes.

In most research on fluid bed spray granulation processes, the importance of fluidised bed hydrodynamics and liquid-solid contacting in the wetting zone is stressed. Several often posed questions regarding the most essential hydrodynamic aspects of process design and operation are:

- How far does the atomised liquid spray penetrate the fluidised bed?
- What is the powder composition in the wetting zone?
- How often do particles pass though the wetting zone?
- How much liquid do they pick up in the wetting zone?
- What is the impact speed in particle-particle and particle-droplet encounters?
- What is the particle exchange rate between the wetting zone and the bulk?
- In which part(s) of the bed do breakage and consolidation take place?

Fundamental hydrodynamic models capable of answering these questions have, to the author's knowledge, not been developed so far. This can on one hand be attributed to the complex hydrodynamics of dense gas-fluidised beds. Hydrodynamic models capable of giving an accurate description of bed dynamics and segregation phenomena are still in an early stage of development (Hoomans et al., 2000b; Goldschmidt et al., 2001b). On the other hand, knowledge about the efficiency and dynamics of liquid-solid contacting and granule formation is also limited. Further complications are caused by the large differences in temporal and spatial scales involved in the process. A typical batch granulation run lasts more than 10 minutes, particle circulation times in the bed are of the order of seconds (McCormack et al., 2001) just as coagulation times for melted liquid binders, whereas particle-particle collision, particle-droplet coalescence and agglomeration are quasi-instantaneous processes, compared to the other relevant time scales.

As for the hydrodynamic modelling of most multi-phase flows, essentially two different types of fundamental hydrodynamic models can be developed for fluidised bed spray

granulation processes. Discrete element methods can be applied to compute the position and motion of every individual particle and droplet, whereby particle collisions and droplet-particle encounters can be taken into account in great detail. However, the number of discrete elements that these models can handle (typically less than 10^6) is orders of magnitude smaller than that encountered in most (industrial) granulation processes. Therefore, continuum models in which all phases are considered as interpenetrating continua, constitute a more appropriate choice for hydrodynamic modelling of engineering scale systems. These models require constitutive relations to take particle-particle collisions, droplet-particle coalescence and granulation kinetics into account. However, little is known about the efficiencies of particle wetting and granule formation, which are required to describe the granulation process within a continuum framework. In this respect more detailed discrete element models can be applied as a valuable research tool to gain more insight and test statistical theories to describe these processes.

In this chapter a two-dimensional discrete element spray granulation model is presented. Simulations on a batch spray granulation process, using a molten liquid binder and 50.000 primary particles, have been performed to demonstrate how process conditions change throughout the granulation process and how hydrodynamic operation conditions may have a severe influence on powder (product) characteristics. The mechanism by which granules grow and the observed influences of process conditions on powder characteristics will be discussed. In the next chapter an outlook on how to proceed towards engineering scale continuum modelling of spray granulation will be presented.

2. Discrete element spray granulation model

The discrete element spray granulation model is based on the hard-sphere discrete particle model for gas-fluidised beds, developed by Hoomans (Hoomans et al., 1996; Hoomans, 2000). The model computes the motion of every individual particle and droplet, whereby the gas phase is considered as a continuum. The gas flow field at sub-particle level is not resolved and empirical relations by Ergun (1952) and Wen and Yu (1966) are applied to describe gas-particle and gas-droplet drag. Particle-particle collisions, particle-droplet coalescence and agglomeration are directly taken into account. The model essentially processes a sequence of encounters in which all particles and droplets are moved under the influence of external forces until the next encounter occurs. For this reason hard sphere models are also referred to as event driven models.

A detailed description of the hard-sphere discrete particle model for gas-fluidised beds has been given in chapter 3. The focus in this chapter will be on the extensions that are needed to describe fluidised bed spray granulation processes. Most necessary modifications regard the addition of droplets, coalescence of particles and droplets, agglomeration and coagulation of the melted liquid binder. These modifications will be discussed in detail in the next paragraphs.

The discrete element spray granulation model basically distinguishes between three different types of entities: dry particles, wetted particles and droplets. All three are assumed to be spherical and encounters are detected as soon as contact occurs at a point on the line joining the centres of two entities. Particle-particle encounters are described by hard sphere collision laws (see chapter 3 or Hoomans 2000a). The same hard-sphere collision model is also applied to describe droplet-droplet encounters, which are assumed to be repulsive for atomised liquid droplets with a typically radius of about 50 μm, whereby the mutual velocity differences are not too large. When a droplet and a dry or wet particle encounter they are supposed to coalesce. A detailed description of the coalescence model is presented in section 2.2. When wetted particles collide with another particle they might either agglomerate or rebound. Which of the two occurs depends on the odds that the particles hit at a wetted spot. The details of the applied granulation model are discussed in section 2.3. Besides their mutual interactions particles and droplets might also hit into the system walls or internals. An overview of all possible interactions and the way they are handled by the discrete element spray granulation model is given in table 7.1.

Table 7.1. Handling of different types of collision.

	Dry particle	**Wetted particle**	**Droplet**	**Wall or internal**
Dry particle	rebound	rebound or agglomeration	coalescence	rebound
Wetted particle	rebound or agglomeration	rebound or agglomeration	coalescence	rebound
Droplet	coalescence	coalescence	rebound	removal of droplet

2.1. Addition of droplets

A striking difference between simulation of gas-fluidised beds and spray granulation is the fact that in most fluidised beds simulations the number of particles is constant, whereas in spray granulation processes new droplets are continuously introduced, followed by the removal of droplets and particles from the system due to coalescence and agglomeration. To simulate a single phase spray nozzle one or more cells of the Cartesian grid applied to calculate the gas phase flow field can be appointed as liquid injection points. New droplets are introduced at the bottom of these cells at regular intervals to maintain a specified liquid mass flow rate. All droplets are given the same initial axial velocity in the downward direction, whereas the radial velocity is imposed according to a Gaussian distribution. The standard deviation of this Gaussian distribution can be varied to modify the width of the spray cone. Further all droplets are randomly distributed over the bottom of the injection cells, whereby a log-normal droplet size distribution is applied. Special care is paid to the droplet placement algorithm to prevent droplet overlaps, which can not be handled by hard-sphere discrete element models.

2.2. Droplet-particle coalescence

When a droplet and a particle encounter the model assumes that coalescence occurs under all circumstances, since droplets hit the particles at the top of the bed at relatively high speed. Eventual break-up of the droplets in such impacts is ignored. More complex descriptions of coalescence and droplet break-up can readily be taken into account, however in this work, that should be regarded as a proof of concept of a new type of hydrodynamic model, it was chosen to stick to a simple description of droplet-particle interaction. Upon droplet-particle coalescence a liquid layer is formed on the surface of the particle and the original particle and droplet continue together as one wetted particle. Within the model the droplet is removed from the simulation and its mass, volume and impulse are added to the particle. If the original particle was a dry particle its identity is changed to that of a wetted particle and the particle is repositioned at the joint mass centre of the droplet and the original particle. This coalescence process is demonstrated in figure 7.1, whereas in formulas it can be described by:

mass conservation: $$m' = m_1 + m_2 \tag{7.1}$$

volume conservation: $$V' = V_1 + V_2 \tag{7.2}$$

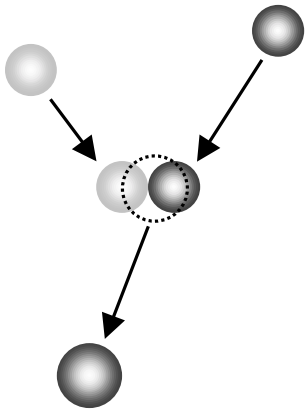

Figure 7.1. Repositioning of particles after coalescence or agglomeration.

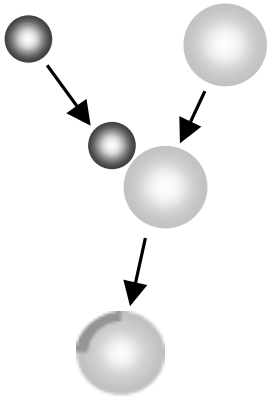

Figure 7.2. Coalescence of a droplet and a particle.

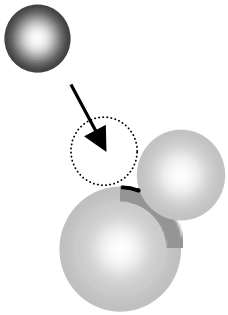

Figure 7.3. Masking of wetted surface for next agglomeration.

momentum conservation:
$$\bar{v}' = \frac{m_1\bar{v}_1 + m_2\bar{v}_2}{m_1 + m_2} \tag{7.3}$$

repositioning of the particle:
$$\bar{r}' = \frac{m_1\bar{r}_1 + m_2\bar{r}_2}{m_1 + m_2} \tag{7.4}$$

In these equations the subscripts 1 and 2 refer to the original particle and droplet and the prime refers to the newly formed wetted particle. Mostly, the amount of liquid supplied by one droplet is not sufficient to cover the whole particle surface and the particle is only partly covered with liquid as shown in figure 7.2. Attinger et al. (2000) performed some pioneering experimental work on the spreading of a highly viscous coagulating liquid fluid, however a model to describe this spreading is not yet available. Therefore it is assumed that a liquid layer of a fixed minimum thickness (l_{min}) forms instantaneously when a droplet and a particle coalesce. This minimum layer thickness will, just as spreading of the liquid, depend upon the viscosity of the liquid, the heat capacity and conductivity of the liquid and the particle, the surface structure of the particle and many other physical properties of binder and particle. A reasonable estimate can however be obtained from SEM photographs of granules obtained from the process of interest.

The total volume of the liquid layer on the newly formed wetted particle is composed of the volume of the amount of melted binder that was already present on the original particle (V_{layer}) and the amount of volume added by the droplet (V_{drop}). The fraction of the

surface of the newly formed particle that is covered by liquid (η') can then be calculated from:

$$\eta' = \frac{6}{\pi} \frac{V_{layer} + V_{drop}}{(d'_p)^3 - (d'_p - 2l_{min})^3} \tag{7.5}$$

When the spread factor η' turns out to be bigger than one the particle is fully covered with liquid, and η' is set equal to one. In this case the liquid layer thickness is no longer equal to the minimum layer thickness l_{min}, but has been calculated according to:

$$2l'_p = d'_p - \sqrt[3]{(d'_p)^3 - \frac{6}{\pi}(V_{layer} + V_{drop})} \tag{7.6}$$

2.3. Agglomeration

When a wetted particle encounters another particle these two particles either agglomerate or rebound. Which of the two processes occurs depends on a combination of many physical properties of the binder liquid, the particle structure and the impact dynamics. Some parameters that will influence the encounter are the viscosity of the binder liquid, the degree of coagulation of the liquid layer, the thickness of the liquid layer, the impact velocity and the impact angle. Again, a detailed model that takes into account all these parameters is not available, although Ennis et al. (1991) give a criterion for rebound/stick as a function of viscosity and particle velocity. A necessary condition that needs to be fulfilled for agglomeration anyhow, is given by the fact that some liquid has to be present at the point of contact, otherwise the particles will simply collide. The odds that the two particles hit each other on a wet spot can be defined in terms of the liquid spreading factors of the involved particles by:

$$P_{aggl} = 1 - (1 - \eta_1)(1 - \eta_2) \tag{7.7}$$

When a wetted particle and another particle encounter the model calculates this chance and compares it to a randomly generated number between 0 and 1. In case P_{aggl} is bigger than the random number the particles are assumed to agglomerate. As in the case of particle-droplet coalescence both particles continue together as a single particle and the agglomeration process is described by equations 7.1–7.4, where after the smallest particle is removed from the simulation.

Unlike droplet-particle coalescence the amount of wetted surface decreases in the case of agglomeration. Through capillary forces the liquid binder is contracted in a liquid bridge between the particles. Also some of the wetted surface can not be reached anymore by other particles because the newly coalesced particle is in the way, as shown in figure 7.3. The decrease of the wetted surface available for possible next agglomeration is in the spray granulation model estimated by:

$$\eta' = \frac{\pi(\eta_1 d_1^2 + \eta_2 d_2^2) - \frac{\pi}{4} d_{small}^2}{\pi (d')^2} \tag{7.8}$$

which shows that the total wet surface that was available before agglomeration is decreased by the projected area of the smaller particle on the bigger particle. The thickness of the liquid layer on the newly formed particle is subsequently calculated from:

$$l' = \frac{V_{layer,1} \cdot l_1 + V_{layer,2} \cdot l_2}{V_{layer,1} + V_{layer,2}} \tag{7.9}$$

2.4. Coagulation of the binder

The melted liquid binder applied in this work is injected at a temperature just above its melting point, whereas the temperature of the fluidising gas is below the melting point of the binder. Therefore the liquid will coagulate after a (short) while, either as a droplet, as a liquid layer on the outside of a particle or as a solid bridge between two or more particles within a granulate. The total energy to be removed per unit mass (ΔH) to cool the liquid to its melting point plus the heat of fusion, has to be transferred from the surface of the droplet to the gas-phase or the particle with which it coalesces. In the current model it is assumed that the main resistance to heat transfer is located outside the droplet in the gas phase, so the average heat transfer coefficient $<\alpha>$ can be determined from the Ranz-Marshall correlation (Ranz and Marshall, 1952):

$$< Nu >= \frac{<\alpha> d_p}{\lambda_g} = 2.0 + 0.6\,\mathrm{Re}^{1/2}\,\mathrm{Pr}^{1/3} \tag{7.10}$$

where:

$$\mathrm{Re} = \frac{\rho_g \bar{v}_p d_p}{\mu_g} \qquad 1 < \mathrm{Re} < 7\text{1}0^{\,4} \tag{7.11}$$

$$\mathrm{Pr} = \frac{\mu_g C_p}{\lambda_g} \qquad 0.6 < \mathrm{Pr} < 400 \tag{7.12}$$

Then the heat flux Φ_h between the droplet at temperature T_d and the fluidising gas with temperature T_g can be estimated by:

$$\Phi_h = <\alpha> \pi d_p^2 (T_d - T_g) \tag{7.13}$$

Applying these equations the coagulation time for every droplet is determined at the time of injection, according to:

$$t_{coag} = \frac{\Delta H \cdot m_d}{\Phi_h} \tag{7.14}$$

Hereby velocity of the fluidising gas is inserted in the calculation of the Reynolds number, because the time a droplet spends in the high velocity jet is relatively short compared to the coagulation time, for most granulation processes. Since a heat balance for the gas phase is not included in the model a constant gas phase temperature is assumed throughout the bed. Furthermore the particle temperature is set equal to the melting temperature in the calculation of the heat flux, because it is assumed that the droplet cools down to this temperature relatively quickly, whereas most heat transfer is required to remove the heat of fusion from the particle.

From the moment of injection the coagulation time is continuously counting down. When t_{coag} reaches zero, the droplet (or liquid layer) has fully coagulated and the droplet (or particle) is treated as a dry particle ($\eta = 0, l = 0$). When a droplet and a wetted particle coalesce or when two particles agglomerate, the coagulation time of the newly formed particle is set to the liquid volume weighted average coagulation time. In the case of granulation (e.g.) the new coagulation time is obtained by:

$$t'_{coag} = \frac{V_{layer,1} \cdot t_{coag,1} + V_{layer,2} \cdot t_{coag,2}}{V_{layer,1} + V_{layer,2}} \tag{7.15}$$

2.5. Encapsulation of gas and binder inside granules

In most granulation processes the porosity and liquid composition of the granules are important powder characteristics, which have to be controlled within specified limits. During the formation of agglomerates binder and gas are encapsulated between the particles. Thus, the total volume of a granule is composed of the solids volume of the primary particles (V_{prim}), the volume of the pores (V_{pore}) and the volume of binder in the layer on the exterior surface of the particle. The pore volume is either filled by encapsulated binder (V_{pore}^{binder}) or gas (V_{pore}^{gas}), whereas the layer volume is composed of melted (V_{layer}) and solidified binder.

From a modelling perspective little is known about the encapsulation of gas and liquid binder inside porous granules, though detailed discrete element or Monte Carlo methods in combination with interface tracking methods may be able to produce granules from which granule composition and porosity can be calculated. For accurate prediction of bed dynamics and segregation patterns in fluidised bed spray granulation processes, the particle composition is however of importance, since the encapsulation of air significantly reduces the density of agglomerates. Therefore a simple model to account for encapsulation of gas and binder inside granules is incorporated in the discrete element spray granulation model. This model is based upon the following approximations:

1. for pores to be formed a granule should contain at least four primary particles (see figure 7.4),
2. every particle that agglomerates with a granule containing at least three primary particles creates extra pore volume,
3. the minimum porosity of an agglomerate of infinite size is 0.36 (=ε_{rcp}), the porosity of a randomly close packed system of mono disperse spheres.

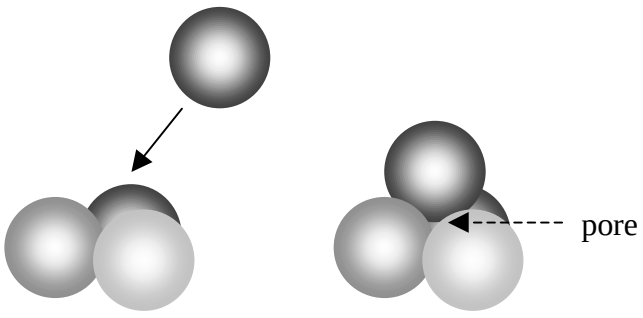

Figure 7.4. Formation of pores by agglomeration.

These assumptions lead to the following estimate of the total pore volume for a granule containing n_p (> 3) primary particles:

$$V_{pore} = \frac{\varepsilon_{rcp}}{1-\varepsilon_{rcp}} \frac{n_p - 3}{n_p} V_{prim} \tag{7.16}$$

The volume of encapsulated gas inside the granule is subsequently calculated from:

$$V_{pore}^{gas} = V_{pore} - V_{pore}^{binder} \tag{7.17}$$

where the amount of binder in the pores is obtained by subtraction of the layer volume from the total amount of binder present in the granule.

3. Numerical solution

The numerical solution strategy applied by the discrete element spray granulation model to solve the sequence of encounters follows the lines of Hoomans (2000) and will not be discussed in detail here. To solve the Navier-Stokes equations for the gas phase a finite differencing technique, employing a staggered grid to improve numerical stability, is used. For calculation of the convective mass and momentum fluxes, the second order accurate Barton method (Centrella and Wilson, 1984; Hawley, 1984) is applied to reduce numerical diffusion. Further the model applies full two-ways coupling for momentum transfer between gas and suspended particles.

3.1. Solving possible overlaps

A weak spot of the hard-sphere approach applied by the discrete particle spray granulation model is that it can not handle overlap of particles. As soon as overlap is detected the simulation terminates. Therefore special care has to be taken when particles grow due to coalescence or agglomeration, to prevent overlaps after repositioning of the newly formed particle. In figure 7.5a it is demonstrated how, because of the increase in size and repositioning of the new particle to the centre of mass of the original entities, overlap with other particles or droplets may occur. Figure 7.5b illustrates the repositioning strategy that has been implemented to overcome this weakness of the model. If positioning of the new particle at the centre of mass is not successful, a second and eventual third attempt will be made to position the new particle closer to the position

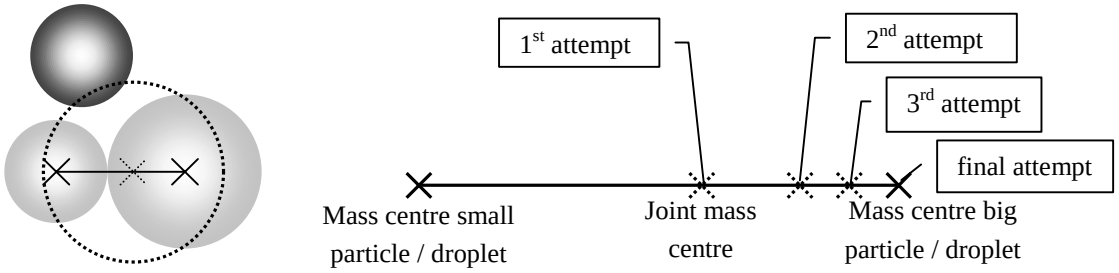

a. Overlap due to growth and repositioning. **b.** Repositioning sequence.

Figure 7.5. Solving overlaps due to coalescence and agglomeration.

of the biggest particle/droplet involved in the encounter. If necessary, a final attempt will be made to reposition the particle at the position of the biggest particle. If overlap still occurs at that position growth of the particle is postponed. The new particle gets the new mass, momentum, etc. as described in section 2, but it is placed at the position of the biggest particle and keeps the volume of that particle. The volume of the smallest particle and the eventual additional pore volume generated by agglomeration are stored in a so called ghost particle. The ghost particle's volume is added to the new particle as soon as sufficient space is available around that particle. The amount of ghost particles is monitored constantly to make sure that delaying of volume addition is an exceptional event, since excessive postponement of volume addition will result in a reduction of collision frequency and growth efficiency. In the simulations presented in this work the average number of ghost particles present in the simulation at a time varied between 0.02 and 0.06.

3.2. Modification of the neighbour lists

A detailed discussion on the optimisation of hard-sphere discrete element codes is presented by Hoomans (2000a). A key step in the optimisation of the hard-sphere strategy is the minimisation of the number of particles/droplets that have to be scanned for possible encounters by definition of a neighbour list. A suitable choice of the size of the neighbour list it is critical for the efficiency of the simulation and depends on the type of system that is simulated. If the neighbour list is chosen too small it is possible that an encounter is not detected and overlap can occur. On the other hand if the neighbour list is chosen to be rather large all collisions will be detected, but this will go at the cost of computational speed.

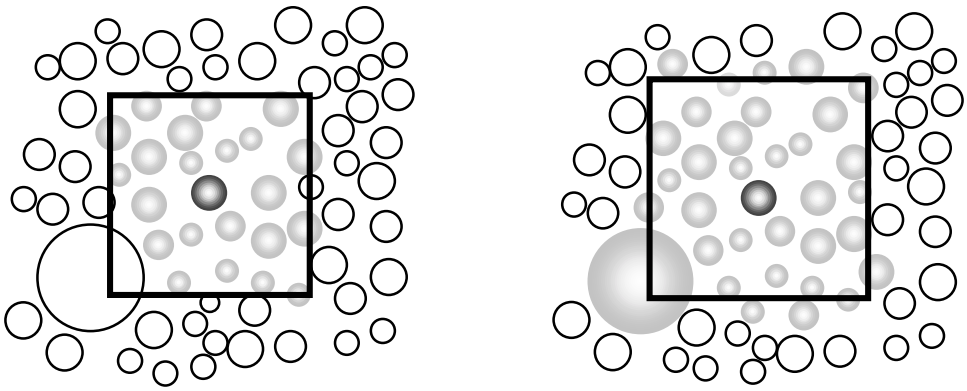

a. Mass centre based neighbour lists for mono-disperse systems.

b. Neighbour list for systems with large size distributions based on particle perimeters.

Figure 7.6. The neighbour list principle.

For mono-disperse systems all particles whose mass centres are found within a square of size D_{nblist} with particle *a* located in the centre, are stored in the neighbour list of particle *a* (see figure 7.6a). The size of the neighbour list is related to the diameter of the particle. For a bubbling bed a relatively small neighbour list ($D_{nblist} = 3 \cdot d_{p,a}$) can be used, whereas a larger perimeter of the neighbour list has to be used in more dilute systems where particle velocities are larger as well. However, when the size of the square is only related to the diameter of particle *a* and the selection of particles is based on the position of their centre of mass, the risk exists that large particles are not placed in the neighbour lists of smaller particles, while they are close enough to be a possible collision partner. Therefore the neighbour list principle applied in the discrete element spray granulation model is based on the particle perimeters in stead of the centres of mass. The neighbour list of particle *a* includes all particles *i* around particle *a* for which one of the following conditions holds (as shown in figure 7.6b):

$$2\left|x_a - x_i\right| - \left(d_{p,a} + d_{p,i}\right) \leq D_{nblist} \tag{7.18}$$

$$2\left|y_a - y_i\right| - \left(d_{p,a} + d_{p,i}\right) \leq D_{nblist} \tag{7.19}$$

When composing the neighbour lists it is further not necessary to scan all particles in the system. For each grid cell required for the solution of the gas flow field, the particles whose centres can be found in that cell are stored in a cell list. So when updating the neighbour lists, only the cell where the particle centre is found and the three nearest

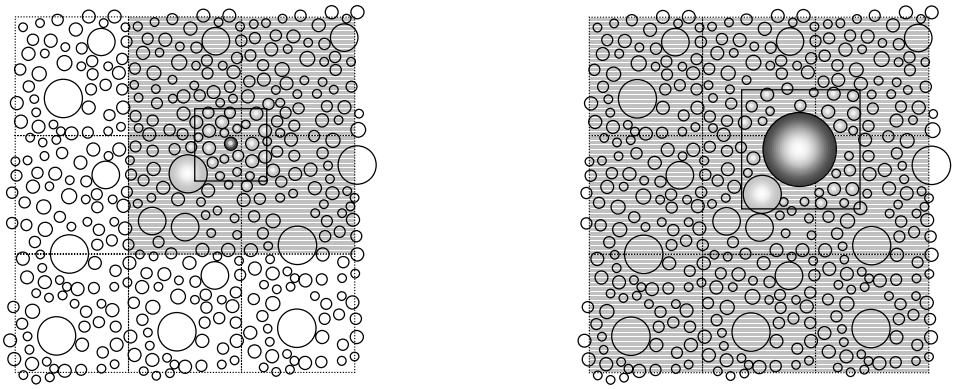

a. Area usually scanned for neighbours **b.** Area scanned for very big particles

Figure 7.7. Area scanned for possible neighbours when updating neighbour lists.

adjacent cells have to be scanned for possible neighbours, as indicated in figure 7.7a. For very big particles, (fast moving) droplets and walls some adjustments have been introduced in the discrete particle spray granulation model:

- for very big particles (d_p > ½grid cell size) all adjacent cells are scanned for neighbours (see figure 7.7b),
- if droplets are scanned in the adjacent cells they are always stored in the neighbour list of a particle irrespective of criteria 7.18 and 7.19. Vice versa all particles and droplets in the scanned adjacent cells are stored in a droplets neighbour list,
- if a scanned adjacent cell contains a wall, this wall is always stored in the neighbour list.

Applying the presented modifications, the optimised hard-sphere simulation strategy presented by Hoomans (2000a) could be applied for the fluidised bed spray granulation simulations, using a neighbour list diameter (D_{nblist}) equal to three times the diameter of the primary particles.

4. Spray granulation simulations

To study the influence of several key operating conditions on the spray granulation process, two-dimensional simulations of a small laboratory scale batch spray granulator have been performed. The initial turbulent fluidised bed shown in figure 7.8 was obtained after fluidising 50,000 primary particles for 3 seconds at the superficial gas velocity of 1.6 m/s. As the simulation starts droplets of melted binder are sprayed onto the bed from a centrally positioned single phase nozzle. The width of the spray pattern in the simula-

Table 7.2. Simulation settings for base case.

System geometry (2D):	
Granulator width	0.20 m
Granulator height	0.50 m
Number of grid cells in horizontal direction	41
Number of grid cells in vertical direction	101
Horizontal position of spray nozzle	0.10 m
Vertical position of spray nozzle	0.25 m
Width of nozzle	0.005 m
Operation conditions:	
Number of primary particles	50000
Fluidisation velocity	1.6 m/s
Droplet spray rate	$2.77 \cdot 10^{-6}$ kg/s
Droplet injection velocity	-40 m/s
Standard deviation in radial direction	0.5 m/s
Runtime	10 s
Final liquid/solid ratio	0.03
Gas phase properties:	
Freeboard pressure	101325 Pa
Gas phase temperature	313 K
Gas phase shear viscosity	$1.8 \cdot 10^{-5}$ Pa·s
Heat conductivity	$2.883 \cdot 10^{-2}$ W/(m·K)
Particle properties:	
Mean diameter of primary particles	250 µm
Standard deviation of size distribution	50 µm
Particle density	2440 kg/m^3
Particle shape factor	1
Coefficient of normal restitution	0.97
Spray properties:	
Mean droplet diameter	100 µm
Standard deviation of size distribution	50 µm
Binder density	1228.0 kg/m^3
Droplet shape factor	1
Coefficient of normal restitution	0.50
Minimum liquid layer thickness	20 µm
Binder injection temperature	353.0 K
Binder melting point	328.0 K
Heat of fusion + cooling enthalpy (353.0 - 328.0 K)	227.6 J/g

tions can be controlled by defining the standard deviation of a Gaussian velocity distribution function for the initial droplet velocity in the radial direction. In most simulations the spray pattern is relatively narrow to simulate a nozzle with a flat spray pattern. Since particle and droplet size distributions are mostly not mono-disperse, a logarithmic size distribution function is applied for primary particles and droplets. It should further be noted that in this first proof of concept particle and droplet rotation is not taken into account. An extensive overview of all simulation conditions applied in this work for the base case simulation is presented in table 7.2, the chosen properties essentially equal those of glass ballotini and PEG, for purpose of future validation.

Figure 7.8. Initial situation.

4.1. Results of base case

The evolution of the particle size distribution that results from the base case simulation described in the previous paragraph is presented in figure 7.9. To obtain this figure the particle size distribution was divided into discrete size classes compliant with a $\sqrt[4]{2}$ sieve set, which is often applied for particle size characterisation. Figure 7.10 shows the development of the number of primaries and granules during the simulation. Further the total number of agglomerations and coalescences are shown. The smooth evolution of the particle size distribution and the straightness of the lines representing the decrease of the number of primary particles and the number of agglomerations indicate that layering is the prevailed granule growth mechanism in this simulation. The straight line for the number of coalescences is a result of the constant flow of droplets into the system, where the ratio of the number of coalescences to the number of agglomerations shows that typically 1.55 droplets are needed for every agglomeration.

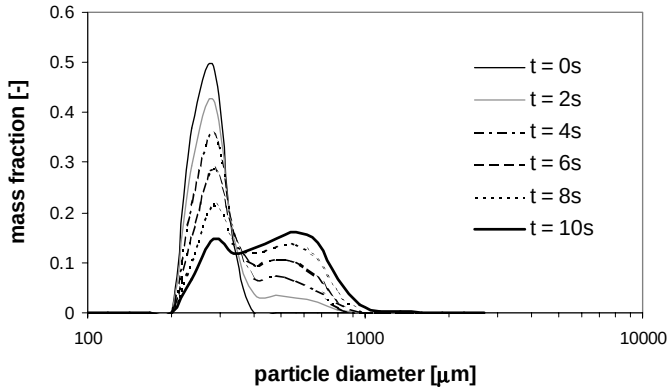

Figure 7.9. Evolution of particle size distribution during the base case simulation.

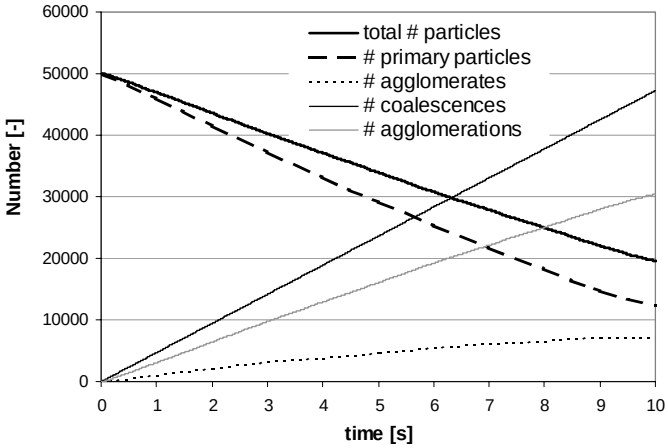

Figure 7.10. Monitoring of key numbers during the base case simulation.

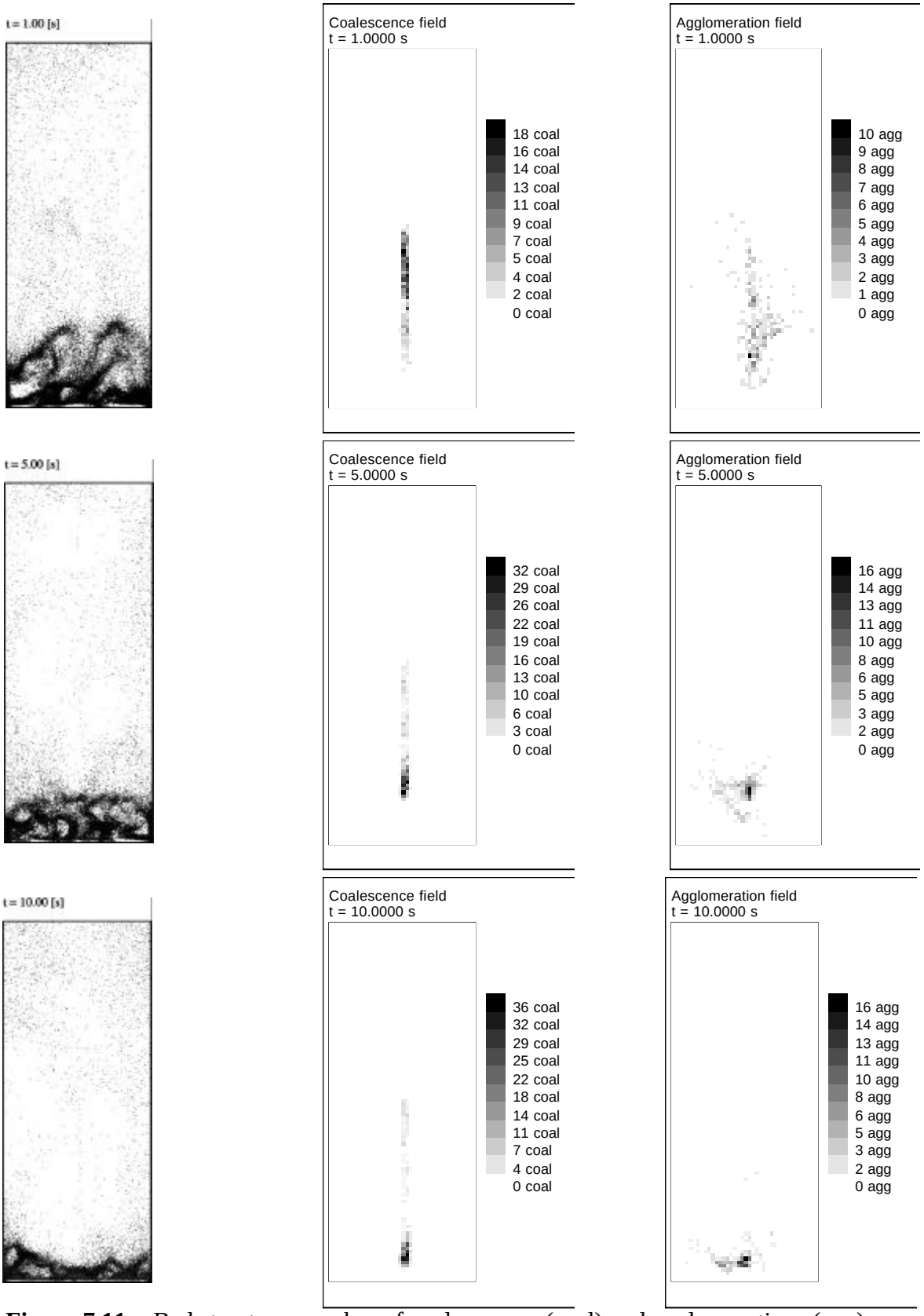

Figure 7.11. Bed structure, number of coalescences (coal) and agglomerations (agg) logged during several 0.1 second intervals for the base case simulation.

To gain insight in the fluidised bed structure and the regions where droplet-particle coalescence and agglomeration take place, figure 7.11 shows some 'snapshots' of bed structures, coalescence and agglomeration fields. The coalescence and agglomeration fields represent the number of coalescences and agglomerations for each computational cell during a 0.1 second interval just before the presented snapshots of the bed structure were taken. These snapshots show how the bed height decreases during the simulation. As a consequence of the increase of the average particle diameter, the fluidised bed dynamics shifts from typical turbulent fluidisation behaviour to the behaviour of a violently bubbling shallow gas-fluidised bed. The coalescence fields show that droplet-particle coalescence initially takes place in the freeboard, whereas as the bed quiets down and the bed height decreases the area where most coalescence takes place shifts more towards the top of the dense bed. Although the spray influences the fluidised bed dynamics (it directs particles present in the spray region back into the bed and sometimes stifles eruption of bubbles), severe penetration of the fluidised bed by droplets is not observed. As shown in figure 7.11 agglomeration exclusively takes place in the freeboard near the top of the fluidised bed during the entire process.

Figure 7.12 shows the average height of droplets and particles of several size classes during the simulation. Since droplets and granules are not present at the beginning of the simulation the corresponding curves in this figure start after 1 second. The top curve in the figure shows how the average height of droplets (diameter 100-119 micron) decreases as the simulation proceeds, reflecting the lowering of the region where coalescence takes place. The figure clearly shows that severe size segregation takes place. The average height of the smallest primary particles (200-238 micron) strongly rises near the end of

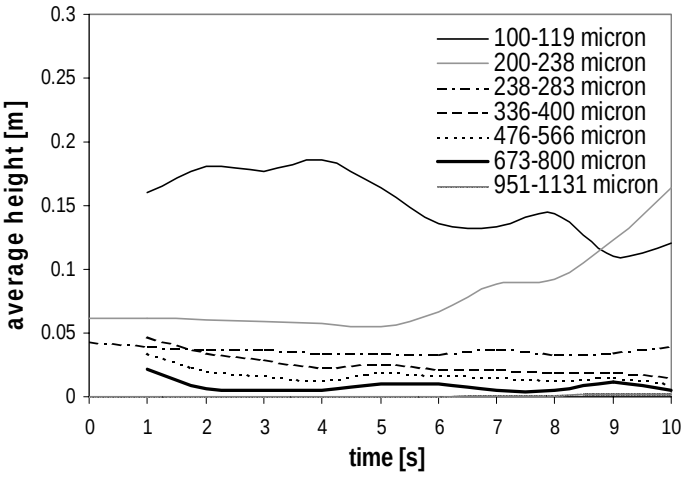

Figure 7.12. Particle size segregation and average droplet height.

the simulation. This is caused by depletion of this type of particles in the bottom of the fluidised bed, while many primary particles are still present in the freeboard above the nozzle. Small primary particles will only occasionally descend from the top of the bed in clusters, because of the relatively high fluidisation velocity. So the simulation illustrates the often encountered efficiency problem of improving the conversion of primary particles to larger granules in a (batch) granulation process, without lowering the fluidisation velocity so far that defluidisation and wet quenching may occur.

The observed segregation pattern confirms a layered growth mechanism. Besides the fact that primary particles by far have the highest number density in the spray granulation system, coalescence of droplets with primaries is favoured by the segregation pattern. Therefore most binder droplets coalesce with primary particles in the spray zone. These primary particles subsequently agglomerate with the first particle that they have a successful encounter with on a wetted spot, which causes a gradual particle growth by layering. Since particles are directed back into the bed where the encounter frequency is high compared to the coagulation time of the binder, most binder is encapsulated inside granules by agglomeration before it solidifies. In experimental systems granules will therefore deform and/or break before reaching their final composition and shape. These two effects are not taken into account in the (current) hydrodynamic model, though they will certainly influence the particle size distribution and granule composition.

The average composition of the produced granules is presented in figure 7.13. The obtained granule composition is clearly a result of the simple porosity model and the layered growth mechanism, which causes particles to pick up a small amount of liquid during their short residence in the spray zone before they agglomerate. If particle residence times in the spray zone would be longer so they would pick up several droplets

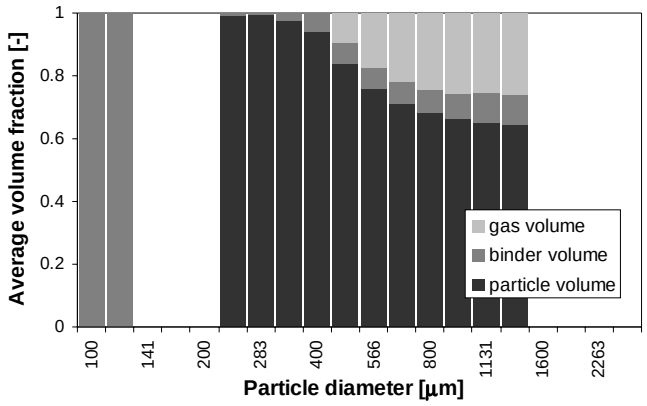

Figure 7.13. Particle composition per size class at the end of the simulation (t = 10 s.).

or particles would pick up more liquid at once, clearly the pores would be much more filled with liquid. In this proof of concept the particle composition model is mainly incorporated to reduce size driven segregation by the lower effective density of larger particles. Though such simple models may not provide accurate information on the exact particle composition, they can be very helpful to study the hydrodynamic influences on the distribution of different liquid components in systems where staged or multi-point injection is applied.

4.2. Influence of spray rate

The influence of the liquid spray rate on the powder characteristics was studied with two simulations. In the 'fast spray' simulation the spray flux was doubled compared to the 'base case', whereas in the 'slow spray' simulation the spray rate was halved. In order to retain the same final liquid/solid ratio the runtimes were respectively halved and doubled. Figure 7.14 shows the particle size distribution of the granulation product. Interestingly, a mono modal sizes distribution results from the slow spray case, whereas a bimodal distribution is obtained in the fast spray case. The figure shows that a higher conversion of the primary particles into granules is obtained at low spray rates, whereas the granules which are formed are bigger at high spray rates. Thus the modelling results are consistent with experimental results, showing that the granule size is proportional to the spray rate (Kristensen and Schaefer, 1987; Boerefijn et al, 2001). At low spray rates particles pick up less liquid while they are in the wetting zone where coalescence and agglomeration mainly take place. Consequently less agglomerations are required to cover all wetted particle area and agglomerates grow more gradually. Further the 'slow spray' simulation takes twice as long as the 'base case', so there is more opportunity for primary particles in the top of the bed to descend and participate in the granulation process.

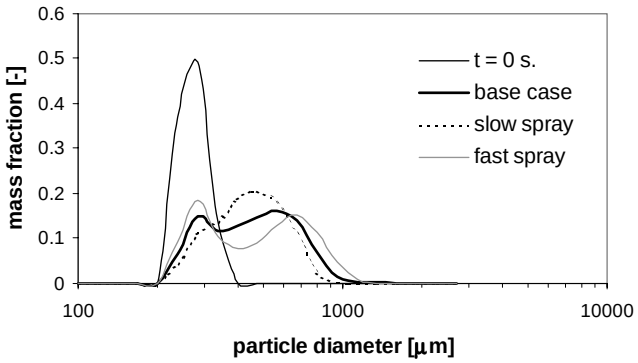

Figure 7.14. Influence of spray rate on final particle size distribution.

4.3. Influence of spray pattern

The influence of the spray pattern on the agglomeration process is examined with a 'wide spray' simulation. In this simulation the standard deviation of the initial radial droplet velocity is set to 5.0 m/s, 10 times higher than the standard deviation in the base case. Figure 7.15 shows some typical snapshots of the bed structure, the spray cone and the droplet-particle coalescence field. Just as in the base case liquid-particle contacting and agglomeration basically take place in the freeboard, just above the top of the bed. The liquid however is spread over a much bigger area, which makes that the particles pick up less liquid before they coalesce and causes a growth pattern that is quite similar to that obtained in the 'slow spray' simulation. This is shown in figure 7.16. In the 'wide spray' case the primary particles are more involved in the granulation process because elutriation is harder through the wider spray zone.

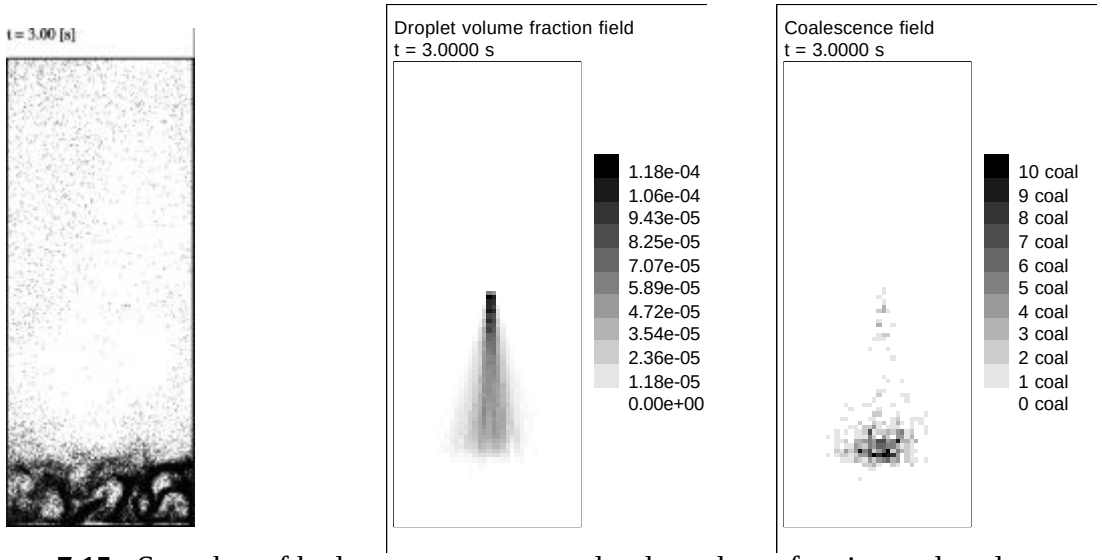

Figure 7.15. Snapshot of bed structure, average droplet volume fraction and coalescence field in the interval t = 2.9 - 3.0 s.

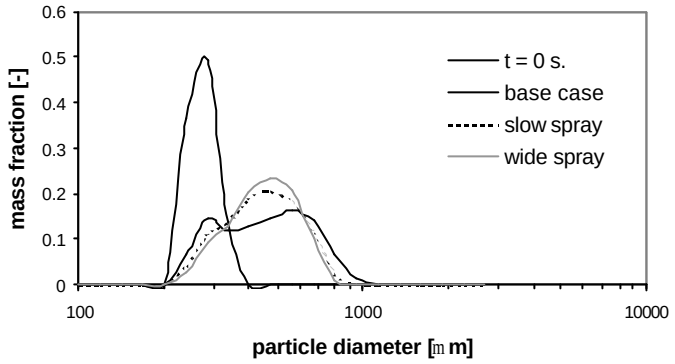

Figure 7.16. Influence of spray pattern on final particle size distribution.

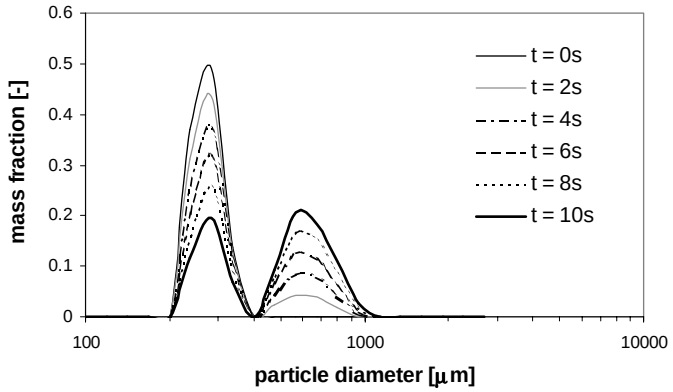

Figure 7.17. Evolution of the particle size distribution for the 'big droplet' case.

4.4. Influence of droplet size

The droplet size of the atomised binder is one of the most important process variables in fluidised bed granulation, by which the granule size can often be varied in a simple and reproductive manner. In general the granule size increases as the droplet size increases (Kristensen and Schaefer, 1987). Therefore a 'big droplet' simulation was performed in which the mean droplet diameter was set to 200 µm, twice the droplet diameter applied in the 'base case', whereby the standard deviation of the log-normal size distribution was maintained at 50 µm. The evolution of the particle size distribution obtained in this simulation is shown in figure 7.17. The final granule size is indeed bigger than for the 'base case', but the obtained growth pattern is somewhat unusual. It can be understood when realising that the droplets are now so big that the complete outer area of a primary particle will be covered with a layer of liquid upon coalescence. It will thus take a couple of agglomerations before all liquid area is covered and wet granules of intermediate size will only shortly exist.

4.5. Influence of fluidisation velocity

In a fluidised bed granulator the air distribution plate and the shape of the container influence the particle motion in the bed. Also the gas velocity has an extensive influence on the fluidised bed behaviour and is therefore expected to influence the granulation process. To study the influence of the gas velocity on the granulation process two simulations at different homogeneous fluidisation velocities were performed.

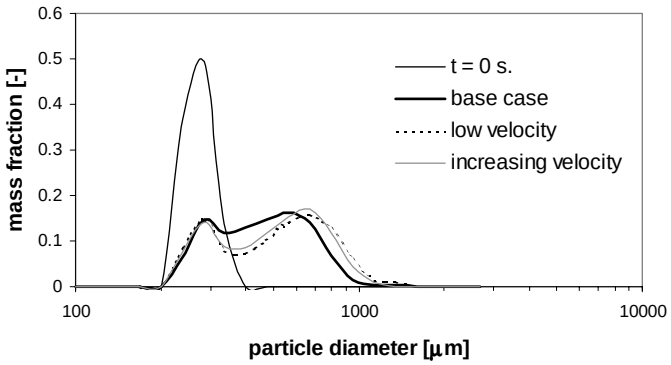

Figure 7.18. Influence of the fluidisation velocity on the final particle size distribution.

In the 'low velocity' simulation a constant fluidisation velocity of 1.0 m/s is applied (1.6 m/s in the 'base case'), whereas in the 'increasing velocity' simulation the gas velocity is linearly increased from 0.6 m/s at the beginning of the simulation to 1.6 m/s at the end. In both simulations the bed was operated in the bubbling regime during the entire granulation process. The resulting particle size distributions are shown in figure 7.18. The particle size distributions obtained in both simulations are quite similar, but they differ significantly from the 'base case'. About the same amount of primary particles seems to be converted into granules, but the size of the produced granules is bigger. This can be explained by reduced mixing of the bed at lower gas velocities, which causes the granule residence time in the wetting zone to rise and consequently bigger granules to be formed.

4.6. Influence of minimum liquid layer thickness

In the applied coalescence model the spreading of the liquid is solely determined by the minimum liquid layer thickness (l_{min}). The value of 20 µm applied in the base case was estimated from SEM photographs of granules composed of glass ballotini and melted polyethylene glycol (PEG) binder. Since the growth of granules in all performed simulations seems to be terminated by covering of the available wetted area, where after the encapsulated binder solidifies inside the granules, the growth pattern will strongly depend on the applied liquid layer thickness. This is clearly shown by the results of a 'thin layer' simulation, in which the minimum liquid layer thickness was set to 15 µm. The results presented in figure 7.19 show that more primary particles have agglomerated and bigger granules are formed when the liquid spreads in a thinner layer, but over a larger area. The explanation for this observation is the same as for the 'big droplet' simulation, though in this case the depletion of particles of intermediate size is not that extreme.

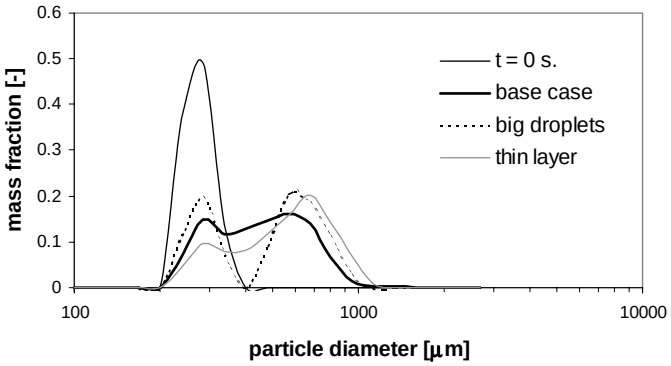

Figure 7.19. Influence of the liquid layer thickness on the final particle size distribution.

Though the presented liquid spreading model is a crude simplification of reality, the observed sensitivity to the minimum liquid layer thickness indicates the influence that parameters influencing liquid spreading, such as binder viscosity, particle structure and wettability, can have on the product composition.

Discussion and conclusions

A novel discrete element spray granulation model that captures the key features of fluidised bed hydrodynamics, liquid-solid contacting and agglomeration has been presented. Simulations of a batch granulation process containing 50.000 primary particles correctly predict the experimentally observed increase in granule size as the binder flow rate or droplet size increases. Further significant effects of the spray pattern and the fluidisation velocity are observed, which can be explained from the perspectives of liquid-solid contacting and bed mixing. Clearly the explanation of the different product characteristics from a hydrodynamic point of view can contribute to better understanding of spray granulation processes, where a mixture of apparatus design, operation conditions and physical properties of binder and primary particles determines the granular product characteristics.

The presented discrete element model contains (far too) simple closures to describe particle-droplet coalescence and agglomeration. Also the number of particles is much lower than that in systems of experimental relevance and the model is limited to a 2D Cartesian geometry which will have caused the prediction of somewhat too vigorous fluidised bed dynamics by the model. Obviously the presented model should be regarded as a proof of concept and further research is required to incorporate more detailed closure

relations that give a more realistic description of coalescence, liquid spreading, agglomerate (de)formation, breakage of agglomerates and droplets, etc. etc. Though expansion to 3D and more complex geometries is readily possible, the number of particles that can (currently) be handled by discrete element codes will limit the application of the model to small laboratory scale systems. Therefore, the model should be considered as a valuable learning tool that can be applied to describe fluidised bed dynamics and liquid-solid contacting in the wetting zone in great detail. In respect of the multi-level modelling strategy presented in chapter 1, the discrete element model can be applied as a valuable research tool to gain more insight into particle growth kernels and liquid-solid contacting efficiencies that are required to describe granulation processes in engineering scale models. Further, the model can be a very useful tool to provide more detailed contact mechanical models with typical droplet-particle and particle-particle encounter characteristics, such as the impact velocities, which are hard to obtain from experiments. However, validation of discrete element spray granulation model with dedicated experiments is required in the near future, to gain more thrust in the model predictions and indicate which improvements need to be made to the model.

Chapter 8.

General conclusions and outlook on future research

Abstract

This chapter briefly summarises the work presented in this thesis. The conclusions regarding the current 'state of the art' in hydrodynamic modelling of dense gas-fluidised beds and spray granulation processes are summarised by topic. Challenges for future research are indicated and a priority amongst them is suggested. Further an outlook on how to proceed towards engineering scale continuum modelling of fluidised bed spray granulation is presented.

1. Introduction

It has been shown in this thesis that the development of fundamental hydrodynamic models for complex multi-phase flows, such as encountered in fluidised bed spray granulation, requires a truly multi-disciplinary approach. Input from the fields of (statistical) physics, (numerical) mathematics, computer science, mechanical and chemical engineering is required to construct and validate detailed CFD models which can be applied for design and scale-up of fluid bed spray granulation processes. Since relevant time and length scales in such processes vary over several decades, a multi-level modelling approach for fundamental hydrodynamic modelling of spray granulation processes is presented in chapter 1. Similar approaches have been presented for hydrodynamic modelling of complex multi-phase flows in gas-fluidised beds (Hoomans, 2000) and gas-liquid bubble columns (Delnoij, 1999). The essence of a multi-level modelling approach is that higher level (continuum) models which are applicable at engineering scale, can be verified and further improved with more detailed (e.g. discrete element) models. So, apart from the development of physically accurate and numerically efficient models at every separate level, it is important to develop statistical theories and sampling techniques that can be applied to link the different modelling levels. As in any modelling approach, one of the most crucial steps is the validation of models at all different levels with accurate measurement data on relevant hydrodynamic phenomena that have to be captured by these models.

In respect of the presented multi-level modelling strategy, the following aspects have been treated in this thesis:

- development of a novel numerical method, dedicated to more efficient solution of two-fluid continuum models with kinetic theory closure laws (chapter 2),
- study of the effect of the coefficient of restitution on bubble dynamics in dense gas-fluidised beds, which was earlier predicted by discrete particle models, with a continuum model with kinetic theory closures (chapter 2),
- critical comparison and validation of a two-fluid continuum model and a 3D hard-sphere discrete particle model with novel experimental results (chapter 3),
- development of a novel sampling technique which enables verification of kinetic theory closures for continuum models with more detailed discrete particle models (chapter 4),
- use of discrete particle models to critically assess assumptions underlying the kinetic theory of granular flow applied in continuum models (chapter 4),

- development of a new set of statistical mechanical closure relations according to the kinetic theory of granular flow for continuum modelling of dense gas-fluidised beds containing multi-component particle mixtures (chapter 5),
- development of a new digital image analysis technique for non-invasive measurement of bed expansion and segregation dynamics in pseudo two-dimensional gas-fluidised beds (chapter 6),
- presentation of an extensive set of measurement data on bed expansion and segregation dynamics, suitable for validation of fundamental hydrodynamic models (chapter 6),
- development of a novel discrete element model for hydrodynamic modelling of fluidised bed spray granulation, which captures the key features of fluidised bed hydrodynamics, liquid-solid contacting and agglomeration (chapter 7).

In this final chapter the conclusions regarding the current 'state of the art' and challenges for hydrodynamic modelling of dense gas-fluidised beds are summarised and priorities for future fluidised bed modelling research are indicated. With regard to engineering scale hydrodynamic modelling of fluidised bed spray granulation processes, two methods for combining the discrete population balance model of Hounslow et al. (1988) and the multi-fluid continuum model presented in chapter 5 are presented. Furthermore, the applicability of the discrete element spray granulation model presented in chapter 7 and the sampling strategy presented in chapter 4 for further development of the engineering scale spray granulation models will be discussed.

2. Dense gas-fluidised bed modelling

The main objective of this research has been the development and validation of a fundamental hydrodynamic model, which accurately predicts the behaviour of particle mixtures in engineering scale dense gas-fluidised beds. Because bubble dynamics play a dominant role in particle mixing, segregation and elutriation in such gas-fluidised beds, the research presented in this thesis has mainly focused on the correctness of the predicted bubble dynamics by fundamental hydrodynamic models. In this section the main conclusions drawn from this work will be discussed topic wise.

2.1. Effect of collision parameters on dense gas-fluidised bed dynamics

In earlier work using detailed discrete particle models, Hoomans et al. (1996, 1998a) observed a strong dependence of bubble dynamics in dense gas-fluidised beds on the

particle collision parameters. Applying a two-fluid model with closure laws according to the kinetic theory of granular flow, similar results were obtained from an engineering scale continuum model, presented in chapter 2 of this thesis. As the coefficient of restitution decreases and the amount of energy dissipated in collisions increases, a strong increase in bubble intensity and consequent pressure drop fluctuations was observed. It can therefore be concluded that, in order to obtain realistic fluidised bed dynamics from fundamental hydrodynamic models, it is of prime importance to correctly take into account the effect of energy dissipation due to non-ideal particle interactions.

In chapter 3 a hard-sphere discrete particle model and a two-fluid continuum model were compared to experiments using 2.5 mm spherical glass beads for which all particle collision parameters were accurately known. In all comparisons with the experimental results the discrete particle model gave superior resemblance. The difference between both models was mainly caused by neglect of particle rotation in the kinetic theory closures applied in the two-fluid model. Energy balance analysis for the discrete particle model showed that over 80% of the total energy dissipation was caused by sliding friction. Introduction of an effective coefficient of restitution in the continuum model, incorporating the additional energy dissipation due to frictional interactions, significantly improved the agreement between both models.

A simple single parameter collision model, that can be applied in the kinetic theory of granular flow to account for the effect of rotation on the centre of mass rebound velocity, is briefly discussed in appendix 4a. A direct relationship between the single collision parameter in this model and the three measurable collision parameters e_n, μ and β_0 could not be established. Therefore information on the correlation between the translational and rotational particle velocities is required, for which, to the author's knowledge, a statistical mechanical theory is currently not available. However, discrete particle models can be applied to obtain an estimate of the collision parameter in the simple model for a specific set of measured collision parameters and bed operation conditions, as demonstrated in chapter 4.

Clearly more research into the effect of energy dissipation on particle clustering and bubble formation in (dense) gas-fluidised beds is required. The results presented in this thesis show that kinetic energy is dissipated in a cascade in which translational kinetic energy is first transformed into rotational kinetic energy upon collision, where after most energy is dissipated by loss of rotational energy in subsequent collisions. For smaller particles with lower rotational inertia and for more dilute particulate flows, friction with

the interstitial gas phase during the free flight phase of the particles between subsequent collisions will also significantly contribute to the loss of rotational energy. Therefore, further research into the kinetic energy household for smaller particles and at different operating conditions is required to gain more insight in the decay of kinetic energy, which dominates flow patterns and particle structures in suspended particulate flows.

The strong influence of particle collision parameters on fluidised bed dynamics further implies that critical validation of fundamental hydrodynamic models is only possible with experiments for which all collision parameters are accurately known. Despite the fact the a number of research groups are capable of measuring particle collision parameters (Foerster et al., 1994; Bernasconi et al., 1997; Labous et al., 1997; Kharaz et al., 1999) the collision parameters are unfortunately scarcely available in fluidisation studies reported in literature. Therefore, an extensive series of experiments with mono-disperse and binary Geldart D-type particles, for which all collision parameters were accurately known, has been carried out in a laboratory scale pseudo two-dimensional gas-fluidised bed with well-defiend inflow conditions (see chapter 6). Unfortunately, accurate measurement of particle collision parameters for industrially more interesting Geldart A and B-type particles is not (yet) possible. However, since the intensity of pressure drop fluctuations in the bed seems strongly correlated to the amount of energy dissipated in particle-particle interactions, pressure drop fluctuations obtained from a fluidised bed with well known geometry at well controlled flow conditions may be applicable to estimate the particle collisions parameters for this type of particles.

2.2. The mechanical energy balance

In chapter 3 the mechanical energy balances for a hard-sphere discrete particle model and a two-fluid continuum model with kinetic theory closures have been presented. Mechanical energy balance analysis has proven to be a sensitive tool to study the effects of particle-particle, particle-wall and gas-particle interactions on fluidised bed dynamics. The mechanical energy balance combines the total energy of the suspended particulate phase with the energy supplying forces and the energy dissipating mechanisms that dominate gas-fluidised bed dynamics. Therefore, the mechanical energy balance deserves more attention in granular flow modelling in general and in fluidisation research in particular. The mechanical energy balance may play an important role in the continuing search for more insight in flow regime transition and development of scale-up rules for gas-fluidised beds. In this respect, the influence of energy dissipation due to non-ideal

particle collisions on flow patterns and dynamics has only recently been recognised, thanks to the development of fundamental hydrodynamic models.

2.3. Validation of fundamental hydrodynamic models

One of the most crucial steps in the development of fundamental hydrodynamic models is the validation of these models using accurate experimental data on the relevant phenomena to be captured by these models. For dense gas-fluidised beds it is of great importance that bubble patterns and dynamics are accurately predicted, since bubbles play a dominant role in particle mixing, segregation and elutriation. To make sure that the measurement method itself does not influence the measurement results, intrusive techniques should be abandoned as much as possible and non-intrusive techniques such as radiation absorption methods, electrical capacitance methods and image analysis methods should receive more attention. To capture bubble shapes and dynamics the applied measurement technique should (preferentially) cover the whole bed with sufficient spatial (< 1 cm) and temporal (> 10 Hz) resolution. Further, for the purpose of validation of fundamental hydrodynamic models, relevant phenomena such as segregation should occur on a time scale not longer than 1 minute, the bed geometry and all particle characteristics (including particle collision parameters!) should be well defined and the operating conditions should be well controlled.

To overcome the lack of accurate experimental data with particles for which all particle collision parameters were accurately known, the experiments with 1.5 mm and 2.5 mm spherical glass beads presented in chapter 6 were carried out. For quantification of the experimental results, a whole field, non-intrusive digital image analysis technique was developed, which could accurately determine bed expansion dynamics in pseudo two-dimensional gas-fluidised beds. The full power of the technique was demonstrated by conducting experiments using binary mixtures of coloured particles, for which the local mixture concentration could be determined within 10% accuracy in the entire bed. Since the developed image analyses technique allowed for accurate determination of the bubble dynamics as well as segregation rates at the same time, the obtained measurement results can be used as a critical test case for fundamental hydrodynamic models.

In chapter 3 experimental data on bubble patterns, time-averaged particle distributions and bed expansion dynamics for a mono-disperse system were compared to simulation results obtained from a hard-sphere discrete particle model and a two-fluid model using kinetic theory closures. It was concluded that the most critical comparison between

experiments and modelling results could be made by analysis of the bed expansion dynamics. Though both models predicted the right fluidisation regime and trends in bubble sizes and bed expansion height, the simulated bed expansion dynamics differed significantly from the experimental results. Alternative gas-particle drag models produced significantly different bed dynamics, but the gap between modelling and experimental results could not be closed. Visual observation of the experiments made clear that the differences were mainly caused by the formation of densely packed regions in which no particle movement could be observed. Formation of such areas did not occur in the simulations and it was concluded in chapter 3 that long-term particle contacts and multi-particle interactions most likely caused the gap with the experimental results. Hard-sphere discrete particle models cannot account for such contacts and they are neglected in the derivation of the kinetic theory closure relations applied for the two-fluid model. A simple frictional viscosity model adapted from the field of soil mechanics could not improve the simulated bed dynamics.

2.4. Development of closure relations for continuum models

In continuum models for dense gas-fluidised beds besides the governing equations for conservation of mass, momentum and fluctuating kinetic energy, mainly two different kinds of closure relations are required:

- closures for gas-particle interaction,
- closures for particle-particle interaction.

Further an equation of state is required to describe the (temperature dependence of) gas phase density and compressibility.

2.4.1. Closures for gas-particle interaction

The phenomenon of fluidisation and bed expansion are related to drag exerted by the interstitial gas phase on the particulate phase. Though most hydrodynamic models nowadays apply the drag model based on the equations of Ergun (1952) and Wen and Yu (1966), there is no general consensus about the modelling of gas-particle drag. An overview of drag models that have been applied by different authors can be found in Enwald et al. (1996). In chapter 3 it was demonstrated that alternative gas-particle drag models by Foscolo et al. (1983) and Garside and Al-Dibouni (1977) resulted in significantly different bed dynamics but a clear decision which model was the best could not be made. Therefore, further research with more detailed hydrodynamic models (e.g. Lattice Boltzmann models) is required to study the influences of sub-grid scale particle structures and rotation on gas-particle drag in dense gas-fluidised beds. The effects of gas

phase turbulence on the particulate flow patterns could be ignored in this work, since gas phase turbulence on spatial scales larger than the particle diameter is fully dampened, because of the high particle number density. However, for hydrodynamic modelling of more dilute granular flows, such as encountered in risers and downers, gas phase turbulence will play an important role. Despite a lot of research, a generally excepted turbulence model for dispersed gas-particle flows does not exists yet and more research in this area is required. A recent overview of turbulence models for fluid-particle flows is given by Crowe (2000).

2.4.2. Closures for particle-particle interaction

Owing to the continuum representation of the particulate phase, continuum models require additional closure laws to describe the rheology of the fluidised particles. In early two-fluid models (e.g. Tsuo and Gidaspow, 1990; Kuipers et al., 1992a) the flow behaviour of the particulate phase was assumed to be Newtonian using a constant shear viscosity, estimated from experiments. Simple solids elasticity models from the theory of powder compaction were used to model the particle pressure, which prevents the particles from reaching impossibly high packing densities.

2.4.2.1. Kinetic theory of granular flow

In most recent two-fluid continuum models (e.g. Gidaspow, 1994; Balzer et al., 1995; Nieuwland et al., 1996) constitutive equations according to the kinetic theory of granular flow are incorporated. This theory describes the rheologic parameters of the fluidised particulate phase in terns of local particle concentration and (fluctuating) particle motion, owing to the transport mechanisms of free flight of particles and particle-particle collisions. The theory is basically an extension of the classical kinetic theory of dense gases (Chapman and Cowling, 1970) to particulate flows, that takes non-ideal particle-particle collisions and gas-particle drag into account. Pioneering work on the kinetic theory of granular flow was performed by Jenkins and Savage (1983) and Lun et al. (1984), whereas Ding and Gidaspow (1990) were the first to apply this theory for hydrodynamic modelling of gas-fluidised beds.

Most kinetic theory closures which are nowadays applied in two-fluid continuum models for gas-fluidised beds have been derived for smooth, rigid, nearly elastic, spherical particles. However, in many practical systems rough, highly inelastic, non-spherical particles are encountered, which makes application of the kinetic theory questionable.

Therefore, the effects of particle roughness (rotation) and coefficient of restitution on particle velocity distribution, impact velocity distribution, collision frequency and energy dissipation were investigated in chapters 3 and 4, using 3D hard-sphere discrete particle simulations. Attention was thereby paid to the isotropy of the particle velocity distribution, which is implicitly assumed in the derivation of most kinetic theory closures.

2.4.2.2. Collision model

In chapter 3 it was concluded that the single parameter collision model incorporated in the kinetic theory closure laws, which applies to smooth particles and thus only accounts for the coefficient of normal restitution, significantly underestimates the amount of energy dissipated in collisions. Since the amount of energy dissipated in collisions dominates gas bubbles behaviour formation and bed dynamics, it is of great importance to correctly take the effect of frictional energy losses due to particle rotation into account in the continuum model. Therefore, two alternative models for energy dissipation based on an effective coefficient of restitution, which are applicable within the current kinetic theory framework, were introduced in chapter 3 and appendix 4A. Both models show significant improvement of the modelling results. However, further research on the effect of frictional energy losses in (kinetic theory) closures for continuum models is still required, to generate more insight on the effect of particle rotation on (dense) granular flows.

Another limitation concerning the way in which non-ideal particle collisions are accounted for in the current kinetic theory, is introduced by limitations of the mathematical derivation of the closures according to the Chapman-Enskog solution procedure (see Chapman and Cowling, 1970). As discussed in chapter 5, it has to be assumed at several points in this procedure that particle collisions are only slightly inelastic. However, since most particles encountered in industrial applications demonstrate highly inelastic behaviour, there is a great need for the development of new solution strategies for the Boltzmann integral-differential equation, which are also valid for particles with a higher degree of inelasticity. Chou and Richman (1998) and Sela and Goldhirsch (1998) made some interesting contributions in this area, which certainly deserve consideration for the development of new closure laws for fluidised beds in the near future.

2.4.2.3. Effect of long-term and multi-particle contact

In chapter 3 it was concluded that the main difference between experiments and modelling results was most likely caused by the neglect of long term contacts and multi-particle interactions. Incorporation of a simple frictional viscosity model from the field of soil mechanics recommended by Laux (1998), could not improve the simulated bed dynamics. Recently Zhang and Rauenzahn (1997, 2000) employed a novel ensemble averaging technique developed by Zhang and Prosperetti (1994, 1997) to examine the effects of finite particle interaction time and multi-particle contacts in dense granular systems. Their results showed good agreement with the results of the kinetic theory of granular flow at low particle concentrations, while at volume fractions approaching random loose packing a transition in rheologic behaviour occurred. Since this visco-elastic model seems to describe the behaviour that was observed in the experiments very well, it seems worthwhile to implement it into 'next generation' continuum models for dense and slow granular flows.

2.4.2.4. Effect of anisotropy and structure formation

The results of sampling of the particle velocity distribution function from 3D hard-sphere discrete particle simulations of dense gas-fluidised beds with smooth, elastic particles showed excellent agreement with the isotropic Maxwellian particle distribution function assumed in the derivation of the kinetic theory of granular flow. For rough, inelastic particles on the contrary, an anisotropic Maxwellian particle velocity distribution was observed. This anisotropy became more pronounced when the degree of inelasticity of the particles increased. It was concluded that the formation of dense particle structures disturbed spatial homogeneity. This resulted in anisotropic flow behaviour because all impact angles in dense particle clusters were not of equal likelihood, which caused unequal dampening of velocity fluctuations in different directions. This kind of anisotropy is therefore revered to as collisional anisotropy.

Simonin and co-workers (Simonin 1991; He and Simonin 1993; Simonin et al. 1995; Fevrier and Simonin 1998) have also studied anisotropic flow behaviour in dilute granular flows. They observed anisotropy of the particle fluctuating particle motion for dilute particle suspensions in homogeneous turbulent gas shear flows and concluded that anisotropy was introduced by the drag force exerted by the gas phase. The anisotropy of the particle stress tensors was found to increase with the production of fluctuating motion due to the mean shear. A continuum modelling approach for turbulent gas-solid flows

was presented and the results were compared to the statistics of particles tracked in turbulent flows generated by large eddy simulation (LES). Their model gave a satisfactory description of the mechanisms leading to the anisotropy of the particle fluctuating motion. The accuracy of the model predictions was directly related to the modelling of the fluid-particle velocity correlation, which could be calibrated on basis of discrete particle simulations. Further it was noticed that the inter-particle collision influence leads to a return to isotropy at higher particle densities, where gas phase turbulence has a negligible effect on the particulate motion. In conclusion the studies by Simonin and co-workers have shown the need for modification of the kinetic theory of granular flow in order to take into account the gas phase influence for systems of moderate and low particle density. However in their work anisotropy introduced by clustering of inelastic particles at high particle densities has never been identified.

Increasingly anisotropic flow behaviour at decreasing coefficients of restitution was also observed in computer simulations of homogeneous shear flows of granular media (Campbell and Gong, 1986; Walton and Braun, 1986a, 1986b; Lun and Bent 1994). It was noticed that at high solids fractions, above random close packing (~ 0.5), layering effects of particles, formation of high-density microstructures and increase in correlation of particle velocities were the major causes of abrupt changes in flow properties. Interestingly, most particles in the reported simulations were present in such high-density areas, and cluster formation dominates the hydrodynamic behaviour of dense gas-fluidised bed reactors. However, non of these effects that occur at high particle densities are included in the current kinetic theory closures applied in 'state-of-the-art' continuum models, since in the derivation of the kinetic theory it is assumed that particles are homogeneously distributed in space and the effects of structure formation are ignored. Therefore, more attention needs to be paid to the influences of structure formation and anisotropy on the rheologic behaviour of gas-fluidised particulate suspensions and the development of continuum theories that takes these effects into account. In this respect the papers by Chou and Richman (1998), Sela and Goldhirsch (1998) and Zhang and Rauenzahn (1997, 2000) should once again be mentioned, since all presented novel closure theories for granular media predict anisotropic flow behaviour.

2.4.2.5. Kinetic theory of granular flow for multi-component mixtures

To model fluidisation and segregation dynamics of particulate mixtures in engineering scale gas-fluidised beds, multi-fluid continuum models need to be developed. In Goldschmidt et al. (2001b) it was demonstrated that a multi-fluid model with existing

kinetic theory closure relations derived by Manger (1996) and Mathiesen (1997) predicts far too high segregation rates in comparison to those measured using non-intrusive digital image analysis. Despite the aforementioned limitations, kinetic theory closure models have significantly improved continuum modelling of dense gas-fluidised beds. Therefore, the derivation of a novel set of kinetic theory closure relations for multi-component particle mixtures, based on the work of Lopez de Haro et al. (1983) for multi-component gas mixtures and the work of Jenkins and Mancini (1989) for binary particle mixtures, was presented in chapter 5. The main difference between the presented kinetic theory model and the existing model derived by Manger (1996) and Mathiesen (1997) is that segregation is no longer possible in the first (equilibrium) approximation to the particle velocity distribution function, but is introduced as a higher order (non-equilibrium) effect. The new theory seems to give a more realistic physical picture for dense gas-fluidised beds in which the collision frequency is very high. It is therefore expected that the new model will predict more realistic segregation rates, though this remains to be proven.

2.4.2.6. The radial distribution function

Within the framework of the kinetic theory of granular flow, the radial distribution function, which accounts for the increase in the collision frequency due to the volume occupied by the particles themselves, plays an important role. Therefore its selection should receive thorough attention and several relations that are often applied for fluidised bed modelling are discussed in chapter 4. At this point the only simulation data available for comparison of these radial distribution functions has been obtained from molecular dynamics and Monte-Carlo simulations for hard-sphere gases. However, in discrete particle simulations of dense gas-fluidised beds it has been observed that the amount of collisions increased as the particle collisions became less elastic. Therefore a method which can be applied to sample the radial distribution function from discrete particle simulations of fluidised beds with inelastic particles, is discussed in chapter 4.

To obtain a consistent set of closure relations for multi-component mixtures within the kinetic theory of granular flow, the expressions applied for the radial distribution function and the chemical potential should result from the same equation of state. Since most researchers in the fluidisation community are apparently not familiar with the relevant thermodynamic relations between pressure, temperature, chemical potential and radial distribution function for hard-sphere fluids, an overview of the key thermodynamic relations has been presented in appendix 5A. In this appendix expressions for the radial

distribution function and the chemical potential for multi-component particle mixtures are derived, and the excellent agreement of these expressions with available simulation data is shown.

2.5. Linking of different modelling levels

Because of the intrinsically unsteady, non-homogeneous flow behaviour of suspended particulate flows, accurate experimental data to validate the closure laws in engineering scale continuum models is hard to obtain. Therefore, more detailed hydrodynamic models, such as Lattice Boltzmann models and discrete particle models, have to be regarded as a valuable research tools to verify and further develop closure relations for engineering scale continuum models. Lattice Boltzmann models allow for accurate calculation of the gas phase flow field around several hundreds or thousands of suspended particles and can be applied to calculate the corresponding frictional forces acting on those particles. Thus, they should be regarded as a valuable research tool to verify and further develop gas-particle drag relations for suspended particulate flows, such as encountered in dense gas-fluidised beds. Currently, Lattice Boltzmann models are still limited to low Reynolds number flows, but it is expected that extension to higher Reynolds numbers will soon be possible. Then, this type of models might also be of great help to shed some light on gas-particle interactions between a turbulent gas phase and the suspended particulates, which is of great interest for modelling of more dilute gas-particle flows in risers, downers and turbulent fluidised beds.

Since discrete particle models do not require additional closure relations for the rheology of the suspended particulate phase, they can be applied as a valuable research tool to verify and further develop (kinetic theory) closure laws applied by engineering scale continuum models to describe particle-particle interactions. Energy balance analysis of discrete particle and two-fluid continuum simulations presented in chapter 3, showed that the main reason for better resemblance of the discrete particle model to experimental results was neglect of particle rotation and subsequent energy dissipation by the kinetic theory closure relations applied for the continuum model. Further, a novel sampling technique to study particle velocity distributions and collision characteristics during dynamic discrete particle simulations was presented in chapter 4. In that chapter, the hard-sphere discrete particle model has been applied to verify the most important assumptions underlying the kinetic theory of granular flow. Although excellent agreement between simulation results and kinetic theory assumptions was obtained for elastic particles, a violation of these assumptions was found for inelastic particles for

which an anisotropic particle velocity distribution was obtained. Detailed analysis of the discrete particle simulations showed that spatial homogeneity is disturbed in dense particulate structures, because not all impact angles are of equal likelihood. It was also observed that the effects of anisotropy became more pronounced as the degree of inelasticity of the particles increased.

Some first attempts to improve continuum model closures with more detailed discrete particle models were presented in chapter 4. It was demonstrated how a simple single-parameter collision model, which can take the effect of energy dissipation due to particle rotation and friction into account in the kinetic theory of granular flow, can be calibrated with discrete particle simulations. Further it was shown how calibration data for a radial distribution function, applicable to correct the kinetic theory relations for the observed increase in collision frequency in dissipative granular media, can be obtained from the collision frequency observed in discrete particle simulations. Besides the expected dependency on the local particle concentration, the obtained data suggest that the radial distribution function should also depend on the local granular temperature and particle collision parameters. Whether the influences of granular temperature and particle collision parameters need to be incorporated in the radial distribution function, or that they are just observed because of the neglect of anisotropy in the applied kinetic theory relations or because of the neglect of spatial gradients by the sampling strategy, should be a subject of future research.

Altogether, it may be concluded from the work presented in this thesis that discrete element models are an excellent tool to provide information about basic particle flow characteristics such as the individual particle velocity distribution and the collision velocity distribution, which are extremely difficult (if not impossible) to obtain from experiments. Furthermore, although more detailed descriptions of particle collisions and the gas phase flow field will result in more advanced discrete particle models, the presented sampling technique (or refinements of it based on new insights) will be a helpful tool to validate and calibrate constitutive theories for application in continuum models.

2.6. Efficient numerical methods and complex geometries

One of the main disadvantages of fundamental hydrodynamic modelling is the tremendous requirement of (super) computer power. Not only for application to large scale industrial fluidised beds, but also for accurate validation of models using smaller

systems, efficient numerical methods are required to allow for sufficiently long three-dimensional simulations at a spatial resolution high enough to capture all relevant flow structures. As demonstrated in chapter 2, the development of efficient numerical solution methods is strongly coupled to the physical phenomena that dominate the flow pattern. Therefore, development of dedicated algorithms should be an implicit part of the implementation of new physical models in computer codes, to proof the new modelling concepts and allow for their validation with efficient research codes. On the other hand, it is recognised that standardisation of computational methods is a requirement for development of (commercial) multi-phase flow packages, in which case acceptable calculation times can be obtained by application of massive parallel computer power. For validation of new models, simple (well-known) geometries should be preferred, whereas extension to more complex geometries for industrial application should be left to specialised numerical research groups and vendors of commercial CFD software packages.

2.7. Incorporation of chemical reaction, heat and mass transfer

Fluidised bed reactors are often applied for their favourable heat and mass transfer characteristics. However, compared to the number of studies dealing with hydrodynamics of gas-fluidised beds, relatively few studies on reactor modelling have been performed. To simulate chemical reaction, heat and mass transfer in chemical reactors, component mass and heat balances have to be added to the presented hydrodynamic models. Interesting contributions to incorporation of heat transfer models in two-fluid continuum models have been made by amongst others Syamlal and Gidaspow (1985), Kuipers et al. (1992b) and Schmidt and Renz (1999, 2000), whereas chemical reactions have been modelled by Gidaspow et al. (1985), Samuelsberg and Hjertager (1996) and Gao et al. (1999). Recently heat transfer and chemical reaction have also been studied with discrete particle models by Kaneko et al. (1999) and Rong (2000). However, most simulations have been performed on relatively coarse grids, whereas the results of modelling attempts strongly depend on how well the gas-fluidised bed hydrodynamics is captured. Therefore, the development of efficient, reliable hydrodynamic models on which this thesis has focussed is of utmost importance for the prediction of the performance of fluidised bed reactors.

2.8. Priorities for future research

Due to the discrepancies found between the different types of hydrodynamic models and simulation results, it can be concluded that further improvement of the models is required for reliable simulation of engineering scale gas-fluidised bed processes. In this respect the following topics should receive the highest priority:

1. further development of (statistical) analysis methods which can be applied to extract useful data from detailed models within a multi-level modelling strategy,
2. correct prediction of the amount of kinetic energy dissipated due to particle roughness and long term particle interactions,
3. further investigation of the effect of collisional anisotropy and other effects of structure formation on the rheology of dense particle suspensions,
4. verification of closures for gas-particle drag with detailed simulation techniques such as Lattice Boltzmann methods,
5. validation of the predictive capacity for segregation in dense gas-fluidised beds of discrete particle models and the newly developed multi-component kinetic theory model for continuum modelling of gas-fluidised particulate flows.

3. Spray granulation modelling

In this thesis a first start has been made with the development of fundamental hydrodynamic models for fluidised bed spray granulation processes. A multi-level modelling strategy has been proposed in chapter 1 and a novel discrete particle spray granulation model was presented in chapter 7. In that chapter, it was demonstrated how explanation of different granulation product characteristics from a hydrodynamic point of view contributes to better understanding of spray granulation processes. In order to proceed towards engineering scale continuum modelling of fluid bed spray granulation processes, a lot of attention was paid to the validation, verification and development of current ‘state-of-the-art’ hydrodynamic models for dense gas-fluidised beds. A multi-fluid continuum model available from the literature was implemented, but this model predicted far too fast segregation rates. Therefore, a novel multi-fluid model was derived within the statistical mechanical framework of the kinetic theory of granular flow. The developed multi-fluid model only predicts the hydrodynamics of a multi-component fluidised bed and incorporation of fluid spray and particle growth are required to describe fluid bed spray granulation processes. Therefore, a brief outlook on how to proceed with engineering scale modelling by coupling of multi-fluid hydrodynamic models with population balance models capable to describe the particle growth process is given here.

3.1. Linking hydrodynamics and particle growth on engineering scale

With respect to granulation processes, population balances methods have successfully been applied to provide insight into the mechanisms by which particles grow (Waldie et al., 1987; Hounslow, 1998; Cryer, 1999; Lee and Matsoukas, 2000). However, most current population balance methods assume the whole bed content to be ideally mixed. Because of that, hydrodynamic influences on the particle growth mechanism, such as segregation and exchange of particles in the wetting zone and the bulk of the bed, can not be taken into account. As shown in this thesis, an increasing amount of research is focussed on the development of hydrodynamic models capable of describing segregation and particle mixing in gas-fluidised beds. However, attempts to incorporate particle growth in engineering scale continuum hydrodynamics models have to the authors knowledge not been undertaken. Therefore, two different approaches to the integration of population balance models and multi-fluid models are proposed here. Both approaches are based upon the multi-fluid model presented in chapter 5 and the discrete population balance model by Hounslow et al. (1988), which will be briefly introduced first.

3.1.1. Discrete population balance modelling

A population balance is basically a statement of continuity for particulate systems, which accounts for the mechanisms that change a particle property by kinetic expressions. An in depth treatment of population balance methods is given by Randolph and Larson (1991). An extension of the discrete population balance by Hounslow et al. (1988) in which particle motion due to the convection is taken into account is given by:

$$\frac{\partial n_n}{\partial t} + \nabla \cdot (n_n u_n) = -R_n^{agg} \tag{8.1}$$

In this equation, both the particle number density (n_n) and the net rate of change of the number of particles per unit volume in size class n due to agglomeration (R_n^{agg}) are a function of time and position in the fluidised bed spray granulator. Granule breakage is not included in equation 8.1, because a very good fit of particle size distributions measured in a fluidised bed spray granulator was obtained by Boerefijn et al. (2001) without taking breakage into account, although expressions for breakage are available (Hill and Ng, 1995; Hounslow, 1998).

The discrete population balance model divides the particle size distribution into a discrete number of NP intervals, in a geometric series such that:

$$d_{n+1} = d_n \sqrt[3]{2} \tag{8.2}$$

This definition of the discretisation interval makes that particles can only aggregate into a given size interval if one of the particles, prior to forming the aggregate, was in the size interval immediately smaller than the interval of interest. Further, should an aggregate be formed by particles both from the same interval it will always be counted in the next interval. Then, if only binary particle interactions are considered, the rate of change of a particle property ϕ which is conserved in collisions, in the n^{th} interval, is determined by four mechanisms (Hounslow et al., 1988):

Mechanism **1.** Birth in the n^{th} interval can occur only when a particle in the $(n\text{-}1)^{th}$ interval aggregates with a particle in the first to $(n\text{-}1)^{th}$ intervals. The total rate of change of particle property ϕ in the n^{th} interval by this mechanism is given by:

$$S_n^{[1]}(\phi) = n_{n-1} \sum_{p=1}^{n-2} 2^{p-n+1} K_{n-1,p} n_p (\phi_{n-1} + \phi_p) \tag{8.3}$$

The agglomeration kernel $K_{n\text{-}1,p}$ is a measure of the frequency of collisions between particles of volumes $V_{n\text{-}1}$ and V_p that are successful in producing a particle of volume V_n. It is a crucial parameter in the agglomeration model and will be discussed in more detail in the next paragraph.

Mechanism **2.** A similar process may be used for aggregates formed in the n^{th} interval by collisions between particles both in the $(n\text{-}1)^{th}$ interval. In this case a leading factor of ½ is included to avoid counting collisions twice:

$$S_n^{[2]}(\phi) = K_{n-1,n-1} n_{n-1}^2 \phi_{n-1} \tag{8.4}$$

Mechanism **3.** Death by aggregation will occur to a particle in the n^{th} interval should it collide and adhere to a particle of sufficient size for the resultant aggregate to be larger than the upper size limit of the n^{th} interval, leading to:

$$S_n^{[3]}(\phi) = -n_n \sum_{p=1}^{n-1} 2^{p-n} K_{n,p} n_p \phi_n \tag{8.5}$$

Mechanism **4.** If a particle in the n^{th} interval aggregates with a particle from that or a higher interval, a death occurs in the n^{th} interval, which is quantified as:

$$S_n^{[4]}(\phi) = -n_n \sum_{p=n}^{NP} K_{n,p} n_p \phi_n \tag{8.6}$$

The overall rate of change of a particle property ϕ for species n may be computed by collecting the terms resulting from the separate independent mechanisms:

$$S_n^{agg}(\phi) = S_n^{[1]}(\phi) + S_n^{[2]}(\phi) + S_n^{[3]}(\phi) + S_n^{[4]}(\phi) \tag{8.7}$$

Since mass and momentum are conserved in agglomerations, source terms for mass and momentum conservation equations of species n in a hydrodynamic model can readily be obtained from equation 8.7 by substitution m and $m\bar{u}$ respectively for ϕ. However, to obtain the agglomeration source term in the population balance equation for species n, it should be realised that the number of particles is halved in agglomerations. The net rate of change of the particle number density of species n due to agglomeration can then be obtained by substituting ϕ = 0.5 in both birth mechanisms and ϕ = 1 in the death mechanisms:

$$R_n^{agg} = S_n^{[1]}(½) + S_n^{[2]}(½) + S_n^{[3]}(1) + S_n^{[4]}(1) \tag{8.8}$$

With this regularly applied agglomeration source term, the population balance equations warrant the conservation of the total particle volume in the system. However, it should be noted that the population balance model presented here only holds for particles with a constant density, to also guarantee mass conservation.

3.1.2. Kinetic theory agglomeration kernel

In contrast to nucleation and growth, aggregation is a poorly understood phenomenon (Hounslow, 1998). It is usual to assume that agglomeration involves only two-body interactions and so may be described by a second order rate constant, or kernel, as it is

often known. The rate of agglomeration events per unit volume, for particles of types n and l is given by:

$$R_{n,p}^{agg} = K_{n,p}(\overline{x}_e, \overline{x}_{i,1_n}, \overline{x}_{i,2_p}, t) n_n n_p \tag{8.9}$$

where x_e and x_i are the external and internal co-ordinates commonly used in population balances, after the work of Hulbert and Katz (1964). The starting perspective of population balance modelling is that a particle can be unambiguously described by its internal co-ordinates (e.g. volume, shape, composition and even age) in combination with its co-ordinates in physical space (external co-ordinates). Little is known about the prediction of the agglomeration rate constants. In some applications it is assumed that the rate of agglomeration is independent of particle size, while in others quite complicated empirical dependencies are fitted to experimental results. Often the rate 'constant' is found to be time dependent. Mostly the granulation system is assumed to be well-mixed and dependence of the growth rate on the local hydrodynamic conditions (the external co-ordinates) is neglected. However, for spray granulation processes, where a binding liquid is locally sprayed on top of a dense gas-fluidised bed, the growth rate will most certainly depend on the position in the bed. Growth will be localised near the spray zone, where most wetted particles capable of forming agglomerates are located. Since the agglomeration rate is related to the amount of particle encounters the kinetic theory of granular flow can be applied to derive an expression for the agglomeration kernel.

According to the kinetic theory of granular flow (see chapter 5) the number of collisions between particles of phases n and p per unit volume per unit time equals:

$$N_{np} = \pi n_n n_p \sigma_{np}^3 g_{np} \left[\frac{4}{\sigma_{np}} \left(\frac{\theta_s}{\pi} \frac{m_n + m_p}{2 m_n m_p} \right)^{\frac{1}{2}} - \frac{2}{3} (\nabla \cdot \overline{u}_s) \right] \tag{8.10}$$

Applying definition 8.9 and multiplying with an agglomeration success-factor ψ then results in the following expression for the growth kernel:

$$K_{n,p} = \psi \cdot \pi \sigma_{np}^3 g_{np} \left[\frac{4}{\sigma_{np}} \left(\frac{\theta_s}{\pi} \frac{m_n + m_p}{2 m_n m_p} \right)^{\frac{1}{2}} - \frac{2}{3} (\nabla \cdot \overline{u}_s) \right] \tag{8.11}$$

The success-factor for agglomeration (ψ) is not a constant but a function of (e.g.) particle wetness, particle collision velocity, particle composition and position in the bed. Determination of an exact expression for ψ is beyond the scope of this thesis, but clearly the discrete element spray granulation model presented in chapter 7 can play an important role in the development of such an expression. At this point it is interesting to compare the obtained expression for the growth kernel to the kernel assuming equi-partition of kinetic energy derived by Hounslow (1998) and applied by Boerefijn et al. (2001):

$$K_{n,p} = K_0(t) \cdot (d_n + d_p)^2 \sqrt{\frac{1}{d_n^3} + \frac{1}{d_p^3}} \tag{8.12}$$

Neglecting the divergence of the particle velocity field, assuming all particles are of equal density ($\rho_n = \rho_p = \rho$) and performing some rewriting, equation 8.11 can be transformed into:

$$K_{n,p} = \psi \cdot g_{np} \sqrt{\frac{3\theta_s}{\rho}} (d_n + d_p)^2 \sqrt{\frac{1}{d_n^3} + \frac{1}{d_p^3}} \tag{8.13}$$

Which shows that the time dependent part $K_0(t)$ of the growth kernel derived by Hounslow can be given by:

$$K_0(t) = \psi \cdot g_{np} \sqrt{\frac{3\theta_s}{\rho}} \tag{8.14}$$

3.1.3. Engineering scale spray granulation modelling method 1

Many spray granulation processes are operated in batch mode. Typically, batch runs last longer then one minute, which is the maximum process time that can be captured by fundamental hydrodynamic models within acceptable computation times. Therefore, the first method for integration of population balance models and multi-fluid hydrodynamic models is based on separated calculation of hydrodynamics and particle growth. In this modelling approach, presented in figure 8.1, the multi-fluid model is applied to calculate the characteristic hydrodynamics for a bed of which the composition is known during a short time period (Δt_{MFM}), typically a couple of seconds. During the flow simulation the particle flow patterns and number of collisions between particles of different species,

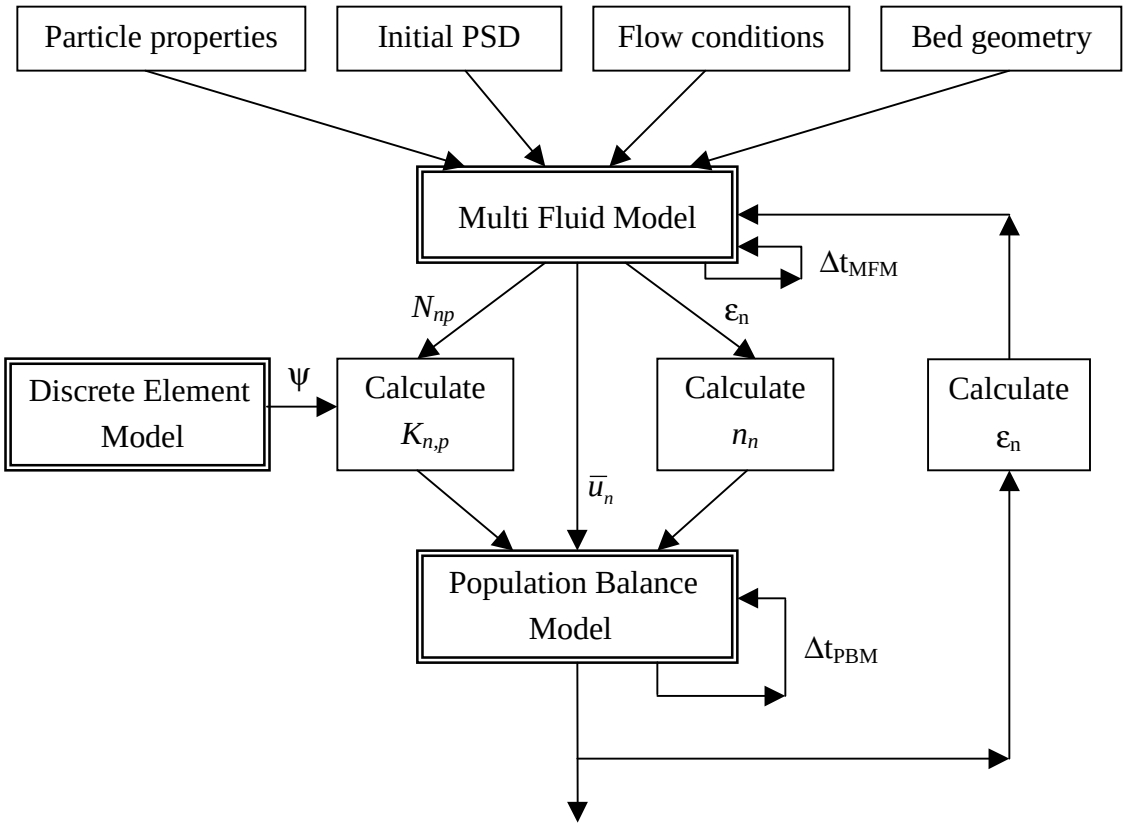

Figure 8.1. Schematic representation of model integration method 1.

required for description of particle circulation and growth in the population balance, model are collected. At the end of the hydrodynamic simulation, the flow pattern, the particle number density and the growth kernels for the a population balance simulation are initialised, where after the population balance model is applied to calculate the development of the particle size distribution over a longer period of time (Δt_{PBM}), e.g. 1 minute. Next, the evolved particle size distribution is returned to the multi-fluid model which calculates the new hydrodynamic characteristics, etc., etc. So this model integration method makes use of the fact that the particle size distribution only evolves gradually with regard to the particle circulation times in the bed. Therefore, the bed hydrodynamics will also change gradually and the same flow characteristics may be applied by the population balance model for a relatively long period before the particle size distribution has evolved so far that the flow behaviour has to be adjusted.

The problem in this approach is the computation of a 'pseudo steady' flow field to be applied in the population balance model. This needs to be a conservative flow field to prevent 'false' mass sources during the population balance simulation, which requires:

$$\nabla \cdot (\varepsilon_n \rho_n \bar{u}_n) = 0 \tag{8.15}$$

for all particle species in every computational cell in the flow domain. However, condition 8.15 is only fulfilled in a steady state, while the multi-fluid model is an intrinsically transient model. The computed flow pattern changes continuously and though all species are globally conserved, locally accumulation takes place at every moment in time. It is therefore impossible to directly generate a conservative 'pseudo steady' hydrodynamic state from the multi-fluid model (not even if a very long averaging period is applied), and the characteristic flow pattern supplied by the multi-fluid model will have to be corrected for the 'false' mass sources.

3.1.4. Engineering scale spray granulation modelling method 2

In the second approach to the integration of population balance methods and multi-fluid hydrodynamic models, no separation of time scales is made. In this approach the agglomeration source terms are directly incorporated in the governing equations of the multi-fluid model, as shown in table 8.1. The presented conservation equations are essentially the same as the ones presented in table 5.1. The source term in the mass conservation equation for species n is given by substitution of $\phi = m$ in equations 8.3-8.7. Similar source terms do not appear in the momentum and granular energy equations for

Table 8.1. Solids phase governing equations for a multi-fluid spray granulation model.

Solids phase continuity equations for species n

$$\frac{\partial(\varepsilon_n \rho_n)}{\partial t} + \nabla \cdot \left[\bar{J}_n + \varepsilon_n \rho_n \bar{u}_s \right] = S_n^{agg}(m) \tag{8.1.1}$$

Solids phase momentum equation

$$\frac{\partial(\varepsilon_s \rho_s \bar{u}_s)}{\partial t} + \nabla \cdot (\varepsilon_s \rho_s \bar{u}_s \bar{u}_s) = -\nabla P_s^s - \nabla \cdot \bar{\bar{\tau}}_s - \varepsilon_s \nabla P_g + \sum_{n=1}^{NP} \beta_{ng} (\bar{u}_g - \bar{u}_n) + \varepsilon_s \rho_s \bar{g} + S^{spray} \tag{8.1.2}$$

Granular energy equation

$$\frac{3}{2}\left\{ \frac{\partial(n_s \theta_s)}{\partial t} + \nabla \cdot (n_s \theta_s \bar{u}_s) \right\} = -(P_s^s \bar{\bar{I}} + \bar{\bar{\tau}}_s) : \nabla \bar{u}_s - \nabla \cdot \bar{q}_s - \sum_{n=1}^{NP} 3 \frac{\beta_{ng}}{m_n} \theta_n - (1-\psi)\gamma_s - \psi \gamma^{agg} \tag{8.1.3}$$

the mixture, since these equations result from summing over all species and the contributions of the source terms then sum to zero. An extra source term (S^{spray}) has to be included in the momentum equation to account for the significant amount of momentum introduced by the liquid spray. Further, far more kinetic energy is dissipated in agglomerations then in collisions. Therefore, the agglomeration success-factor has been taken into account in the calculation of the amount of energy dissipated by collisions (γ_s) and a new term (γ^{agg}) for the rate of energy dissipation due to agglomerations needs to be introduced. Considering agglomerations as collisions in which all fluctuating kinetic energy is dissipated, an estimate for this rate of energy dissipation can be obtained by setting the coefficient of restitution in equation 5.84 equal to zero:

$$\gamma^{agg} \approx \pi\theta_s \sum_{n=1}^{NP}\sum_{p=1}^{NP} n_n n_p \sigma_{np}^3 \frac{m_p}{m_n + m_p} g_{np} \left[\frac{4}{\sigma_{np}} \left(\frac{(m_n + m_p)\theta_s}{2 m_n m_p \pi} \right)^{\frac{1}{2}} - \nabla \cdot \bar{u}_s \right] \tag{8.16}$$

The main advantages of this modelling approach are that there will be no 'false' momentum sources due to the divergence of the flow field and that particle growth can be instantaneously taken into account using the kinetic theory growth kernel. Further the model can be applied for direct comparison with more detailed discrete element spray granulation models, such as the one presented in chapter 7, which will be helpful for verification and further development of closure models for liquid-solid contacting and particle growth. The main disadvantage of this modelling approach is however that the simulations will be limited to relatively short runs, which is no problem for simulation of continuous spray granulation processes but makes the model not suitable for modelling of batch granulation processes, which are often applied in laboratory scale studies.

3.2. Priorities for future research

Clearly the development of fundamental hydrodynamic models for first principle modelling of fluidised bed spray granulation has just started. In respect of the multi-level modelling approach presented in chapter 1 the following developments should receive the highest priority:

1. development of engineering scale hydrodynamic models by integration of population balance models and multi-fluid continuum fluidised bed models,
2. development of statistical analysis techniques which can be applied to extract information on particle-droplet interaction, particle growth and breakage for engineering scale models from more detailed discrete element models,

3. more detailed description of granulation and coalescence in the discrete particle spray granulation model,
4. design of well-defined experimental systems which can be applied to validate all steps in the multi-level modelling approach.

Nomenclature

a	Sonine coefficient
	Helmholtz free energy per particle, J
A	constant, s/m
	Helmholtz free energy, J
$A_{bubbles}$	area convered by bubbles, m^2
A_{solids}	area convered by particles, m^2
A^n	explicit term in the x-momentum balance, $kg/(m^2s)$
$A(C)$	function, defined in equation 5.58
b	Sonine coefficient
B	constant, s^2/m^2
B^n	explicit term in the y-momentum balance, $kg/(m^2s)$
$B(C)$	function, defined in equation 5.58
B_1	collision constant, $1/kg$
B_2	collision constant, $1/kg$
c	particle velocity, m/s
c_{12}	centre of mass impact velocity, m/s
$c`_{12}$	centre of mass rebound velocity, m/s
C	fluctuating component of particle velocity (peculiar velocity), m/s
C^n	explicit term in the z-momentum balance, $kg/(m^2s)$
C_d	drag coefficient, -
C_g	fluctuating component of local gas phase velocity, m/s
C_p	heat capacity, $J/(kgK)$
$C(C)$	function, defined in equation 5.58
□	dimensionless peculiar velocity, -
d	Sonine coefficient
d_p	particle diameter, m
dt	time step, s
D	quantity to be fluxed
	mass residual, kg/m^3

D_{nblist}	diameter of neighbour list, *m*
e	coefficient of restitution in KTGF collision model, -
e_n	coefficient of normal restitution, -
e_t	coefficient of tangential restitution, -
E	energy, *J*
f	particle velocity distribution function, s^3/m^6
	normalised particle velocity distribution function, *s/m*
f_{12}	pair distribution function, s^6/m^{12}
	normalised pair distribution function, *s/m*
f_{bed}	bed expansion frequency, *Hz*
f_{np}	pair distribution function, s^6/m^{12}
F	external force, *N*
	collision frequency, *Hz*
g	gravitational acceleration, m/s^2
g_0	radial distribution function for mono-disperse system, -
g_{np}	radial distribution function for mixture, -
G	Gibbs free energy, *J*
G_s	solids elasticity modulus, *Pa*
h	height, *m*
	Sonine coefficient
	Planck's constant, $6.626081\cdot10^{-34}$ *Js*
H	Enthalpy, *J/kg*
$H(C)$	function, defined in equation 5.58
I	momentum of inertia, $kg\cdot m^2$
	collision integral
J	impulse vector, *kg·m/s*
	Jacobi matrix
	diffusion flux, $kg/(m^2s)$
k	unit vector along the line of centres at collision, -
K	agglomeration kernel
k_b	Boltzmann's constant, $1.380661\cdot10^{-23}$ *J/K*
ℓ	mean free path, *m*
l	liquid layer thickness, *m*
l_{min}	minimum liquid layer thickness, *m*
m	mass of particle, *kg*
M	molecular mass, *kg/mol*
M_{np}	reduced mass, -

n	number of particles per unit volume, $1/m^3$
n	normal unit vector, -
nx	number of grid cells in x-direction, -
nz	number of grid cells in z-direction, -
N	order of Enskog approximation
	number of particle, -
N_{12}	collision frequency per unit volume, $1/(m^3 s)$
N_{np}	collision frequency per unit volume, $1/(m^3 s)$
N_{cell}	number of computational cells, -
N_{coll}	number of collisions during time interval, -
N_{part}	total number of particles, -
$N_{part,k}$	number of particles in k^{th} computational cell, -
Nu	Nusselt number, -
P	pressure, Pa
P_{aggl}	odds of agglomerate formation, -
Pr	Prandtl number, -
P_s	particle pressure, Pa
q	summation index
q_s	pseudo Fourier flux of kinetic fluctuating energy, $kg/(m \cdot s)$
r	position, m
	summation index
R	radius, m
	gas constant, $J/(mol \cdot K)$
R^{agg}	rate of agglomeration, $1/s$
Re	Reynolds number, -
s	percentage of segregation, -
S	Sonine polynomial
	degree of segregation, -
	agglomeration source term
S^{spray}	momentum source term, $kg/(m^2 s^2)$
S_p	particle drag source term, Pa
t	time, s
	tangential unit vector, -
T	Temperature, K
u	continuum velocity, m/s
u_s	ensemble average particulate velocity, m/s
v	velocity of particle, m/s

U_{mf}	minimum fluidisation velocity, *m/s*
v_{12}	impact velocity at the point of contact, *m/s*
V	volume, m^3
	flux velocity, *m/s*
V_{cell}	cell volume, m^3
W	work, *W*
x	particle number fraction (chapter 5)
	particle mass fraction (chapter 6)
	x-position, *m*
y	y-position, *m*
z	compressibility, -

Greek symbols

α	dimensionless function of solids fraction and other dimensionless quantities,
	specularity coefficient, -
	heat transfer coefficient, $W/(m^2K)$
β	inter-phase momentum transfer coefficient, $kg/(m^3 \cdot s)$
	$1/\theta$ (appendix 5A), *1/J*
β_0	coefficient of tangential restitution, -
γ	dissipation rate due to inelastic particle-particle collisions, $kg/(m \cdot s^3)$
δ_{np}	Kronecker delta
ε	volume fraction, -
η	fraction of particle surface covered by liquid, -
θ	granular temperature, m^2/s^2 (Chapter 2-4)
	granular temperature, $kg \cdot m^2/s^2 = J$ (Chapter 5)
θ_{np}	collisional flux
κ	pseudo conductivity, $kg/(m \cdot s)$
λ	bulk viscosity, $kg/(m \cdot s)$
	heat conductivity, *W/mK*
Λ	De Broglie wave length, *m*
μ	dynamic friction coefficient, -
μ	shear viscosity, $kg/(m \cdot s)$
	chemical potential, *J*
ρ	density, kg/m^3
σ	particle diameter, *m*

σ_{np}	inter-particle distance, *m*
τ	stress tensor, *Pa*
ϕ	particle property
	shape factor, -
ϕ_I	internal angle of friction, ^{0}
Φ	impact angle, ^{0}
Φ_0	critical impact angle, ^{0}
$\Phi^{(1)}$	first order perturbation function, -
Φ_h	heat flux, *W*
χ_{np}	collisional source
ψ	success factor for agglomeration, -
ω	angular velocity, rad/*s*

Subscripts

0	prior to collision
ab	indices of colliding particle pair
bed	averaged over whole bed
coag	coagulation
conv	convection of ensemble
drag	contribution due to gas-particle drag
drop	droplet
eff	effective
f	fluid
fric	contact friction
g	gas
	gravity
gran	fluctuating granular motion
h	heat
i	particle index number
	granular temperature class index
	discretisation index x-direction
j	discretisation index y-direction
k	computational cell index number
	discretisation index z-direction
kin	kinetic
layer	liquid layer on surface of particle

lim	limit
max	maximum
Maxwell	based on Maxwellian velocity distribution
min	minimum
n	normal direction of impact velocity
	partcile species index
p	particle
	particle species index
pore	pore
pot	potential
press	contribution due to gas-phase pressure
rcp	random closest packing
rest	normal restitution
rot	rotation
s	solids
sliding	sliding collision
small	small 1.5 mm particles
sticking	sticking collision
t	time-average
	tangential direction of impact velocity
tot	total
wall	particle-wall interaction
x	x-direction (directed from left to right)
y	y-direction (directed from bottom to top)
z	z-direction (directed from front to back)
θ	average weighted according to equation 4.49

Superscripts

`	after collision / agglomeration
(0)	first approximation in Chapman Enskog solution procedure
(1)	second approximation in Chapman-Enskog solution procedure
c	collisional
id	ideal gas state
ex	excess state
k	kinetic
max	maximum packing density

Mathematical notation

-	vector quantity
=	tensor quantity
^{0}	non-divergent tensor
< >	ensemble average
×	vector cross product
	multiplication (at line break)
·	vector dot product
	multiplication
Σ	summation
∇	gradient, *1/m*
∇·	divergence, *1/m*
δ_{np}	Kronecker delta
δ*t*	finite difference time step size, *s*
δ*x*	finite difference mesh size in x-direction, *m*
δ*y*	finite difference mesh size in y-direction, *m*
δ*z*	finite difference mesh size in z-direction, *m*
D/Dt	substantial time derivative, *1/s*
I	unit tensor
min	minimum
n	normal unit vector
t	tangential unit vector
T	transpose

Abbreviations

2D	two-dimensional
3D	three-dimensional
CCD	Charge Coupled Device
CFD	Computational Fluid Dynamics
DPM	Discrete Particle Model
ICCG	Incomplete Choleski Conjungated Gradient
KTGF	Kinetic Theory of Granular Flow
MC	Monte-Carlo
MD	Molecular Dynamics
MFM	Multi-Fluid Model

PEG	Poly-Ethylene Glycol
RMS	Root Mean Square
SEM	Scanning Electron Microscopy
SIMPLE	Semi-Implicit Method for Pressure Linked Equations
TFM	Two-Fluid Model

Bibliography

Agarwal P.K., Hull A.S., Lim K.S., 1996, 'Digital image analysis techniques for the study of bubbling fluidized beds' in *Non-invasive monitoring of multiphase flows* edited by Chaouki J., Larachi F. and Dudukovic M.P., **Chapter 12**, 407-454

Alder B.J. and Wainright T.E., 1960, Studies in molecular dynamics. II. Behavior of a small number of elastic spheres, *J. Chem. Phys*., **33**, 1439-1451

Anderson T. and Jackson R., 1967, A fluid mechanical description of fluidized beds, *Ind. Eng. Chem. Fundam*., **6**, 527-539

Arnarson B.O. and Willits J.T., 1998, Thermal diffusion in binary mixtures of smooth, nearly elastic spheres with and without gravity, *Phys. Fluids*, **10**, 1324-1328

Attinger D., Zhao Z., Poulikakos D., 2000, An experimental study of molten microdroplet surface deposition and solidification: transient behaviour and wetting angle dynamics, *ASME J. Heat Transfer*, **122**, 544-556

Bagnold R.A., 1954, Experiments on a gravity free dispersion of large solid spheres in a Newtonian fluid under shear, *Proc. R. Soc. Lond*., **A225**, 49-63

Balzer G., Boelle A., Simonin O., 1995, Eulerian gas-solid flow modelling of dense fluidized bed, in *'Fluidization VIII'* edited by J.-F. Large and C. Laguérie, Engineering Foundation, New York, 409-418

Banks M. and Aulton M.E., 1991, Fluidized bed granulation: A chronology, *Drug Dev. Ind. Pharm.*, **17**, 1437-1463

BarošováM., MalijevskýA., Labík S., Smith W.R., 1996, Computer simulation of the chemical potentials of binary hard-sphere mixtures, *Mol. Phys.*, **87**, 423-439

Becher R.-D. and Schlüder E.-U., 1998, Fluidized bed granulation –the importance of a drying zone for the particle growth mechanism, *Chem. Engng Proc*., **37**, 1-6

Bemrose C.R. and Bridgwater J., 1987, A review on attrition and attrition test methods, *Powder Technol.*, **49**, 97-126

Bernasconi D.J., Fandrich M.E., Hogue C., 1997, Experimental 3-D impact analysis, *Mulitbody System Dynamics*, **1**, 361

Bińk A., Warych J., Komorowski R., 1985, The batch granulation process in a fluidised bed, *Powder Technol*., **41**, 1-11

Boelle A., Balzer G. and Simonin O., 1995, Second-order prediction of the particle-phase stress tensor of inelastic spheres in simple shear dense suspensions, Proceedings 6^{th} *int. symp. on gas-solid flows, ASME FED*, **Vol. 228**, 9-18

Boemer A., Qi H., Renz U., 1997, Eulerian simulation of bubble formation at a jet in a two-dimensional fluidized bed, *Int. J. Multiphase flow*, **23**, 927-944

Boerefijn R., Buscan M., Hounslow M.J., 2001, Effects of non-ideal powder properties on granulation kinetics, in '*Fluidization X*' edited by M. Kwauk, J. Li and W.-C. Yang, Engineering Foundation, New York, 629-636

Boublĸ T., 1970, Hard-sphere equation of state, *J. Chem. Phys.*, **53**, 471-472

Campbell C.S. and Gong A., 1986, The stress tensor in a two-dimensional granular shear flow, *J. Fluid Mech*., **164**, 107-125

Carnahan N.F. and Starling K.E., 1969, Equation of state for nonattracting rigid spheres, *J. Chem. Phys*., **51**, 635-636

Centrella J. and Wilson J.R., 1984, Planar numerical cosmology. II**.** The difference equations and numerical tests, *Astrophys. J. Suppl*. *Ser.*, **54**, 229-249

Chapman S. and Cowling T.G., 1970, *The mathematical theory of non-uniform gases*, 3rd edition, Cambridge university press, Cambridge

Chou C.-S. and Richman M.W., 1998, Constitutive theory for homogeneous granular shear flows of highly inelastic spheres, *Physica A*, **259**, 430-448

Crowe C.T., 2000, On models for turbulence modulation in fluid-particle flows, *Int. J. Multiphasse Flow*, **26**, 719-727

Cryer S.A., 1999, Modeling agglomeration processes in fluid-bed granulation, *AIChE J*., **45**, 2069-2078

Davidson J.F., Clift R., Harrison D., 1985, *Fluidization*, Academic press, London

Delnoij E., 1999, *Fluid dynamics of gas-liquid bubble columns: A theoretical and experimental study*, Ph.D. Thesis, Twente University, The Netherlands

Detamore M.S., Swanson M.A., Frender K.R., Hrenya C.M., 2001, A kinetic theory analysis of the scale-up of circulating fluidized beds, *Powder Technol.*, **116**, 190-203

Ding J. and Gidaspow D., 1990, A bubbling fluidization model using kinetic theory of granular flow, *AIChE J*., **36**, 523-538

Ennis B.J., Tardos G., Pfeffer R., 1991, A microlevel-based characterization of granulation phenomena, *Powder Technol*., **65**, 257-272

Ennis B.J. and Litster J.D., 1997, *The science and engineering of granulation processes*, Blackie Academic Ltd., London, U.K.

Enwald H., Peirano E., Almstedt A.E., 1996, *Int. J. multiphase flow*, **22**, Suppl., 21-66

Ergun S., 1952, Fluid flow through packed columns, *Chem. Engng Prog*., **48**, 89-94

Fedors R.F., Landel R.F., 1979, An empirical method of estimating the void fraction in mixtures of uniform particles of different size, *Powder Technol*., **23**, 225-231

Février P. and Simonin O., 1998, Constitutive equations for fluid-particle velocity correlations in gas-solid turbulent flows, *3rd Int. Conf. On Multiphase Flow, ICMF'98*, Lyon, France

Foerster S.F., Louge M.Y., Chang H., Allia K., 1994, Measurements of the collision properties of small spheres, *Phys. Fluids,* **6**, 1108-1115

Foscolo P.U., Gibilaro L.G., Waldram S.P., 1983, A unified model for particulate expansion of fluidised beds and flow in fixed porous media, *Chem. Eng.Sci*., **38**, 1251-1260

Ferziger J.H. and Kaper H.G., 1972, *Mathematical theory of transport processes in gases*, North-Holland, Amsterdam, The Netherlands

Gao J., Xu C., Lin S., Tang G., Guo Y., 1999, Advanced model for turbulent gas-solid flow and reaction in FCC riser reactors, *AIChE J.*, **45**, 1095-1113

Garside J. and Al-Dibouni M.R., 1977, Velocity-Voidage Relationships for fluidization and sedimentation in Solid-Liquid systems, *Ind. Eng. Chem., Process Des. Dev.*, **16**, 206-214

Geldart D., 1973, Types of gas fluidization, *Powder Technol*., **7**, 285-292

Gidaspow D., 1994, *Multiphase flow and fluidization: Continuum and kinetic theory descriptions*, Academic press, Boston

Gidaspow D., Ettehadieh B., Bouillard J., 1985, Hydrodynamics of fluidization: bubbles and gas compositions in the U-gas process, *AIChE. Symp. Series*, **80**, 57-64

Gilbertson M.A. and Eames I., 2001, Segregation patterns in gas-fluidized systems, *J. Fluid. Mech.*, **433**, 347-356

Goldschmidt M.J.V., Hoomans B.P.B., Kuipers J.A.M., 2000, Recent progress towards hydrodynamic modeling of dense gas-particle flows, *Recent Res. Devel. Chemical Engng*, **4**, 273-292

Goldschmidt M.J.V. and Van Sint Annaland M., 2001, On the derivation of the kinetic theory of granular flow for multi-component mixtures, Internal Report, Twente University, The Netherlands

Goldschmidt M.J.V., Kuipers J.A.M., Van Swaaij W.P.M., 2001a, Hydrodynamic modelling of dense gas-fluidised beds using the kinetic theory of granular flow: effect of the coefficient of restitution on bed dynamics, *Chem. Eng.Sci.*, **56**, 571-578

Goldschmidt M.J.V., Kuipers J.A.M., Van Swaaij W.P.M., 2001b, Segregation in dense gas-fluidised beds: Validation of a multi-fluid continuum model with non-intrusive digital image analysis measurements, in '*Fluidization X'* edited by M. Kwauk, J. Li and W.-C. Yang, Engineering Foundation, New York, 795-802

Gorham D.A. and Kharaz A.H., 1999, Results of particle impact tests, *Impact Research Group IRG 13*, The Open University, Milton Keynes, UK

Grace J.R., 1970, The viscosity of fluidised beds, *Can. J. Chem. Engng*, **48**, 30-33

Grad H., 1949, On the kinetic theory of rarefied gases, *Comm. pure Appl. Math*., **2**, 331-407

Grad H., 1963, Asymptotic theory of the Boltzmann equation, *Phys. Fluids*, **6**, 147-181

Gradshteyn I.S. and Ryzhik I.M., 1980, *Table of integrals, series, and products*, Academic Press, London

Harlow F.H. and Amsden A.A., 1974, *Kachina: An Eulerian computer program for multi-fluid flows*, Los Alamos, LA-5680

Harlow F.H. and Amsden A.A., 1975, Numerical calculation of multiphase fluid flow, *J. Comput. Phys*., **17**, 19-52

Hawley J.F., Smarr L.L., Wilson J.R., 1984, A numerical study of nonspherical black hole accretion. II. Finite differencing and code calibration, *Astrophys. J. Suppl. Ser*., **55**, 211-246

He J. and Simonin O., 1993, Non-equilibrium prediction of the particle-phase stress tensor in vertical pneumatic conveying, Proceedings *5th int. symp. on gas-solid flows*, ASME FED, **vol. 166**, 253-263

Hill P.J. and Ng K.M., 1995, New discretization procedure for the breakage equation, *Proc. Systems Engng*, **41**, 1204-1216

Hoffmann A.C. and Romp E.J., 1991, Segregation in a fluidised powder of a continuous size distribution, *Powder Technol*., **66**, 119-126

Hoomans B.P.B., Kuipers J.A.M., Briels W.J., Van Swaaij W.P.M., 1996, Discrete particle simulation of bubble and slug formation in a two-dimensional gas-fluidised bed: a hard sphere approach, *Chem. Eng.Sci*., **51**, 99-118

Hoomans B.P.B., Kuipers J.A.M., Van Swaaij W.P.M., 1998a, The influence of particle properties on pressure signals in dense gas-fluidised beds: a computer simulation study, *World Congress on Particle Technology 3*, Brighton, UK

Hoomans B.P.B., Kuipers J.A.M., Van Swaaij W.P.M., 1998b, Granular dynamics simulation of cluster formation in riser flow, *Third international conference on multiphase flow, ICMF'98*, Lyon, France

Hoomans B.P.B., Kuipers J.A.M., Briels W.J., Van Swaaij W.P.M., 1998c, Discrete particle simulation of segregation phenomena in dense gas-fluidized beds, in *Fluidization IX* edited by Fan L.-S. and Knowlton T.M., Engineering Foundation, New York, 485-492

Hoomans B.P.B., 2000a, *Granular dynamics of gas-solid two-phase flows*, Ph.D. Thesis, Twente University, The Netherlands

Hoomans B.P.B., Kuipers J.A.M., Van Swaaij W.P.M., 2000b, Granular dynamics simulation of segregation phenomena in bubbling gas-fluidised beds, *Powder Technol*., **109**, 41-48

Hounslow M.J., Ryall R.L., Marshall V.R., 1988, A discrete population balance model for nucleation, growth and aggregation, *AIChE J*., **34**, 1821-1832

Hounslow M.J., 1998, The population balance as a tool for understanding particle rate processes, *KONA Powder and Particle*, **16**, 179-193

Hrenya C.M. and Sinclair J.L., 1997, Effects of particle-phase turbulence in gas-solid flows, *AIChE J*., **43**, 853-869

Hulbert H.M. and Katz S., 1964, Some problems in particle technology. A statistical mechanical formulation, *Chem. Eng.Sci.*, **19**, 555-574

Ishii M., 1975, *Thermo-fluid dynamic theory of two phase flow*, Eyrolles, Paris

Jackson G., Rowlinson J.S., Van Swol F., 1987, Computer simulation of mixtures of hard spheres, *J. Phys. Chem.*, **91**, 4907-4912

Jackson R., 1997, Locally averaged equations of motion for a mixture of identical spherical particles and a newtonian fluid, *Chem. Eng.Sci.*, **52**, 2457-2469

Jenkins J.T. and Savage S.B., 1983, A theory for the rapid flow of identical, smooth, nearly elastic, spherical particles, *J. Fluid Mech.*, **130**, 187-202

Jenkins J.T. and Richman M.W., 1985, Kinetic theory for plane flows of a dense gas of identical, inelastic, circular disks, *Phys. of Fluids*, **28**, 3485-3494

Jenkins J.T. and Mancini F., 1987, Balance laws and constitutive relations for plane flows of a dense, binary mixture of smooth, nearly elastic, circular disks, *J. Appl. Mech.*, **54**, 27-34

Jenkins J.T. and Richman M.W., 1988, Plane simple shear flow of smooth inelastic circular disks: the anisotropy of the second moment in the dilute and dense limits, *J. Fluid Mech.*, **192**, 313-328

Jenkins J.T. and Mancini F., 1989, Kinetic theory for binary mixtures of smooth, nearly elastic spheres, *Phys. Fluids A 1*, **12**, 2050-2057

Jenkins J.T., 1992, Boundary conditions for rapid granular flow: flat, frictional walls, *J. Appl. Mech.*, **59**, 120-127

Jenkins J.T. and Zhang C., 2000, Kinetic theory for identical, slightly frictional, nearly elastic spheres, personal communication, *paper to be published*.

Johnson K.L., 1985, *Contact mechanics*, Cambridge University Press, Cambrigde, UK

Kaneko Y., Shiojima T., Horio M., 1999, DEM simulation of fluidized beds for gas-phose olefin polymerization, *Chem. Eng.Sci.*, **54**, 5809-5821

Kawaguchi T., Tanaka T., Tsuji Y., 1998, Numerical simulation of two-dimensional beds using the discrete element method (comparison between the two- and three-dimensional models), *Powder Technol*., **96**, 129-138

Kharaz A.H., Gorham D.A., Salman A.D., 1999, Accurate measurement of particle impact parameters, *Measurement Science and Technology*, **10**, 31-35

Kristensen H.G. and Schaeffer T., 1987, Granulation –A review on pharmaceutical wet-granulation, *Drug. Dev. Ind. Pharm*., **13**, 803-872

Kuipers J.A.M., Van Duin K.J., Van Beckum F.P.H., Van Swaaij W.P.M., 1992a, A numerical model of gas-fluidized beds, *Chem. Eng.Sci*., **47**, 1913-1924

Kuipers J.A.M., Prins W., Van Swaaij W.P.M., 1992b, Numerical simulation of wall-to-bed heat transfer coefficients in gas-fluidized beds, *AIChE J.*, **38**, 1079-1091

Kuipers J.A.M., Van Duin K.J., Van Beckun F.P.H. and Van Swaaij W.P.M., 1993, Computer simulation of the hydrodynamics of a two-dimensional gas-fluidised bed, *Computers Chem. Eng*, **8**, 839-858

Kuipers J.A.M. and Van Swaaij W.P.M., 1998, Computational fluid dynamics applied to chemical reaction engineering, *Adv. in Chem. Eng*, **24**, 227-328

Kunii D. and Levenspiel O., 1991, *Fluidization engineering*, 2nd edition, Butterworth-Heinemann, Boston

Labous L., Rosato A.D., Dave R.N., 1997, Measurements of collisional properties of spheres using high-speed video analysis, *Phys. Rev. E.*, **56**, 5717

Laux H., 1998, *Modeling of dilute and dense dispersed fluid-particle flow*, Ph.D. Thesis, NTNU Trondheim, Trondheim, Norway

Lee K. and Matsoukas T., 2000, Simultaneous coagulation and break-up using constant-N Monte Carlo, *Powder Technol*., **110**, 82-89

Lian G., Thornton C., Adams M.J., 1998, Discrete particle simulation of agglomerate impact coalescence, *Chem. Eng.Sci*., **53**, 3381-3391

Lim K.S., Agarwal P.K., O'Neill B.K., 1990a, Measurement and modelling of bubble parameters in a two-dimensional gas-fluidized bed using image analysis, *Powder Technol.*, **60**, 159-171

Lim K.S. and Agarwal P.K., 1990b, Conversion of pierced lengths measured at probe to bubble size measures: an assessment of the geometrical probability approach and bubble shape models, *Powder Technol.*, **63**, 205-219

Lim K.S. and Agarwal P.K., 1992, Bubble velocity in fluidized beds: the effect of non-vertical bubble rise on its measurement using submersible probes and its relationship with bubble size, *Powder Technol.*, **69**, 239-248

Lim K.S., Gururajan V.S., Agarwal P.K., 1993, Mixing of homogeneous solids in bubbling fluidized beds: theoretical modelling and experimental investigation using digital image analysis, *Chem. Eng.Sci.*, **48**, 2251-2265

Litster J.D., Hapgood K.P., Michaels J.N., Sims A., Roberts M., Kameneni S.K., Hsu T., 2001, Liquid distribution in wet granulation: dimensionless spray flux, *Powder Technol*., **114**, 32-39

López de Haro M., Cohen E.G.D., Kincaid J.M., 1983, Linear transport theory for multicomponent mixtures. I. Linear transport theory, *J. Chem. Phys*., **78**, 2746-2759

Lun C.K.K., Savage S.B., Jeffrey D.J. and Chepurniy N., 1984, Kinetic theories for granular flow: inelastic particles in Couette flow and slightly inelastic particles in a general flowfield, *J. Fluid Mech*., **140**, 223-256

Lun C.K.K. and Savage S.B., 1987, A simple kinetic theory for granular flow of rough, inelastic, spherical particles, *J. Appl. Mech*., **54**, 47-53

Lun C.K.K., 1991, Kinetic theory for granular flow of dense, slightly inelastic, slightly rough spheres, *J. Fluid Mech*., **233**, 539-559

Lun C.K.K. and Bent A.A., 1994, Numerical simulation of inelastic frictional spheres in simple shear flow, *J. Fluid Mech*., **258**, 335-353

Ma D. and Ahmadi G., 1986, An equation of state for dense rigid sphere gases, *J. Chem. Phys*., **84**, 3449-3450

Manger E., 1996, *Modelling and simulation of gas/solids flow in curvelinear coordinates*, Ph. D. Thesis, Telemark College, Department of Technology, Porsgrunn, Norway

Mansoori G.A., Carnahan N.F., Starling K.E., Leland Jr. T.W., 1971, Equilibrium thermodynamic properties of the mixture of hard spheres, *J. Chem. Phys*., **54**, 1523-1525

Mathiesen V., 1997, *An experimental and computational study of multiphase flow behaviour in circulating fluidised beds*, Ph.D. Thesis, Telemark Institute of Technology, Porsgrunn, Norway

Mathiesen V., Solberg T., Hjertager B.H., 2000, An experimental and computational study of multiphase flow behavior in a circulating fluidized bed, *Int. J. Multiphase Flow*, **26**, 387-419

Maw N., Barber J.R., Fawcett J.N., 1981, The role of elastic tangential compliance in oblique impact, *ASME J. Lub. Technol.*, **103**, 74-80

Maxwell, J.C., 1866, On the dynamical theory of gases, *Phil. Trans. R. Soc. Lond*., **157**, 49-88

McCormack A., Greenwood R.M., Seville J.P.K., 2001, The effect of binder viscosity, solidification rate, and distributor plate design in fluidised bed granulation, *Proc. 7th Int. Conf. on Agglomeration*, Albi, France

Nienow A.W., 1995, Fluidised bed granulation and coating: Applications to materials, agriculture and biotechnology, *Chem. Eng.Comm*., **139**, 233-253

Nieuwland J.J., 1995, *Hydrodynamic modelling of gas-solid two-phase flows*, Ph.D. Thesis, Twente University, Enschede, The Netherlands

Nieuwland J.J., Van Sint Annaland M., Kuipers J.A.M., Van Swaaij W.P.M., 1996, Hydrodynamic modeling of gas/particle flows in riser reactors, *AIChE J.*, **42**, 1569-1582

Ogawa S., Unemura A., Oshima N., 1980, On the equations of fully fluidized granular materials, *Z. Angew. Math. Phys. (J. Appl. Math. Phys.)*, **31**, 483-493

Orr C., 1966, *Particulate technology*, Macmillan, New York

Ouyang J. and Li J., 1999, Discrete simulations of heterogeneous structure and dynamic behaviour in gas-solid fluidisation, *Chem. Eng.Sci.*, **54**, 5427-5440

Patankar S.V., Spalding D.B., 1972, A calculation procedure for heat, mass and momentum transfer in three-dimensional parabolic flows, *Int. J. Heat Mass Transfer*, **15**, 1787-1806

Pietsch W., 1992, *Size enlargement by agglomeration*, John Wiley & Sons Ltd., Chichester

Pita, J.A. and Sundaresan, S., 1991, Gas-solid flow in vertical tubes, *AIChE J.*, **37**, 1009-1018

Randolph A.D. and Larson M.A., 1991, *Theory of particulate processes*, 2nd edition, Academic Press. New York

Ranz W.E. and Marshall W.R. Jr., 1952, Evaporation form drops, *Chem. Engng Prog.*, **48**, 141-146, 173-180

Reed T.M. and Gubbins K.E., 1973, *Applied statistical mechanics*, McGraw-Hill, Tokyo, Japan

Richman M.W., 1989, The source of second moment in dilute granular flows of highly inelastic spheres, *J. of Rheol.*, **33**, 1293-1306

Rintoul M.D. and Torquato S., 1996, Computer simulations of dense hard-sphere systems, *J. Chem. Phys.*, **105**, 9258-9265

Rong D., 2000, DEM simulation of hydrodynamics, heat transfer and combustion in fluidized beds, Ph.D. Thesis, Tokyo University of Agric. and Tech., Tokyo, Japan

Rowe P.N., Nienow A.W., Agbim A.J., 1972, The mechanism by which particles segregate in gas fluidised beds - binary systems of near-spherical particles, *Trans. Instn Chem. Engrs*, **50**, 310-323

Rowe P.N. and Nienow A.W., 1976, Particle mixing and segregation in gas fluidised beds. A review, *Powder Technol*., **15**, 141-147

Samuelsberg A. and Hjertager B.H., 1996, Computational fluid dynamics simulation of an oxy-chlorination reaction in a full-scale fluidized bed reactor, *preprint volume for 5th international conference on Circulating Fluidised Beds*, Beijing, China, MSR12 1-6

Santos A., Yuste S.B., López de Haro M., 1999, Preliminary communication: Equation of state of a multicomponent d-dimensional hard-sphere fluid, *Mol. Phys*., **96**, 1-5

Savage S.B. and Jeffrey D.J., 1981, The stress tensor in a granular flow at high shear rates, *J. Fluid Mech*., **110**, 255-272

Savage S.B., 1988, Streaming motions in a bed of vibrationally fluidized dry granular material, *J. Fluid Mech*., **194**, 457-478

Schmidt A. and Renz U. 1999, Eulerian computation of heat transfer in fluidized beds, *Chem. Eng. Sci.*, **54**, 5515-5522

Schmidt A. and Renz U., 2000, Numerical simulation of heat transfer in fluidized beds by a kinetic theory of granular flows, *Int. J. Therm. Sci.*, **39**, 871-885

Schügerl K., Merz M., Fetting F., 1961, Rheologische Eigenschaften von gasdurchströmten Fliessbettsystemen , *Chem. Eng. Sci*., **15**, 1-38

Sela N. and Goldhirsch I., 1998, Hydrodynamic equations for rapid granular flows of smooth inelastic spheres, to Burnett order, *J. Fluid. Mech.*, **361**, 41-71

Simonin O., 1991, Second-moment prediction of dispersed phase turbulence in particle-laden flows, *Proceedings 8th Symp. on turbulent shear flows*, **Vol. 1**, 741–746

Simonin O., Deutsch E., Boivin M., 1995, 'Large eddy simulation and second-moment closure model of particle fluctuating motion in two-phase turbulent flows' in *Selected papers on from the ninth symposium on turbulent shear flows* edited by J.H. Whitelaw, Springer-Verlag, 85-115

Simonin O., 1996, 'Modelling turbulent reactive dispersed two-phase flows in industrial equipments' in Proceedings of the '*Third world conference in applied computational fluid dynamics'* edited by Miller A., Löffler B., Habasi W. Bercovier M., Freiburg, Germany, 17.9

Simons S.J.R., 1995, Imaging techniques for fluidized bed systems: a review, *Chem. Engng J.*, **56**, 83-93

Simons S.J.R. and Fairbrother, 2000, Direct observations of liquid binder-particle interactions: the role of wetting behaviour in agglomerate growth, *Powder Technol*., **110**, 44-58

Sinclair J.L. and Jackson R., 1989, Gas-particle flow in a vertical pipe with particle-particle interactions, *AIChE J*., **35**, 1473-1486

Smith P.G. and Nienow A.W., 1983, Particle growth mechanisms in fluidised bed granulation –II: Comparison of experimental data with growth models , *Chem. Eng. Sci*., **38**, 1233-1240

Song Y., Stratt R.M., Mason E.A., 1988, The equation of state of hard spheres and the approach to random closest packing, *J. Chem. Phys.*, **88**, 1126-1133

Stewart P.S.B., 1968, Isolated bubbles in fluidised beds –theory and experiment, *Trans. Instn Chem. Engrs*, **46**, 60-66

Syamlal M., 1985, *Multiphase hydrodynamics of gas-sold flow*, Ph.D. Thesis, Illinois Institute of Technology, Chicago, U.S.A.

Syamlal M. and Gidaspow D., 1985, Hydrodynamics of fluidization: prediction of wall to bed heat transfer coefficients, *AIChE Journal*, **31**, 127-134

Syamlal M., Rogers W., O'Brien T.J., 1993, *MFIX documentation theory guide*, U.S. Dept. of Energy, Technical Note DOE/METC-94/1004

Tham M.K. and Gubbins K.E., 1971, Kinetic theory of multicomponent dense fluid mixtures of rigid spheres, *J. Chem. Phys*., **55**, 268-279

Thornton C., Ciomocos M.T., Adams M.J., 1999, Numerical simulation of agglomerate impact breakage, *Powder Technol*., **105**, 74-82

Tobochnik J. and Chapin P.M., 1988, Monte Carlo simulations of hard spheres near random closest packing using spherical boundary conditions, *J. Chem. Phys.*, **88**, 5824-5830

Tsuji Y., Kawaguchi T., Tanaka T., 1993, Discrete particle simulation of two-dimensional fluidised bed, *Powder Technol*., **77**, 79-87

Tsuo Y.P. and Gidaspow D., 1990, Computation of flow patterns in circulating fluidized beds, *AIChE J*., **36**, 885-896

Yang W.-C. and Keairns D.L., 1982, Rate of particle separation in a Gas Fluidized Bed, *Ind. Eng. Chem. Fundam.*, **21**, 228-235

Yates J.G., 1983, *Fundamentals of fluidized bed processes*, Butterworths, London

Yau D.H.L., Chan K.-Y., Henderson D., 1996, A further test of the Boublik et al. equations for binary hard sphere mixtures, *Mol. Phys.*, **88**, 1237-1248

Van Wachem B.G.M., Schouten J.C., Krishna R., Van den Bleek C.M., 1999, Validation of the Eulerian simulated dynamic behaviour of gas-solid fluidised beds, *Chem. Eng. Sci*., **54**, 2141-2149

Waldie B., Wilkinson D., Zachra L., 1987, Kinetics and mechnisms of growth in batch and continuous fluidized bed granulation, *Chem. Eng. Sci*., **42**, 653-665

Walton O.R. and Braun R.L., 1986a, Viscosity and temperature calculations for shearing assemblies of inelastic, frictional disks, *J. Rheol*., **30**, 949-980

Walton O.R. and Braun R.L., 1986b, Stress calculations for assemblies of inelastic spheres in uniform shear, *Acta Mech*., **63**, 73-86

Walton O.R., 1993, 'Numerical simulation of inelastic, frictional particle-particle interactions' in *Particulate two-phase flow*, edited by M.C. Roco, Butterworth-Heinemann, London

Wang R.-C. and Chou C.-C., 1995, Particle mixing/segregation in gas-solid fluidized bed of ternary mixtures, *Can. J. Chem. Engng*, **73**, 793-799

Wen Y.C. and Yu Y.H., 1966, Mechanics of fluidization, *Chem. Eng. Prog. Symp. Ser*., **62**, 100-111

Woodcock L.V., 1981, Glass transition in the hard-sphere model and Kauzmann's paradox, Ann. N.Y. Acad. Sci. 37, 274-298

Wurster D.E., 1960, Preparation of compressed tablet granulations by the air-suspension technique II, *J. Am. Pharm. Ass. (Sci. Edn.)*, **49**, 82-84

Zamankhan P., 1995, Kinetic theory of multicomponent dense mixtures of slightly inelastic spherical particles, *Phys. Rev E.*, **52**, 4877-4891

Zhang C., 1993, *Kinetic theory for rapid granular flows*, Ph.D. Thesis, Cornell University, U.S.A.

Zhang D.Z. and Prosperetti A., 1994, Averaged equations for inviscid disperse two-phase flow, *J. Fluid Mech*., **267**, 185-219

Zhang D.Z. and Prosperetti A., 1997, Momentum and energy equations for disperse two-phase flows and their closure for dilute suspensions, *Int. J. Multiphase Flow*, **23**, 425-453

Zhang D.Z. and Rauenzahn R.M., 1997, A viscoelastic model for dense granular flows, *J. Rheol.*, **41**, 1275-1298

Zhang D.Z. and Rauenzahn R.M., 2000, Stress relaxation in dense and slow granular flows, *J. Rheol*., **44**, 1019-1041

Publications

Graduation work

Brilman D.W.F., Goldschmidt M.J.V., Versteeg G.F., Van Swaaij W.P.M., 2000, Heterogeneous mass transfer models for gas absorption in multiphase systems, *Chem. Eng. Sci.*, **55**, 2793-2812

This thesis

Goldschmidt M.J.V., Hoomans B.P.B., Kuipers J.A.M., 2000, Recent progress towards hydrodynamic modeling of dense gas-particle flows, *Recent Res. Devel. Chemical Engng*, **4**, 273-292

Goldschmidt M.J.V., Kuipers J.A.M., Van Swaaij W.P.M., 2001, Hydrodynamic modelling of dense gas-fluidised beds using the kinetic theory of granular flow: effect of the coefficient of restitution on bed dynamics, *Chem. Eng. Sci.*, **56**, 571-578

Gilbertson M.A., Goldschmidt M.J.V., Kuipers J.A.M., 2001, Comparison of Eulerian hydrodynamic models with non-intrusive X-ray measurements in pressurised dense gas-fluidised beds, in '*Fluidization X*' edited by Kwauk M., Li J. and Yang W.-C., Engineering Foundation, New York, 405-412

Goldschmidt M.J.V., Kuipers J.A.M., Van Swaaij W.P.M., 2001, Segregation in dense gas-fluidised beds: validation of a multi-fluid continuum model with non-intrusive digital image analysis measurements, in '*Fluidization X*' edited by Kwauk M., Li J. and Yang W.-C., Engineering Foundation, New York, 795-802

Goldschmidt M.J.V., Beetstra R., Kuipers J.A.M., 2001, Hydrodynamic modelling of dense gas-fluidised beds: Comparison and validation of 3D discrete particle and continuum models, submitted to *Powder Technol.*

Goldschmidt M.J.V., Beetstra R., Kuipers J.A.M., 2001, Hydrodynamic modelling of dense gas-fluidised beds: Comparison of the Kinetic Theory of Granular Flow with 3D hard-sphere discrete particle simulations, submitted to *Chem. Eng. Sci.*

Goldschmidt M.J.V., Link J.M., Mellema S., Kuipers J.A.M., 2001, Digital image analysis measurements of bed expansion and segregation dynamics in dense gas-fluidised beds, submitted to *Powder Technol.*

Goldschmidt M.J.V., Weijers G.G.C., Boerefijn R., Kuipers J.A.M., 2001, Discrete element modelling of fluidised bed spray granulation, submitted to *AIChE J.*

Goldschmidt M.J.V., Weijers G.G.C., Boerefijn R., Kuipers J.A.M., 2002, Discrete element modelling of fluidised bed spray granulation, submitted to *'World congress on particle technology 4'*, 21-25 July, Sydney, Australia

Acknowledgement

And then it is the last night before your thesis goes to press and you still have to write one of the most important parts of it, the acknowledgement, hoping you do not forget anyone. As indicated in the dedication, this thesis would not have been here without the absolute support of my parents. Therefore I would like to thank them in the first place. I also owe a lot to Donna for her love, interest and patience on which I continuously put higher demands during the last year. I'm grateful to my brother Wouter and my friends for their continuous interest when I was telling about my research problems. I am looking forward to catch up with each of you, while we are enjoying a nice glass of beer, a good glass of wine, a delicious dinner, a relaxed run or what so ever.

In particular I want to thank Wim Brilman. His enthusiasm during my graduation project has been a great example for me. He boosted my interest for research and played an important role in my choice to perform my Ph.D.-studies in Twente. I also owe a lot to my promoters, Hans Kuipers and Wim van Swaaij, who in collaboration with Unilever Research offered me the opportunity to perform a scientifically challenging Ph.D.-project with industrial relevance. I have always experienced the collaboration with my mentor, Hans Kuipers, as a very pleasant one. I have learned a lot from his extensive knowledge about fluidised bed modelling and numerical methods and I cherish many good memories about our in-depth discussions, such as the one in Sheffield, when returning from a meeting we were so concentrated on our discussion that we missed the train to the airport, even though we were standing on the right platform (?!) way before departure of the train. I also want to thank Martin van Sint Annaland for his critical contribution and his indispensable perseverance during the derivation of the kinetic theory model, whenever we got stuck because of another mathematical challenge. In the many (late night) hours that went into this derivation we puzzled a lot and had a lot of fun, sentences like "the derivation is left to the reader as a simple exercise" I will remember for a long time. Furthermore the derivation of a complete kinetic theory model would not have been possible without the statistical-thermodynamic contribution of Martin van der Hoef, for which I am grateful to him. I would also like to thank professor Jim Jenkins from Cornell

University for the helpful discussions we had on the derivation of the kinetic theory models and for sending me a copy of the paper Zhang en Jenkins (2000) before publication.

As indicated in the second line of the dedication I would not have been able to perform the research reported in this thesis without the work of many others upon which I could build. Besides the earlier mentioned people, I also think of the work of my colleagues, Bob Hoomans and Erik Delnoij, but also still somewhat further back to the work of Jelle Nieuwland. Under the guidance of Hans Kuipers they founded the basis of a solid research program on modelling of multi-phase flows, from a chemical reactor engineering viewpoint.

Furthermore, I have been able to build upon the work of a couple of excellent graduate students: Renier Braam, who fulfilled the not so easy assignment to incorporate an existing kinetic theory closure model into the multi-fluid code; Siebren Mellema who saw an opportunity to combine his photography and computer hobbies in his graduation assignment, but decided to take the assignment because I offered him free coffee; Renske Beetstra who was looking for a challenging assignment and thus made the first link between the discrete particle model and the kinetic theory of granular flow; Jeanette Mensink who performed her assignment at Unilever Research in Vlaardingen worked on the acquisition of validation data for the models, for which the pilot plant spray granulation batch set-up had to be modified to operate in continuous mode; Jeroen Link who perfected the digital image analysis system and despite severe experimental setbacks, patiently performed the extensive set of measurements and Geert Weijers who, after acquiring the necessary knowledge about spray nozzles at Unilever Research, built the discrete particle spray granulation model in Twente. Furthermore, Paul-Guillaume Schmitt performed the pioneering experimental work into segregation as an international internship and Arnoud Roos studied the influence of different gas-particle drag relations on fluidised bed dynamics as part of his combined technical and Pt-II assignment. Herewith I also want to thank Unilever Research for sharing their research facilities and I want to thank the following people for participating in the several graduation committees: Ties Bos, Wim Briels, Louis van der Ham, Mike Hounslow, Kees Slump, Geert Versteeg, Marijn Warmoeskerken and Ko van der Weele.

Then the practical work would never have been possible without the expertise of the technicians in the Vlugterlab. First of all I want to thank Gerrit Schorfhaar for all the work he performed for me with great dedication. The continuous struggle we had,

together with Hans Kuipers, with the forced contracting at the IMC and the bureaucracy of the department of CT, with all consequences, I will not forget quickly. Furthermore, I am most grateful to Wim Leppink, Benno Knaken en Henk-Jan Moed for their immediate technical assistance in times of need, but especially I want to thank them for the construction of 'De Vlugtheuvel', for which the idea raised during a game of carts in one of the breaks. Of course I would also like to thank Robert Meijer for his electrotechnical assistance for the control of the set-up and for the necessary safety supervision.

For administrative support I could always fall back on Gery Stratingh-Roelofs, Nicole Haitjema, Ria Stegehuis-de Vegte, Brigitte Sanderink en Ria Hofs-Winkelman, whereas Rik Akse and later Martin van Sint Annaland took good care of the project finances. Thanks to all of you! Then, no computer would have been purchased or repaired and no glass bed would have been constructed without the help of the people at TCCT. Therefore I want to thank Mark Hulshof, Wim Platvoet, Jan Jagt, Jan Heezen, Joachim Olde Bolhaar, Joop Snoeyenbos and all others at TCCT for always being there when I needed them most. Furthermore, I want to thank Silicon Graphics for letting me participate in the powergroup meetings and the support for which I could always count on Ronald van Pelt or Peter Michielse.

Furthermore I have had a very good time with all my colleagues and the students of the Chemical Engineering Science research group (later Fundamental Aspects of Chemical Reactor Engineering). Unfortunately playing cards and darts is not going on any more, but sailing in Friesland is still a top activity. Furthermore, I would like to thank Liesbeth Kuipers for the organisation of the pan parties and the perfect organisation of the skiing holidays (what does FAP stand for: Fun and Party?). Of course I cherish good memories about the conferences we visited, but for one reasons or another it seems not appropriate to go into more detail here.

Last but not least I want to thank the people involved with the CREF-granulation research team at Unilever Research, Joop Olieman, Frank van de Scheur, Atze Jan van der Goot, Renee Boerefijn en Terry Instone, for their critical contribution to my Ph.D.-project. Because of the good collaboration we build up within the project I was able to visit professor Mike Hounslow in Sheffield for several weeks in the spring of the year 2000, to get acquainted with the details about population balance modelling. Besides Mike Hounslow I also would like to thank Nynke Wierda and Agba Salman for their hospitality and I would like to see this worthwhile collaboration grow in the near future.

And so you see that writing a Ph.D. thesis does not only demand a lot of knowledge, but also requires that you know a lot of people,

once again many thanks to all of you,

Mathijs

About the author

Mathijs Goldschmidt was born on May 14th, 1973 in Almelo. He grew up in Wierden where he attended grammar school. Subsequent to primary education, from 1985, he attended the "Pius X College" in Almelo. In the spring of 1991 he there obtained the VWO diploma.

In August 1991 he started his Chemical Engineering study at Twente University in Enschede, The Netherlands. During the second year he entered the free doctoral program Chemical Engineering and Computer Science. As part of the engineering education, he performed his internship with Akzo Nobel Corporate Research in Dobss Ferry (New York, U.S.A.), in the autumn of 1995. In February 1997 he defended his graduation project on "Heterogeneous modelling of mass transfer and chemical reaction", which was carried out within the Chemical Reaction Engineering Science research group. In March of the same year he was awarded his engineering degree *cum laude*.

In April 1997 he joined the Chemical Reaction Engineering Science research group (later Fundamental Aspects of Chemical Reaction Engineering) as a Ph.D. student, to perform research on the hydrodynamic modelling of granular flow in gas-fluidised beds and fluidised bed spray granulation processes. The results presented in this thesis reflect that work.

Since August 2001 he is employed by Akzo Nobel Chemicals NV as a process engineer, where he is responsible for carrying out projects in the area of Computational Fluid Dynamics and Chemical Reactor Engineering.

Dankwoord

En zo zit je dan aan de vooravond van het ter perse gaan van je proefschrift nog te typen aan één van de belangrijkste stukjes van het proefschrift, het dankwoord, hopend je niemand zult vergeten. Zoals de opdracht aangeeft zou dit proefschrift niet tot stand zijn gekomen zonder de onvoorwaardelijke steun die mijn ouders mij gedurende mijn gehele studie gegeven hebben. Ik wil hen daarvoor dan ook als eerste van harte bedanken. Tevens ben ik Donna veel dank verschuldigd voor haar liefde en belangstelling en haar geduld dat tijdens het laatste jaar van de promotie steeds meer op de proef werd gesteld. Mijn broertje Wouter en mijn vrienden ben ik dankbaar voor hun vriendschap en hun voortdurende belangstelling bij het aanhoren van mijn promotieperikelen. Ik zie er naar uit om weer eens rustig met eenieder bij te praten, onder het genot van een biertje, een goed glas wijn, een lekkere maaltijd, een ontspannen duurloopje of noem maar op.

In het bijzonder wil ik Wim Brilman bedanken. Door zijn enthousiaste begeleiding en welgemeende belangstelling tijdens mijn afstudeerproject is hij voor mij een groot voorbeeld geweest. Hij heeft mijn belangstelling voor het onderzoek aangewakkerd en een belangrijke rol gespeeld bij mijn keuze om in Twente te gaan promoveren. Veel dank ben ik ook verschuldigd aan mijn promotoren, Hans Kuipers en Wim van Swaaij, die mij samen met Unilever Research de mogelijkheid hebben geboden om een wetenschappelijk uitdagend promotie project met industriële relevantie uit te voeren. De samenwerking met mijn directe begeleider, Hans Kuipers, heb ik altijd als zeer prettig ervaren. Van zijn uitgebreide kennis op het gebied van de wervelbedmodellering en de numerieke methoden heb ik veel mogen opsteken. Aan onze diepgaande discussies koester ik vele goede herinneringen, zoals die ene keer in Sheffield, dat we na afloop van een bijeenkomst zo diep in de discussie opgingen dat we de trein naar het vliegveld misten, terwijl we toch ruim op tijd op het juiste (?!) perron stonden. Tevens wil ik Martin van Sint Annaland van harte bedanken voor zijn kritische inbreng en zijn onmisbare doorzettingsvermogen bij het afleiden van het kinetische theorie model als we weer eens vastliepen op een nieuwe wiskundige uitdaging. In de vele (nachtelijke) uurtjes die in deze afleiding zijn gaan zitten hebben we flink wat afgepuzzeld en gelachen, en zinnetjes

als "de afleiding wordt als eenvoudige oefening aan de lezer overgelaten" zullen mij nog lang bijblijven. Verder zou het opstellen van het volledige kinetische theorie model niet mogelijk zijn geweest zonder de statistisch-thermodynamische inbreng van Martin van der Hoef, waarvoor ik hem dan ook van harte wil bedanken. Tevens wil ik professor Jim Jenkins van Cornell University van harte bedanken voor zijn hulpvaardige commentaar bij de afleiding van de kinetische theorie modellen en het verstrekken van het artikel door Zhang en Jenkins (2000) voordat dit gepubliceerd was.

Zoals reeds aangegeven in de tweede opdracht regel zou ik met dit onderzoek niet zover hebben kunnen komen zonder het vele werk van anderen waarop ik heb kunnen bouwen. Naast de eerder genoemde mensen denk ik dan eveneens aan het werk van mijn collega's, Bob Hoomans en Erik Delnoij, maar ook nog wat verder terug aan het werk van Jelle Nieuwland. Onder begeleiding van Hans Kuipers stonden zij aan de basis van een zeer goed doordachte onderzoekslijn voor de modellering van meerfasenstromingen in de chemische reactorkunde.

Verder heb ik kunnen bouwen op het werk van een aantal uitstekende afstudeerders: Renier Braam, die de niet zo eenvoudige opgave volbracht om reeds in de literatuur beschikbare kinetische theorie sluitingen in de multi-fluid code in te brengen; Siebren Mellema die kans zag om zijn fotografie en computer hobby te combineren in een afstudeeropdracht op het gebied van de digitale beeldanalyse, maar voor wie vooral de gratis koffie de doorslag gaf om bij mij te komen afstuderen; Renske Beetstra die op zoek was naar een uitdagende opdracht en dus als eerste de link legde tussen het discrete deeltjes model en de kinetische theorie; Jeanette Mensink die bij Unilever Research in Vlaardingen aan de slag ging met het vergaren van validatiedata voor de modellen, waarvoor de batch pilotplant granulator geschikt gemaakt diende te worden voor continue operatie; Jeroen Link die het digitale beeldanalysesysteem perfectioneerde en ondanks experimentele tegenslagen geduldig de vele metingen verrichtte en Geert Weijers die, na bij Unilever Research de nodige kennis verzameld te hebben over het sproeien van druppeltjes, in Twente het discrete deeltjes sproeigranulatiemodel heeft gebouwd. Verder heeft Paul-Guillaume Schmitt in het kader van zijn stage veel werk verricht bij het inventariseren van het segregatie gedrag en heeft Arnout Roos in het kader van een gecombineerde technische en PT-II opdracht een studie uitgevoerd naar de invloed van de verschillende relaties voor gas-deeltjes frictie op het fluïdisatiegedrag. Daarbij wil ik ook Unilever Research bedanken voor het aanbieden van hun onderzoeksfaciliteiten voor de verschillende afstudeerprojecten en ben ik de volgende mensen dankbaar voor hun inbreng bij de verschillende afstudeercommissies: Ties Bos, Wim Briels, Louis van der

Ham, Mike Hounslow, Kees Slump, Geert Versteeg, Marijn Warmoeskerken en Ko van der Weele.

Dan zou het praktische werk natuurlijk nooit van de grond zijn gekomen zonder de deskundigheid van de technici in het Vlugterlab. Allereerst wil ik Gerrit Schorfhaar graag bedanken voor het werk dat hij altijd met veel toewijding voor mij heeft verricht. Het voortdurende gevecht dat wij samen met Hans Kuipers voerden tegen de gedwongen winkelnering bij het IMC en de bureaucratische molen van CT, met alle gevolgen van dien, zal ik niet snel vergeten. Verder wil ik Wim Leppink, Benno Knaken en Henk-Jan Moed van harte danken voor de vele hand- en spandiensten die zij mij hebben verleend als er op stel en sprong weer eens iets gebeuren moest, maar vooral wil ik hen bedanken voor het bouwen van de belangrijkste opstelling van het Vlugterlab, 'De Vlugtheuvel', waarvoor het idee onstond tijdens een ontspannend potje klaverjassen in de pauze. Uiteraard wil ik ook Robert Meijer van harte bedanken voor zijn electro-technische ondersteuning bij de aansturing van de opstelling en het noodzakelijke toezicht op de veiligheid.

Voor secretariële ondersteuning heb ik altijd terug kunnen vallen op Gery Stratingh-Roelofs, Nicole Haitjema, Ria Stegehuis-de Vegte, Brigitte Sanderink en Ria Hofs-Winkelman, terwijl Rik Akse en later Martin van Sint Annaland zorg droegen voor de afhandeling van de financiën. Allen daarvoor van harte bedankt! Dan zou er natuurlijk ook geen computer gekocht of gerepareerd zijn en geen glazen bed in elkaar gezet zijn, zonder de ondersteuning van de mensen bij TCCT. Daarom wil ik bij deze Mark Hulshof, Wim Platvoet, Jan Jagt, Jan Heezen, Joachim Olde Bolhaar, Joop Snoeyenbos en de andere medewerkers van TCCT van harte bedanken dat zij altijd voor mij klaar stonden wanneer dat weer eens nodig was. Tevens wil ik Silicon Graphics bedanken voor de mogelijkheid die zij mij hebben geboden om deel te nemen aan de 'powergroup' bijeenkomsten en de geleverde ondersteuning waarvoor ik bij Ronald van Pelt of Peter Michielse altijd terecht kon.

Verder heb ik een bijzonder goede tijd gehad met al mijn collaga's en de studenten van de vakgroep Proceskunde (later Fundamentele Aspecten van de Proceskunde). Helaas is het kaartje leggen en darten de laatste tijd een beetje in verval geraakt, maar het zeilen in Friesland is nog steeds een top activiteit. Verder wil ik Liesbeth Kuipers bedanken voor de gezellige pan-feesten en de vlekkeloze organisatie van de wintersport vakantie (wat betekende FAP ook alweer: Fun And Party?). Natuurlijk koester ik goede herinneringen

aan de conferenties die we met z'n allen hebben bezocht, maar om een of andere reden lijkt het me ongepast om daar op deze plek verder op in te gaan.

En 'last but not least' wil ik de mensen van het CREF-granulation project team bij Unilever Research, Joop Olieman, Frank van de Scheur, Atze Jan van der Goot, Renee Boerefijn en Terry Instone, bedanken voor hun kritische inbreng bij mij promotie project. Door de goede contacten die we binnen het project hebben opgebouwd ben ik in het voorjaar van 2000 enkele weken te gast geweest bij professor Mike Hounslow in Sheffield, om de fijne kneepjes van de populatiebalans modellering te leren. Naast Mike Hounslow wil ik ook Nynke Wierda en Agba Salman bedanken voor de gastvrije ontvangst en spreek ik hierbij de hoop uit dat deze waardevolle samenwerking in de toekomst nog verder uitgebouwd zal worden.

Zo zie je dat er voor het tot stand komen van een proefschrift niet alleen veel kennis nodig is, maar dat er vooral ook veel 'kennissen' nodig zijn, daarom

allemaal nogmaals van harte bedankt,

Mathijs

Levensloop

Mathijs Goldschmidt werd op 14 mei 1973 geboren te Almelo. Hij groeide op in Wierden alwaar het lager onderwijs werd gevolgd. In vervolg op het lager onderwijs bezocht hij vanaf 1985 het Pius X College te Almelo. In het voorjaar van 1991 werd het VWO diploma aldaar in ontvangst genomen.

In augustus 1991 begon hij de studie Chemische Technologie aan de Universiteit Twente te Enschede. In het tweede jaar koos hij voor vrijdoctoraal variant Chemische Technologie en Informatica. In het kader van deze ingenieursopleiding liep hij in het najaar van 1995 stage bij Akzo Nobel Corporate Research te Dobbs Ferry (New York) in de Verenigde Staten. In februari 1997 studeerde hij af bij de vakgroep Proceskunde op het onderwerp "Heterogene modellering van stofoverdracht en chemische reactie in gas-vloeistof-vloeistof systemen". In maart van datzelfde jaar werd het *met lof* behaalde ingenieursdiploma in ontvangst genomen.

Na afloop van zijn studie trad hij in april 1997 in dienst bij de vakgroep Proceskunde (later Fundamentele Aspecten van de Proceskunde) om als assistent in opleiding een promotie onderzoek te verrichten naar de modellering van poeder stroming in wervelbedden en wervelbed sproeigranulatoren. Dit proefschrift geeft een weerslag van dat werk.

Sinds augustus 2001 is hij als medewerker research werkzaam bij Akzo Nobel Chemicals NV, waar hij verantwoordelijk is voor het uitvoeren van projecten op het gebied van "Computational Fluid Dynamics" en Chemische Reactorkunde.